

**DESIGN AND POWER MANAGEMENT OF AN OFFSHORE MEDIUM VOLTAGE
DC MICROGRID REALIZED THROUGH HIGH VOLTAGE
POWER ELECTRONICS TECHNOLOGIES AND CONTROL**

by

Brandon Michael Grainger

B.S. in Mechanical Engineering, University of Pittsburgh, 2007

M.S. in Electrical Engineering, University of Pittsburgh, 2011

Submitted to the Graduate Faculty of
Swanson School of Engineering in partial fulfillment
of the requirements for the degree of
Doctor of Philosophy

University of Pittsburgh

2014

UNIVERSITY OF PITTSBURGH
SWANSON SCHOOL OF ENGINEERING

This dissertation was presented

by

Brandon Michael Grainger

It was defended on

July 7th, 2014

and approved by

Gregory F. Reed, PhD, Professor
Department of Electrical and Computer Engineering

George L. Kusic, PhD, Associate Professor
Department of Electrical and Computer Engineering

Zhi-Hong Mao, PhD, Associate Professor
Department of Electrical and Computer Engineering

Thomas E. McDermott, PhD, Assistant Professor
Department of Electrical and Computer Engineering

William E. Stanchina, PhD, Professor
Department of Electrical and Computer Engineering

William W. Clark, PhD, Professor
Department of Mechanical Engineering and Materials Science

Marius Rosu, PhD, Electromechanical Lead Product Manager, ANSYS Inc.

Dissertation Director: Gregory F. Reed, PhD, Professor
Department of Electrical and Computer Engineering

Copyright © by Brandon M. Grainger

2014

DESIGN AND POWER MANAGEMENT OF AN OFFSHORE MEDIUM VOLTAGE DC MICROGRID REALIZED THROUGH HIGH VOLTAGE POWER ELECTRONICS TECHNOLOGIES AND CONTROL

Brandon M. Grainger, PhD

University of Pittsburgh, 2014

The growth in the electric power industry's portfolio of Direct Current (DC) based generation and loads have captured the attention of many leading research institutions. Opportunities for using DC based systems have been explored in electric ship design and have been a proven, reliable solution for transmitting bulk power onshore and offshore. To integrate many of the renewable resources into our existing AC grid, a number of power conversions through power electronics are required to condition the equipment for direct connection. Within the power conversion stages, there is always a requirement to convert to or from DC.

The AC microgrid is a conceptual solution proposed for integrating various types of renewable generation resources. The fundamental microgrid requirements include the capability of operating in islanding mode and/or grid connected modes. The technical challenges associated with microgrids include (1) operation modes and transitions that comply with IEEE1547 without extensive custom engineering and (2) control architecture and communication. The Medium Voltage DC (MVDC) architecture, explored by the University of Pittsburgh, can be visualized as a special type of DC microgrid.

This dissertation is multi-faceted, focused on many design aspects of an offshore DC microgrid. The focal points of the discussion are focused on optimized high power, high frequency magnetic material performance in electric machines, transformers, and DC/DC power converters – all components found within offshore, power system architectures. A new

controller design based upon model reference control is proposed and shown to stabilize the electric motor drives (modeled as constant power loads), which serve as the largest power consuming entities in the microgrid. The design and simulation of a state-of-the-art multilevel converter for High Voltage DC (HVDC) is discussed and a component sensitivity analysis on fault current peaks is explored. A power management routine is proposed and evaluated as the DC microgrid is disturbed through various mode transitions. Finally, two communication protocols are described for the microgrid – one to minimize communication overhead inside the microgrid and another to provide robust and scalable intra-grid communication.

The work presented is supported by Asea Brown Boveri (ABB) Corporate Research Center within the Active Grid Infrastructure program, the Advanced Research Project Agency – Energy (ARPA-E) through the Solar ADEPT program, and Mitsubishi Electric Corporation (MELCO).

TABLE OF CONTENTS

NOMENCLATURE.....	XIX
ACKNOWLEDGMENTS.....	XXIII
1.0 INTRODUCTION.....	1
1.1 MOTIVATION FOR RESEARCH PURSUITS.....	2
1.1.1 Electric Ship Design.....	3
1.1.2 Explorations in Offshore Wind Generation Potential and Oil Drilling Reservoirs	5
1.1.3 Challenges and Opportunities with Microgrids	8
1.1.4 Increased Interest in Microgrid Operations for AC and DC Architectures	9
1.1.5 Microgrid Hierarchical Control Terminology.....	11
1.2 SIGNIFICANCE AND CONTRIBUTIONS	13
1.3 DISSERTATION OUTLINE.....	18
2.0 POWER DENSITY IMPROVEMENTS UTILIZING HIGH FREQUENCY MAGNETIC NANOCOMPOSITE MATERIALS IN POWER APPLICATIONS....	20
2.1 MOTIVATION FOR DESIGNING BIDIRECTIONAL CHARGERS WITH HIGH FREQUENCY MAGNETIC COMPONENTS	23
2.2 OPTIMIZING BIDIRECTIONAL CHARGER MAGNETIC DESIGN FOR KILOWATT SCALE POWER APPLICATIONS USING ANSYS	26
2.2.1 Analytical Methodology for Optimizing Transformer Parameters.....	26

2.2.2	Optimal Ferrite Core Transformer Parameters Analyzed through ANSYS PExprt	30
2.2.3	Optimal HTX-012B Nanocomposite Core Transformer Parameters Analyzed through ANSYS PExprt	34
2.2.4	Results Comparison between Analytical Ferrite Core, Computer Simulated Ferrite Core, and Computer Simulated Nanocomposite Core41	
2.3	ELECTRIC MACHINE POWER DENSITY IMPROVEMENT USING NANOCOMPOSITE MATERIALS	42
2.3.1	Power Density Improvement of Induction Motors Utilizing HTX-012B: Design Considerations	43
2.3.2	Power Density Improvement of Induction Motors Utilizing HTX-012B: Motor Optimization Study	47
2.4	APPROXIMATE UTILITY SCALE TRANSFORMER CORE SIZE REDUCTION EMPLOYING NANOCOMPOSITE MAGNETIC MATERIALS	51
3.0	MODULAR MULTILEVEL CONVERTER BASED HIGH VOLTAGE DC MODELING, COMPONENT SENSITIVITY ANALYSIS, AND SCALING APPROXIMATIONS	55
3.1	MODULAR MULTILEVEL CONVERTER MODELING AND CONTROL	60
3.1.1	Generalized Mathematical Model of the MMC Converter	61
3.1.2	MMC Converter Inner Loop Controllers: Current Regulators and Tuning	63
3.1.3	MMC Converter Outer Loop Controllers: AC and DC Regulators.....	65
3.1.4	Capacitor Balancing Algorithm	66
3.1.5	System Parameters and Dynamic Performance Evaluation.....	67
3.2	MODULAR MULTILEVEL CONVERTER COMPONENT SENSITIVITY ANALYSIS ON FAULT CURRENTS.....	71
3.2.1	Transformer Impedance Impact on Peak DC Current	73
3.2.2	Bypass Switch Impact on Peak DC Current.....	73

3.2.3	Reactor Impact on Peak DC Current	74
3.3	ELECTRIC CHARACTERISTIC PREDICTION WITH REDUCED SUBMODULE COUNT IN CONVERTER ARMS.....	76
4.0	MODEL REFERENCE CONTROLLER DESIGN FOR STABILIZING CONSTANT POWER LOADS IN A MEDIUM VOLTAGE DC MICROGRID	78
4.1	FUNDAMENTALS OF BIDIRECTIONAL DC/DC CONVERTERS.....	80
4.1.1	Converter Dynamics.....	82
4.1.2	System Description with Constant Power Load Assumption	83
4.2	STABILITY ASSESSMENTS USING MODEL REFERENCE CONTROL THEORY	85
4.2.1	Attempt to Stabilize Plant with PD Controller	85
4.2.2	Model Reference Control Definitions and Assumptions.....	88
4.2.3	Attempt to Stabilize Second-Order Plant with Model Reference Control.....	90
4.2.4	Stabilized Third Order Plant with Model Reference Control.....	91
4.3	COMPENSATOR DESIGN AND PARAMETER SELECTION.....	93
4.3.1	Simulation Results – Control Block Diagram Response.....	94
4.3.2	Simulation Results – Circuit Response.....	98
5.0	MODELING AN OFFSHORE MEDIUM VOLTAGE DC MICROGRID.....	102
5.1	FULL CONVERTER WIND TURBINE MODEL.....	102
5.1.1	Simplified Model of a Permanent Magnet Synchronous Machine	103
5.1.2	Aerodynamic Model of Wind Source.....	104
5.1.3	Maximum Power Point Tracking Control Implementation	105
5.1.4	Wind Turbine Model Validation.....	107
5.2	POWER ELECTRONIC CONVERTER MODELING	109

5.2.1	Mathematical Modeling of Power Electronic Converters: The Average Model.....	109
5.2.2	Average Model of Pulse Width Modulated Rectifier with Open Loop PQ Control.....	113
5.2.3	Average Model Implementation of Neutral Point Clamped Converter in Simulink.....	118
5.2.4	Average Model of Bidirectional DC/DC Converter	119
5.3	VARIABLE FREQUENCY DRIVE MODEL	121
5.3.1	Machine Current Control.....	123
5.4	SYSTEM PARAMETERS AND ASSEMBLED DC MICROGRID VALIDATION.....	125
5.4.1	System Power Balance and DC/DC Converter Power Handling Capability	127
5.4.2	Motor Drive Responses	130
6.0	DYNAMIC POWER MANAGEMENT AND DC/DC CONVERTER CURRENT SHARING EVALUATION UNDER VARIOUS MODE TRANSITIONS.....	135
6.1.1	Power Management Routine	136
6.1.1	DC/DC Converter Dynamic Response under a Grid Disconnection	139
6.1.2	DC/DC Converter Dynamic Response under a Grid Connection.....	144
7.0	CONSIDERATIONS FOR DESIGNING THE COMMUNICATION NETWORK ARCHITECTURE OF THE OFFSHORE DC MICROGRID	146
7.1	COMMUNICATION NETWORKS	147
7.1.1	Microgrid Communication Network	148
7.1.2	Wide-Area Control Network	151
7.2	PERFORMANCE ANALYSIS OF THE DISTRIBUTED COMMUNICATION ARCHITECTURE	152
7.2.1	Availability and Reliability.....	153

7.2.2	Packet Size and Overhead	154
7.2.3	Transmission Delays.....	154
7.2.4	Security.....	155
8.0	CONCLUSIONS AND FUTURE WORK.....	157
	APPENDIX A.....	161
	APPENDIX B.....	165
	APPENDIX C.....	168
	Permanent Magnet Synchronous Generator (PMSG) Implementation in Simulators.....	168
	APPENDIX D.....	173
	BIBLIOGRAPHY.....	176

LIST OF TABLES

Table 2.1: Geometrical Relationships Associated with Transformer Core	27
Table 2.2: Optimal Core Results for DAB Benchmark Case with Available Commercial Core Metrics [51]	29
Table 2.3: Ferrite Material Properties	30
Table 2.4: Top Ten Core Solutions Rated for 1 kW Utilizing Ferrite Core	31
Table 2.5: Dimensions, Mass, and Permeability of Experimentally Tested Cores.....	35
Table 2.6: Core Loss Measurements at Varying Frequencies and Induction Levels for Experimental Toroids.....	35
Table 2.7: Steinmetz Coefficients Associated with Tested Cores	36
Table 2.8: HTX-012B Nanocomposite Material Properties	40
Table 2.9: Top Ten Core Solutions Rated for 1 kW Utilizing Nanocomposite HTX-012B	40
Table 2.10: Comparison of Optimized Core Results	41
Table 2.11: Motor Geometric Variables	48
Table 2.12: Motor Constraints	48
Table 2.13: Two Pole Motor Output.....	48
Table 2.14: Eight Pole Motor Output	48
Table 2.15: Parameters Associated with Core and Winding Loss Calculation	52
Table 2.16: System Constraints to Optimize 100 kW Transformer.....	53

Table 2.17: Transformer Optimization Results with Varying Frequency	53
Table 3.1: HVDC System Parameters for a US Market Installation	68
Table 3.2: Circuit Breaker and BPS Operating Sequence after Fault Occurs	72
Table 4.1: Cable Parameters	84
Table 4.2: Rated System Parameters	95
Table 5.1: Wind Turbine and Permanent Magnet Synchronous Machine Parameters [96]	103
Table 5.2: Operating States of Pulse Width Modulated Boost Rectifier	114
Table 5.3: Induction Machine Parameters [76].....	131
Table 5.4: Predicted Motor Simulation Results.....	134
Table 7.1: Telecommunication Protocols and Media Options for Microgrid and Wide-Area Networks [117]	153

LIST OF FIGURES

Figure 1.1: Electric Ship Power System Architecture [5].....	4
Figure 1.2: Semi-Submersible Drilling Rig [7]	6
Figure 1.3: Location of Oil Drilling Opportunities between 2012 and 2017 [5].....	7
Figure 1.4: Available Wind Generation Onshore and Offshore in the United States [9]	7
Figure 1.5: Offshore Platforms – Siemens Offshore Design (Left), [10]& ABB Offshore Design (Right), [11].....	7
Figure 1.6: Block Diagram of Microgrid Control Layers Operating in Unison [27]	12
Figure 1.7: Hierarchical Control Architectures for an AC and DC Microgrid [28]	12
Figure 1.8: DC Microgrid - Local Wind Power being supplied to Offshore Platform	14
Figure 2.1: 2010 Power Electronic Opportunities for Improvements [34].....	21
Figure 2.2: Offshore Medium Voltage DC Microgrid Emphasizing Magnetic Intensive Areas.	22
Figure 2.3: Bidirectional DC/DC Converter Topology	24
Figure 2.4: Voltage and Current Waveforms of DAB DC/DC while Operating in Charging (Buck) Mode.....	25
Figure 2.5: Single-phase Transformer Core for Dual-Active Bridge Converter [46].....	27
Figure 2.6: Magnetics 0P44125UC [54].....	29
Figure 2.7: Optimal Manufacturer Core Volume Solutions	31
Figure 2.8: Notable Parameters associated with the ETD49 Ferrite Core Design for the 1 kW DAB.....	32

Figure 2.9: ETD49 Core: Simulation Results and Manufactured Component from Magnetics [56].....	33
Figure 2.10: Cross Section of 72 Windings Configured in Two Parallel Turns around ETD49 Core.....	34
Figure 2.11: Core Loss for Annealed, Impregnated, and Impregnated Cut Cores ($f = 20\text{kHz}$) [57]	37
Figure 2.12: Core Loss for Annealed, Impregnated, and Impregnated Cut Cores ($f = 50\text{kHz}$) ..	37
Figure 2.13: Core Loss for Annealed, Impregnated, and Impregnated Cut Cores ($f = 100\text{kHz}$)	38
Figure 2.14: Core Loss for Annealed, Impregnated, and Impregnated Cut Cores ($B = 0.1\text{T}$)	38
Figure 2.15: Steinmetz Coefficients Provided by PExprt for HTX-012B Based on Experimental Loss Data	39
Figure 2.16: Notable Parameters associated with the ETD49 Nanocomposite Core Design for the 1 kW DAB	40
Figure 2.17: Size Reduction of 10 kW PPMT Motor Using HTX-005C Fe-Co Nanocomposite Material [59].....	42
Figure 2.18: B-H Curve for HTX-012B	43
Figure 2.19: M600-50A B-H Curve [62].....	45
Figure 2.20: Core Loss Data for M600-50A [62].....	45
Figure 2.21: Machine Power Factor Adjustments as Number of Machine Poles Increase [63] ..	46
Figure 2.22: Motor Geometry, Winding Configuration and Slot Dimensions	47
Figure 2.23: Two Pole Motor Flux Distribution.....	49
Figure 2.24: Eight Pole Motor Flux Distribution.....	49
Figure 2.25: Two Pole Motor Torque vs. Speed Curve.....	50
Figure 2.26: Eight Pole Motor Torque vs. Speed Curve.....	50
Figure 2.27: C-Core Transformer Design [64]	51
Figure 2.28: Core Volume vs. Frequency for 100 kW Rated Transformer Core	54

Figure 3.1: Planned HVDC Installations within North America through 2019	55
Figure 3.2: Planned HVDC Installations in China through 2020 [67]	56
Figure 3.3: Definition of a Multilevel Inverter [68]	57
Figure 3.4: Modular Multilevel Converter Topology	58
Figure 3.5: Multi-Terminal DC Application within the Offshore DC Microgrid Environment..	59
Figure 3.6: Submodule States of the Modular Multilevel Converter	60
Figure 3.7: Circuit Synthesis of 6 Cell per Arm MMC Converter	61
Figure 3.8: Current Controller of MMC Converter	64
Figure 3.9: Illustration of Modulated Case with Third Harmonic Injection [77]	65
Figure 3.10: THD Voltage Distortion Limits [82].....	68
Figure 3.11: Top-Level View of HVDC Model Development in PSCAD.....	69
Figure 3.12: HVDC Model Waveforms: (a) DC voltage (b) Capacitor Voltage Ripple, (c) Δ - side AC Voltage / Y-Side AC Voltage / Reference Signal and (d) Power Flow ..	70
Figure 3.13: Pole-to-Pole Fault in a Monopolar HVDC System.....	71
Figure 3.14: Transformer Reactance Impact on Peak DC Current.....	73
Figure 3.15: Bypass Switch Speed Impact on Peak DC Current.....	74
Figure 3.16: DC Line Inductor Impacts on Peak DC Current	75
Figure 3.17: Asymmetrical Arm Reactor Impact on Peak DC Current.....	75
Figure 3.18: Comparison between Electrical Characteristics for 6 and 10 Cell MMC Converter Systems.....	77
Figure 4.1: Model Reference Controller Design Application within the Offshore DC Microgrid Environment.....	79
Figure 4.2: Dual Active Bridge Bidirectional DC/DC Converter.....	80
Figure 4.3: Current Traces of DAB DC/DC Converter	81
Figure 4.4: Operating Waveforms of the Dual Active Bridge DC/DC Converter.....	82

Figure 4.5: System Model for Studying CPL Scenario	83
Figure 4.6: Simplified System Model for Evaluating CPL Scenario (Third Order System).....	84
Figure 4.7: Pole-zero plot associated with unstable output impedance for various constant power loads.....	85
Figure 4.8: Second-order System Model of a Simplified Motor Drive Model (Second-Order)..	86
Figure 4.9: PD Control of Plant.....	86
Figure 4.10: Controller Structure to Stabilize Constant Power Load [93]	89
Figure 4.11: Pole Placement of the Reference Model	94
Figure 4.12: Pole-zero plot for unstable plant with lumped network capacitors (right) and neglected (left).....	96
Figure 4.13: Pole-zero Plot for Model, $M(s)$	96
Figure 4.14: Simulation Model of Designed Control Structure Utilizing Model Reference Control.....	97
Figure 4.15: Closed Loop Controller Performance Based Upon Model Reference Control Design	97
Figure 4.16: Closed Loop Controller Performance Based Upon PD Design	97
Figure 4.17: Circuit Diagram for Proving Model Reference Control Capability	98
Figure 4.18: Circuit Response with Step Change in DC/DC Converter Control Input at 0.5 seconds	99
Figure 4.19: Average Circuit Model Representation of Plant Model under Study	100
Figure 4.20: Comparison of Circuit Simulation and Control Block Diagram Response.....	101
Figure 5.1: Offshore Wind Turbine Collection System.....	102
Figure 5.2: Maximum Power Point Tracking Implementation and Control of Wind Turbine ..	105
Figure 5.3: Wind Turbine Controller Responses	107
Figure 5.4: Wind Turbine Aerodynamic Responses and Output Power.....	108
Figure 5.5: Simplified Half-Bridge Inverter	109

Figure 5.6: Switched Equivalent Circuit Model of the Half-Bridge Converter.....	110
Figure 5.7: Averaged Equivalent Circuit of the Half-Bridge Converter	113
Figure 5.8: Pulse Width Modulated Boost Rectifier.....	114
Figure 5.9: Average Model of Pulse Width Modulated Inverter/Rectifier	117
Figure 5.10: Open Loop PQ Regulator of Pulse Width Modulated Boost Rectifier	117
Figure 5.11: Average Model of Neutral Point Clamped Converter.....	118
Figure 5.12: Detailed and Average Model Output Voltage Waveform of NPC Inverter	119
Figure 5.13: Average Model of Bidirectional DC/DC Converter.....	120
Figure 5.14: Illustration of Detailed and Average Model Currents for the Bidirectional DC/DC Converter	120
Figure 5.15: Variable-Frequency Voltage Sourced Converter for Controlling Induction Machine	121
Figure 5.16: Magnetization Current Alignment in a dq Axis Frame.....	123
Figure 5.17: Machine Current Control.....	125
Figure 5.18: Interconnected DC Based Microgrid Computer Model	126
Figure 5.19: Generation Sources in Microgrid	128
Figure 5.20: Bus DC Voltages and Currents in DC Microgrid.....	128
Figure 5.21: dq Flux Linkages of Wind Turbine Generator after Grid Disconnect	129
Figure 5.22: dq Current Regulation of Induction Motors	131
Figure 5.23: Axes Orientation for Current Controller and Motor	132
Figure 5.24: Relationship between the dq and abc Quantities for Generating and Motoring Operation[97].....	132
Figure 5.25: dq Stator Currents and Motor Torque	134
Figure 5.26: Motor Load Power and Modulation Index of Motor Inverters	134
Figure 6.1: Power Signals and Coordination through Centralized Computer	136

Figure 6.2: Power Management Routine for Adjusting DC/DC Converters in Microgrid.....	137
Figure 6.3: Microgrid Computer Model with Implementation of Power Management Scheme	138
Figure 6.4: System Generation Response During a Grid Disconnect.....	140
Figure 6.5: DC/DC Converter Duty Cycle Response	140
Figure 6.6: DC Bus Voltages and Current Flows in Case of Grid Disconnect.....	141
Figure 6.7: Zoomed-In Intervals of Figure 6.6 Providing Finer Electrical Characteristics.....	141
Figure 6.8: Output Currents of DC/DC Converters for Grid Disconnect Scenario – 60% / 40 % Weighting.....	142
Figure 6.9: Wind Generator Currents and Grid Connected Converter Current for Grid Disconnect Scenario.....	143
Figure 6.10: System Generation Response During a Grid Connection	145
Figure 6.11: Duty Cycles and Output Currents of DC/DC Converters – 60% / 40% Weighting	145
Figure 7.1: Architecture of Microgrid Communication Networks	148
Figure 7.2: Secondary Controller's Inside and Outside Communication Cycles.....	150
Figure 7.3: Architecture of Wide-Area Communication Network	151
Figure 8.1: Portable Motor Units (Left) and Motor Control Center (Right)	159
Figure 8.2: LVRT Requirement per Appendix G of FERC's LGIA	160

NOMENCLATURE

\bar{x}	Average DC Value
\tilde{x}	Small Signal AC Value
\vec{x}	Dimensional Vector
\underline{x}	Phasor
x^*	Complex Conjugate
A	Area Swept by Wind Turbine Blades
A_c	Cross Sectional Area of Transformer
A_i	Equipment Availability
A_t	Transformer Thermal Area
A_w	Window Area of Transformer
B	Magnetic Induction
B_s	Saturation Magnetic Induction
B_{Tx}	Transformer Magnetic Induction
C	Capacitance
C_{dc}	DC/DC Converter Output Capacitor
C_p	Power Coefficient of Wind Turbine
D	Diode
E_{rms}	RMS Transformer Voltage
F	Machine Friction Factor
F_r	Litz Wire Loss Factor
$G(s)$	Closed Loop Transfer Function
H	Magnetic Field Strength
I	General DC Current
I_g	DC/DC Converter Input Current
I_L	Inductor Current
J	Machine Moment of Inertia
K_{DC}	DC/DC Converter Plant Gain
K_P	Proportional Gain of DC/DC Converter Controller
K_D	Derivative Gain of DC/DC Converter Controller
K_{pc}	Proportional Gain of HVDC Converter
K_{ic}	Integral Gain of HVDC Converter
L	General Inductance
L_{ds}	Permanent Magnet Machine Direct Axis Inductance
L_{qs}	Permanent Magnet Machine Quadrature Axis Inductance

L_m	Induction Machine Magnetizing Inductance
L_s	HVDC Converter Arm Inductance
L_{Tx}	Transformer Inductance
M	Mutual Inductance
$M(s)$	Reference Model Transfer Function
N	Turns Ratio of Transformer, Submodules per HVDC Converter Arm
P	Real Power, Machine Poles
$\hat{P}(s)$	Plant Transfer Function
P_L	Power Loss
P_T	Turbine Power
P_c	Core Loss
P_t	Terminal Power
P_s	Sending Power
Q	Reactive Power, Semiconductor Module
R	Resistance, Length of Wind Turbine Blade
S	Apparent Power
T	Transpose
T_e	Electrical Torque
T_m	Mechanical Torque
T_{rise}	Temperature Rise of Transformer
T_s	Switching Period
$T(\theta)$	Park Transformation
V	General DC Voltage, Transformer Volume
V_H	Medium Voltage DC Bus Voltage
V_L	Offshore Production Platform DC Bus Voltage
V_{LL}	Line-to-Line Voltage
V_W	Wind Velocity
V_c	Core Volume
V_g	DC/DC Converter Input Voltage
V_p	Primary Side Voltage
V_s	Secondary Side Voltage, Stator Voltage
V_r	Rotor Voltage
V_t	Terminal Voltage
V_{sm}	Submodule Voltage
X	Reactance
Y	Wye side of Transformer, Constant Power Load
Z	Total Impedance
Z_{out}	Output Impedance
a	Width of Main Flux Path in Transformer
a_h	Fourier Coefficient
b_h	Fourier Coefficient
a_x	Polynomial Coefficients of Reference Model Numerator, $\hat{n}_m(s)$; $x = 0,1,2,3 \dots n$
b	Width of the Transformer Window
b_x	Polynomial Coefficients of Reference Model Denominator, $\hat{d}_m(s)$; $x = 1,2,3 \dots n$

d	Transformer Thickness, General Duty Cycle
d_c	Copper Wire Diameter
d_d	Direct Axis Duty Cycle
d_q	Quadrature Axis Duty Cycle
d_h	DC/DC Converter Duty Cycle
$\hat{d}_p(s)$	Plant Denominator
f	System Frequency
f_0	Ratio between Model and Plant Gains
f_s	Switching Frequency
f_{abc}	Variable f in abc frame
f_{dqk}	Variable f in dq frame
h	Height of Half of the Transformer Window, harmonic number
i	AC Current
i_d	Direct axis current
i_k	AC Current in Converter Arm k
i_q	Quadrature Axis Current
i_s	Stator Current
i_r	Rotor Current
i_{mr}	Machine Magnetizing Current
k	Steinmetz Relationship Gain, Field Distribution Constant
k_m	Reference Model Gain
k_α	Scaling factor of DC/DC Converter No. 1
k_β	Scaling factor of DC/DC Converter No. 2
k_p	Plant Gain
l	Magnetic Effective Length
l_o	Mean Length per Turn
l_1	Transformer Width
l_2	Transformer Thickness
l_3	Transformer Height
m	Modulation Index
m_d	Direct Axis Modulation Index
m_q	Quadrature Axis Modulation Index
n	Turns Ratio of DC/DC Converter, Wire Strands, Multilevel Converter Levels
$\hat{n}_p(s)$	Plant Numerator
$\hat{n}_m(s)$	Reference Model Numerator
p_x	Polynomial Coefficients of Plant Denominator, $\hat{d}_p(s)$; $x = 0,1,2,3\dots n$
q_x	Polynomial Coefficients of Plant Numerator, $\hat{n}_p(s)$; $x = 1,2,3\dots n$
$\hat{r}(s)$	Reference Model Input
s	Laplace Operator, Switching Function, Switch
t	Ribbon thickness, Time
u	Phase voltage of HVDC Converter, Control signal
u_d	Direct Axis Control Input
u_q	Quadrature Axis Control Input
$\hat{u}(s)$	Control System Input

v	AC voltage
v_d	Direct Axis Voltage
v_q	Quadrature Axis Voltage
$\hat{y}_p(s)$	Plant Output
$\hat{y}_m(s)$	Reference Model Output
α	Steinmetz Exponent on Frequency
β	Steinmetz Exponent on Induction, Wind Turbine Pitch Angle
δ	Phase of Voltage
λ	Flux or Tip Speed Ratio of Wind Turbine
λ_d	Direct Axis Flux
λ_q	Quadrature Axis Flux
λ_{opt}	Optimal Tip Speed Ratio
λ_m	Permanent Magnet Flux
λ_s	Stator Flux
λ_r	Rotor Flux
μ	Permeability
ω	Circular Frequency
ω_l	Model Pole Location
ω_e	Excitation Frequency
ω_n	Natural Frequency
ω_o	Nominal Frequency
ω_r	Rotor Mechanical Speed
ϕ	Phase Delay, Transformer Geometric Constant
ρ	Resistivity, Air Density, Angle between Rotor and Stator Machine Axis
ρ	Copper Resistivity
σ	Total Leakage Factor
σ_s	Stator Leakage Factor
σ_r	Rotor Leakage Factor
θ	Phase of Impedance, System Angle
θ_r	Rotor Angle
τ	Closed Loop Transfer Function Time Constant
τ_s	Stator Time Constant
ζ	Damping Coefficient
Δ	Delta side of transformer
Φ	HVDC Converter Energy Ratio

ACKNOWLEDGMENTS

The race towards achieving an advanced engineering degree is not a simple task but requires perseverance and endurance to breakthrough life's challenges and trials to reach the end goal. The path towards completion cannot be achieved without the support of others because the journey, without question, is an emotional rollercoaster with heights and valleys. Acknowledgments are meant to show gratitude to those who have encouraged or supported my efforts and are not listed in any particular order.

First, I want to thank my parents – Douglas and Nancy Grainger – who didn't have the same opportunities as I had growing up and ensured that I received a solid education and supported my efforts along the way. The drive, undistracted attention and focus, and perfectionist mentality comes from my dad and the ability to organize, manage, and listen comes from my mom – all qualities that are valuable in engineering.

Second, I want to thank the financial support from ABB Corporate research, ARPA-E, and MELCO. From ABB, special thanks go to Dr. Le Tang and Dr. Zhenyuan "John" Wang from the United States and Dr. Jan Svensson from Vasteras, Sweden who funded our efforts at the university in medium voltage DC microgrids. From ARPA-E, Dr. Tim Heidel who program managed the research efforts being done on the advanced magnetic material development. From MELCO, Ryo Yamamoto for partnering with Pitt, funding and encouraging our HVDC research and development, and touring me around Japan to see MELCO's engineering facilities. I also

want to thank the Richard K. Mellon foundation for providing substantial funds in supporting the Center for Energy at Pitt and awarding me one of the first endowed graduate student fellowships.

A special thank you to Dr. Gregory Reed for selecting me as his first PhD student in 2009 to help build the electric power program; instilling in my mentality the importance of networking; relationship building; and close collaboration with industry. As our relationship grew, the faculty/student hierarchy began to dissolve and, from my viewpoint, we became engineering colleagues using each other's strengths to reach a common goal. Using a very untraditional academic model, the opportunities, engineering skillsets, and company interactions have molded me into, spoken humbly, a sought-after engineer who has the analytical foundation and communication attributes to be successful in this field all in thanks to his guidance.

Thanks to Dr. Zhi-Hong Mao for his willingness to meet often to discuss control theory, listen to my thoughts and concerns, and enhanced my research abilities over the years and to Dr. Thomas McDermott for always having his office door open for "on-the-fly" technical discussions. Thanks to Dr. George Kusic, Dr. William Stanchina, Dr. William Clark, and Dr. Marius Rosu for serving as committee members.

I want to thank many of my friends who have helped pave the success of the electric power engineering research group since its initiation and who really have / make the group something special. Past and present members include Hashim Al-Hassan, Ansel Barchowsky, Dr. Hussain Bassi, Alvaro Cardoza, Dr. Shimeng Huang, Dr. Bob Kerestes, Dr. Raghav Khanna, Dr. Matthew Korytowski, Patrick Lewis, Rusty Scioscia, Zachary Smith, Adam Sparacino and Dr. Emmanuel Taylor. Also, thanks to Velin Kounev for partnering with me and applying his communications knowledge to solving microgrid communication issues.

Special recognition to various members of Pitt's staff including Danielle Ilchuk, Suzan Dolfi, James Lyle, Bill McGahey and Sandy Weisburg for making the Center for Energy and ECE Department operate as smooth as possible on a daily basis and Paul Kovach for helping to publically market our research program and team.

Engineering difficulty arises not because of the nature of the work but *strictly* because engineers and scientists have *finite* minds attempting to understand one, *infinite* mind. For nothing could explain how the equations, from the perspective of man, eloquently break down, when used correctly, to predict the phenomena of this world without acknowledging a higher, creative power who designed this world. All the engineer does is invents or manipulates what has already been created. With this perspective, I express sincere thanks to God who knows the plans for my life and secures my future.

A thank you is in order for Godly men in the faith who have prayed for me and serve as weekly encouraging mechanisms during weekly studies. These men include Dr. Stephen Wilson, Scott Marton, Ojo Nwabara, Don Schell, Warren Keyes, Paul Dougherty, Vince Schmidt, Terry Colabrese, Todd Lewandowski, Paul De La Torre, and others. Special recognition goes to Dr. Stephen Wilson for two years of prayer support for my future employment endeavors.

Finally, great appreciation is expressed towards those organizations and individuals within those organizations that continuously help to support, volunteer their time, and train the next generation of electric power engineers at the University of Pittsburgh.

Brandon M. Grainger

1.0 INTRODUCTION

Corporate research centers, universities, power equipment vendors, end-users and other market participants around the world are beginning to explore and consider the use of DC in future transmission and distribution system applications. Recent developments and trends in electric power consumption indicate an increasing use of DC-based power and constant-power loads. In addition, growth in renewable energy resources requires DC interfaces for optimal integration. A strong case is being made for intermeshed AC and DC networks, with new concepts emerging at the medium voltage level for Medium Voltage DC (MVDC) infrastructure developments.

At the turn of the 20th century, the use of AC transmission, as opposed to DC, was a justifiable decision for many reasons. Looking toward the future of transmission and distribution, this decision must be reevaluated, in light of the changes taking place throughout the United States electric grid at all levels – generation, transmission and distribution, and end-use. In 2006, EPRI presented a number of valid arguments that strengthened the case for DC infrastructure in the 21st century [1]. Modern advances in the transportation industry have often come through the application of electronics (electric vehicles and magnetic levitation trains, for example). These innovations utilize DC power, requiring an AC to DC conversion within the current grid infrastructure. We are living in the emerging era of the microgrid, composed of distributed generation (such as photovoltaic systems) and energy storage systems that produce DC power. Finally, solutions for integrating renewable energy with storage devices are

attempting to be developed at the utility scale to deliver DC power. These advances will make utility scale energy storage more economical and efficient.

Power electronics technology is an efficient, powerful, and reliable solution for integrating large amounts of renewable generation into existing grid infrastructure. Increased renewable integration with aggressive growth targets is a mandate set forth by the United States government with a deadline in 2030. Growing developments in the area of power electronics, including the application of novel semiconductor devices and materials, have unlocked the potential for higher capacity, faster switching, lower-loss conversion, inversion, and rectification devices. In recent years the advent of silicon carbide solid state electronic devices, which have lower switching and conduction losses compared to silicon devices, have made DC/AC conversion more promising in the near-term timeframe. Virtually all voltage and current ratings are possible by utilizing series and parallel combinations of discrete semiconductors. All of these factors combine to form an opportunity for the development and further deployment of DC technology throughout the electric grid at all levels.

1.1 MOTIVATION FOR RESEARCH PURSUITS

Before a problem statement is defined, it is important to investigate areas where DC technology is currently being utilized. Electric ship design, trends and exploration in offshore renewable energy integration (specifically wind power) in the United States, and the concept of the microgrid is lightly defined in this section. Utilizing the local, offshore wind power to supply power to the offshore production platforms is a new concept being explored and explained in this section as well.

1.1.1 Electric Ship Design

The concept of an integrated power system (IPS) is familiar terminology for the Office of Naval Research and research groups within universities [2],[3]. A generic layout of an electric ship using a DC backbone is provided in Figure 1.1. The idea of IPS is to enable all the energy generated to be used by all the ship systems. Earlier IPS concepts showed that the energy within the ship propulsion system would be enough to supply traditional ship operation needs so that service generators could be eliminated, yielding significant fuel savings. Efficient use of generated energy is important, but another critical factor in ship design is space savings. Traditionally, every marine load or load circuit was interfaced with a transformer strictly for galvanic isolation. Transformers have two main functions in addition to providing galvanic isolation – impedance matching and voltage scaling [4]. Although vital and a workhorse of past and current electric power systems, transformers rated for 60 Hz are large and heavy. For these reasons, research organizations like the Advanced Research Projects Agency – Energy (ARPA-E) are providing funds for investigating new magnetic materials for transformer cores so the unit can operate at much higher frequencies. The size and weight of the transformer is inversely proportional to the operating frequency.

Historically, DC has had protection issues limiting DC distribution systems to a maximum rating of 1,000 V level on naval ships. Traditional electromechanical switchgear is slow and DC voltage collapse can be much faster than AC collapse. Amongst power engineering professionals, it is well known that AC circuit breakers make use of zero crossing points to clear faults, but in DC systems there are no zero crossings. Today, solid-state devices and power converters are making DC a more attractive and feasible option. Rectifier and inverter sets found in today's modern motor drives have the capability of identifying faults in microseconds. Motor

controllers handle faults, maintain the DC link between the rectifier and inverter in various circumstances, and monitor over-voltage and under-voltage while using appropriate protection schemes for a specific occurrence. If the technology and knowledge within the motor drives industry is mapped to future DC architectures, it is expected that the same benefits in controller performance and protection will be inherit in these systems.

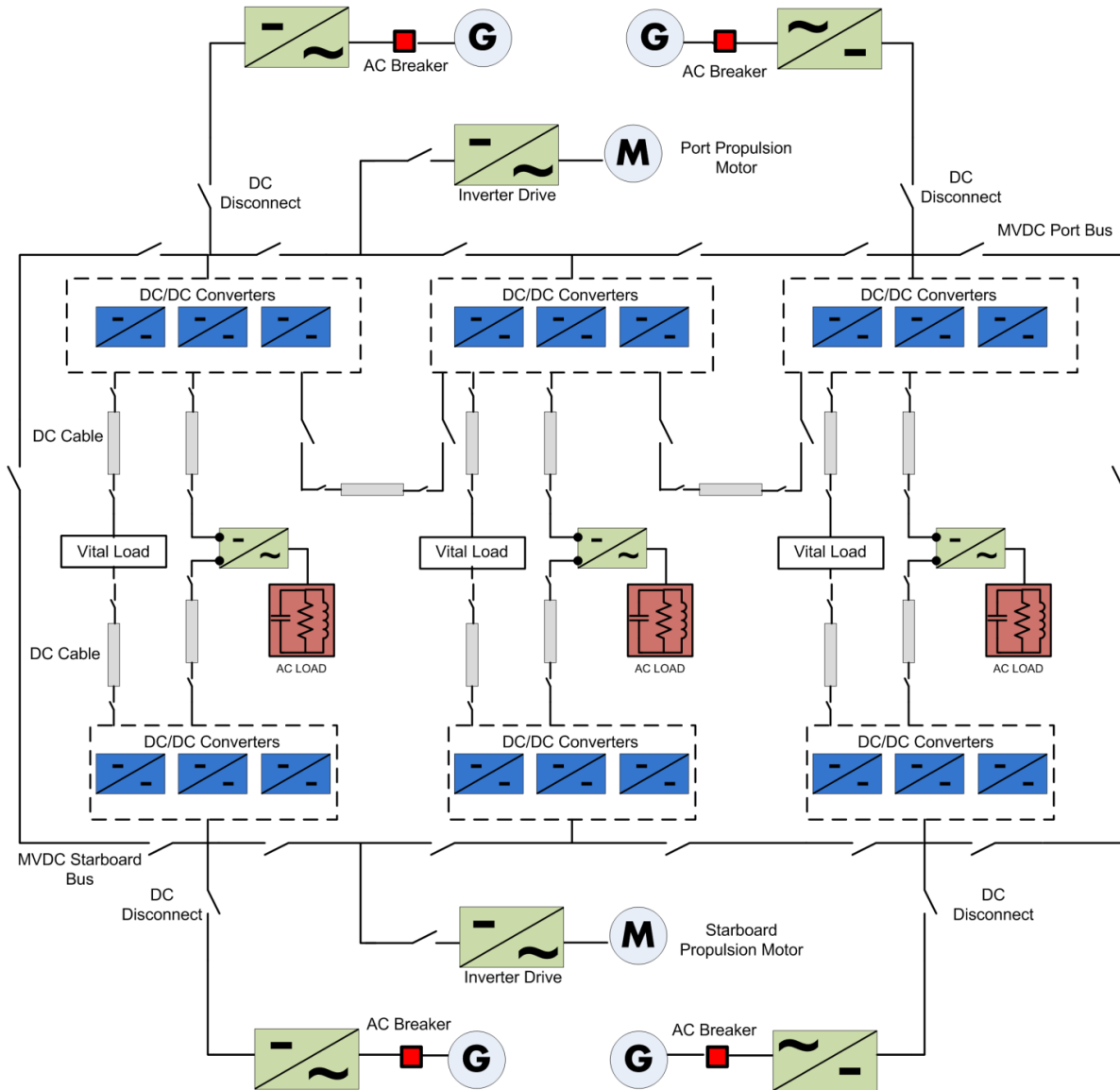


Figure 1.1: Electric Ship Power System Architecture [5]

1.1.2 Explorations in Offshore Wind Generation Potential and Oil Drilling Reservoirs

A better understanding of onshore wind behavior has been the attention of many engineers in the last several years. The Department of Energy (DOE), through FOA-414, has found great interest in exploring the integration of *offshore* wind and has funded a team of organizations to explore the wind speed behaviors at sea and determine the optimal location for placing large wind turbines around the perimeter of the United States. Not only is optimal wind turbine placement important, but investigating ways of integrating the power into the grid is being considered [6].

Drilling rigs, as those shown in Figure 1.2, and *offshore* production platforms rely heavily on AC variable frequency drives for applications such as propulsion, station keeping, drilling, and pumping product to the surface. In drilling rigs, drill-ships, and offshore production platforms, the non-linear variable speed drive load makes up 85% of the installed kW. The typical installed drive power for a drilling package is 5000-12,000 HP (3.7 to 9 MW), [7]. Drilling rigs and oil platforms are placing considerable harmonic strain on generators and degrading the quality of the voltage supplies. As stated in [7], the power quality is degraded due to harmonic currents produced during the *conversion from AC to DC for VFDs*. The harmonic spectrum of an oil production platform can be found in [7]. The harmonic mitigation methods include the use of passive LC filters, multi-pulse drives, active filters and active front end rectifiers. But the additional equipment requires additional space, often where space is at a premium, and also increases the weight of the platforms. A host of disadvantages for each of the mitigation methods is also provided in [7].



Figure 1.2: Semi-Submersible Drilling Rig [7]

Today, domestic offshore oil drilling takes place in the Gulf of Mexico and Northern Alaska, as shown in Figure 1.3. The eastern seaboard, from North Carolina through Maine, are locations with the greatest potential for offshore oil and gas drilling. Considering a few results in Figure 1.4 from the Department of Energy wind turbine placement study mentioned earlier showing available wind generation along the east coast, readers will observe a strong overlap between high wind penetration and oil drilling areas approved by the United States government when comparing Figure 1.3 and Figure 1.4.

The offshore production platform is an opportunity for a more innovative application while taking advantage of the offshore wind turbine power generation locally. The directions that many manufacturers of power system equipment are exploring with offshore technologies, Figure 1.5, to harness and transmit electric power provides further encouragement that the direction proposed is viable [8].

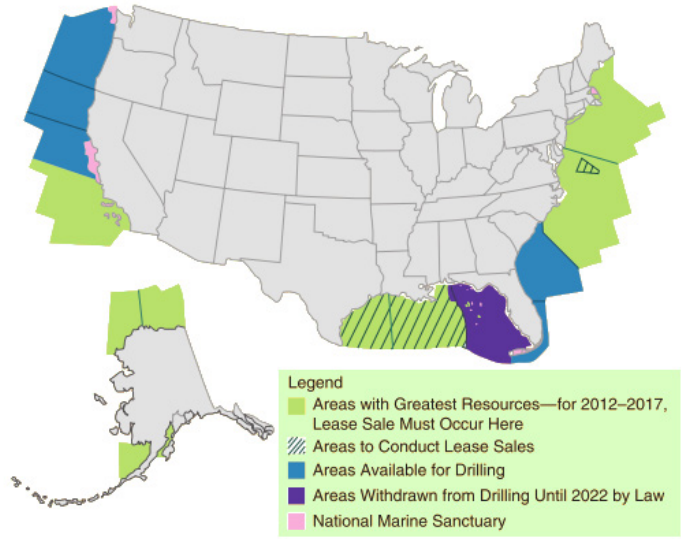


Figure 1.3: Location of Oil Drilling Opportunities between 2012 and 2017 [5]

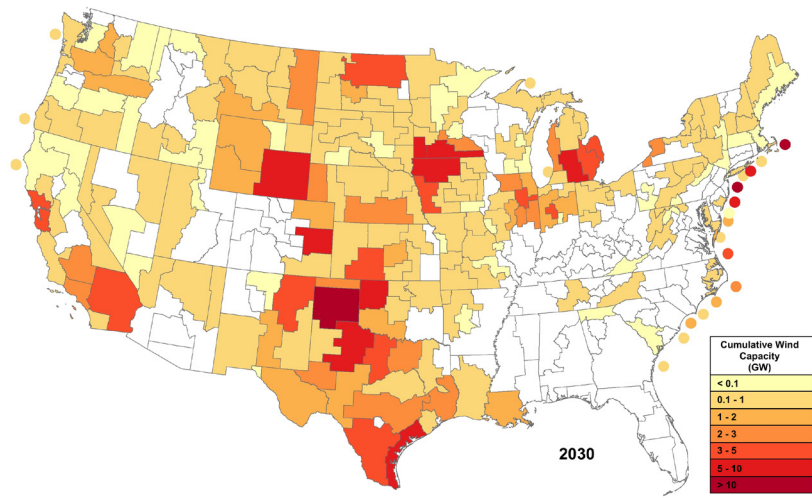


Figure 1.4: Available Wind Generation Onshore and Offshore in the United States [9]

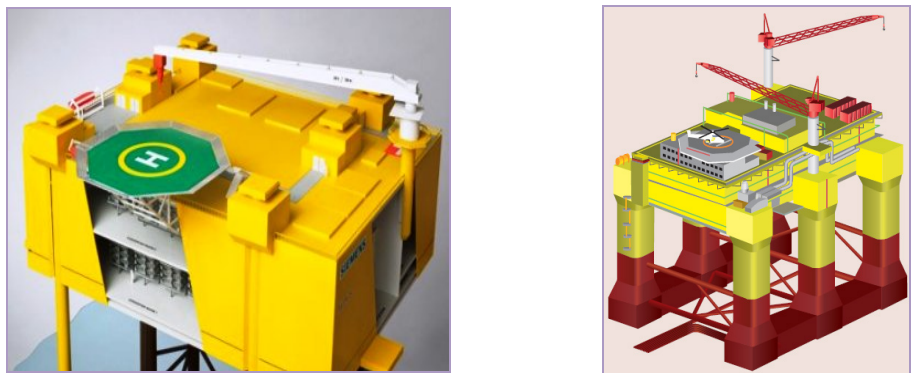


Figure 1.5: Offshore Platforms – Siemens Offshore Design (Left), [10]& ABB Offshore Design (Right), [11]

1.1.3 Challenges and Opportunities with Microgrids

The MVDC architecture, [1], [5], has often been referred to as a type of microgrid upon first view. The microgrid concept was first proposed in 2002 as a better way to implement the emerging potential of distributed generation. During disturbances, the generation and corresponding loads can separate from the disturbed grid, maintain service, and not harm the overall grid's integrity. As pointed out by [12], the difficult task is to achieve the microgrid functionality without extensive custom engineering and still have high system reliability and generation placement flexibility.

The fundamental microgrid requirements include the capability of operating in islanding and/or grid connected modes with high stability, mode switching with minimum load disruption and shedding during transitions, and after a transition, stabilize in a certain amount of time. The high-level technical challenges associated with microgrids include (1) operation modes and transitions that comply with IEEE1547 (Standard for Interconnecting Distributed Resources with Electric Power Systems), [13], and (2) control architecture and communication. For the case of an AC based microgrid, the following items are considered by various research teams:

- **Islanding mode:**
Frequency and Voltage Stability, Optimal Power Flow
- **Grid to Islanding mode:**
Transition and Stabilization, Minimum load shedding and disruption
- **Islanding to Grid mode:**
Re-synchronization and Re-connection, Minimum impact on sensitive loads and electronics as transients evolve during state transitions

Key research and development needs are centered upon operational inverter improvements (harsh environment design, robust operation during fault conditions, improved overload, volume

and weight reduction) and improved system yields (micro and mini converters). A listing of topics referred to as advanced concepts provided in [14] focused on (1) an integrated storage inverter, (2) direct medium voltage inverter design and (3) DC microgrid subsystems. These components are extremely important but protection is also one of the most vital challenges facing the deployment of microgrids.

1.1.4 Increased Interest in Microgrid Operations for AC and DC Architectures

A plug-and-play property of the microgrid is defined as a unit (either generation source or load) that can be placed at any point without re-engineering the system or controls. Ideally, the microgrid should maintain system operation even if one component is lost [12] and operate without communications [15] because of the long distance between generation units [16].

The ability of the microgrid to transition to an islanded state smoothly or automatically reconnect to the bulk power delivery system (and vice versa) is an important operational property [12]. This feature also supports the fact that the reference frequency in a microgrid application is not fixed and depends on the magnitude of the load and power frequency curves of the sources [15]. These transitions from one system state to another will be referred to as a *mode transition* throughout this dissertation. Other transition modes are application specific. Handling internal fault ride-through in the case of wind turbine systems is a prime example. The authors in [17] designed a phase-locked loop controller for grid failure detection and automatic mode switching between stand-alone and grid-connected modes for a 11 kW, full converter, wind turbine. In [18], the authors investigated parallel microgrid inverters with the design challenge of ensuring precision power flow control, current sharing between the converters and smooth transition between grid-tie and islanding modes. An adaptive droop control method is formulated for

inverters operating in grid-connected and islanded modes in [19] and a control strategy to handle transient disturbances and faults in [20].

Most of the research conducted so far has concentrated on AC microgrids [21]. The DC microgrid has a similar network structure compared to a single phase AC microgrid. The fundamental differences include the existence of a frequency component and reactive power flow control is not necessary in a DC system. Power flow is controlled by voltage droops in AC [22],[23],[24],[25] and DC systems [26]. Droop control is extensively found in the literature and is worthy of explaining here. Consider a two generator system with grid impedance, \underline{Z} , between both units. The apparent power, \underline{S} , flowing from the reference generator to the next can be described with (1.1). The real and reactive power components from (1.1) are described by (1.2) and (1.3), respectively.

$$P + jQ = \underline{S} = \underline{V}_1 I^* = \underline{V}_1 \left(\frac{V_1 - V_2}{\underline{Z}} \right)^* = V_1 \left(\frac{V_1 - V_2 e^{j\delta}}{Z e^{-j\theta}} \right) \quad (1.1)$$

$$P = \frac{V_1^2}{Z} \cos \theta - \frac{V_1 V_2}{Z} \cos(\theta + \delta) \quad (1.2)$$

$$Q = \frac{V_1^2}{Z} \sin \theta - \frac{V_1 V_2}{Z} \sin(\theta + \delta) \quad (1.3)$$

Utilizing the fact, $Z e^{j\theta} = R + jX$, (1.2) and (1.3) can be rewritten as (1.4) and (1.5).

$$P = \frac{V_1}{R^2 + X^2} [R(V_1 - V_2 \cos \delta) + X V_2 \sin \delta] \quad (1.4)$$

$$Q = \frac{V_1}{R^2 + X^2} [-R V_2 \sin \delta + X(V_1 - V_2 \cos \delta)] \quad (1.5)$$

Relationships (1.4) and (1.5) can be simplified to (1.6) and (1.7). By utilizing a small angle approximation and neglecting line resistance; one arrives at (1.8) and (1.9).

$$V_2 \sin \delta = \frac{XP - RQ}{V_1} \quad (1.6)$$

$$V_1 - V_2 \cos \delta = \frac{RP + XQ}{V_1} \quad (1.7)$$

$$\delta \cong \frac{XP}{V_1 V_2} \quad (1.8)$$

$$V_1 - V_2 \cong \frac{XQ}{V_1} \quad (1.9)$$

From (1.8) and (1.9), the angle δ can be controlled by regulating P and the voltage V_l is controllable through Q . Control of the frequency dynamically controls the power angle and thus, the real power flow. By adjusting P and Q , frequency and amplitude of the grid voltage are determined.

1.1.5 Microgrid Hierarchical Control Terminology

Only a few works conceived the microgrid as a whole problem taking into account the different control levels. In the literature, [27] and [28] provide exceptional overviews of the three control layers within microgrids – primary control, secondary control, and tertiary control. The primary control – droop control discussed earlier – is often used to emulate physical behaviors to make the system stable and more damped. The primary control maintains voltage and frequency

stability of the microgrid prior to islanding. The secondary control ensures that the electrical signals through the microgrid are within the required values compensating voltage and frequency deviations toward zero when necessary caused by the operation of the primary controls. Finally, the tertiary layer controls the power flow between the microgrid and main grid. Figure 1.6 is an illustration showing the interoperability of the primary, secondary, and tertiary control within a microgrid set-up. Figure 1.7 shows the reduced controller complexity for a DC microgrid with respect to an AC microgrid.

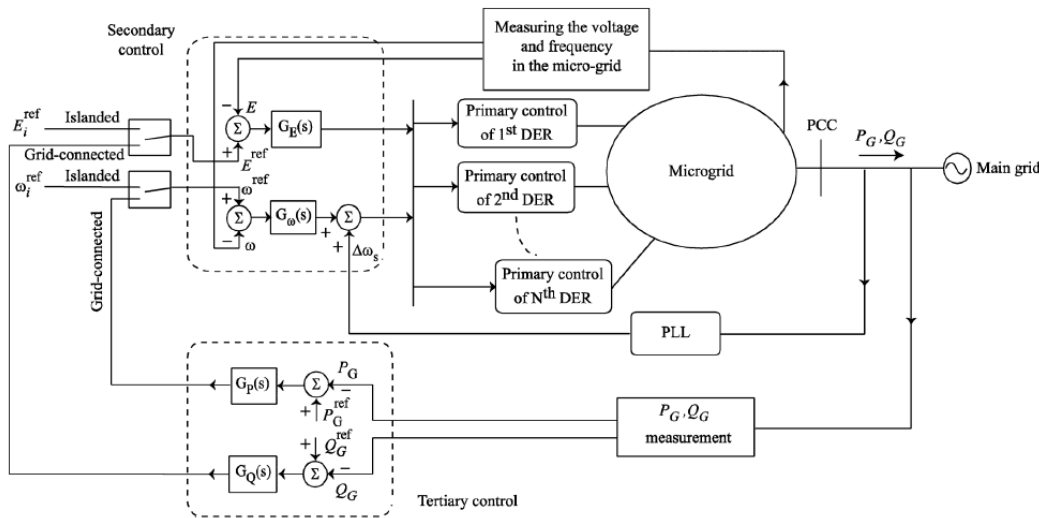


Figure 1.6: Block Diagram of Microgrid Control Layers Operating in Unison [27]

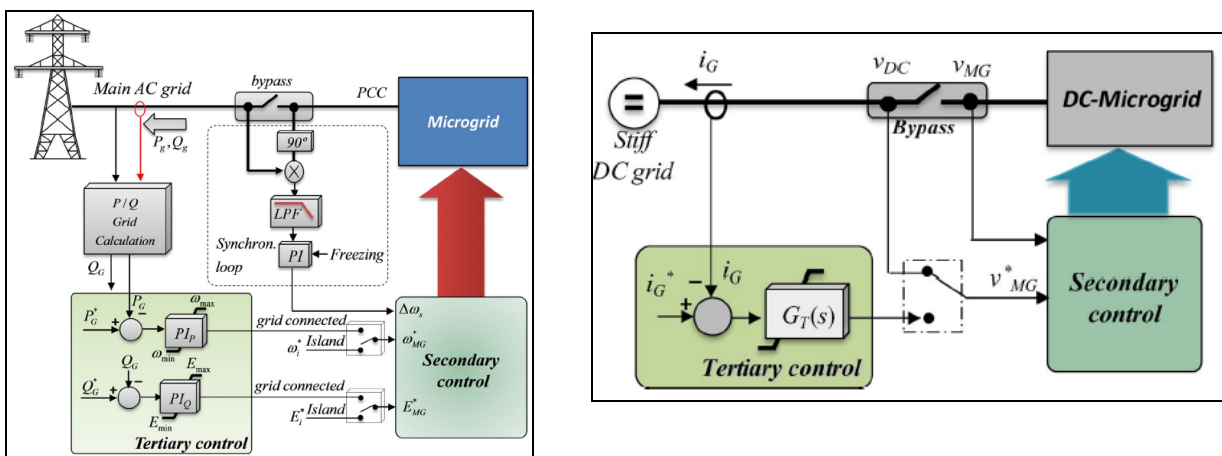


Figure 1.7: Hierarchical Control Architectures for an AC and DC Microgrid [28]

1.2 SIGNIFICANCE AND CONTRIBUTIONS

With improvements in power electronics technology, renewable energy resources are experiencing wider adoption and commercial facilities are considering new infrastructure options with the vast increase in IT hardware. These movements are allowing research teams to propose ideas centered around high and low voltage DC grids. As examples, reference [29] studied a multi-terminal HVDC system for transferring power between (1) one wind farm to two grid connected points and (2) multiple wind turbines to one grid connected point. Reference [30] studied the eight different operation modes within a DC data center environment. Variable wind turbines and energy storage systems coupled through a DC microgrid are explored in [21]. The microgrid, currently, is also being considered for more efficient disaster recovery [31], [32].

With the motivation and current industry/academia pursuits established, one main goal of this study is to investigate offshore, power management strategies within a medium voltage DC microgrid as various network components transition from one state (grid-connected or islanded) to another while adequately serving critical industrial processes. The approach is to understand that there are research needs at the power system level but determine a remedy for the problem at the component/equipment level. For this reason, detailed model development in ANSYS PExprt, PSCAD/EMTDC, and Matlab/Simulink is required. The chosen package is dependent on the problem being evaluated in the forthcoming chapters.

The DC microgrid developed and analyzed throughout this dissertation is found in Figure 1.8. The main source of generation serving the offshore production platform composed of electric motor drives includes offshore wind power, potential utility feed from an onshore substation, and backup generators on the platform. Interfacing many of the generation sources

and loads are a number of power electronic interfaces – one key component being the bidirectional DC/DC converter.

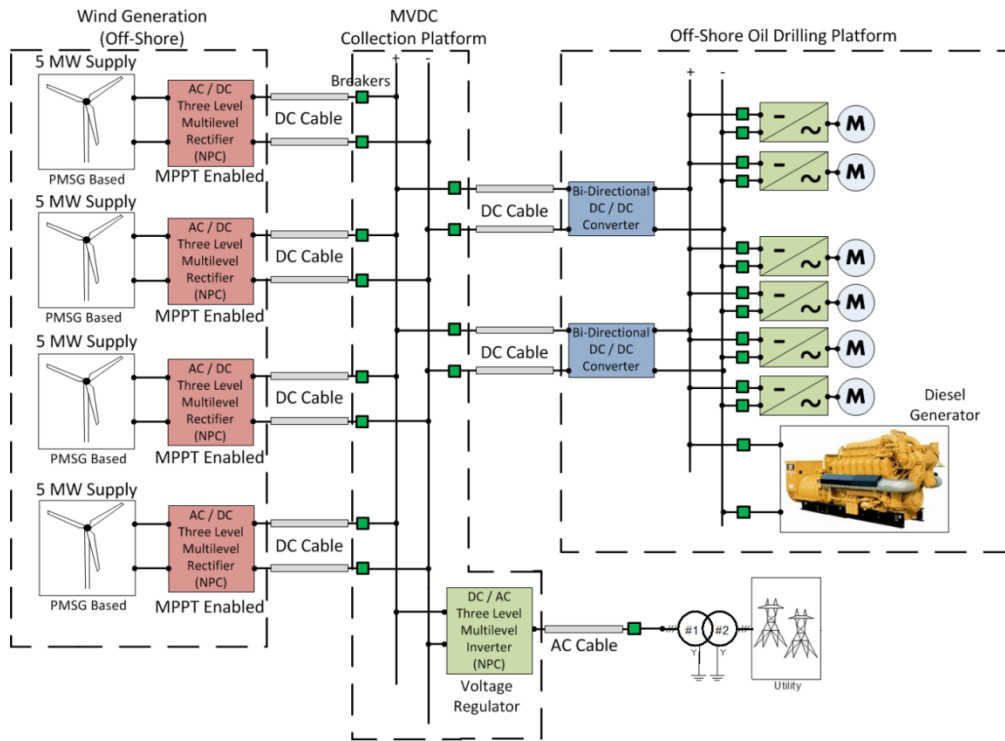


Figure 1.8: DC Microgrid - Local Wind Power being supplied to Offshore Platform

The research contributions, from the author’s perspective, include the following:

- Proposed offshore DC and, potentially, practical microgrid architecture that utilizes offshore renewables to supply the local load. Average models of all components assembling the microgrid are mathematically provided and combined to form the overall architecture in the Matlab/Simulink environment.
- Performance evaluation of new magnetic materials utilized in high frequency and high power environments showing size reductions of these magnetic components (bidirectional chargers, transformers, and electric machines) that will indeed be utilized in the offshore production

platform or other environments where size and weight restrictions are common. This optimized analysis is conducted in ANSYS PExprt or RMxprt.

- The offshore microgrid offers an opportunity for a multi-terminal application that will be explained in Chapter 3. Therefore, a model of a high voltage DC system utilizing modular multilevel converters is developed in PSCAD/EMTDC to evaluate component sensitivities on peak DC fault currents. Physical systems of this size and power rating are difficult for any computer to simulate, thus, discussions are presented on how to scale computer models, from a system energy perspective, to predict electrical quantities of interest.
- Constant power loads are inherently unstable and common in power systems. The electric motor drives are constant power consuming entities due to their speed regulation. This work lays out the mathematical details showing that PD controllers, traditionally used for stabilizing systems, are inadequate and proposes a model reference control design ensuring stability. Although the analysis is based on linear methods (small perturbations from the operating point), the control architecture can be readily upgraded to include adaptation capabilities following model reference adaptive control (MRAC) design – a discussion point in the future work.
- Our objective is to develop a simplified power management strategy between the available renewable generation and onshore utility to provide adequate power to the platform under various mode transitions while still maintaining continuous and seamless power to the electric machines. Although wind turbines out at sea have higher output power potential for transmission compared to onshore wind turbines, the engineer cannot say with 100% confidence that the critical load can always be served by the wind generation alone. In

systems like Figure 1.8, the available power production is also a system constraint. At times, the wind potential may be too high allowing for power to be transferred to the utility and at other times too low requiring the wind turbines to disconnect and allow the utility and onsite diesel generation to supply the critical motor loads. Ultimately, our desire is to use the diesel generation supply at a minimum.

- Finally, communication protocols are described and proposed. One protocol is for within the microgrid itself and another protocol for communication between other microgrids in the same geographical location. This portion of the dissertation required discussions between electrical engineers and telecommunication engineers speaking the same dialogue showing that the microgrid problem is truly multidisciplinary in nature.

The proposed research objectives will have a number of profound impacts and technological advancements in the following areas listed, in no particular order:

1. Enhancement in DC System Operation and Understanding. Changes being made to the power system architecture and layout are drastic with increased renewable generation penetration and power electronic equipment. From previous sections, strong arguments have been made that support new developments in DC areas. As many have been focused on improving AC architectures, this body of work shall go beyond the norm and enhance the engineering community's knowledge in DC microgrid operation.

2. Microgrids: Conceptual to Practical. Throughout the last decade, the microgrid was conceptualized as a potential solution to improve power system reliability by having the ability to detach from the main grid under a major disturbance. Usually, microgrids have some kind of

connection with a larger electrical network but this is not necessarily always the case. This dissertation has distinct applications to help improve disaster relief procedures, future military operating bases used for short time periods, and in non-developed nations where a strong electric grid is non-existent.

3. Numerical Insights into Advantages of MVDC compared to MVAC. Pursuing DC system design is a challenge when the legacy of the electric power industry has primarily been based on AC. This dissertation area will try to disclose some of the advantages that have been hypothesized, through a simulation environment, or perhaps reveal the challenges with DC based grids.

4. Diagnosis of Power Electronic Operation and Equipment Interaction in a DC Environment. Presently 30% of all electric power generated uses power electronics technologies somewhere between the point of generation and end-use. By 2030, 80% of all electric power will flow through power electronics, [33]. The need to understand how equipment, like power electronics, in the grid responds, interacts and delivers power to changing loads due to operational mode transitions is a valuable exploratory effort because this will be a future scenario that will need to be handled appropriately both in AC and DC system design.

5. Exploratory Offshore Renewable Generation Utilization. Traditionally, engineers have strictly focused on transporting offshore renewable energy, specifically wind power, to the shore and utilizing the remaining power, after losses have been considered, to power equipment on land. The system described in the proposal body is a unique application that uses offshore wind generation, locally, to power an offshore production platform (a heavy industrial environment). Although conceptual at first, the oil and gas industry could potentially benefit from this study.

As stated earlier, many global manufacturers are pursuing initiatives and funding offshore power equipment design.

6. Evolving Application for High Voltage DC. The increasing need for high voltage, grid-scale power electronics (HVDC & FACTS) and growth is astonishing. Also, multi-terminal HVDC is a concept that has been proposed but, in practice, has not been implemented to date. The medium voltage DC concept is an application of a multi-terminal scenario *and* microgrid packaged into one unit which will be explored.

1.3 DISSERTATION OUTLINE

This dissertation provides a thorough treatment (but not complete!) for an offshore, medium voltage DC microgrid power system design. This dissertation is organized in 7 chapters, as follows:

Chapter 2 looks into power density improvements for electric machines, transformers and bidirectional DC/DC converters utilizing novel nanocomposite magnetic materials capable of performing at high switching frequency. The analysis is conducted in various ANSYS packages.

Chapter 3 investigates the design of a modular multilevel converter based HVDC system with key analysis focused upon component sensitivities to system fault currents. Scaling the HVDC system for large submodule count per inverter arm is also emphasized. The analysis is conducted in PSCAD/EMTDC.

Chapter 4 presents the argument that the motor drives on the offshore platform can be modeled as constant power loads. First, it is shown that traditional proportional-derivative

control cannot be used to stabilize constant power loads and a new, small signal model reference control is analytically derived for stabilizing the constant power load. The analysis is primarily conducted in Matlab/Simulink.

Chapter 5 explores the detail model development for all components of the DC microgrid power system described in Chapter 1 including wind turbine models, detailed variable frequency electric drive model, average converter models, and associated controls for each component. Model development was entirely developed in Matlab/Simulink using the SimPowerSystems toolbox.

Chapter 6 presents a power management routine implemented within the model developed in Chapter 5. A few mode transitions are evaluated and results presented including grid connected to islanding mode and islanding to grid connected mode. Low voltage ride through studies conducted with the wind generation is considered a future work item. Emphasis is placed on the behavior of the components on the offshore platform and behavior of the bidirectional DC/DC converters in the model.

Chapter 7 demonstrates the necessary communication requirements for the offshore DC microgrid. A multi-disciplinary partnership was established between the research groups of the electric power initiative in the Swanson school of engineering and the department of telecommunications to adequately research this microgrid problem. Lite details are only provided for completeness with more extensive results published collaboratively between both parties.

Chapter 8 concludes the dissertation by summarizing the major takeaways of this document while also providing a few suggestions for future work including experimental verification in the electric power systems laboratory at the University of Pittsburgh.

2.0 POWER DENSITY IMPROVEMENTS UTILIZING HIGH FREQUENCY MAGNETIC NANOCOMPOSITE MATERIALS IN POWER APPLICATIONS

The need for the advancement of soft magnetic materials for applications in high-frequency, medium-voltage, MW-scale power electronics and grid integration technology is conveyed by recent DOE reports [34]. Figure 2.1 provides a comprehensive summary of the power electronic programs that the Advanced Research Project Agency – Energy (ARPA-E) has found interest in funding. Increases in DC power conversion and DC loads also motivate research into new topologies containing high-frequency DC-to-DC power converters. The soft magnetics used in these power electronics can occupy significant space, require extensive cooling, and limit designs [35]. Operation at higher frequencies allows for reductions in converter size and weight [36],[37]. Current commercial magnetic core materials are limited by low saturation inductions, in the case of ferrites, or limited to low-frequency applications because of unacceptable losses at high frequencies, in the case of silicon steels. Nanocomposites contain both the soft magnetic strengths of amorphous core materials with the more attractive saturation inductions of crystalline metals, a combination naturally well suited for high-frequency converter applications [37],[38].

The operation of power converters at higher frequencies is limited by increased losses, a trend accounted for by the Steinmetz Equation, (2.1), which relates the operating frequency, f , and saturation induction, B_s , to power loss. In (2.1), the material-dependent, empirically-found

$$P_L = kf^\alpha B^\beta \quad (2.1)$$

Steinmetz Coefficients, $\alpha(\sim 2)$ $\beta(\sim 1-2)$, account for all core losses, in which hysteretic, anomalous and conventional eddy current losses are predominant. Eddy current losses depend on electrical resistivity, sample geometry, and dimensions. The operating frequency of a transformer can be chosen by considering the tradeoffs at high switching frequencies, namely, reduced converter size at the expense of reduced efficiency.

Exhaustive development of nanocomposites, such as FINEMET, NANOPERM, and HITPERM, has shifted focus to optimizing these materials' properties specifically for their use in state-of-the-art power converters, [39],[40],[41]. Combinations of compositional additions and novel processing techniques have produced nanocomposites with permeability, $\mu > 10^5$, saturation induction, $B_s > 1.6T$, resistivity, $\rho > 150\mu\Omega\text{-cm}$, thickness, $t < 15 \mu\text{m}$, temperature stability up to 300°C , and overall core losses less than 20 W/kg at 10 kHzT , a unit convention set by the ARPA-E. Note that T in the metric is Tesla.

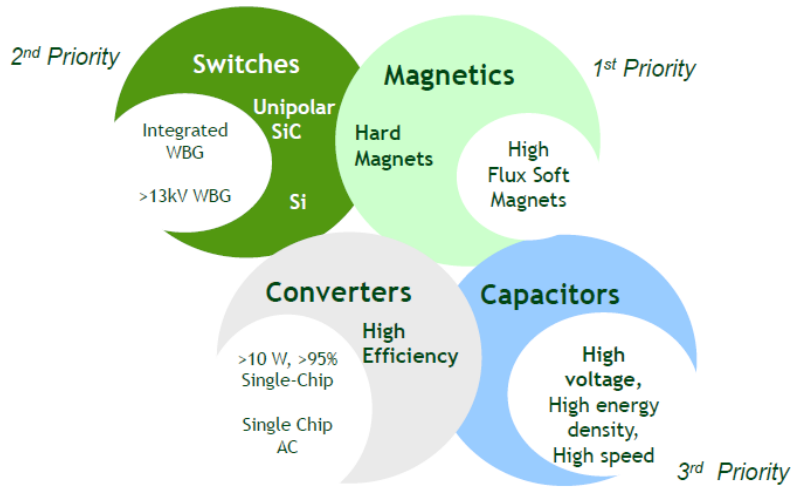


Figure 2.1: 2010 Power Electronic Opportunities for Improvements [34]

The unique material properties possessed by nanocomposites also present challenges. Converter designs developed for ferrites or silicon steels may not be the ideal designs for new

nanocomposites. With currently available soft magnetic materials, thermal management requirements limit converter power density below levels that could otherwise be achieved with advanced switching circuits [35]. The research presented here is focused on a HTX-012B, a novel nanocomposite magnetic material whose iron based chemistry has been optimized to have low coercivity and low permeability. The material’s performance will be evaluated in three major power engineering applications including electric machines, transformers, and bidirectional chargers with higher emphasis on the latter two applications. Continuing with the offshore medium voltage DC microgrid theme, the yellow encircled components found in Figure 2.2 can take advantage of these high frequency magnetic materials.

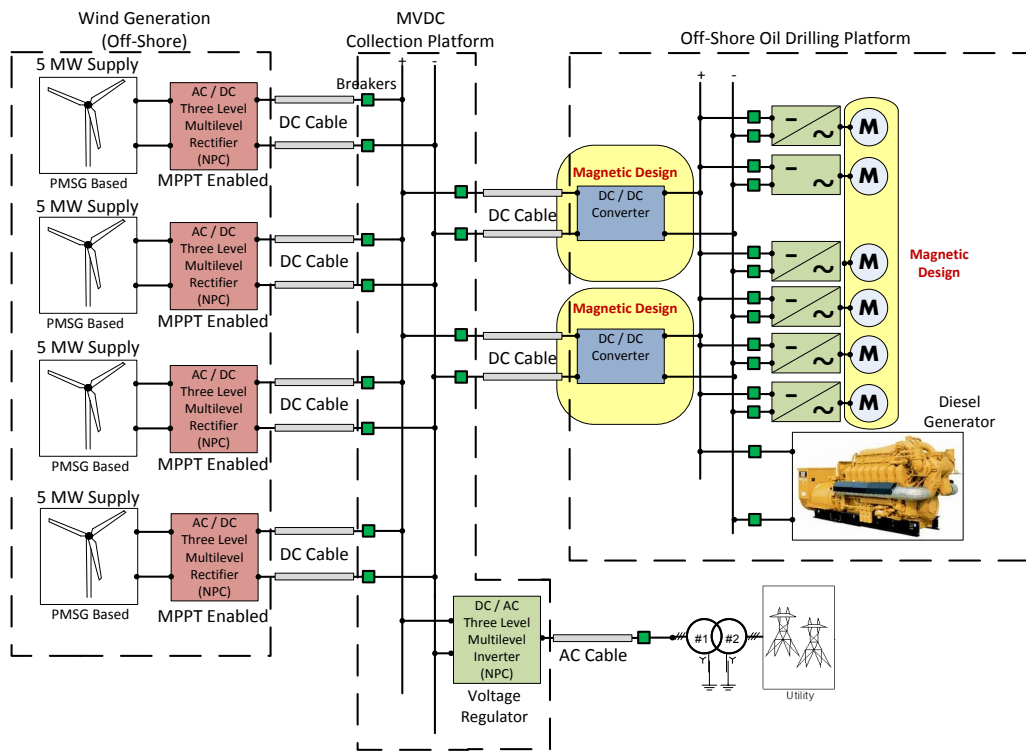
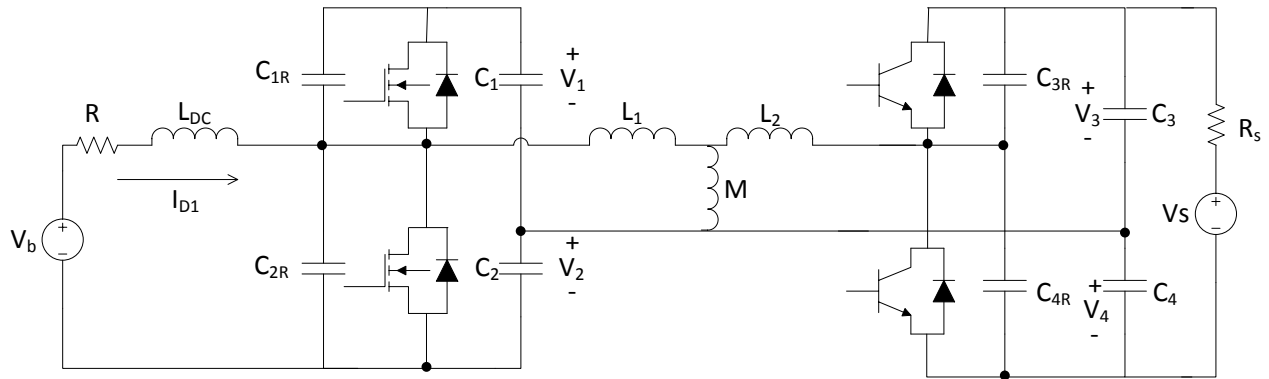


Figure 2.2: Offshore Medium Voltage DC Microgrid Emphasizing Magnetic Intensive Areas

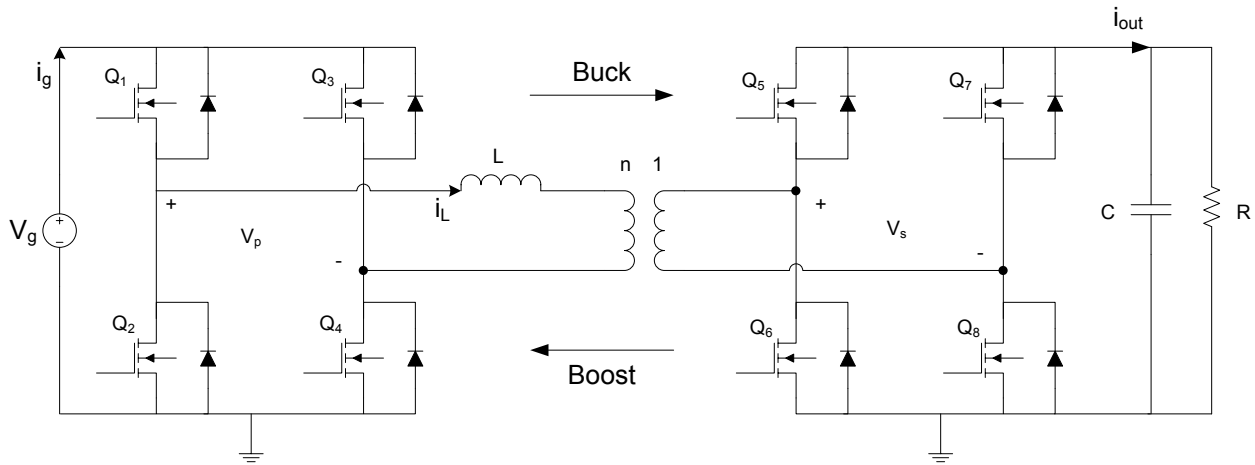
2.1 MOTIVATION FOR DESIGNING BIDIRECTIONAL CHARGERS WITH HIGH FREQUENCY MAGNETIC COMPONENTS

The topology chosen for the DC/DC converter first proposed in [42] is the dual active bridge (DAB) DC/DC converter. Multiple configurations have been proposed with two of the most common provided in Figure 2.3. Half-bridge converters, as shown in Figure 2.3 (a) consist of a single phase leg in parallel with a split capacitor bus. These converters have been applied in uninterruptible power supply systems, electric vehicle applications, and photovoltaic arrays. Although the half-bridge converters offer a reduced switch count in comparison to the full-bridge configuration, their primary drawback is the size and cost of the DC capacitors (C_1 - C_4) required. Half-bridge topology ratings are limited to below 400 V and 2 kW, which is not applicable for a medium voltage design (kV rating) [42],[43].

The single phase, full-bridge, DAB topology found in Figure 2.3 (b) is very attractive because of its zero-voltage switching capability, low component stresses (increased phase legs), high-power density applications [42],[44],[45],[46] and accommodates voltage levels up to 1 kV and higher [47]. The configuration has found widespread use in shipboard power systems because of its galvanic isolation property between two voltage levels through a transformer [48]. In recent literature, [49] explored controller designs for varying loads with the full-bridge DAB operating in the megahertz operating regime while maintaining high efficiency operation. The ARPA-E has also funded work to investigate bidirectional, battery-to-grid charger applications using GaN devices [50]. With growing trends towards higher switching frequency based bidirectional charger applications which utilize transformers, the motivation is set to perform an analysis using ANSYS PExprt to quantify the potential benefits of using HTX-012B in the charger transformer.



(A) Single Phase, Half-bridge Based Dual Active Bridge Converter



(B) Single Phase, Full-bridge Based Dual Active Bridge Converter

Figure 2.3: Bidirectional DC/DC Converter Topology

The bidirectional DC/DC converter shown in Figure 2.3 can operate as a buck converter with power flowing from the MVDC input, V_g , to the local load, or a boost converter with power flowing from the local load towards the MVDC bus. Net power will flow from the primary side of the converter to the secondary side if a delay exists between the primary and secondary side voltages. More specifically, if ϕ lies between 0 and 90 degrees as shown in Figure 2.4, power will flow from the primary side to the secondary side. If ϕ is between 90 and 180 degrees, power will flow from the secondary side to the primary side under the assumption that the load is a

voltage source like a battery. The waveforms illustrated are ideal and neglect the resonant transitions that may occur between the substrate capacitances of the semiconductors and line inductance. The numbers associated with each of the four intervals shown in Figure 2.4 correspond to the active switches shown in Figure 2.3.

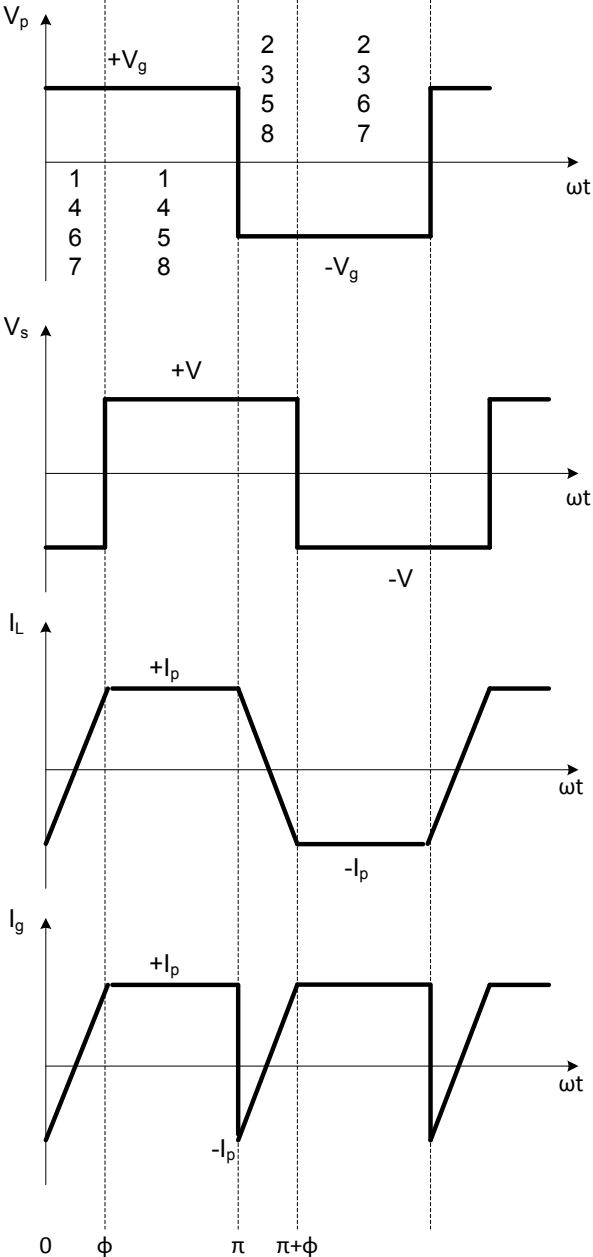


Figure 2.4: Voltage and Current Waveforms of DAB DC/DC while Operating in Charging (Buck) Mode

2.2 OPTIMIZING BIDIRECTIONAL CHARGER MAGNETIC DESIGN FOR KILOWATT SCALE POWER APPLICATIONS USING ANSYS

With the understanding of the DAB circuit behavior, procedures for evaluating the magnetic performance of HTX-012B against traditional ferrites using ANSYS PExprt are explored. A benchmark circuit platform used for the analysis is taken from [46],[51]. The single phase DAB converter was experimentally prototyped and rated for 300 V input, 1-to-1 turns ratio, 20 kHz operating frequency, and 1 kW rated output power.

2.2.1 Analytical Methodology for Optimizing Transformer Parameters

Consider the single phase core found in Figure 2.5. The graphic shows appropriate dimensions from the front and side views of the transformer core with windings appropriately colored – a is the width of the main flux path, b is the width of the transformer window, h is the height of half of the transformer window, and thickness d .

Traditionally, modeling every winding associated with the core is not of interest unless AC resistance is of concern resulting in model approximations [52]. For the analysis presented, it is assumed that (1) the windings are fully filled in the window area of the core and (2) the volume model of the transformer can be simplified by assuming the coils are densely packed (high fill factor). The volume of the transformer (core + windings) can be expressed with the geometric parameters of the latter paragraph as shown in Table 2.1.

The cost function (transformer volume), optimized variables (geometric dimensions of transformer) and constraints of interest are listed as (2.2). The design constraints are functions of the geometric dimensions of the transformer as well as driving frequency as indicated by (2.3),

Table 2.1: Geometrical Relationships Associated with Transformer Core

Geometric Property	Mathematical Relationship with Geometric Dimensions
Cross Sectional Area	$A_c = ad$
Window Area	$A_w = 2bh$
Mean Length per Turn	$l_o = 2(a + b + d)$
Transformer Width	$l_1 = 2(a + b)$
Transformer Thickness	$l_2 = d + b$
Transformer Height	$l_3 = 2a + 2h$
Transformer Volume	$V = l_1 l_2 l_3$
Core Volume	$V_c = (2a + b)(2a + 2h)d - 2hbd$
Transformer Thermal Area	$A_t = 2(l_1 l_2 + l_1 l_3 + l_2 l_3)$

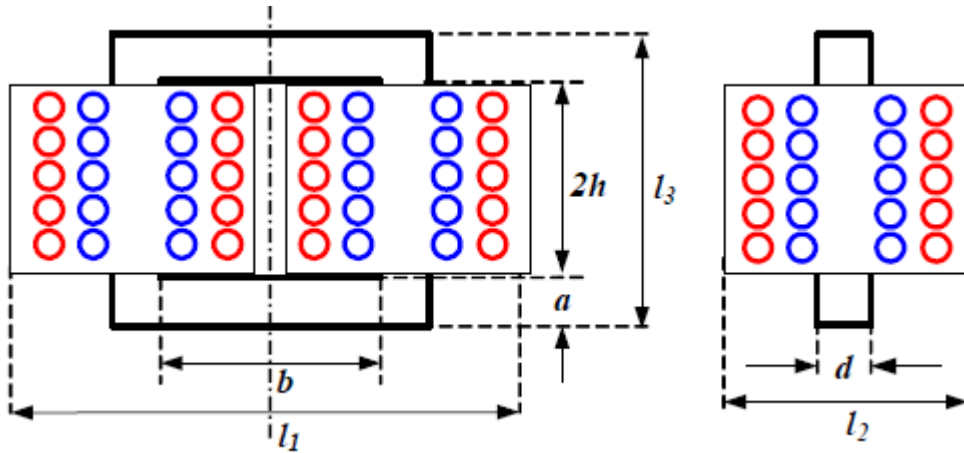


Figure 2.5: Single-phase Transformer Core for Dual-Active Bridge Converter [46]

(2.4), and (2.5). Equation (2.3) is the transformer universal EMF equation assuming the core is driven by a sinusoid, (2.4) is the standard Steinmetz relationship describing transformer core loss for nanocomposite materials, (2.5) is a relationship describing transformer winding losses [35], and (2.6) is an estimate on the temperature rise within the core, [53]. Note that α , β , and k are standard Steinmetz coefficients, l is a magnetic effective length, and ϕ is a geometric constant. Equation (2.2) through (2.6) establishes the basis for an optimization problem with given constraint that can be solved using Matlab optimization algorithms. The benchmark results for our study are provided in Table 2.2 - both numerical results and available core selected, [51].

$$B_{Tx} < B_{\max}; T_{rise} < T_{\max} \quad (2.2)$$

$$B_{\max} = \frac{\sqrt{2}E_{rms}}{2\pi f N a d} \quad (2.3)$$

$$P_{core} = V_{core} k f^{\alpha} B^{\beta} \quad (2.4)$$

$$P_{winding} = \frac{1}{2} \left(\frac{B_{\max} l}{\mu \phi N} \right) \frac{\rho l}{A_c} \quad (2.5)$$

$$T_{rise} = 450 \left(\frac{P_{core} + P_{winding}}{A_t} \right)^{0.826} \quad (2.6)$$

The existing literature provides a nice basis for sizing cores of any size. However, the research team in [51] had to select a bobbin from a different manufacturer with given design constraints. Utilizing ANSYS PExprt, a solution was found that achieves a smaller magnetics volume with parts (core and bobbin) that can be purchased from the same manufacturer. This analysis will be shown next.

Table 2.2: Optimal Core Results for DAB Benchmark Case with Available Commercial Core Metrics [51]

Transformer Property	Optimized Numerical Result (Single Phase)	Commercial Core (Magnetics: 0P44125UC)
Volume (mm ³)	85376	105204
B _{max} (T)	0.3	0.25
Core Loss (W)	1.79	2.16
Winding Loss (W)	7.02	2.84
Total Loss (W)	8.81	5.0
Transformer Turns	82	78
a (mm)	11.7	11.94
b (mm)	13.0	18.8
d (mm)	13.0	11.94
h (mm)	21.6	15.9

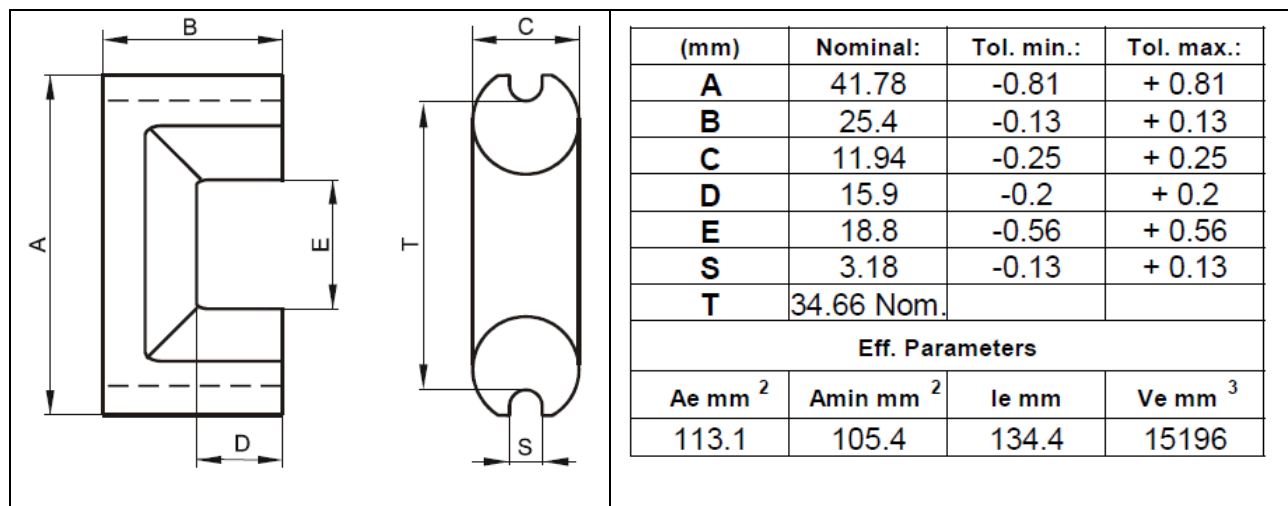


Figure 2.6: Magnetics 0P44125UC [54]

2.2.2 Optimal Ferrite Core Transformer Parameters Analyzed through ANSYS PExprt

The transformer core uses P material that is commonly used for low to medium frequency general-purpose power converters and is engineered for lowest loss at 95°C, [55]. The parameters required by the software are provided in Table 2.3. AWG22 gauge wire was chosen for this application. With a 300 V peak-to-peak, 20 kHz square wave voltage defined having a duty cycle of 50%, the computer software is able to optimize a transformer core rated for 1 kW using stock libraries. PExprt optimizes based on reducing the total system loss associated with the core and windings towards a minimum. The vendors incorporated into the program include AVX, Electrical Steel, Epcos, Ferroxcube, Magnetics, Metglas, Micrometals, Steward, and TDK. Only one stock library can be selected to be evaluated per solution set, thus, Magnetics was chosen. The top ten cores selected for a 1 kW rated core are provided in Table 2.4. Figure 2.7 provides the volume for each core relative to each other for the ten proposed solutions.

Table 2.3: Ferrite Material Properties

Ferrite Material Property	Quantity
Core Resistivity	5 Ω -m
Relative Permittivity	10000
Initial Permeability	2500
Magnetic Flux Density Saturation	0.375 T
Steinmetz Coefficient α	2.1
Steinmetz Coefficient β	2.65
Steinmetz Coefficient k	0.0015 kW/m ³

Table 2.4: Top Ten Core Solutions Rated for 1 kW Utilizing Ferrite Core

Core Name	Volume (mm ³)	Turns	Temperature (°C)	Parallel Turns	Power Losses (W)
ETD49	24510	72	58.91	2	5.2485
ETD49	24510	72	74.55	1	8.3685
EC70	39621	55	42.84	2	4.6319
EC70	39261	55	51.26	1	7.2212
EE45528	43050	44	50.03	2	5.4129
EE47228	50416	42	45.32	2	5.0993
EE47228	50416	42	54.36	1	7.7417
ETD59	51152	42	42.92	2	4.7803
ETD59	51152	42	50.65	1	7.3051
EE48020	68265	42	43.71	2	6.1329

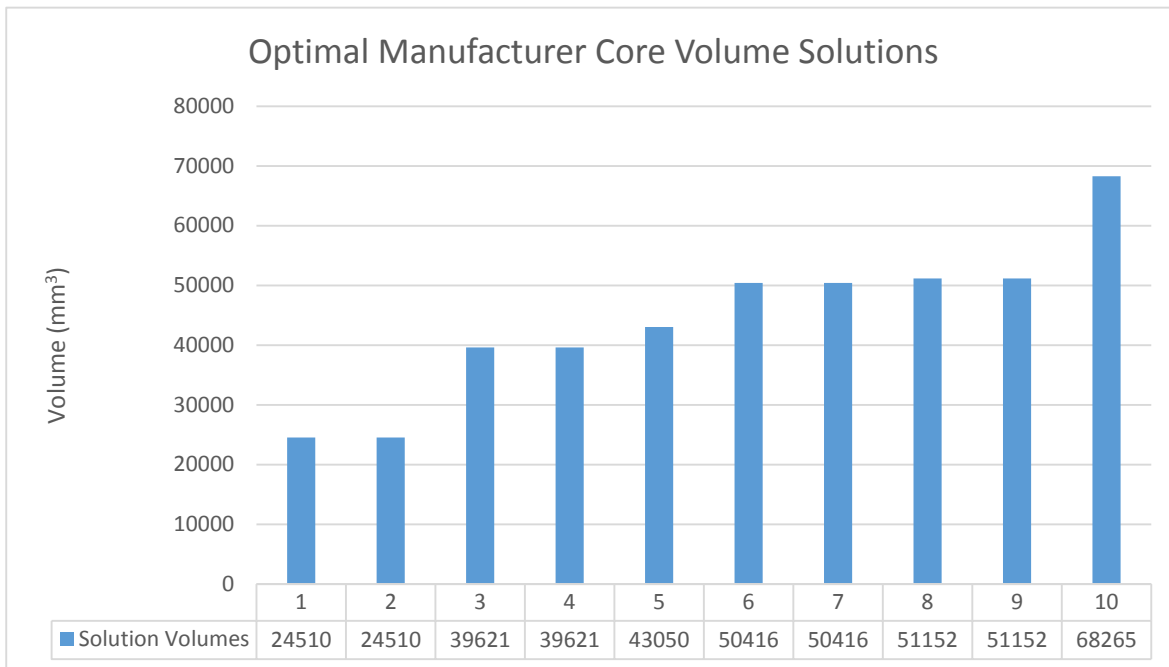


Figure 2.7: Optimal Manufacturer Core Volume Solutions

The advantages of operating at higher switching frequency include component volume reductions resulting in improved power density, one of the key drivers behind the ARPA-E program. Hence, the core volume, total loss, and number of wire turns around the core are parameters of interest in this analysis with core volume being of highest priority. Evaluating the solutions in Table 2.4, the core selected for the 1 kW application is the ETD49. Two solutions are associated with the ETD49 core – the solution with 5.25 W total loss, 2 parallel turns, and maximum temperature rise of 58.91°C is chosen. Other valuable parameters associated with this design including current density and maximum flux density are included in Figure 2.8.

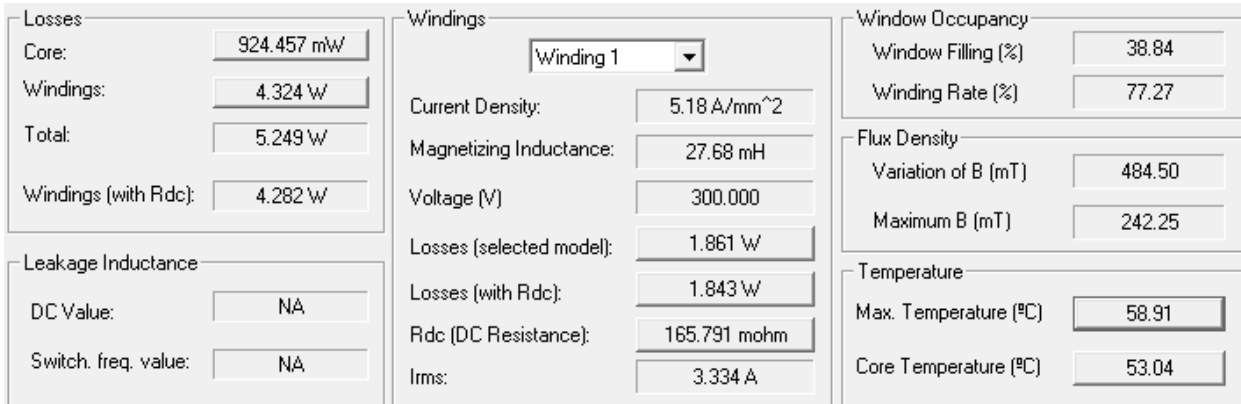
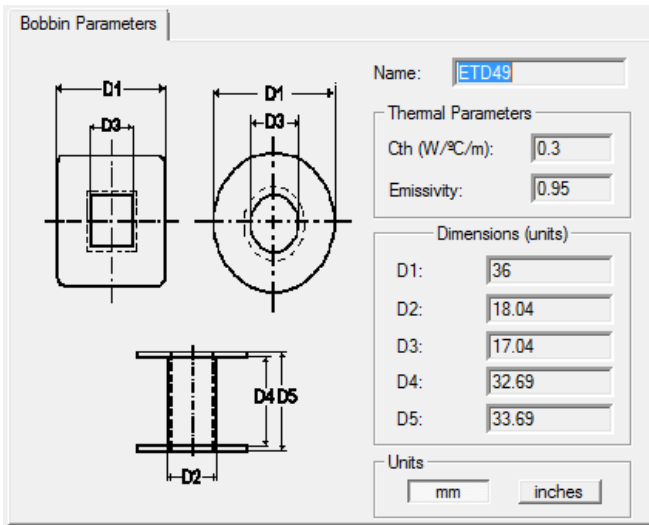
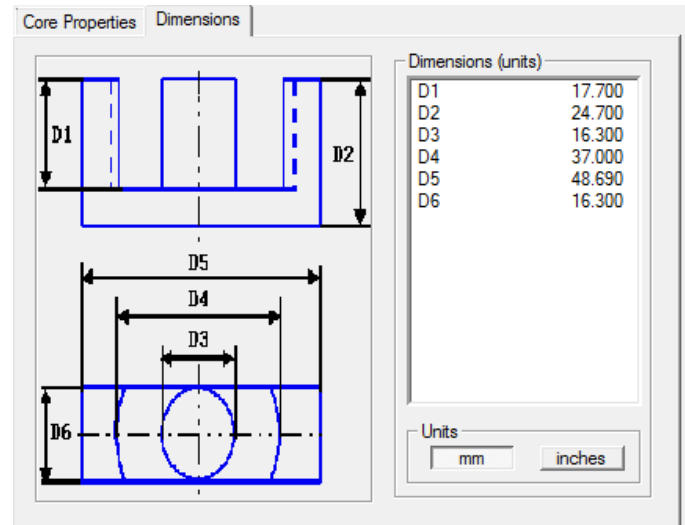


Figure 2.8: Notable Parameters associated with the ETD49 Ferrite Core Design for the 1 kW DAB

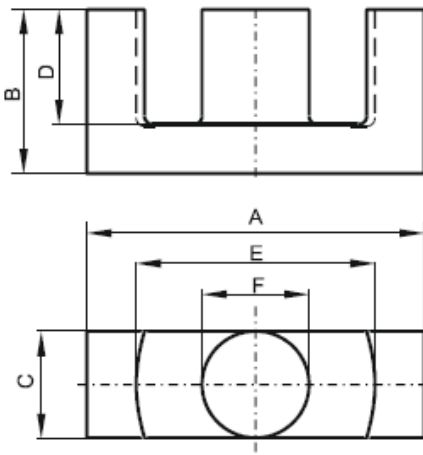
The dimensions associated with the core and bobbin is provided in Figure 2.9. Figure 2.9 (a) provides the dimensions of the bobbin, Figure 2.9 (b) provides the dimensions of the core, Figure 2.9 (c) and (d) provide the schematic and dimensions associated with a readily available core from Magnetics, respectively. A cross sectional view of the core with winding arrangement is found in Figure 2.10. This schematic is the geometry that can be used to conduct a finite element analysis upon if quantities such as current density distribution, flux distribution, power loss vs. time, and other variables that might be of interest.



(A) PExprt Bobbin Dimensions



(B) PExprt Core Dimensions



(C) Magnetics Manufactured Core

(mm)	Nominal:	Tol. min.:	Tol. max.:
A	49.8	-2.2	0.0
B	24.7	-0.2	+0.2
C	16.7	-0.6	0.0
D	17.7	0.0	+0.8
E	36.1	0.0	+1.8
F	16.7	-0.6	0.0
Eff. Parameters			
Ae mm ²	Amin mm ²	le mm	Ve mm ³
211.0	209.0	114.0	24000

(D) 2014 Manufactured Core Dimensions

Figure 2.9: ETD49 Core: Simulation Results and Manufactured Component from Magnetics [56]

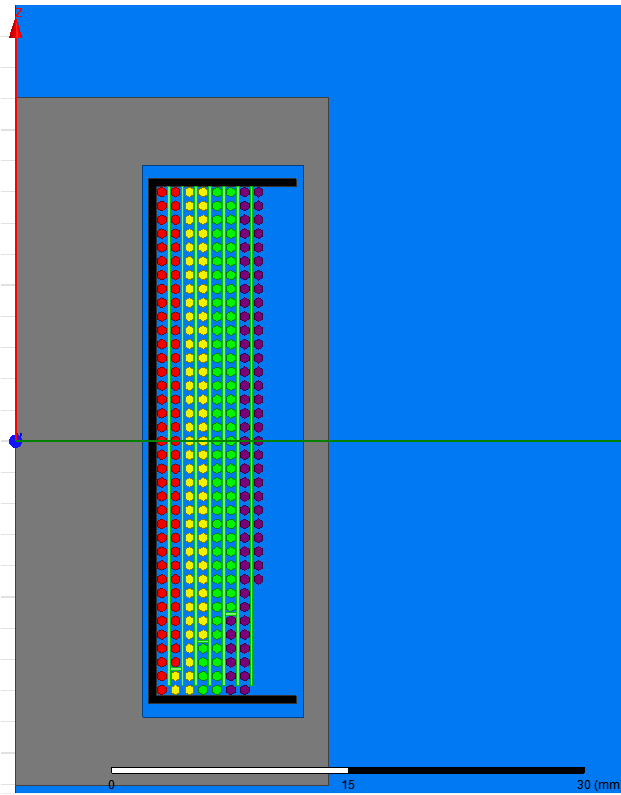


Figure 2.10: Cross Section of 72 Windings Configured in Two Parallel Turns around ETD49 Core

2.2.3 Optimal HTX-012B Nanocomposite Core Transformer Parameters Analyzed through ANSYS PExprt

HTX-012B is a material whose chemistry has been optimized for high switching frequency, tunable permeability depending on desired application, capable of operating at high temperature (above 200°C), and designed for high power applications (kW to MW scale magnetic core designs). A few disadvantages of the material are that the alloy saturates between 1 and 1.2 T and is mechanically brittle. Throughout this section, the same analysis is conducted as in Section 2.2.2 except the ferrite has been replaced with HTX-012B.

Before the magnetic material could be evaluated in a charger application, loss characteristics of various cores had to be obtained experimentally as a function of frequency and

induction level. Once these parameters were obtained, the Steinmetz coefficients could be evaluated and used as inputs into the software.

Six circular cores made of HTX-012B were manufactured, annealed, then impregnated, and tested by technicians at Spang & Company – Magnetics division. Two sets of cores were fabricated – uniform cores and cut cores having outside diameters of 1.25 inch (small), 2.81 inch (medium), and 6.25 inch (large). As the cores were scaled, the ratio between the inside and outside diameter was fixed at 0.80 to reduce flux crowding. The size of the cut in the cores is 0.002 inches. General properties associated with the cores are provided in Table 2.5 with core loss measurements associated with the cores for three different frequencies in Table 2.6.

Table 2.5: Dimensions, Mass, and Permeability of Experimentally Tested Cores

Core #	Dimensions	Mass (g)	Remarks	Permeability μ
1	1.25"x1.0"x1.0"	47.4	Annealed	64,544
2	1.25"x1.0"x1.0"	46.0		69,846
3	2.81"x2.25"x1.0"	215.0		70,507
4	2.81"x2.25"x1.0"	216.9		68,118
5	6.25"x5.0"x1.0"	1023		69,407
6	6.25"x5.0"x1.0"	1068		77,567
1	1.25"x1.0"x1.0"	42.7	Impregnated	21,169
2	1.25"x1.0"x1.0"	43.4	Impregnated, cut	2,843
3	2.81"x2.25"x1.0"	214.3	Impregnated	21,109
4	2.81"x2.25"x1.0"	215.0	Impregnated, cut	3,458
5	6.25"x5.0"x1.0"	1016	Impregnated	45,356
6	6.25"x5.0"x1.0"	1067	Impregnated, cut	12,398

Table 2.6: Core Loss Measurements at Varying Frequencies and Induction Levels for Experimental Toroids

Core #	Dimensions	Remarks	Watt loss at 20 kHz, W/kg			Watt loss at 50 kHz, W/kg			Watt loss at 100 kHz, W/kg		
			0.1 T	0.2 T	0.5 T	0.05 T	0.1 T	0.2 T	0.025 T	0.05 T	0.1 T
1	1.25"x1.0"x1.0"	Annealed	0.8	3.2	18.2	0.9	3.7	14.0	0.8	3.1	11.7
2	1.25"x1.0"x1.0"		0.8	3.2	17.7	1.0	3.7	13.9	0.8	3.1	11.8
3	2.81"x2.25"x1.0"		0.8	3.0	17.5	0.9	3.5	13.3	0.7	2.9	11.2
4	2.81"x2.25"x1.0"		0.8	3.1	18.4	0.9	3.6	13.7	0.8	3.0	11.5
5	6.25"x5.0"x1.0"		0.8	3.1	18.8	0.9	3.5	13.6	0.7	2.9	11.2
6	6.25"x5.0"x1.0"		0.7	3.0	17.9	0.9	3.4	13.2	0.7	2.8	11.0
1	1.25"x1.0"x1.0"	Impregnated	1.5	5.6	37.3	1.4	5.7	23.0	1.1	4.5	17.7
2	1.25"x1.0"x1.0"	Impregnated, cut	1.2	4.6	25.1	1.5	5.9	22.2	1.1	4.6	17.8
3	2.81"x2.25"x1.0"	Impregnated	1.5	6.2	37.9	1.4	5.5	21.9	1.1	4.2	16.9
4	2.81"x2.25"x1.0"	Impregnated, cut	1.6	6.5	34.1	1.6	6.2	24.3	1.2	4.8	19.0
5	6.25"x5.0"x1.0"	Impregnated	0.9	3.5	21.3	0.9	3.7	14.4	0.8	3.1	12.0
6	6.25"x5.0"x1.0"	Impregnated, cut	1.0	3.9	23.1	1.0	4.2	16.2	0.8	3.4	13.2

The core loss results of Table 2.6 have been plotted to show various trends as the cores are geometrically scaled. Figure 2.11, Figure 2.12, and Figure 2.13 are the core loss results for fixed frequency excitation of 20 kHz, 50 kHz, and 100 kHz, respectively. Figure 2.14 are the results for fixed induction. A few trends can be observed. Consider Figure 2.11 although the following observation can be seen in Figure 2.12 and Figure 2.13. The annealed core loss remains constant (left to right in the plots) as the size of the cores increases for a given frequency. This is not the case for the cores that were impregnated and impregnated with cut. For the latter core conditions, the losses increase with increasing core size. Interestingly, the losses are lower in magnitude for the large cores compared to the small and medium-sized cores. This trend is related to the mechanical stress states of the cores. Consider the loss trends from top to bottom for each figure. As induction levels increase, losses consistently increase. Finally, consider when the applied induction level is fixed and frequency varies as shown in Figure 2.14. The losses measured appear to be independent of core size and consistent from core to core if applied induction is fixed and frequency is varied. The experimentally determined Steinmetz coefficients based off of this data is provided in Table 2.7.

Table 2.7: Steinmetz Coefficients Associated with Tested Cores

Core #	Dimensions	Remarks	Steinmetz coefficients		
			K	a	b
1	1.25"x1.0"x1.0"	Annealed	0.5186	1.6295	1.9090
2	1.25"x1.0"x1.0"		0.4806	1.6435	1.9012
3	2.81"x2.25"x1.0"		0.4722	1.6537	1.9360
4	2.81"x2.25"x1.0"		0.5026	1.6509	1.9473
5	6.25"x5.0"x1.0"		0.5349	1.6430	1.9715
6	6.25"x5.0"x1.0"		0.4944	1.6510	1.9628
1	1.25"x1.0"x1.0"	Impregnated	1.4684	1.5467	2.0281
2	1.25"x1.0"x1.0"	Impregnated, cut	0.5927	1.6945	1.8964
3	2.81"x2.25"x1.0"	Impregnated	1.9061	1.4548	1.9877
4	2.81"x2.25"x1.0"	Impregnated, cut	1.2957	1.5314	1.9004
5	6.25"x5.0"x1.0"	Impregnated	0.6904	1.5967	1.9689
6	6.25"x5.0"x1.0"	Impregnated, cut	0.7305	1.6059	1.9630

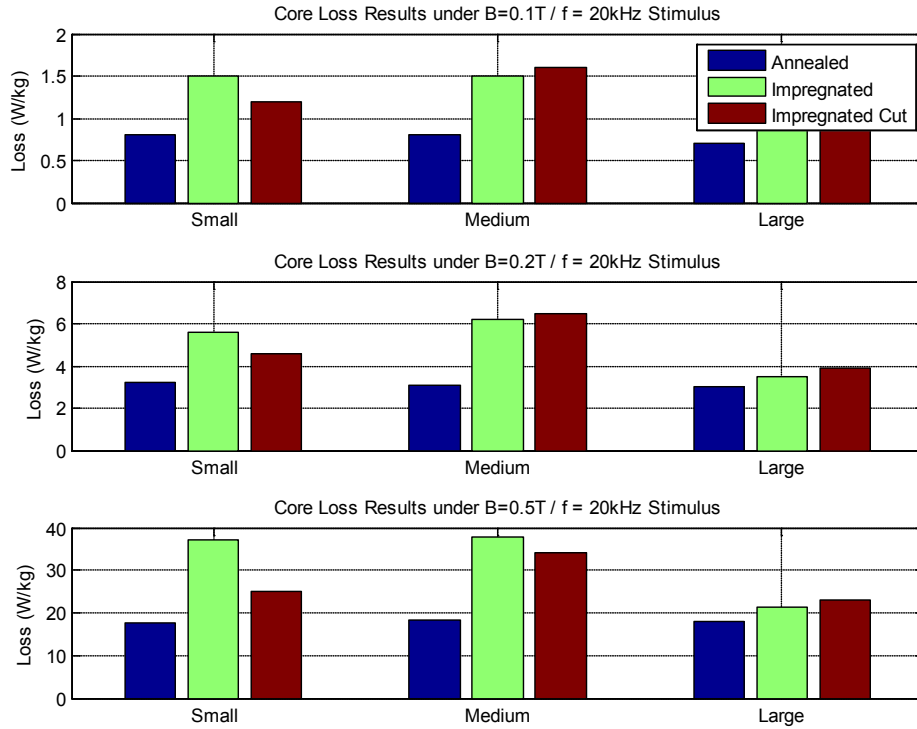


Figure 2.11: Core Loss for Annealed, Impregnated, and Impregnated Cut Cores ($f = 20\text{kHz}$) [57]

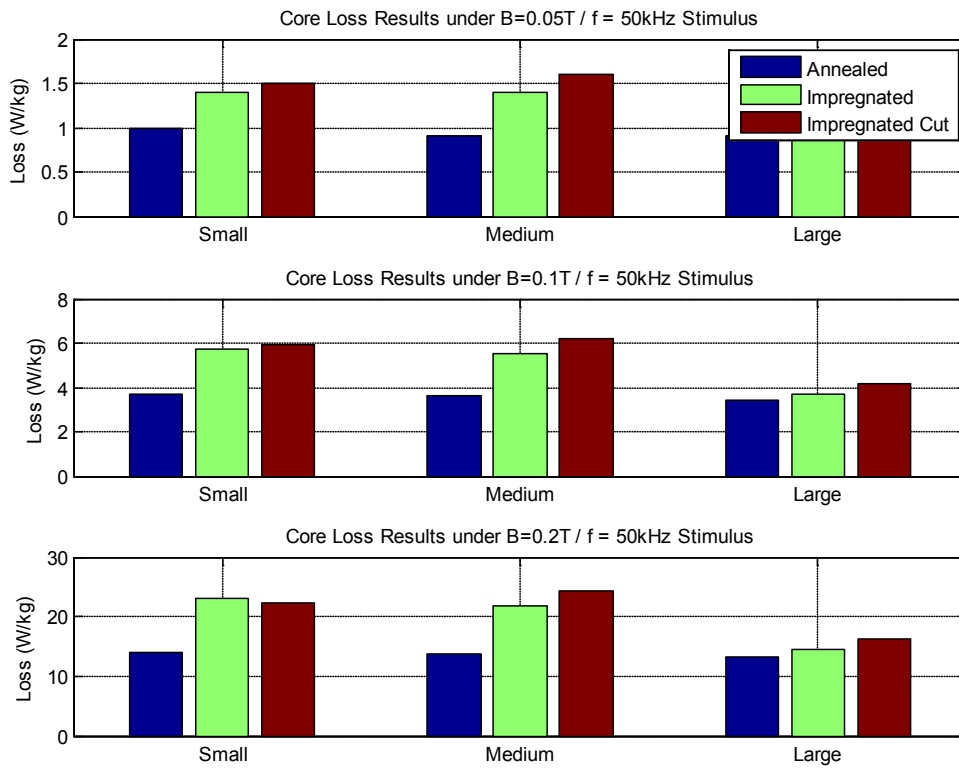


Figure 2.12: Core Loss for Annealed, Impregnated, and Impregnated Cut Cores ($f = 50\text{kHz}$)

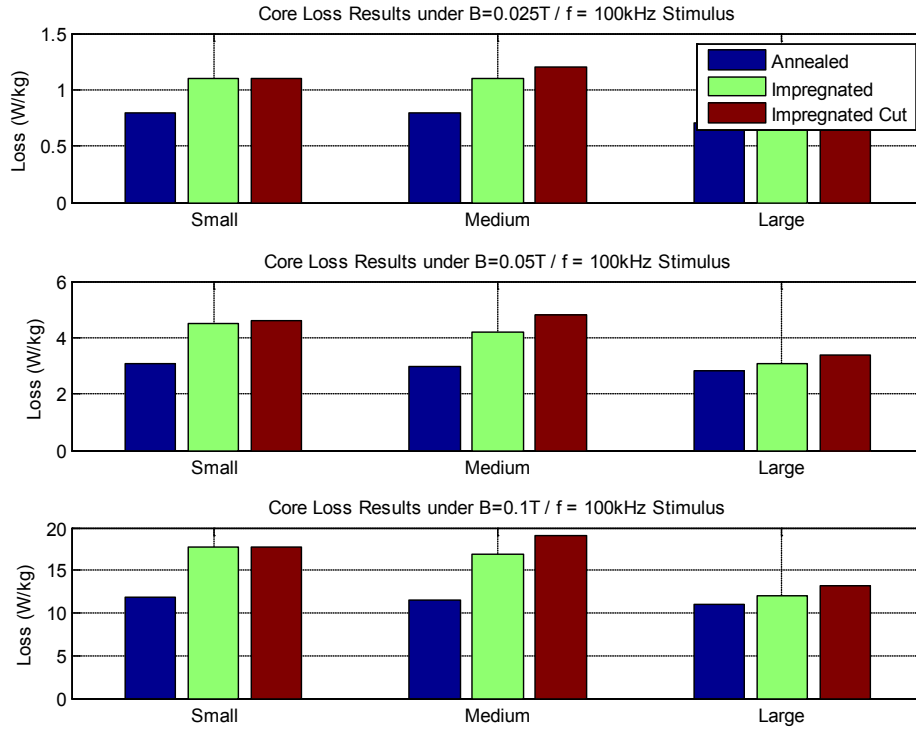


Figure 2.13: Core Loss for Annealed, Impregnated, and Impregnated Cut Cores (f = 100kHz)

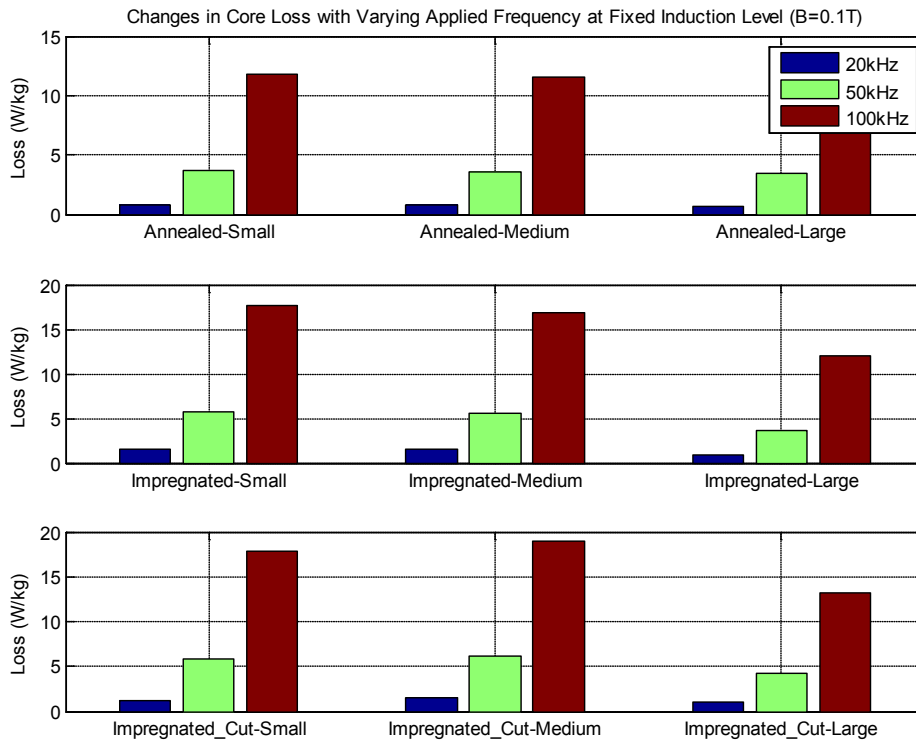


Figure 2.14: Core Loss for Annealed, Impregnated, and Impregnated Cut Cores (B = 0.1T)

The next task at hand is to introduce the material properties from the tested cores into the simulation software. The bobbin for the core (Figure 2.9) will likely have an outside diameter of 36 mm (1.41 inches). From the experimental cores, Core #2 has an outside diameter of 1.25 inches and a measured permeability of 2,843. This permeability value is relatively close to the ferrite design. The experimental core loss information of Core #2 at (20 kHz, 0.1 T), (20 kHz, 0.2 T), (50 kHz, 0.1 T), (50 kHz, 0.2 T) from Table 2.6 were inputs into the core loss definition and Steinmetz coefficients extracted as shown in Figure 2.15. For Core #2, the effective area of the core is 0.657 cm².

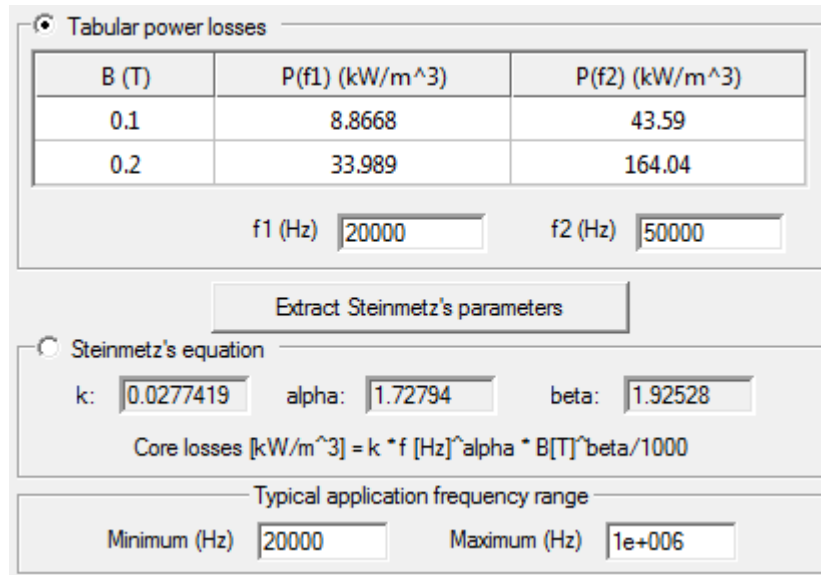


Figure 2.15: Steinmetz Coefficients Provided by PExprt for HTX-012B Based on Experimental Loss Data

The remaining material definition parameters are provided in Figure 2.8. Although permeability is a function of frequency, it is assumed that the permeability is relatively constant for the frequency range of operation. For very high switching frequencies, this assumption is not valid,[58].

Table 2.8: HTX-012B Nanocomposite Material Properties

HTX-012B Material Property	Quantity
Core Resistivity	1 Ωm
Relative Permittivity	10000
Initial Permeability	2843
Magnetic Flux Density Saturation	1.08 T

Table 2.9: Top Ten Core Solutions Rated for 1 kW Utilizing Nanocomposite HTX-012B

Core Name	Volume (mm ³)	Turns	Temperature (°C)	Parallel Turns	Power Losses (W)
EE44022	23321	40	66.08	2	5.9785
ETD49	24510	49	56.98	2	5.1987
ETD49	24510	40	68.78	1	7.5634
EC70	39621	46	47.43	2	5.6100
EC70	39621	37	57.28	1	8.4266
EE45528	43050	37	53.17	2	6.0570
EE47228	50416	39	47.94	2	5.7826
ETD59	51152	41	45.34	2	5.3978
ETD59	51152	33	54.41	1	8.1681
EE48020	68265	42	45.95	2	6.8988

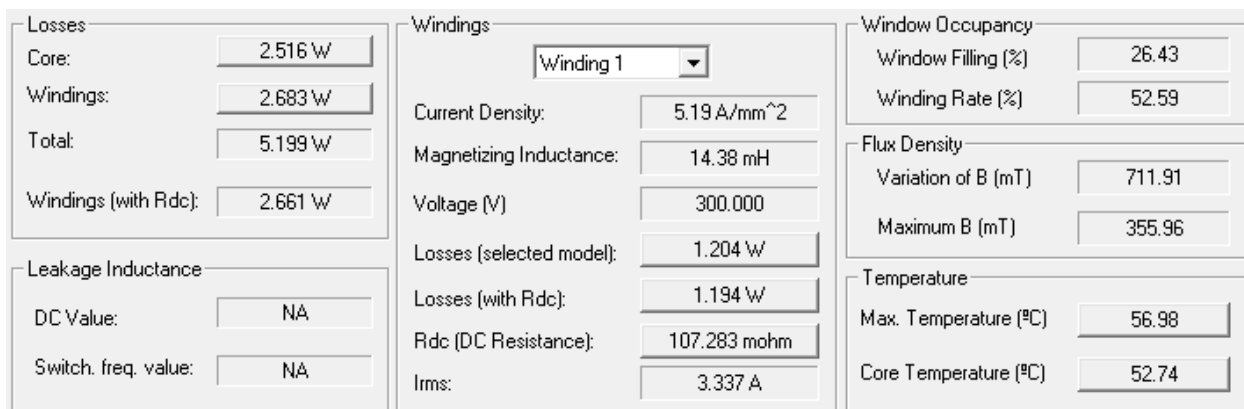


Figure 2.16: Notable Parameters associated with the ETD49 Nanocomposite Core Design for the 1 kW DAB

The top ten optimized core results for a 1 kW DAB core utilizing HTX-012B is provided in Table 2.9 with other parameters of interest associated with the core in Figure 2.16. For reasons listed previously, the best suitable design is the ETD49 core using two parallel turns. Although the same core is utilized in this design compared with the ferrite design, there are some advantages to using the HTX-012B material that will be pointed out in the next section.

2.2.4 Results Comparison between Analytical Ferrite Core, Computer Simulated Ferrite Core, and Computer Simulated Nanocomposite Core

Table 2.10 provides a side by side comparison of the ferrite core results (benchmark) with the results when utilizing HTX-012B in the core. Realize that the analytical result is an approximation from the originally proposed geometry whereas PExprt provides a more formal solution from a larger family of core shapes and sizes that are widely available for purchase. By utilizing a nanocomposite material, the losses are more evenly distributed between the core and windings. The number of turns required to achieve the DAB ratings (1 kW, 300 V, 20 kHz) is reduced in comparison to the ferrite design as well as the core's magnetizing inductance. The ferrite material does not exhibit any noticeable advantage in comparison to HTX-012B from an electrical engineering design perspective. Note that economics have not been taken into account.

Table 2.10: Comparison of Optimized Core Results

Transformer Property	Analytical Result (Square Core)	Optimized / Commercial Ferrite Core	Optimized / Commercial HTX-012B Core
Volume (mm ³)	85376	24510	24510
B _{max} (T)	0.3	0.242	0.355
Core Loss (W)	1.79	0.924	2.516
Winding Loss (W)	7.02	4.324	2.683
Total Loss (W)	8.81	5.249	5.199
Turns	82	72	49
Core Temperature (°C)	--	53.04	52.74

2.3 ELECTRIC MACHINE POWER DENSITY IMPROVEMENT USING NANOCOMPOSITE MATERIALS

Colleagues on the ARPA-E project have explored a new class of Fe-Co based amorphous and nanocomposite materials in permanent magnet machine applications. Co-rich compositions offer the benefits of Fe-rich alloys but are not nearly as brittle and offer an alternative for high frequency operation when material strength is critical, [59]. Frequencies in excess of 1000 Hz can be achieved. However, Co-rich materials have lower saturation inductions, which ultimately impact overall torque production from a machine.

Novel materials contribute to improved machine power density but also novel motor architectures. Reference [59] chose the Parallel Path Magnetic Technology (PPMT) architecture because peak power density can be achieved with little or no rare earth material. For 10 kW rated machines, the team showed that a 70% size reduction can be achieved if HTX-005C (novel Fe-Co nanocomposite material) was utilized in comparison to M-19 G29 (non-oriented silicon steel) while using 83% less rare earth permanent magnet. Reductions are shown in Figure 2.17.

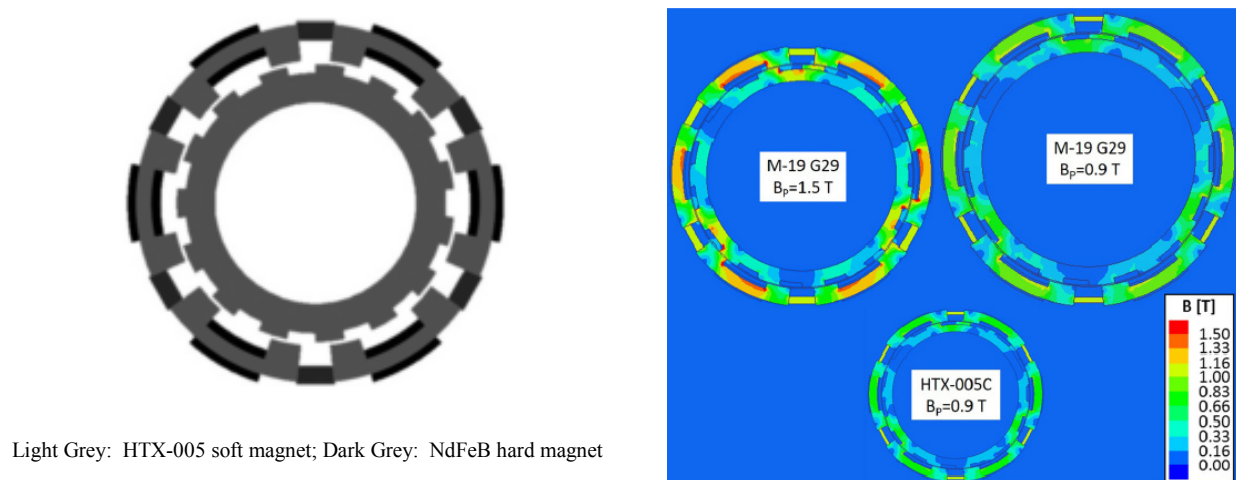


Figure 2.17: Size Reduction of 10 kW PPMT Motor Using HTX-005C Fe-Co Nanocomposite Material [59]

2.3.1 Power Density Improvement of Induction Motors Utilizing HTX-012B: Design Considerations

All machine designs require mechanical, electrical, and thermal analysis. Although HTX-012B is an iron rich alloy, the intent is to show power density improvements for induction motor applications. The B-H loop associated with HTX-012B is provided in Figure 2.18.

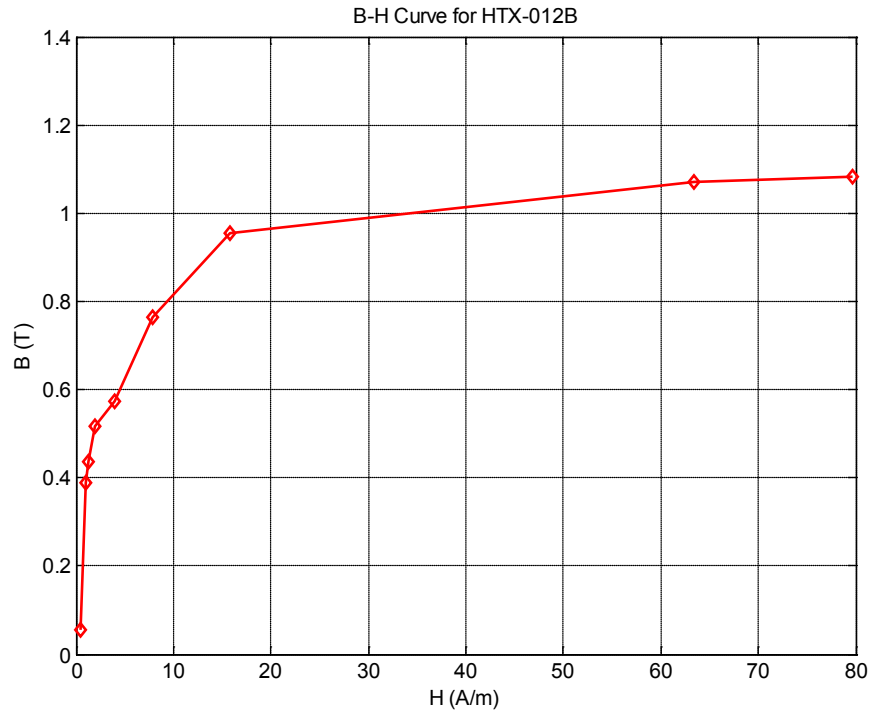


Figure 2.18: B-H Curve for HTX-012B

To observe possible power density improvements for induction motors, an example motor model is selected from the ANSYS RMxprt motor library. The model reflects an existing motor and ensures validity of the operational characteristics for the base case. By increasing the driving frequency of the motor, the motor's size can be decreased, as described by Faraday's Law. This is shown mathematically for a toroidal core assuming a sinusoidal current excitation and constant voltage in (2.7) – both the cross sectional area, A , and driving frequency, ω , are inversely proportional to each other. Note that N and l are the number of turns and effective

length, respectively. When increasing the driving frequency without changing any other parameters of the motor, the mechanical speed of the motor increases proportionally. For this reason, the number of poles of the motor must be altered in order to maintain the same mechanical speed. This concept is described by (2.8) where P is the number of pole pairs and ω_e and ω_r is notation for the excitation frequency and rotor frequency, respectively.

$$V = -NA \frac{dB}{dt} = -L \frac{dI}{dt} = \frac{-\mu N^2 A}{l} I_o \omega \cos(\omega t) \quad (2.7)$$

$$\omega_r = \frac{\omega_e}{P/2} \quad (2.8)$$

The number of poles of the original motor is reduced from 8 poles to 2 poles. The voltage, driving frequency (50 Hz), and rated speed are all kept constant. A second motor model is then created with all the same characteristics; however, the driving frequency is *changed* to 200 Hz requiring an increase in pole number to keep the same rotational speed between both cases. The number of poles was altered to 8 for the second case.

The nanocomposite material, HTX-012B, replaces the stator material but not the rotor material for both motor models to maintain mechanical integrity. The original motor model utilizes an electric steel listed as M19-24G in the rotor. Because the original motor model is only rated for 50 Hz operation we cannot be sure the loss data for M19-24G is valid for higher frequencies. For this reason, a new material, M600-50A is used to replace M19-24G in the rotor. The core loss/material data and B-H curves were obtained from [60],[61],[62] and can be seen in Figure 2.19 and Figure 2.20, respectively. The core loss data for M600-50A is represented by the dashed lines in Figure 2.20.

With the new materials in the rotor and stator, a non-linear optimization algorithm is performed on the geometry of the 8 pole motor. Parameters such as the outer diameter of the stator, air gap size, slot length, and a general scaling factor are allowed to vary so as to decrease the overall size of the motor. The objective of the algorithm is to reduce size while keeping the efficiency and power factor high. In addition, the algorithm is run to keep the output power and the rotational speed for the 8 pole design, the same as the 2 pole design.

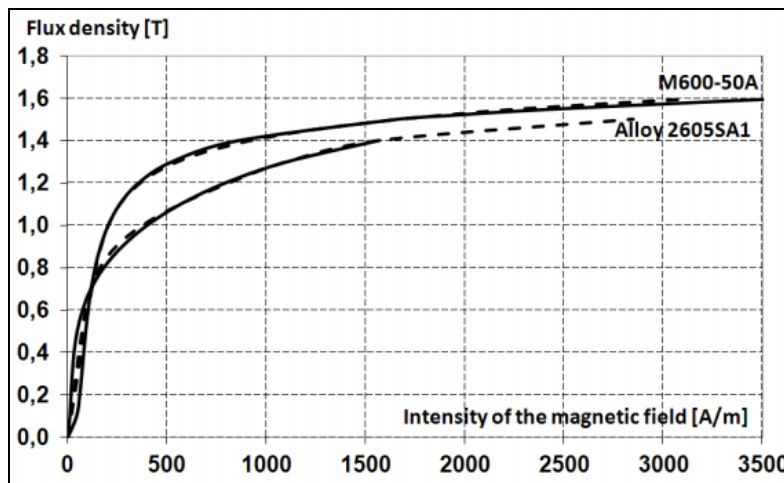


Figure 2.19: M600-50A B-H Curve [62]

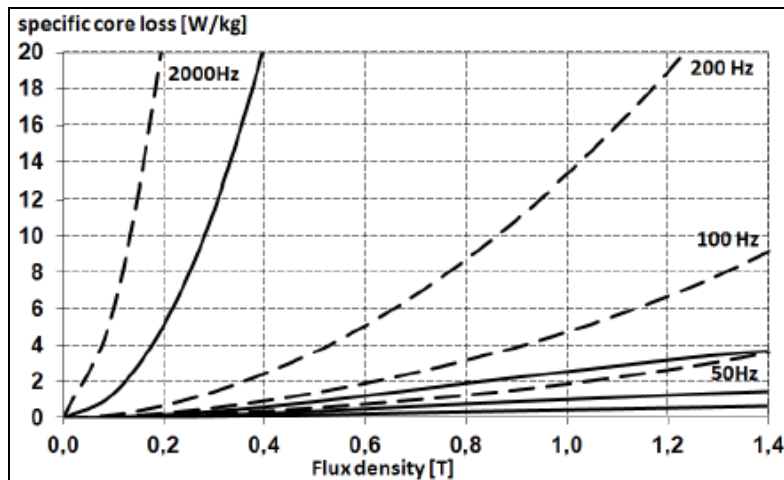


Figure 2.20: Core Loss Data for M600-50A [62]

When increasing the number of poles, it is critical to take into account how the magnetizing current, and therefore, the power factor (P.F.) are both impacted. As the number of poles in a motor increases, the magnetic flux has less distance to travel to get from one end of a pole to the other. There is an inverse relationship between the number of poles and the necessary thickness or width of the return path in the stator core. If the thickness is not increased, flux crowding will occur and will diminish the motor's ability to produce torque; additionally the magnetizing current will also increase. This increases the full load current and, therefore, the primary I^2R losses. In order to maintain the same output power, the current through the rotor cannot diminish. Therefore, the stator current must increase to provide more magnetizing current. As the magnetizing current increases, the power factor of the motor decreases. The machine power factor trend as machine poles increase is shown in Figure 2.21, [63].

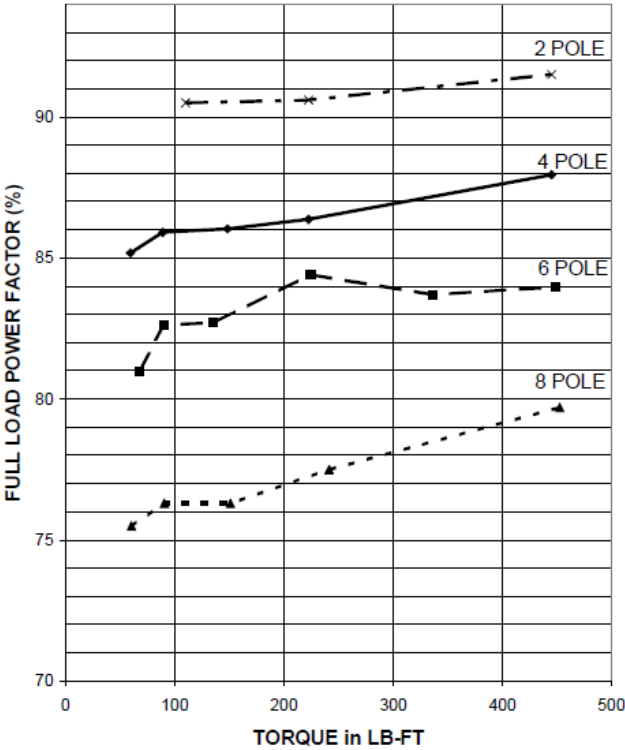


Figure 2.21: Machine Power Factor Adjustments as Number of Machine Poles Increase [63]

2.3.2 Power Density Improvement of Induction Motors Utilizing HTX-012B: Motor Optimization Study

The motor model for this study is depicted in Figure 2.22 and the geometric data is listed in Table 2.11. The geometry and winding configuration is fixed for the 2 pole design operating at 1.3 kW, 50 Hz and 2800 RPM. In order to run an optimization algorithm for the 8 pole design, adjustable parameters are assigned to the dimensions of the rotor and stator outer diameters, rotor and stator slots, motor length, and a scaling factor for the motor at a whole. Every geometric variable of the motor was multiplied by the scaling factor except for the stacking factor and the number of slots. This scaling factor was used to allow the optimization algorithm to change the motor's size. These variables and their constraints are listed in Table 2.12. A nonlinear optimization algorithm is run to reduce the size of the motor while keeping the same output power and rotational speed. The constraints of the optimization algorithm are as follows: Efficiency $\geq 77\%$; Power Factor ≥ 0.93 ; Slot fill factor $\leq 79\%$. These constraints were chosen to make the machine power factor the highest priority.

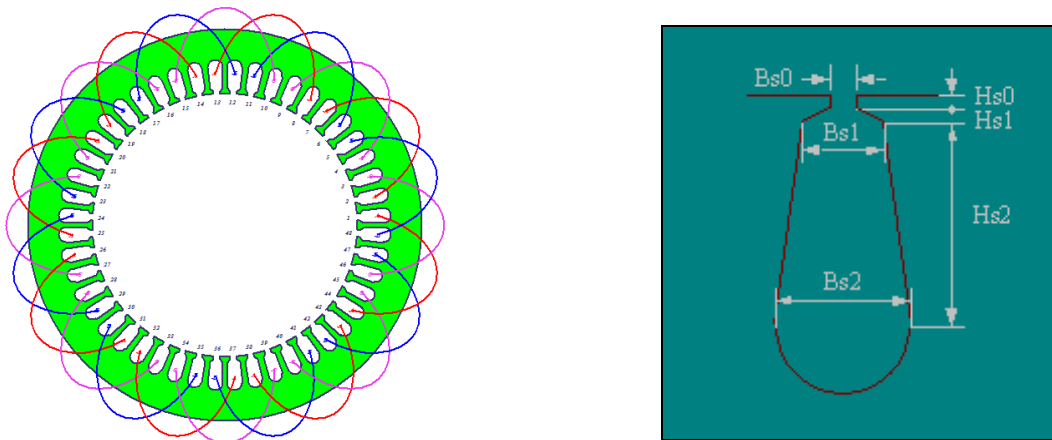


Figure 2.22: Motor Geometry, Winding Configuration and Slot Dimensions

Table 2.11: Motor Geometric Variables

Parameter	Stator	Rotor
Outer Diameter (mm)	210	147.3
Inner Diameter (mm)	148	48
Length (mm)	250	250
Stacking Factor	0.92	0.92
Number of Slots	48	44
Hs0 (mm)	0.8	0.5
Hs01 (mm)	NA	0
Hs1 (mm)	1.05	1.2
Hs2 (mm)	12.9	12
Bs0 (mm)	2.8	1
Bs1 (mm)	4.9	5.2
Bs2 (mm)	6.7	3.5

Table 2.12: Motor Constraints

Parameter	Min	Max
Outer Diameter Stator (mm)	190	210
Outer Diameter Rotor (mm)	137	147.9
Length (mm)	125	375
Hs2 Stator (mm)	4	14
Hs2 Rotor (mm)	4	14
Scaling Factor	0.4	1

Operating characteristics for the two pole and eight pole motor are provided in Table 2.13 and Table 2.14, respectively. A 56% size reduction and a 57% reduction in weight can be visually seen through the magnetic field plots shown in Figure 2.23 and Figure 2.24 for the two pole and eight pole machine, respectively. While there is a 7.6% reduction in power factor between these models, the output power, rated torque, and efficiency are all similar. Figure 2.25

Table 2.13: Two Pole Motor Output

Machine Parameter	Quantity
Outer Diameter Stator (mm)	210
Outer Diameter Rotor (mm)	147.3
Length (mm)	250
Hs2 Stator (mm)	14
Hs2 Rotor (mm)	12
Scaling Factor	1
Stator Ohmic Loss (W)	21.965
Rotor Ohmic Loss (W)	29.444
Iron-Core Loss (W)	0.000564
Output Power (W)	1300.1
Input Power (W)	1519.94
Efficiency	85.53
Power Factor	0.967
Rated Torque (N-m)	4.222
Rated Speed (RPM)	2940.52
Rated Slip	0.01982
Stator Phase Current (A)	1.3668
Magnetizing Current (A)	0.2922
Rotor Phase Current (A)	1.329
Total Net Weight (kg)	54.987
Total Size (m³)	0.00866

Table 2.14: Eight Pole Motor Output

Parameter	Quantity
Outer Diameter Stator (mm)	196.6
Outer Diameter Rotor (mm)	147.9
Length (mm)	125
Hs2 Stator (mm)	14
Hs2 Rotor (mm)	8.55
Scaling Factor	1
Stator Ohmic Loss (W)	9.87
Rotor Ohmic Loss (W)	10.4
Iron-Core Loss (W)	0.0011288
Output Power (W)	1299.3
Input Power (W)	1490.02
Efficiency	87.1997
Power Factor	0.8931
Rated Torque (N-m)	4.16534
Rated Speed (RPM)	2978.72
Rated Slip	0.007
Stator Phase Current (A)	1.451
Magnetizing Current (A)	0.4377
Rotor Phase Current (A)	1.3378
Total Net Weight (kg)	23.448
Total Size (m³)	0.00379

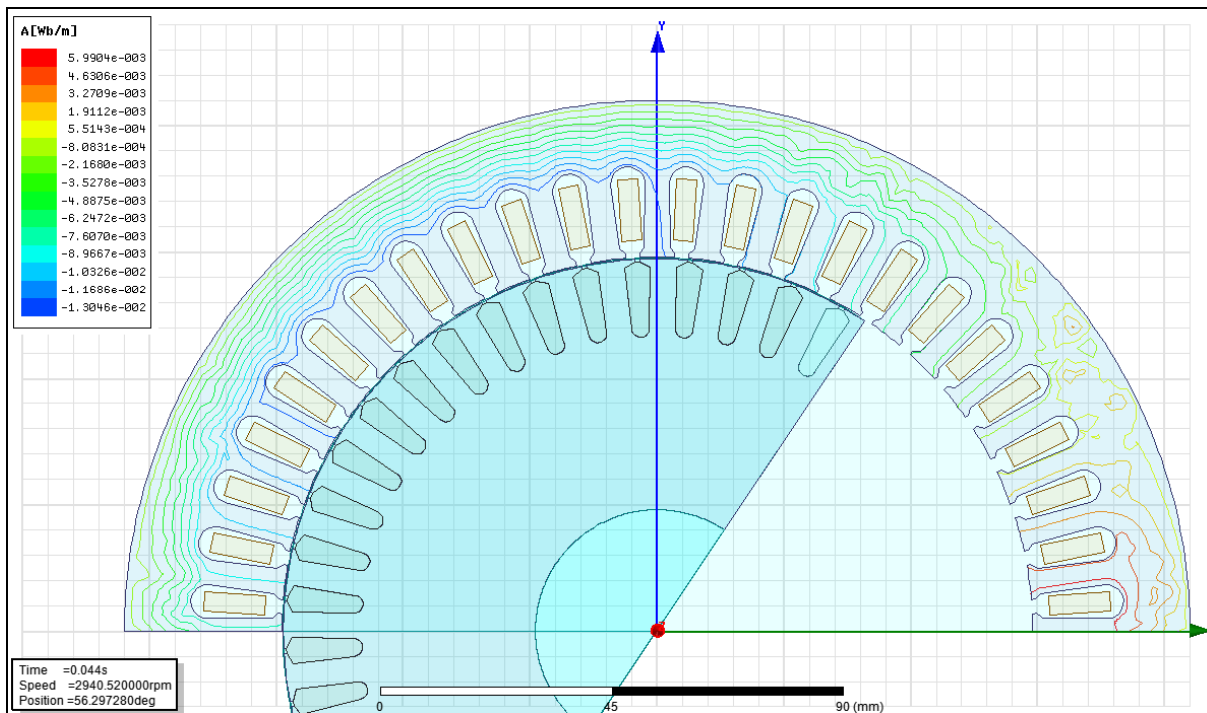


Figure 2.23: Two Pole Motor Flux Distribution

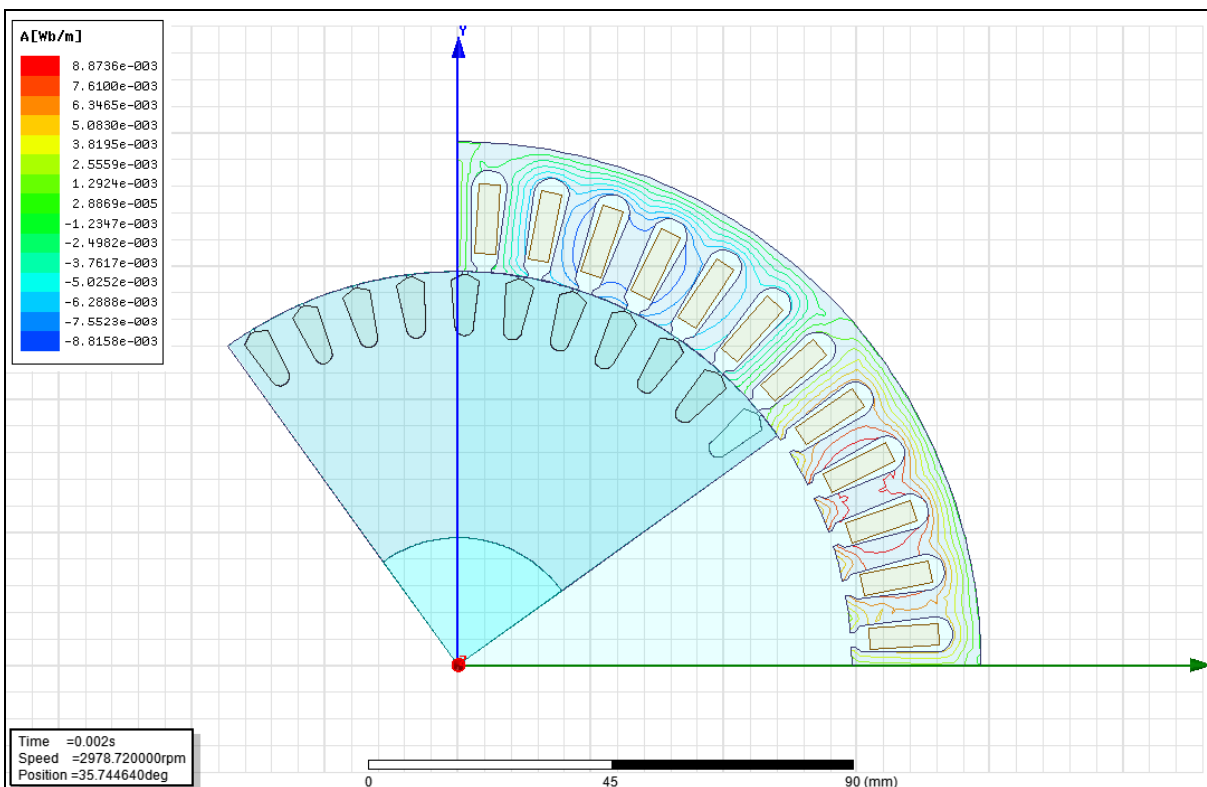


Figure 2.24: Eight Pole Motor Flux Distribution

and Figure 2.26 show a reduction in the maximum torque for the motor from 40 Nm to 37.2 Nm; however, rated torque remains the same. If HTX-012B is used in the stator, simulations show improved power density and improved operating efficiency, with a minimal loss in power factor.

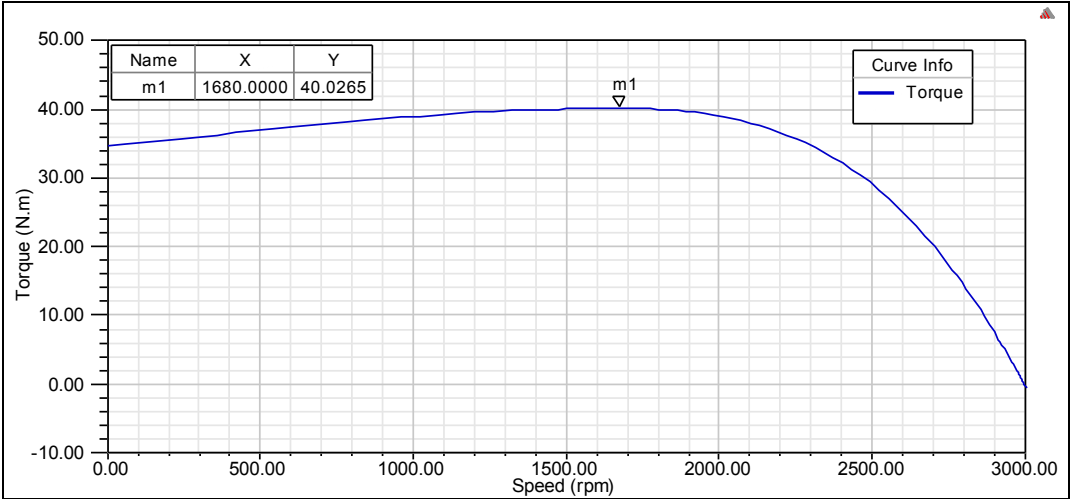


Figure 2.25: Two Pole Motor Torque vs. Speed Curve

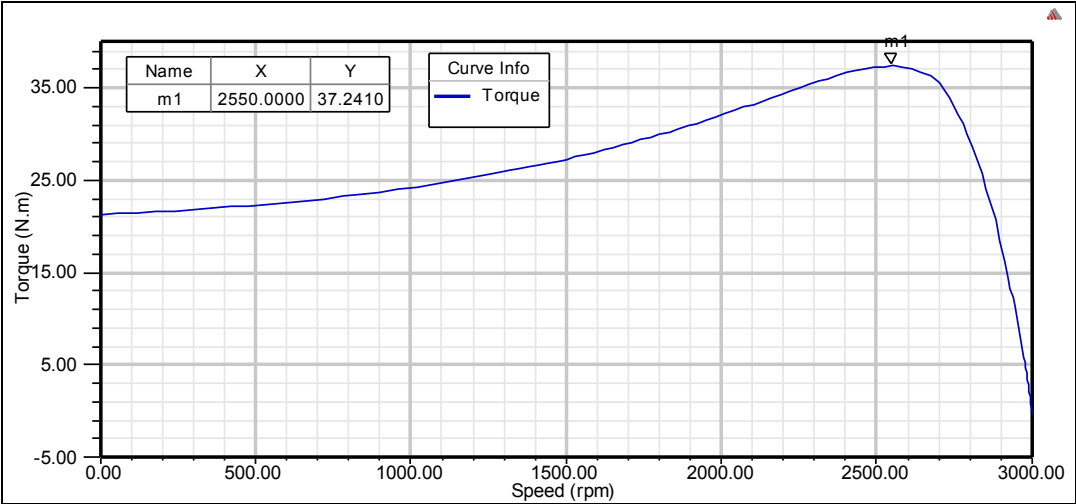


Figure 2.26: Eight Pole Motor Torque vs. Speed Curve

2.4 APPROXIMATE UTILITY SCALE TRANSFORMER CORE SIZE REDUCTION EMPLOYING NANOCOMPOSITE MAGNETIC MATERIALS

The optimization objective of any transformer design is decided by the application of the power transformer and specification of the design. Various factors such as the weight, volume of the transformer, cost, minimum loss, or combination of all four are often considered. Design constraints are from the limit of the magnetic, electrical, and mechanical properties of the materials used in transformers. Usually system constraints include the maximum flux density, maximum allowable temperature rise and sometimes current density as shown previously. The objective of this brief section is to optimize a 100 kW transformer core and quantify volume reductions with increased switching frequency. The C-core design to be optimized is shown in Figure 2.27 (dark gray component).

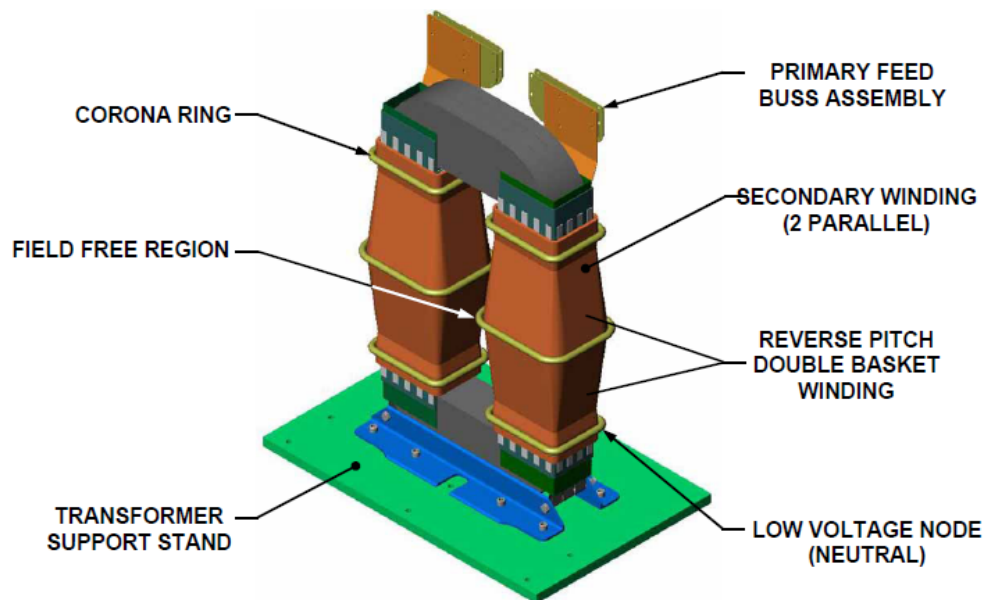


Figure 2.27: C-Core Transformer Design [64]

The design details of the 100 kW, 13.8 kV (primary) / 7.7 kV (secondary) rated transformer will be kept to a minimal. The transformer is to operate with an efficiency greater than 99% with a power factor of 0.93 and weighing 15 lbs. There are 8 primary circuits and 1 secondary all using multi-filar windings. All winding groups are in parallel to one another. On the primary side and secondary side, 12 AWG Litz wire and 22 AWG magnet wire is used, respectively.

The loss model associated with the Litz wire is described by (2.9) and (2.10), [65]. In (2.10), ω is the transformer driving frequency, μ_o is the permeability constant, N is the transformer turns, n is the number of strands, d_c is the diameter of the copper strand, k is a factor accounting for field distribution in multi-winding transformers, ρ_c is the resistivity of copper at 100°C, and b_c is the depth of the core window. Data contributing to core loss or winding loss computation utilized in the optimization algorithm is provided in Table 2.15.

$$P_{Loss,Litz} = F_r I_{ac}^2 R_{dc} \quad (2.9)$$

$$F_r = 1 + \frac{\pi^2 \omega^2 \mu_o^2 N^2 n^2 d_c^6 k}{768 \rho_c^2 b_c^2} \quad (2.10)$$

Table 2.15: Parameters Associated with Core and Winding Loss Calculation

Loss Variable	Value
Steinmetz Coefficient, α	1.695
Steinmetz Coefficient, β	1.967
Steinmetz Coefficient, k	0.787 W/kg
Number of Turns, N	32
Number of Strands, n	420
Diameter of Strand, d_c	0.000102 m
Resistivity of Copper, ρ_c	$23 \times 10^{-9} \Omega\text{-m}$
Transformer Depth, b_c	0.110 m
Litz Wire DC Resistance, R_{dc}	0.323 Ω
Solid Wire DC Resistance, R_{dc}	0.0104 Ω

Table 2.1 provides the geometric relationships associated with the transformer and (2.3) through (2.6) describe the physics associated with the transformer. Equations (2.3) through (2.6) are function of system frequency and core geometry. The system constraints provided in Table 2.16 and latter relationships establish the necessary mathematics to optimize the transformer core, as was demonstrated in the charger application. The Matlab optimization toolbox was utilized to optimize the core volume and the codes that were written are provided in Appendix A. The frequency of the core varied from 1000 Hz to 40 kHz resulting in six sets of results for six distinct frequencies. These results are provided in Table 2.17. A plot of core volume versus frequency is also provided in Figure 2.28.

Table 2.16: System Constraints to Optimize 100 kW Transformer

Loss Variable	Value
B_{Tx}	0.65 T to 0.75 T
T_{max}	150°C
a	0.008 to 0.08 m
b	0.04 to 0.36 m
d	0.008 to 0.08 m
h	0.09 to 0.51 m
N	25 to 32

Table 2.17: Transformer Optimization Results with Varying Frequency

Case Number	1	2	3	4	5	6
B_{Tx} (T)	1.90	0.75	0.75	0.75	0.73	0.67
T_{rise} (°C)	13.63	41.40	59.70	88.53	116.29	134.33
$I_{rms,primary}$	1.25	1.25	1.25	1.25	1.25	1.25
P_{core} (W)	113.24	13.23	26.87	64.77	111.80	150.30
$P_{winding}$ (W)	89.85	89.85	89.85	89.86	89.87	89.88
Powerloss (W)	203.09	103.09	116.72	154.63	201.68	240.18
a (m)	0.080	0.041	0.022	0.011	0.008	0.008
b (m)	0.263	0.040	0.040	0.040	0.040	0.040
d (m)	0.080	0.080	0.075	0.075	0.075	0.075
h (m)	0.146	0.090	0.090	0.090	0.090	0.090
N	32	32	32	32	31	26
V_{core} (m ³)	0.1064	0.0050	0.0032	0.0024	0.0021	0.0021
Frequency (Hz)	1000.00	5000.00	10000.00	20000.00	30000.00	40000.00

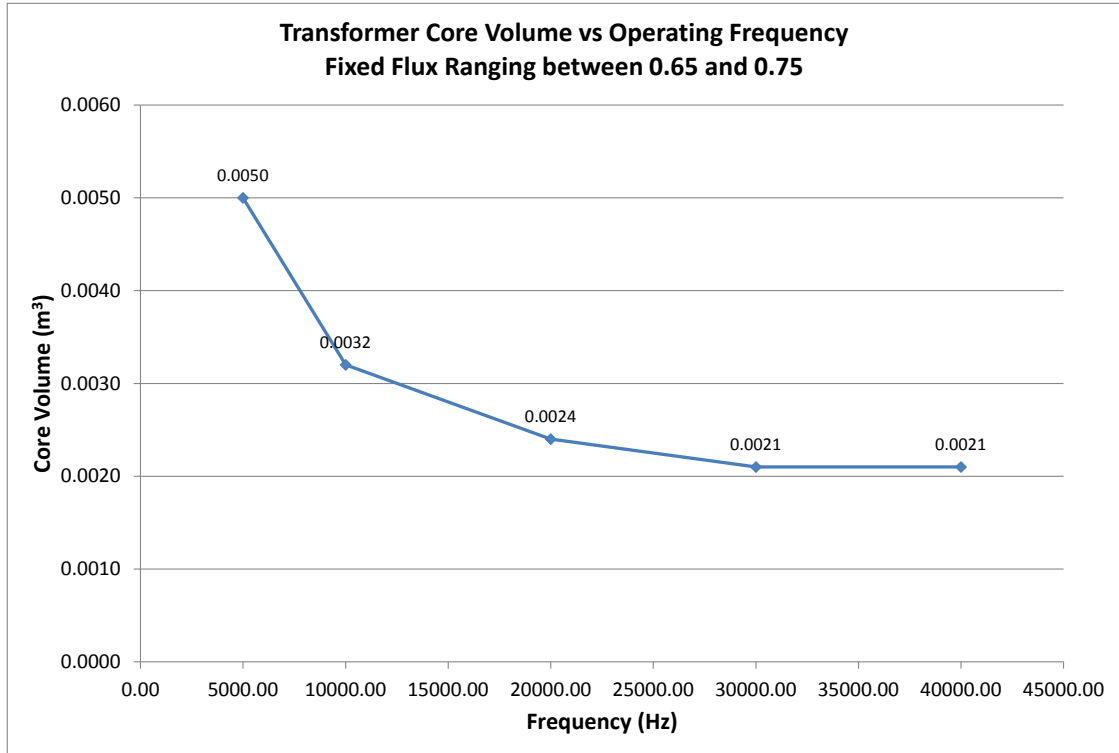


Figure 2.28: Core Volume vs. Frequency for 100 kW Rated Transformer Core

3.0 MODULAR MULTILEVEL CONVERTER BASED HIGH VOLTAGE DC MODELING, COMPONENT SENSITIVITY ANALYSIS, AND SCALING APPROXIMATIONS

There are a number of advantages associated with Voltage-source converter High Voltage DC (VSC-HVDC) technology including: (1) more efficient power transfer over long distances, (2) carrying capacity of up to 2 to 5 times that of an AC line of similar voltage, (3) interconnection of two AC systems, where AC lines would not be possible due to stability problems or both systems having different nominal frequencies (as in Japan), (4) underwater power transfer if cables are longer than 50 km and (5) rapid and accurate power flow control, [66]. For these reasons, it's not surprising to see the number of planned installations taking place in North America and China as shown in Figure 3.1 and Figure 3.2, respectively.

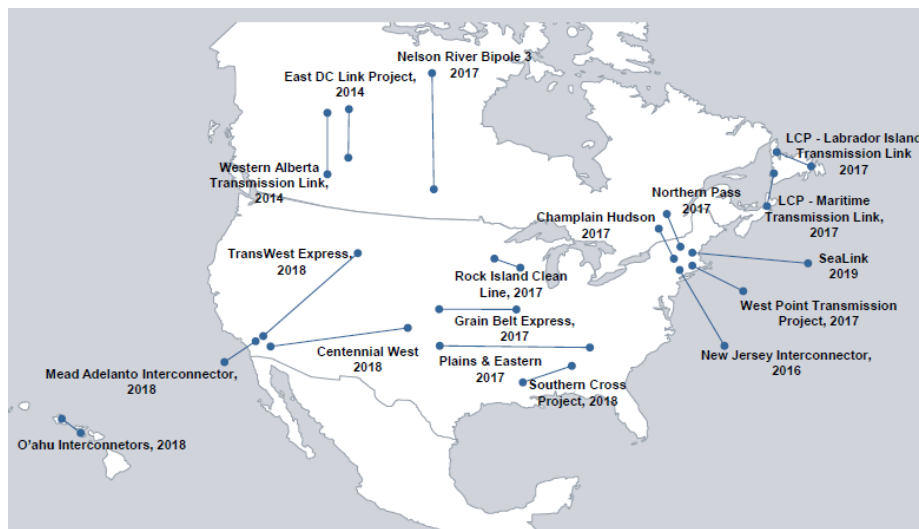


Figure 3.1: Planned HVDC Installations within North America through 2019



Figure 3.2: Planned HVDC Installations in China through 2020 [67]

Multilevel converters are power conversion systems composed of an array of power semiconductors and capacitive voltage sources that, when properly controlled, can generate a multiple-step voltage waveform with variable and controllable frequency, phase and amplitude [68]. The number of levels, n , of a converter is defined as the number of steps or constant voltage values that can be generated by the converter between the output terminal and any internal reference node (the DC-link node) within the converter.

A qualification of a multilevel converter to be referred to as being multilevel is that each phase of the converter has to generate at least three different voltage levels. Figure 3.3 contains three inverter structures. The topology on the far left is an inverter, but it is not a multilevel inverter because the output is that of a classical voltage source inverter. The middle and far right topologies are three and five-level topologies and are classified as multilevel inverters.

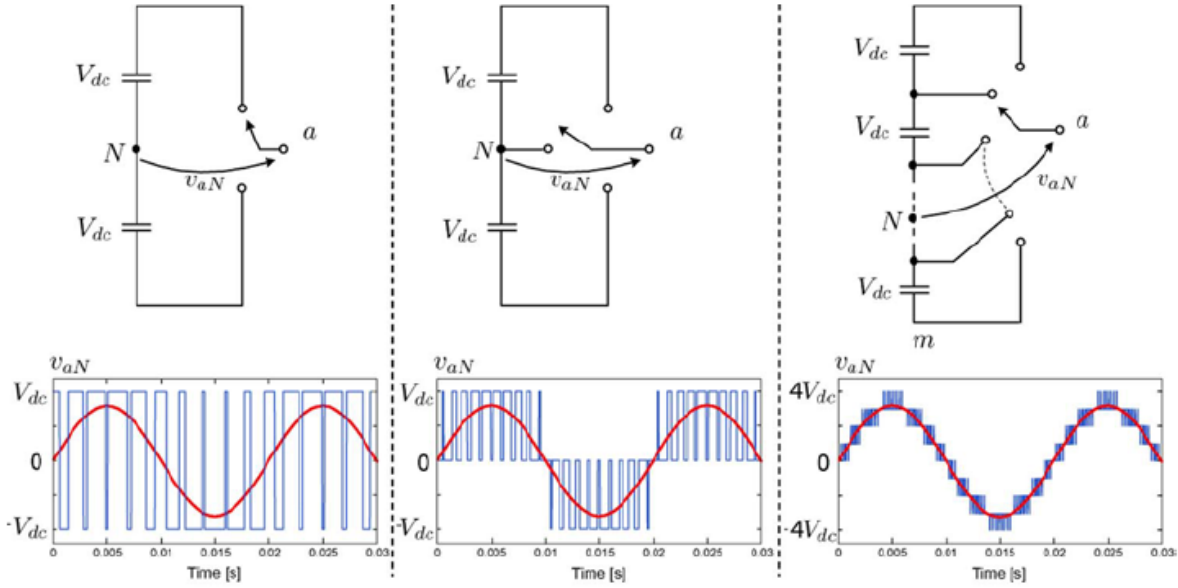


Figure 3.3: Definition of a Multilevel Inverter [68]

The number of levels is always defined by the number found in the line-to-neutral voltage output, which are equally distant from each other. When considering a three-phase system, the levels of one phase are combined with those of the other phases generating $(2n - 1)$ voltage levels in the line-to-line voltage waveform, where n is the phase to neutral voltage levels. The levels that are produced by the inverter add a new degree of freedom, from the control perspective, giving more alternatives to generate the desired output waveform. For this reason, multilevel inverters have the capability of improving power quality resulting in lower voltage distortion and reduced dv/dt [68].

The modular multilevel converter (MMC) topology design for an HVDC converter station is shown in Figure 3.4. The topology boasts a number of advantages over traditional multilevel designs including its high modularity in hardware and software, low generation of harmonics, lower switching frequency of semiconductor devices, easily scalable, and, most importantly, a stronger approximation of a sinusoidal output with increasing submodules [69].

An extensive literature review on the MMC topology, modulation, and control is provided in [70], controller design in [71], and protection needs given a pole-to-pole fault occurrence in [72].

Missing from the literature is a sensitivity analysis of the various components that make up the converter topology and their impacts on system currents and fault currents. The study presented in this chapter focuses on (i) the arm reactor, L_s , sizing and configuration layout (symmetrical vs. asymmetrical) depicted in Figure 3.4, (ii) transformer impedance, and (iii) bypass switch (BPS) speed of response on fault current magnitudes.

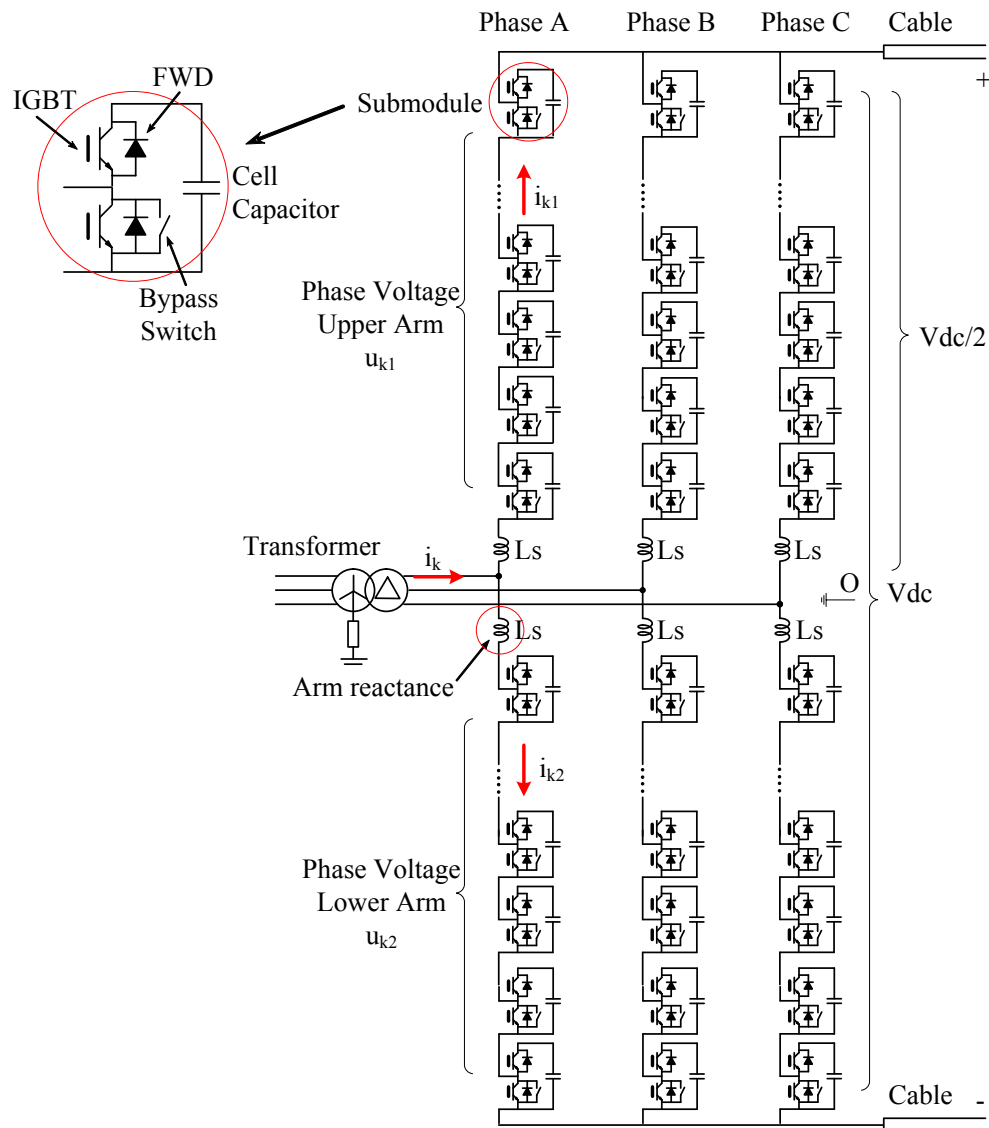


Figure 3.4: Modular Multilevel Converter Topology

Many research teams have also investigated approaches for simulating systems with hundreds of submodules per converter arm, [73],[74]. In this work, 10 submodules per arm are used to perform the majority of the sensitivity analysis. Reasons for this will be stated. A transient analysis of a 6 submodule per arm system with appropriately sized capacitors will be shown to predict circuit phenomena comparable to a 10 submodule per arm design.

Although the system ratings of a HVDC system are on the order of 100's of kilovolts and 100's of megawatts, the presence of the multi-terminal "HVDC" concept is an apparent characteristic of the offshore medium voltage DC microgrid concept as shown in Figure 3.5.

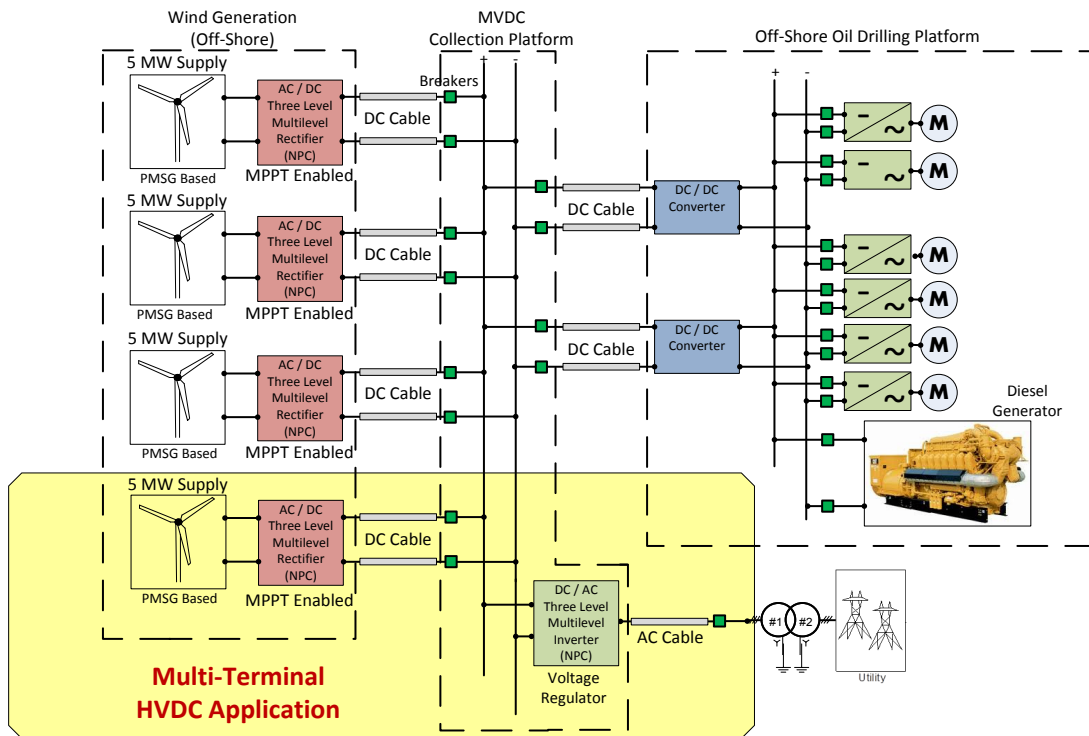


Figure 3.5: Multi-Terminal DC Application within the Offshore DC Microgrid Environment

3.1 MODULAR MULTILEVEL CONVERTER MODELING AND CONTROL

The MMC in Figure 3.4 consists of n series-connected half-bridge submodules on each of the six arms, two arms per phase. For the validated model presented, the number of submodules, or n , is 10. For the entire HVDC system, there are 120 submodules. Each MMC submodule consists of a half bridge cell where its output voltage is either equal to its capacitor voltage or zero depending on the switching states (two states). The two switches per submodule are complimentary in nature. The submodule voltage V_{sm} takes on the value of 0 volts or the voltage on the capacitor depending upon which switch is ON and which is OFF. Figure 3.6 demonstrates this submodule operation. The operation directly depends upon the binary input to the IGBT switches (S_1 and S_2) specific to each submodule. When $V_{sm} = V_C$ the submodule as a whole is considered ON. When $V_{sm} = 0$ the submodule is considered OFF.

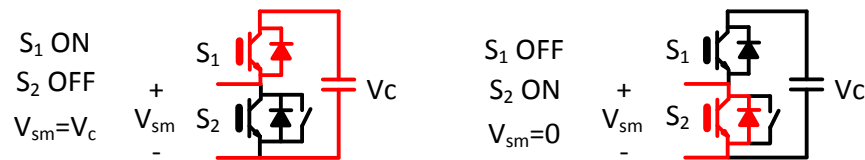


Figure 3.6: Submodule States of the Modular Multilevel Converter

Circuit synthesis of the MMC topology is worthy of noting. Consider a theoretical example system with 6 submodules ($n = 6$), the system is considered a 7 voltage level system ($n + 1$). To achieve Level 7 all upper switches of one arm must be turned ON ($V_{sm} = V_C$) while all lower switches of the same arm must be turned OFF ($V_{sm} = 0$). To achieve Level 6, the first 5 upper switches closest to the arm reactor must be turned ON and one lower switch closest to the arm reactor must be turned ON with all other switches OFF. Figure 3.7 provides a visual aid of these voltage level changes on the Phase A branch of the MMC. This pattern continues until the approximate sinusoidal waveform is established based upon 7 levels.

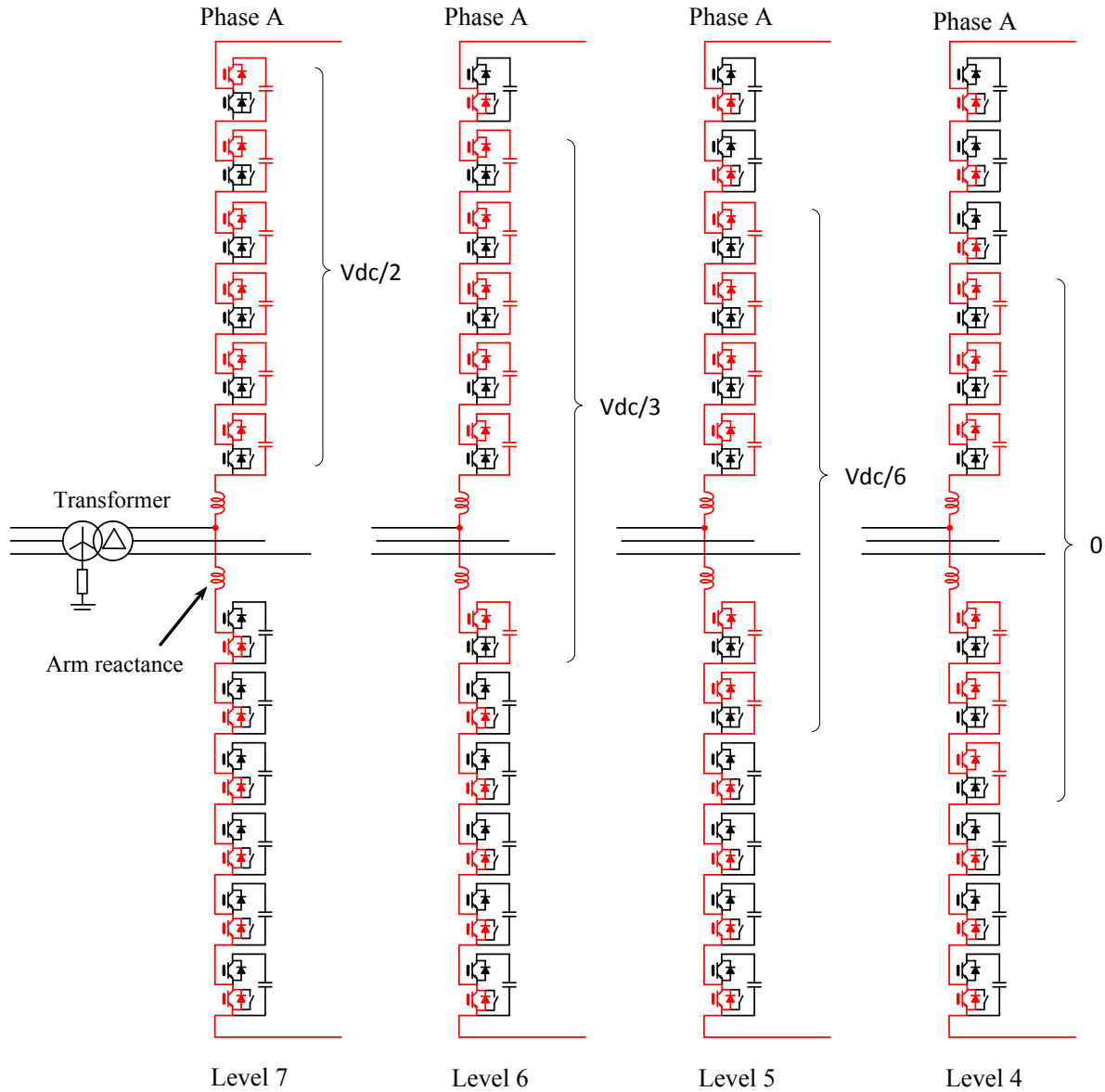


Figure 3.7: Circuit Synthesis of 6 Cell per Arm MMC Converter

3.1.1 Generalized Mathematical Model of the MMC Converter

In Figure 3.4, i_{k1} and i_{k2} represent the upper and lower arm currents of phase- k ($k = a, b, c$) with their sum being composed of the total line current, i_k . Mathematically, this is expressed as (3.1).

$$i_{k1} + i_{k2} = i_k \quad (3.1)$$

Because the capacitors within the top arm and bottom arm are never equally balanced for *all* system conditions, a current difference can exist that circulates through each phase. This current difference is expressed as (3.2). The circulating currents within the three phases must sum to zero as described by (3.3). The circulating currents have no effect on the DC or AC-side of the converter but perform a role in the sizing of the MMC components and capacitor ripple, [71].

$$i_{kz} = \frac{i_{k1} - i_{k2}}{2} \quad (3.2)$$

$$\sum i_{kz} = i_{ka} + i_{kb} + i_{kc} = 0 \quad (3.3)$$

Writing Kirchoff's voltage law for phase- k in Figure 3.4, equations (3.4) and (3.5) can be deduced for the upper and lower converter arms, respectively. Note that point "O" is a fictitious dc-side mid-point associated with v_o . This term can often be neglected if the system is balanced. Also, u_k is the terminal voltage associated with the AC-side of the converter.

$$u_k - \left(v_o + \frac{V_{dc}}{2} - u_{k1} \right) = (2L_s + L_{Tx}) \frac{di_{k1}}{dt} \quad (3.4)$$

$$u_k - \left(v_o - \frac{V_{dc}}{2} + u_{k2} \right) = (2L_s + L_{Tx}) \frac{di_{k2}}{dt} \quad (3.5)$$

The sum of (3.4) and (3.5) divided by 2 leads to (3.6). Equation (3.6) describes the dynamics of the MMC converter on the AC-side for any phase- k , [75], with the transformer inductance, L_{Tx} , assumed to be much larger than the arm inductances. Utilizing Park's transformation, (3.7), the dq -axis relationships can be shown to be (3.8). In (3.8), f can be three phase voltage or current.

$$u_k - \left(\frac{u_{k2} - u_{k1}}{2} + u_o \right) = u_k - (v_k - u_o) = L_{Tx} \frac{di_k}{dt} \quad (3.6)$$

$$T(\theta) = \frac{2}{3} \begin{bmatrix} \sin \theta & \sin(\theta - 2\pi/3) & \sin(\theta + 2\pi/3) \\ \cos \theta & \cos(\theta - 2\pi/3) & \cos(\theta + 2\pi/3) \end{bmatrix} \quad (3.7a)$$

$$\theta = \int_0^t \omega(t) dt \quad (3.7b)$$

$$f_{dqk} = T(\theta) f_{abc} \quad (3.7c)$$

$$\frac{di_d}{dt} = \omega i_q + \frac{1}{L_{Tx}} u_d - \frac{1}{L_{Tx}} v_d \quad (3.8)$$

$$\frac{di_q}{dt} = -\omega i_d + \frac{1}{L_{Tx}} u_q - \frac{1}{L_{Tx}} v_q$$

3.1.2 MMC Converter Inner Loop Controllers: Current Regulators and Tuning

Inner loop current controls are found on the sending end and receiving end converters in the HVDC system. On the sending end converter, the outer loop provides DC voltage regulation. On the receiving end, the outer loop regulates real power flow. The equations expressed by (3.8) are coupled together but can be decoupled through a change of variable. Defining (3.9) and substituting into (3.8), the result can be shown to be (3.10). Equation (3.10) represents two first-order, decoupled subsystems with inputs being i_d and i_q .

$$v_d = u_d + \omega L i_q - \left(k_{pc} (i_{d,ref} - i_d) + k_{ic} \int (i_{d,ref} - i_d) dt \right) \quad (3.9)$$

$$v_q = u_q - \omega L i_d - \left(k_{pc} (i_{q,ref} - i_q) + k_{ic} \int (i_{q,ref} - i_q) dt \right)$$

$$L \frac{di_d}{dt} = k_{pc} (i_{d,ref} - i_d) + k_{ic} \int (i_{d,ref} - i_d) dt \quad (3.10)$$

$$L \frac{di_q}{dt} = k_{pc} (i_{q,ref} - i_q) + k_{ic} \int (i_{q,ref} - i_q) dt$$

Throughout the analysis, it has been assumed that line resistance, R , is small. If R were considered, (3.10) would be appropriately adjusted as shown with (3.11). The closed loop transfer function can be shown to be (3.12) if the gains are chosen to be $k_{pc} = L / \tau$ and $k_{ic} = R / \tau$. The time constant, τ_i , ranges between 1 and 5 milliseconds, [75],[76]. The current regulator for each converter station is found in Figure 3.8.

$$Ri_d + L \frac{di_d}{dt} = k_{pc} (i_{d,ref} - i_d) + k_{ic} \int (i_{d,ref} - i_d) dt \quad (3.11)$$

$$Ri_q + L \frac{di_q}{dt} = k_{pc} (i_{q,ref} - i_q) + k_{ic} \int (i_{q,ref} - i_q) dt$$

$$G(s) = \frac{i_d}{i_{d,ref}} = \frac{1}{1 + \tau_i s} \quad (3.12)$$

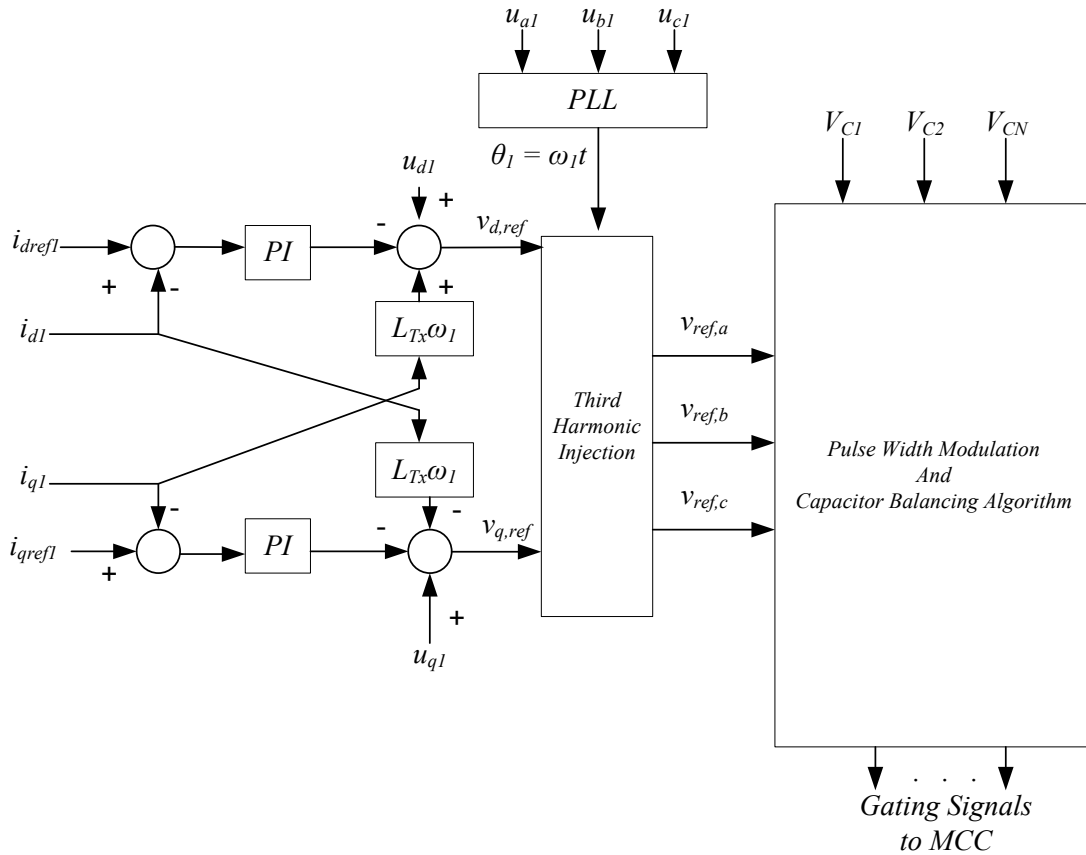


Figure 3.8: Current Controller of MMC Converter

To obtain the desired DC voltage, it may be required to increase the fundamental line-to-line voltage by adding a third harmonic component to the three-phase sinusoidal modulating wave without causing overmodulation. This technique is illustrated in Figure 3.9. Essentially, the peak *fundamental* component can be higher than the peak triangular carrier wave, which boosts the fundamental voltage. At the same time, the *modulated* wave can be kept lower than the carrier signal avoiding problems caused by overmodulation. This technique is referred to as third harmonic injection, [77]. The reference signal generated is a combination of the three-phase sinusoidal modulated wave signal generated by the current controller based upon $v_{d,ref}$ and $v_{q,ref}$ and a signal composed of a third harmonic.

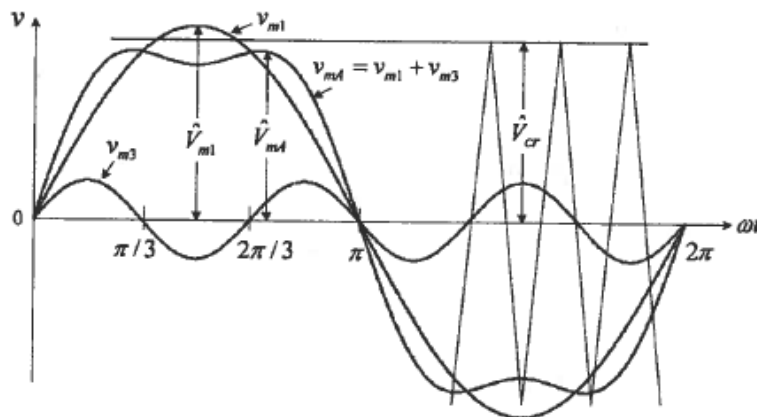


Figure 3.9: Illustration of Modulated Case with Third Harmonic Injection [77]

3.1.3 MMC Converter Outer Loop Controllers: AC and DC Regulators

The outer control loops in the HVDC model include the AC voltage regulator and DC voltage regulator. The adjusted error difference established by the PI controller between the measured line-to-ground voltage on the wye-side of the transformer and reference is regulated to establish $i_{q,ref}$. AC voltage regulation is a feature of both converter stations. The adjusted error difference

established by the PI controller between the measured DC voltage and reference is regulated to establish $i_{d,ref}$ for only one converter station. Mathematically, the latter is described by (3.13). Stronger mathematical details for tuning the DC regulators are provided in [71],[78]. For our application, $k_{pdc} = 10$ and $k_{idc} = 200$.

$$i_{d,ref} = k_{pdc}(V_{d,ref} - V_d) + k_{idc} \int (V_{d,ref} - V_d) dt \quad (3.13)$$

In the monopolar HVDC system, one converter acts as the sending end and the other as the receiving end at any given time. The converter controlled by the DC voltage regulator can be seen as the sending end. The receiving end must then be controlled by a real power regulator, ensuring proper power transfer through the system. The $i_{d,ref}$ command for the receiving end converter is described by (3.14), [79].

$$i_{d,ref} = \frac{P_{ref}}{1.5u_d} \quad (3.14)$$

3.1.4 Capacitor Balancing Algorithm

A problem that arises if left unaddressed is a voltage imbalance between the various capacitors in a given arm. This is due to the different rates at which the capacitors are switched, resulting in more charge being stored in the capacitors that are switched the least frequently. To remedy this problem, an algorithm was implemented based on that demonstrated in [71], which relies on the selection of cells based on capacitor voltage and the direction of current flow. The strategy can be separated into three distinct portions: determination of the number of conducting cell capacitors per arm, sorting of cells based on capacitor voltage, and selection of the conducting cells based on current direction.

3.1.5 System Parameters and Dynamic Performance Evaluation

Megawatt scale HVDC systems require hundreds of submodules per arm. The key challenge for systems of this size is simulating all power semiconductor switching events without exhausting computational resources. A detailed article written by an IEEE task force addresses various average models associated with the MMC, [80]. Since fault studies are critical for evaluating protection design, a detailed switching model of the modular multilevel converter is required. The primary objective from this point forward is to adequately scale the system down from hundreds of submodules per converter arm to about ten submodules per arm. This is done by equating the energies of both systems and scaling the capacitance accordingly.

The ratio of the total energy stored and the rated capacity of the converter should be maintained when converter parameters are scaled. The ratio of the total capacitor energy to the rated capacity of the converter, Φ , is listed as (3.15). With the understanding that the DC voltage is evenly distributed between each submodule, the energy stored per arm is defined by (3.16). Finally, the ratio, Φ , can be shown to be (3.17). Note that the number of arms is 6 for three phase systems and the number of cells per arm is defined as N . Variable S is the system apparent power. Ratio Φ must be maintained while parameters C , N , V_{DC} , and S are varied allowing (3.18) to be written. As long as the large scale system parameters are known, (3.18) can be used to determine the necessary capacitance for an adequately scaled simulation model.

$$\Phi = \frac{(\text{Number of arms})(\text{Number of cells per arm})(\text{Energy stored per arm})}{\text{Rated Capacity of Converter}} \quad (3.15)$$

$$E_{Arm} = \frac{1}{2} C \left(\frac{V_{DC}}{N} \right)^2 \quad (3.16)$$

$$\Phi = \frac{3CV_{DC}^2}{NS} \quad (3.17)$$

$$\Phi = \frac{3C_1V_{DC,1}^2}{N_1S_1} = \frac{3C_2V_{DC,2}^2}{N_2S_2} \quad (3.18)$$

A deeper treatment on energy storage requirements in modular multilevel converters can be found in [81] and similar capacitor sizing analysis as presented here in [73].

In order to select the number of submodules, the following criteria are considered. First, the total harmonic distortion (THD) measured on the wye-side of the transformer must be below the limits set by IEEE 519-1992. If the THD was found to be too high through simulation studies, the number of cells would need to be increased. Second, the capacitor voltage ripple must be less than 10%. The THD voltage distortion limits are found in Figure 3.10. Ten cells per arm was found to be adequate. The HVDC system parameters are found in Table 3.1.

Table 3.1: HVDC System Parameters for a US Market Installation

Parameter	Numerical Quantity
Tx Primary Winding	500 kV - Wye
Tx Secondary Winding	500 kV - Delta
Transformer Reactance	0.25 p.u.
Transformer MVA Rating	1050 MVA
X/R Ratio of Transformer	100
Rated System Capacity	1000 MW
Rated DC Voltage	+/- 500 kV
Nominal Frequency	60 Hz
Switching Frequency	2.5 kHz
Submodule Capacitor	300 μ F
Arm Reactor	0 to 100 mH
Cable Length	800 to 1200 km

Bus Voltage at PCC	Individual Voltage Distortion (%)	Total Voltage Distortion THD (%)
69 kV and below	3.0	5.0
69.001 kV through 161 kV	1.5	2.5
161.001 kV and above	1.0	1.5

NOTE: High-voltage systems can have up to 2.0% THD where the cause is an HVDC terminal that will attenuate by the time it is tapped for a user.

Figure 3.10: THD Voltage Distortion Limits [82]

Figure 3.11 provides a schematic layout of the HVDC model developed in PSCAD/EMTDC. The cable parameters are taken from [83]. System dynamic / steady-state results are provided in Figure 3.12. Although attempts were made to initialize the system at steady-state (charging capacitors with ideal sources, controller reference points, etc.), reviewers will still notice some initial dynamics occurring from 0 to 1.0 seconds into the simulation. PSCAD does not initially compute the steady-state solution but always starts from 0 in its computational procedures. All results from 0 to 1.0 seconds should be ignored. A commanded step change at 2.6 seconds is initiated by the author.

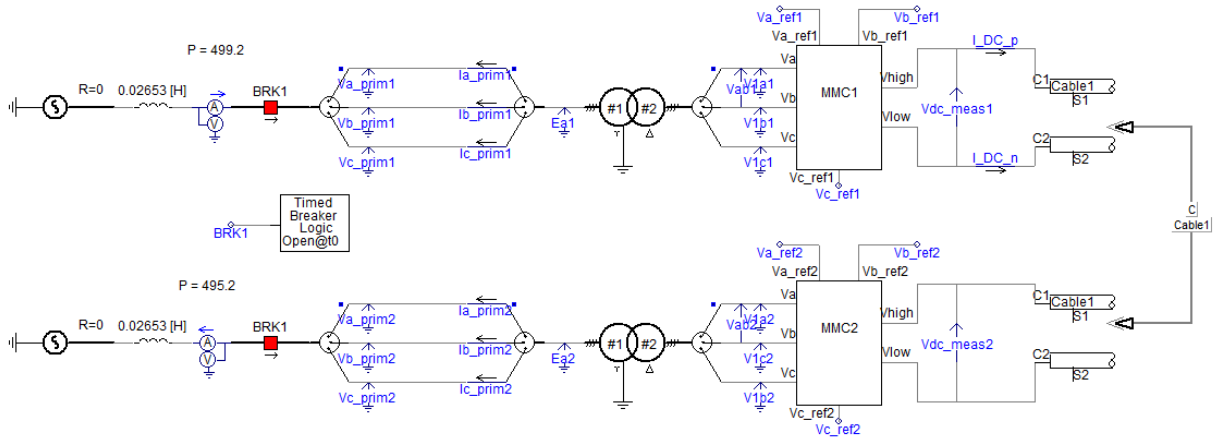
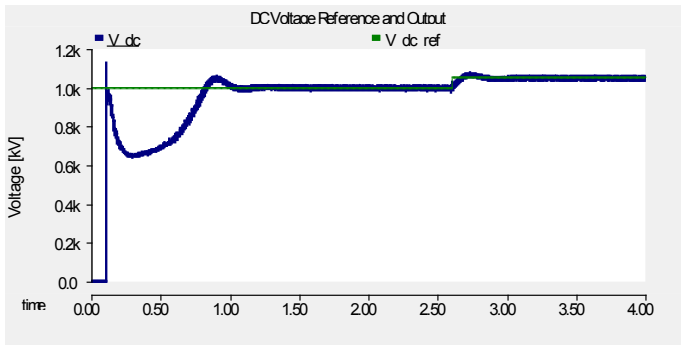


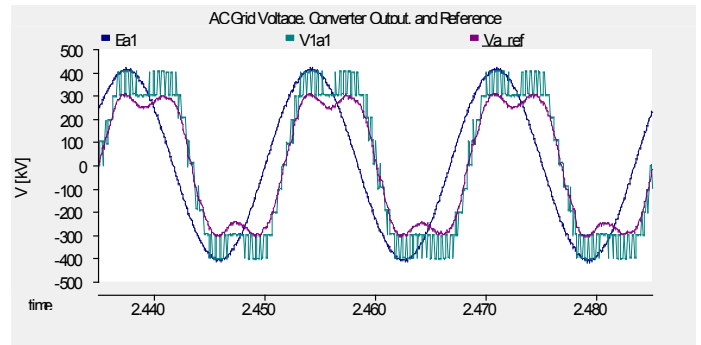
Figure 3.11: Top-Level View of HVDC Model Development in PSCAD

The DC voltage over the course of the simulation can be seen in Figure 3.12(a) and capacitor ripple in Figure 3.12(b). It is clear that after the initial transient, the DC voltage settles near the demanded 1000 kV value and, after a reference change, to 1050 kV at 2.6 seconds. The DC steady-state error was calculated to be 0.6% and calculation of the voltage fluctuation on the capacitors was found to be 1.39%. Note that both quantities are well below their specified limits mentioned earlier.

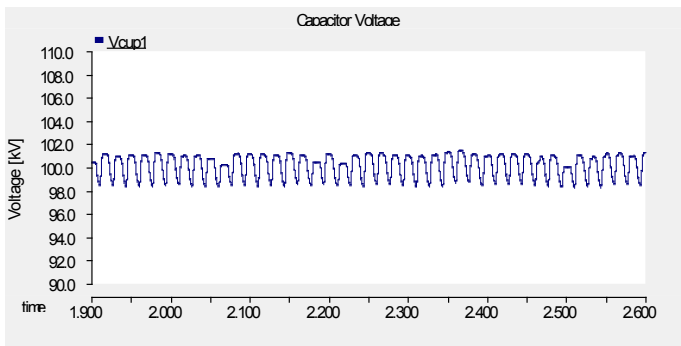
Figure 3.12(c) shows that the HVDC system model is working satisfactorily – all circuitry, capacitor balancing algorithm, and system controls. Note that the slight phase shift between the grid side and the Δ -side is expected due to the Y- Δ transformer (30 degree phase shift). According to IEEE 519-1992, the total harmonic distortion (THD) at the point of interconnection can be no more than 1.5%. Utilizing 10 cells per arm for the base case, the grid side AC voltage THD was found to be 0.49%. The final portion of this analysis presents the power flow characteristics. The steady-state DC power flow is 1000 MW as expected and shown in Figure 3.12(d).



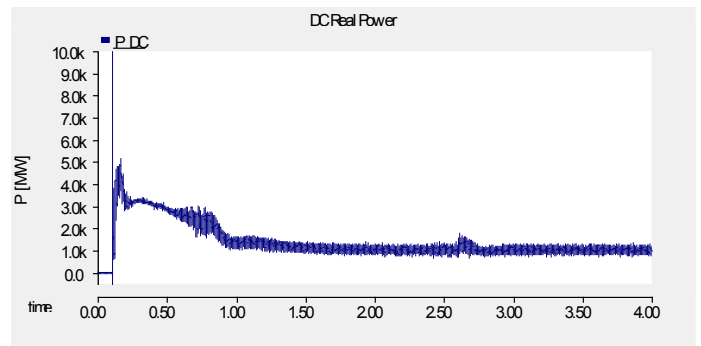
(a)



(c)



(b)



(d)

Figure 3.12: HVDC Model Waveforms: (a) DC voltage (b) Capacitor Voltage Ripple, (c) Δ -side AC Voltage / Y-Side AC Voltage / Reference Signal and (d) Power Flow

3.2 MODULAR MULTILEVEL CONVERTER COMPONENT SENSITIVITY ANALYSIS ON FAULT CURRENTS

When considering system faults, the pole-to-ground DC-link fault is more likely compared to the pole-to-pole DC-link fault. However, the pole-to-pole fault is more critical in the symmetrical monopole HVDC configuration and needs evaluated for worst case peak currents, [72]. The pole-to-pole fault is located in Figure 3.13. The important features of Figure 3.13 for the explanation to follow include the bypass switch (BPS) and AC circuit breaker – the two mechanisms of mechanical protection in the circuit. Some details of the analysis are purposely omitted with only observations noted.

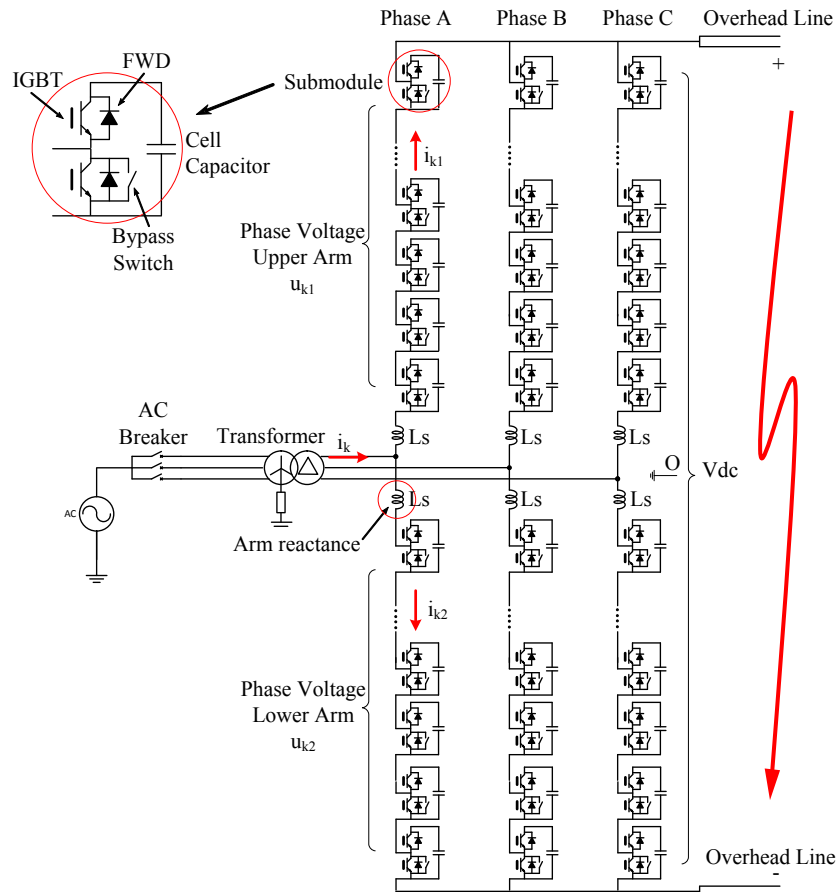


Figure 3.13: Pole-to-Pole Fault in a Monopolar HVDC System

When a fault is identified in the system, the AC circuit breaker (ACCB) and BPS are introduced into the circuit and converter controllers do not regulate any longer but gate block. Assume the HVDC system is operating at steady-state and suddenly a pole-to-pole fault occurs. The first action of the controllers is to gate block (microsecond time scale), the BPS close on all submodules to protect the semiconductors (millisecond time scale), and finally the ACCB open on both ends of the system isolating the unit from the rest of the grid. For pole-to-ground faults, the bypass switches are not needed since a natural ground occurs for current to flow towards. For the pole-to-pole fault, bypass switches are necessary because the current is continuously circulating through the unit. The component operating sequences are provided in Table 3.2.

Table 3.2: Circuit Breaker and BPS Operating Sequence after Fault Occurs

Fault	Voltage Source Converter 1			Voltage Source Converter 2		
	ACCB	BPS	Controller	ACCB	BPS	Controller
OFF	Close	Open	DC Regulation	Close	Open	Power Regulation
ON	Close	Open	DC Regulation	Close	Open	Power Regulation
ON	Close	Open	GB	Close	Open	GB
ON	Close	Close	GB	Close	Close	GB
ON	Open	Close	GB	Open	Close	GB
ON	Open	Close	GB	Open	Close	GB

The analysis presented from this point forward shows the sensitivity of transformer reactance, BPS speed response, and lumped inductance (arm and DC line reactance) on fault current magnitudes. A 25% transformer reactance, 0 mH DC line reactance, 10% arm reactance along the lower arms (asymmetric configuration), and 10 ms BPS operation speed is utilized to establish the base case DC peak current of 13.4 kA. The overhead line parameters associated with the study are taken from [84] and an electro-geometric model was built within PSCAD. Only pole-to-pole fault studies are evaluated and peak DC currents emphasized. Other variables

often considered by manufacturers include (1) the time to reach the maximum peak current, (2) rate of change in the current, (3) peak currents through the submodule diodes, and (4) I^2T for the diodes.

3.2.1 Transformer Impedance Impact on Peak DC Current

The transformer reactance was varied from 10% to 25% per unit impedance with increments of 5% resulting in four cases. The peak DC currents for the four scenarios evaluated are provided in Figure 3.14. From experience, transformers within the United States market typically are designed for 25% impedance. These results support this design criteria. Peak DC current when pole-to-pole faults are applied are quite sensitive to the transformer impedance rating.

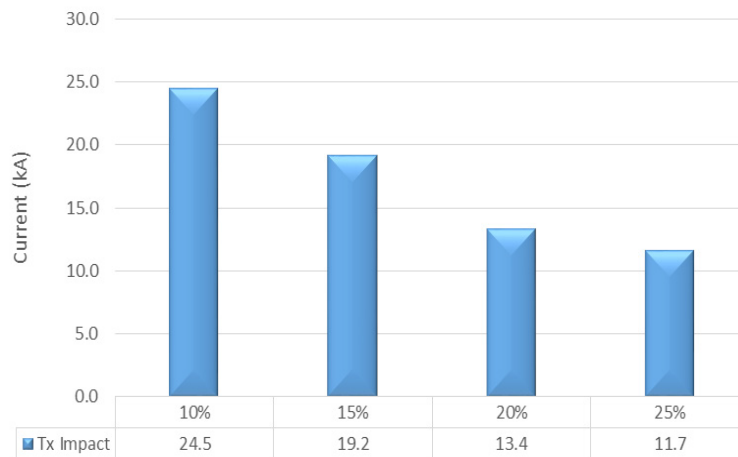


Figure 3.14: Transformer Reactance Impact on Peak DC Current

3.2.2 Bypass Switch Impact on Peak DC Current

The BPS speed of operation was varied from 5 ms to 11 ms. The peak DC currents for the seven scenarios evaluated are provided in Figure 3.15. Intuitively, these results make sense. The longer the BPS is inactive in the circuit, the more time the DC current has to reach its peak

potential. The purpose of the BPS is to protect the submodules by introducing an alternative path (short circuit) for the current to flow. The faster the BPS can be introduced into the network, the quicker the transient current can be suppressed resulting in a faster decay towards zero from which system restart could then be achieved. Peak DC current when pole-to-pole faults are applied are quite sensitive to BPS operation speed.

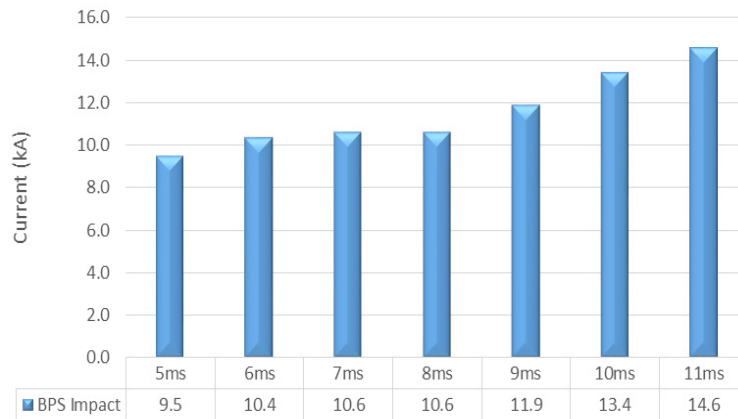


Figure 3.15: Bypass Switch Speed Impact on Peak DC Current

3.2.3 Reactor Impact on Peak DC Current

There are two reactor sets introduced into the MMC HVDC converter design – arm reactors placed either in an asymmetrical configuration (only along the bottom arm of each phase) or symmetrical configuration (both upper and lower arm placement) and the DC line reactors. Figure 3.16 provides the sensitivity results on the DC positive rail current if the DC line reactor varies from 0 to 100 mH. Similarly, Figure 3.17 provides the peak DC current results if the arm reactor varies from 5% to 10% per unit impedance. Interestingly, the peak DC currents are insensitive to changes in arm reactor size. Before the onset of the study, it is well known that DC line reactors contribute to fault current control – hence the name current limiting reactors (CLR) – and was conducted for completeness.

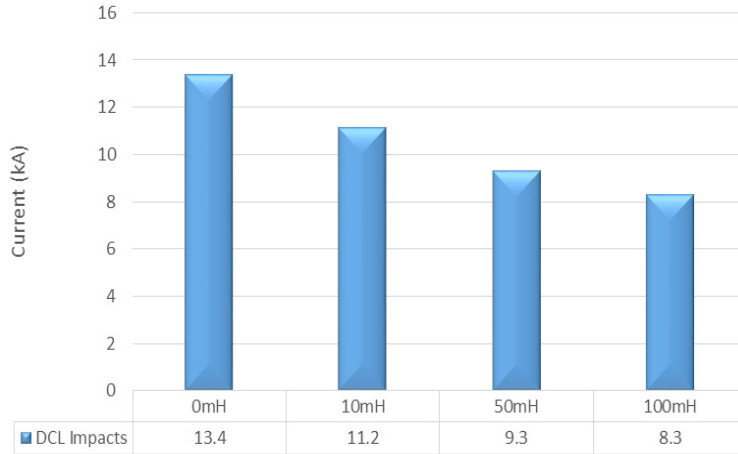


Figure 3.16: DC Line Inductor Impacts on Peak DC Current

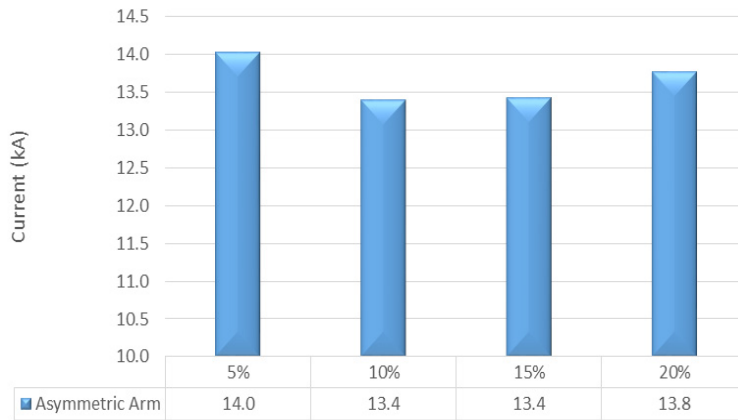


Figure 3.17: Asymmetrical Arm Reactor Impact on Peak DC Current

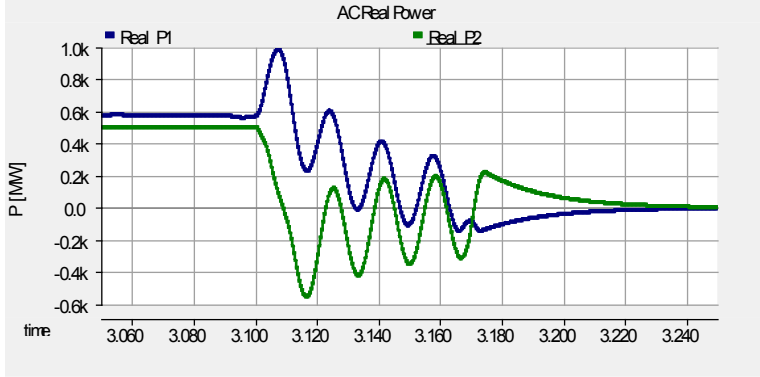
Other exhaustive system studies on circuit component sensitivities can be evaluated including impacts of increasing overhead line length, system strength, and many others. These were conducted but only the most dramatic results from particular system components have been shown. Although not related to high power design (utility scale), a nice study was conducted in [85] showing the fault current dependence on cable length, chosen bus voltage, and number of interconnected sources within a meshed DC system.

3.3 ELECTRIC CHARACTERISTIC PREDICTION WITH REDUCED SUBMODULE COUNT IN CONVERTER ARMS

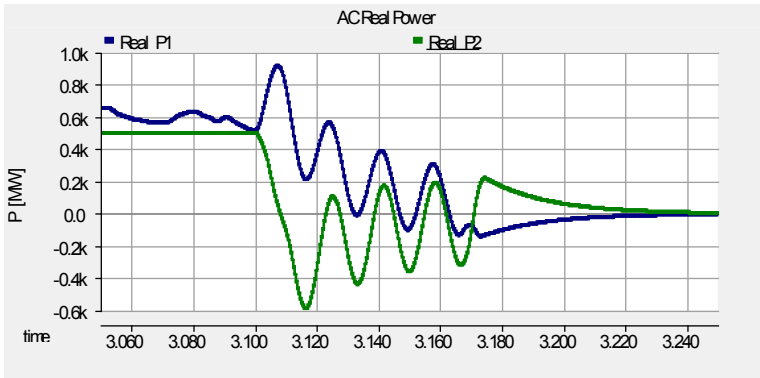
Utilizing the case with 10% reactor sizing with asymmetrical arm configuration, no DC line reactors, and a line-to-line fault applied, the task at hand is to draw comparisons of peak DC current transients and HVDC power flow dynamics for both a 6 and a 10 cell per arm system. Indirectly, the capacitor value also changes with the number of cells utilized per arm.

Recall that the THD level on the wye-side of the transformer is of greatest importance – remaining below the set value provided by IEEE 519-1992 while minimizing submodules but predicting peak currents adequately. For the 6 cell and 10 cell system, the submodule capacitance is 180uF and 300uF, respectively. The arm reactor is the same in both cases. A line-to-line fault occurs at 3.1 seconds and the sequence of circuit operations described by Table 3.2 occurs throughout the simulation time. The solution time step for both simulations is set to 10 microseconds and channel plot time to 25 microseconds.

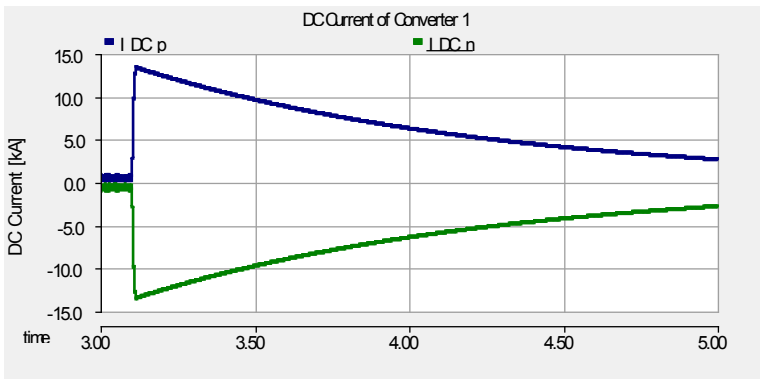
Comparing the peak DC fault current flowing through the HVDC overhead line model and power flow dynamics, the 6 cell system strongly predicts the same transient behavior in comparison to the 10 cell system. The 6 cell system also serves as a suitable approximation for the system dynamics but the THD levels are higher than the maximums set by IEEE standards.



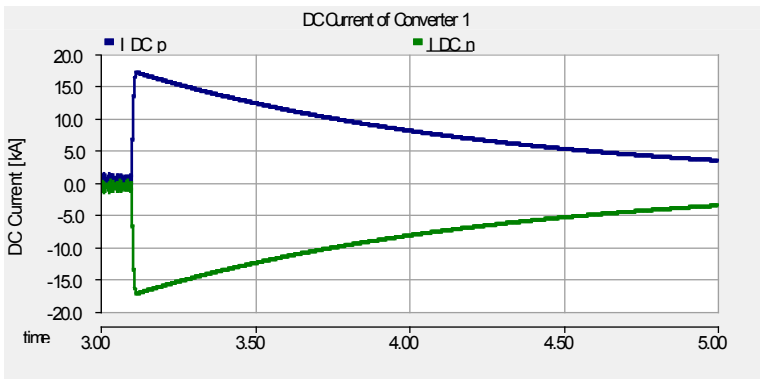
10 Cell Per Arm Power Flow Dynamics after Fault



6 Cell Per Arm Power Flow Dynamics after Fault



10 Cell Per Arm DC Voltage Decay after Fault



6 Cell Per Arm DC Voltage Decay after Fault

Figure 3.18: Comparison between Electrical Characteristics for 6 and 10 Cell MMC Converter Systems

4.0 MODEL REFERENCE CONTROLLER DESIGN FOR STABILIZING CONSTANT POWER LOADS IN A MEDIUM VOLTAGE DC MICROGRID

Constant power loads (CPL) exhibit negative incremental impedance characteristics contributing to destabilizing effects in power systems [86]. Power electronic converters and motor drives, when tightly regulated, behave as CPLs. For the case of a motor drive, the inverter drives the motor and tightly regulates the speed to achieve constant speed. Assuming a linear relationship between torque and speed, motor torque will remain constant resulting in constant power consumption by the motor. For CPLs, the instantaneous value of impedance is positive ($V/I > 0$), but the incremental impedance is always negative ($dV/dI < 0$). In the literature, the latter is referred to as negative incremental impedance instability [86],[87],[88].

As pointed out in [87], CPL induced instability or oscillations can be resolved by modifying the DC system's hardware structure, by adding resistors, filters, or energy storage elements, but approaches based on feedback control can offer more practical and efficient solutions. In addition to linear controllers featured by simple architectures and designs, many research teams have chosen nonlinear based control approaches to stabilize CPL scenarios to avoid limitations of linearization (operating closely to the system equilibrium point) and large-signal stability is guaranteed [88]. The primary nonlinear approaches include the use of Lyapunov-based design, hysteresis control, nonlinear passivity-based techniques, and boundary control. However, some of the disadvantages of these techniques include the use of

proportional-derivative (PD) controllers which can be sensitive to noise, current and voltage transient overshoots, and difficulty with implementation.

In this chapter, a model reference controller is proposed for stabilizing CPLs. Model reference control has the advantages of allowing the designer to select the pole and zero placements to adequately tune system behavior. The controlled closed-loop system with naturally unstable plant replicates the dynamic system behavior of the designed reference model to ensure stable output. Moreover, this control architecture can be readily upgraded to include adaptation capabilities following model reference adaptive control (MRAC) design.

This chapter provides a review of the fundamentals of bidirectional DC/DC converters and develops the plant model to be controlled through model reference control approaches. An in-depth treatment of how model reference control techniques can be used to stabilize CPLs through the design of a controller compensator for a third-order plant model will be analytically shown. Finally, a demonstration of the closed loop response showing compensator performance through a Matlab/Simulink simulation using the proposed control scheme will be provided. A diagram emphasizing the focus of this chapter is highlighted in Figure 4.1.

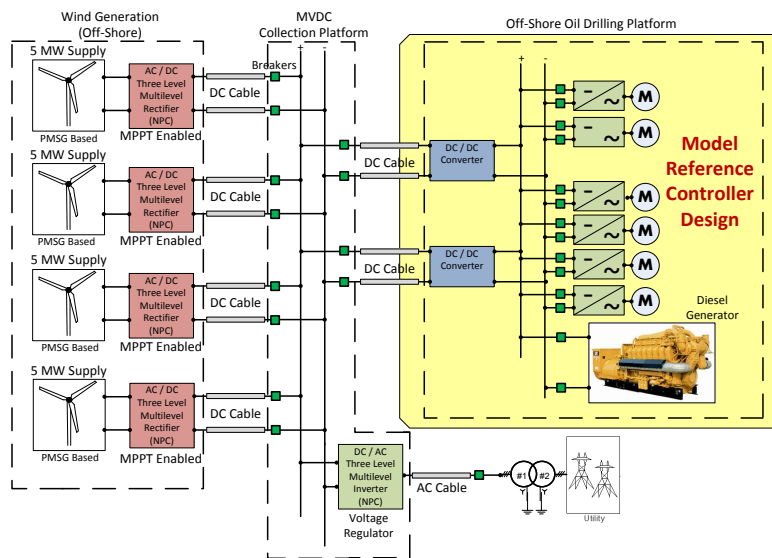


Figure 4.1: Model Reference Controller Design Application within the Offshore DC Microgrid Environment

4.1 FUNDAMENTALS OF BIDIRECTIONAL DC/DC CONVERTERS

The dual active bridge DC/DC converter shown in Figure 4.2 was first proposed in [42]. The converter topology has grown in popularity as demand in bidirectional power flow capability has increased in research pursuits such as battery charger applications for electric vehicles. Research teams have devised new control techniques for improving system efficiencies [49] and using state of the art semiconductor devices for high frequency operation of the topology [89]. Research efforts have been primarily centered upon low power applications. In this work, we utilize the dual active bridge as an interface between two medium voltage (kV) DC busses.

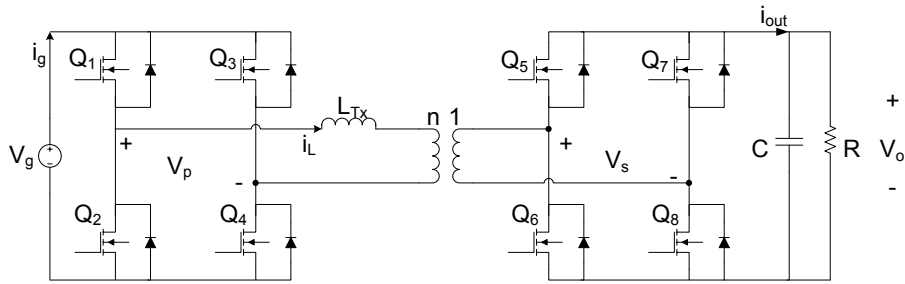
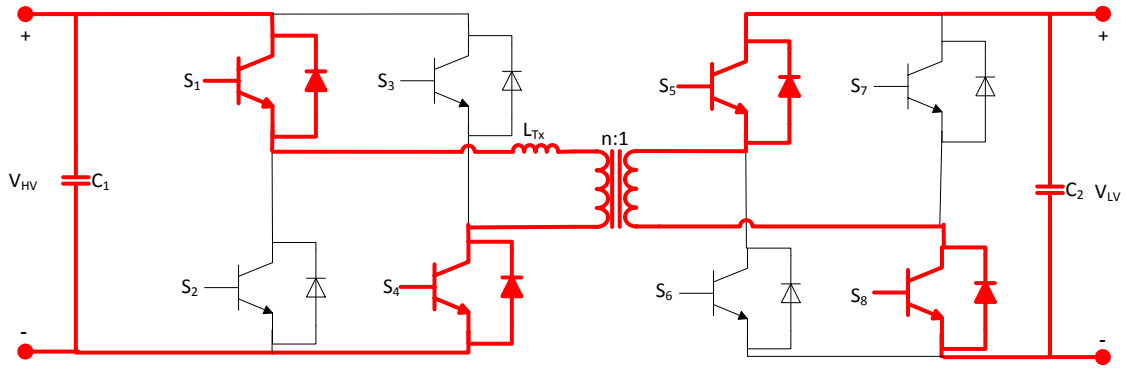


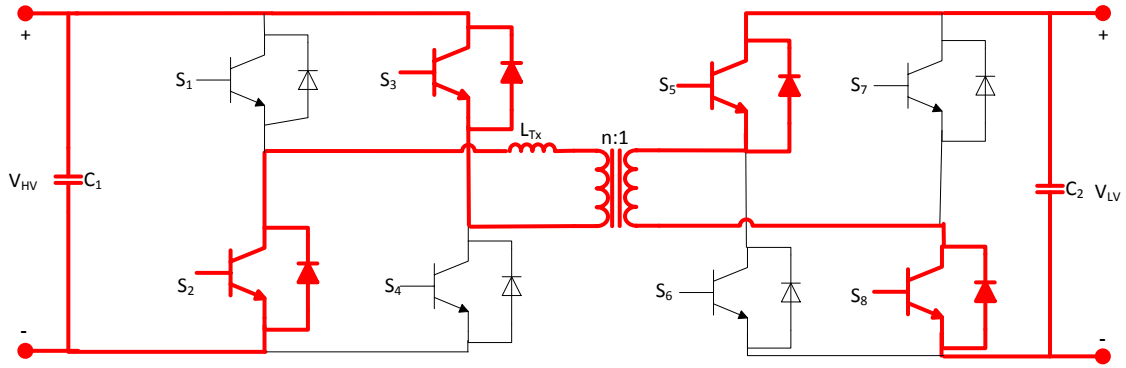
Figure 4.2: Dual Active Bridge Bidirectional DC/DC Converter

The current traces and operating waveforms of the dual active bridge DC/DC converter are provided in Figure 4.3 and Figure 4.4, respectively. Plots correspond to the primary side voltage, V_p , secondary side voltage, V_s , inductor current, I_L , and input current, I_g . The active devices within the circuit for each subinterval are labeled according to the convention found in Figure 4.2. The most notable characteristic is the phase delay, ϕ , between both bridges, which controls the allowable power flow in the circuit. The relationship between the phase delay and duty cycle, d_h , is described by (4.1). Note that T_s is the switching period.

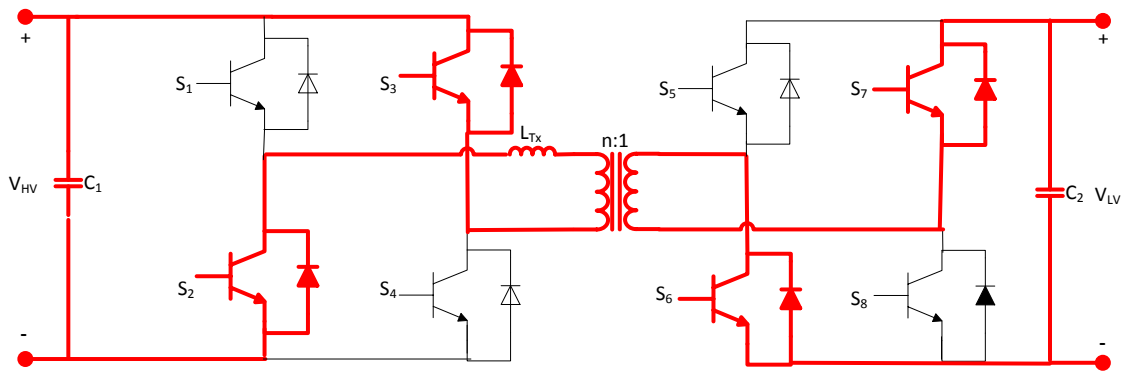
$$\phi = \frac{d_h T_s}{2} \quad (4.1)$$



(A) $V_p = V_g$; $V_s = V$



(B) $V_p = -V_g$; $V_s = V$



(C) $V_p = -V_g$; $V_s = -V$

Figure 4.3: Current Traces of DAB DC/DC Converter

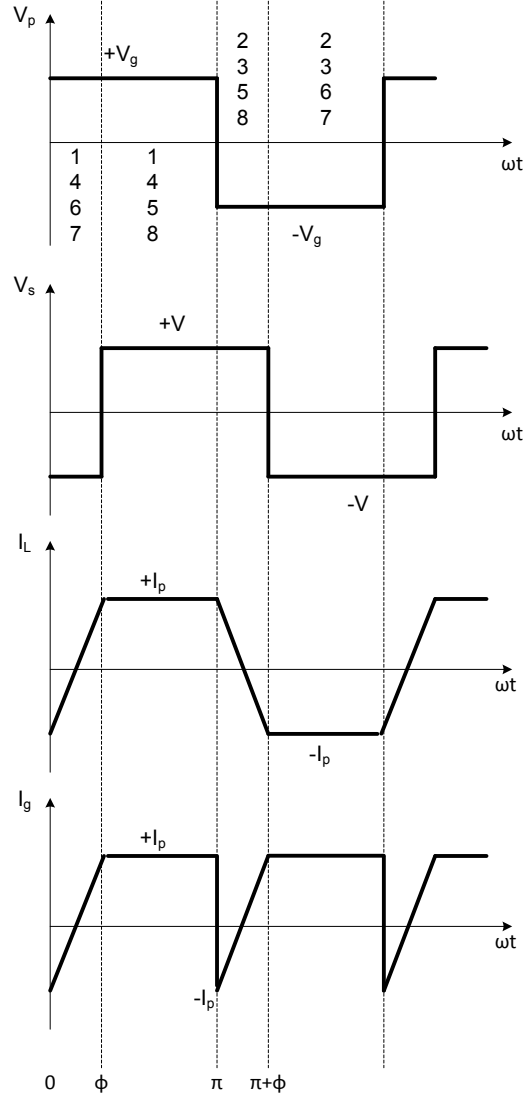


Figure 4.4: Operating Waveforms of the Dual Active Bridge DC/DC Converter

4.1.1 Converter Dynamics

The average inductor current can be described by (4.2), [90]. The output voltage as a function of the converter duty cycle and output impedance, Z_{out} , of the converter is described by (4.3). If we apply a small perturbation to both the output voltage, \hat{V} , and duty cycle, \hat{d}_h , of (4.3) and linearize, the linear small signal transfer function between the output voltage and duty cycle can

be shown to be (4.4) where K_{DC} denotes $nV_{DC}T_s(1-2d_h)/(2L_{Tx})$. Equation (4.4) is the plant that will be shown to be naturally unstable.

$$I_{avg} = \frac{nV_{DC}T_s}{2L_{Tx}} d_h(1-d_h) \quad (4.2)$$

$$V = I_{avg}Z_{out} = \frac{nV_{DC}T_s}{2L_{Tx}} d_h(1-d_h)Z_{out} \quad (4.3)$$

$$\frac{\hat{V}}{\hat{d}_h} = \frac{nV_{DC}T_s}{2L_{Tx}}(1-2d_h)Z_{out} \equiv K_{DC}Z_{out} \quad (4.4)$$

4.1.2 System Description with Constant Power Load Assumption

Figure 4.5 is a key segment of the overall power system found in Figure 4.1 and will be studied thoroughly in this work. Starting from left to right, the medium voltage DC bus has been replaced with an ideal voltage source (assuming a well regulated DC bus) and a bidirectional DC/DC converter interfaces the medium voltage DC bus with the induction motor inverter. A 7.2 kV rated, single core, XLPE insulated, PVC sheathed, unarmoured cable bridges the power converters and is modeled as a coupled pi circuit as shown [91].

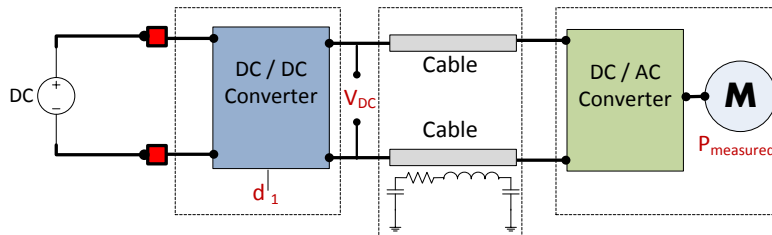


Figure 4.5: System Model for Studying CPL Scenario

As described in [92], a common constant power load is a DC/AC inverter that drives an electric motor and tightly regulates the speed of the machine to be constant. Assuming a linear relationship between torque and speed, for every speed there is one and only one torque. For

constant speed, torque will be constant as well as power. Therefore, the motor/inverter combination presents a constant power load characteristic to the DC/DC converter. With the understanding that the average current of the bidirectional DC/DC converter can be described by (4.2) and assuming that the DC/AC inverter and motor can be approximately represented as a constant power load (whose time constant is much smaller than that of the DC/DC converter), Figure 4.5 can be simplified to Figure 4.6.

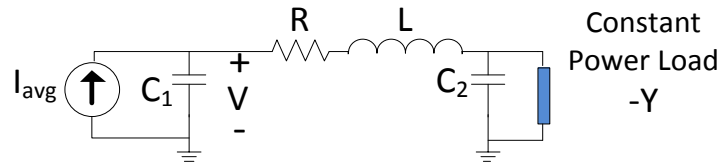


Figure 4.6: Simplified System Model for Evaluating CPL Scenario (Third Order System)

The output impedance associated with the simplified system model is described by (4.5) where the circuit parameters are defined in Figure 4.6. The pole-zero placements of the naturally unstable transfer function is found in Figure 4.7. For higher power applications, the poles and zeros shift further into the unstable region of the complex plane. Line parameters used for this observation are provided in Table 4.1.

$$Z_{out} = \frac{LC_2 Y s^2 + (RC_2 Y - L)s + (Y - R)}{(LC_1 C_2 Y)s^3 + (RC_1 C_2 Y - LC_1)s^2 + (C_1 Y - RC_1 + C_2 Y)s - 1} \quad (4.5)$$

Table 4.1: Cable Parameters

Parameter	Numerical Quantity
Line Resistance, R	0.0176 Ω /km
Line Inductance, L	0.248 mH/km
Line Capacitance, $2C_{1,2}$	0.923 μ F/km
Cable Distance	0.005 km (16 feet)

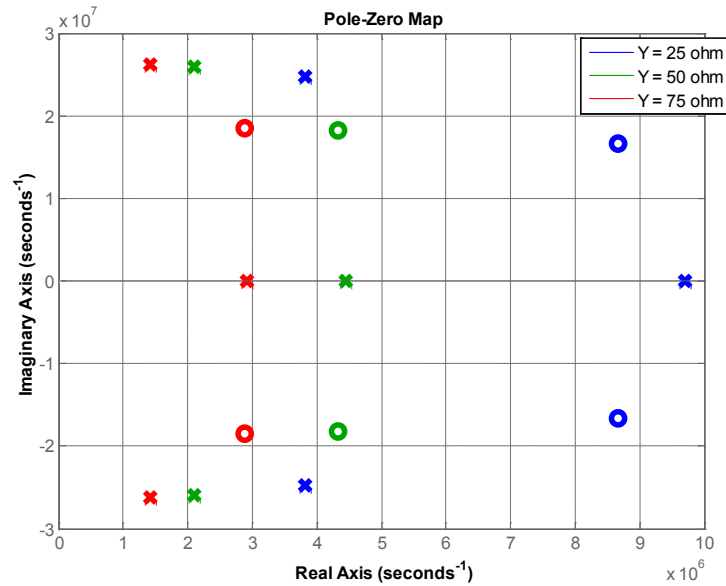


Figure 4.7: Pole-zero plot associated with unstable output impedance for various constant power loads

4.2 STABILITY ASSESSMENTS USING MODEL REFERENCE CONTROL THEORY

Based on the previous analysis, the task at hand is to design a controller compensator. Power system engineers are accustomed to using some form of PID controller. The integral (I) control is often used to eliminate steady-state error, while derivative (D) control to improve stability and system damping. This section will first show that the proportional derivative (PD) controller cannot achieve satisfactory steady-state performance and stable response at the same time. The principles of model reference control (MRC) are used to stabilize the CPL scenario.

4.2.1 Attempt to Stabilize Plant with PD Controller

To appreciate the damping control effect of a PD controller, we first consider a simplified second-order model of the plant. Because the distance between the DC/DC converter and motor

inverter is short (application being on an offshore platform), the cable can be approximated with a line resistance and inductance in series (Figure 4.8), [93]. Noting the output capacitor of the dual active bridge DC/DC converter, the system model can be approximated as a second-order system with output impedance transfer function described by (4.6), where $Z_{2,out}$ represents the simplified second-order output impedance, the meaning of K_{DC} is given in (4.4), and the other circuit parameters are defined in Figure 4.6. The line resistance is assumed to be small.

$$\frac{\hat{V}}{\hat{d}_h} = K_{DC} Z_{2,out}(s) = K_{DC} \frac{Ls - Y}{LCs^2 - YCs + 1} \quad (4.6)$$

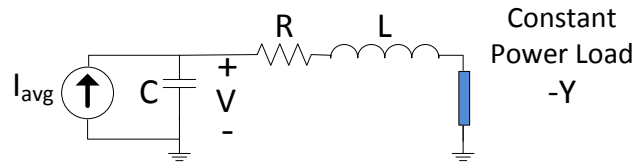


Figure 4.8: Second-order System Model of a Simplified Motor Drive Model (Second-Order)

The first choice of controller compensator would be the PD controller because this type of compensation provides a phase lead, which creates a stabilizing effect. Generally for a second-order plant, the derivative (D) part of the PD control can act on the damping component of the closed-loop system and thus stabilize the plant. Figure 4.9 shows a diagram with PD control in the closed loop.

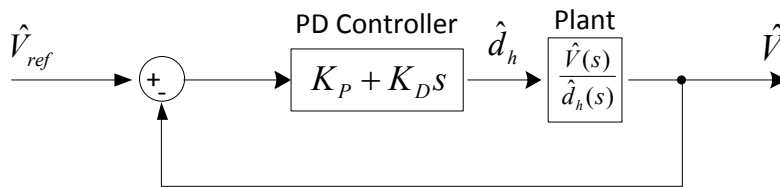


Figure 4.9: PD Control of Plant

The closed-loop transfer function of the system in Figure 4.9 can be written as (4.8) where a standard PD compensator of the form $K_P + K_D s$ is used to control the plant in (4.6), and K_P and K_D are the proportional and derivative gains, respectively. A couple of observations can be made on the performance of the PD control. First, under the premise of stability, from (4.9), as K_P increases the damping ratio, ζ , increases. As K_D increases, the natural frequency, ω_n , and damping ratio decrease. This behavior of PD control is different from the conventional effect of PD control when applied to a stable and minimum-phase plant where, for example, bigger K_D and K_P usually achieve larger damping ratio and higher natural frequency, respectively. From (4.10), as K_P increases the natural frequency decreases.

The DC gain of the system is listed as (4.11a). In order for the closed-loop system to be stable, both (4.9) and (4.10) need to be greater than 0, i.e., $K_{DC}K_P L - K_{DC}K_D Y - YC > 0$ and $K_{DC}K_P Y < 1$. However, as $K_{DC}K_P Y < 1$, the system's DC gain is always negative. Therefore, the PD controller here cannot achieve satisfactory steady-state performance while maintaining system stability.

$$\frac{\hat{V}(s)}{\hat{V}_{ref}(s)} = \frac{K_{DC}(K_P + K_D s)(Ls - Y)}{(K_{DC}K_D L + LC)s^2 + (K_{DC}K_P L - K_{DC}K_D Y - YC)s + (1 - K_{DC}K_P Y)} \quad (4.8)$$

$$2\zeta\omega_n = \frac{K_{DC}K_P L - K_{DC}K_D Y - YC}{K_{DC}K_D L + LC} \quad (4.9)$$

$$\omega_n^2 = \frac{1 - K_{DC}K_P Y}{K_{DC}K_D L + LC} \quad (4.10)$$

$$DC_{Gain} = \frac{-K_{DC}K_P Y}{1 - K_{DC}K_P Y} \quad (4.11a)$$

We now consider the third-order model of the plant including the line resistance R and an added capacitor C_2 in parallel with the constant power load. It can be derived that the DC gain of the closed-loop system with PD control equals (4.11b).

$$DC_{Gain} = \frac{K_{DC}K_p(Y - R)}{K_{DC}K_p(Y - R) - 1} \quad (4.11b)$$

Under the premise of stability (here a necessary condition for stability is $K_{DC}K_p(Y - R) > 1$), the system's DC gain is always greater than 1. Therefore, the PD controller still cannot achieve satisfactory steady-state performance even with a capacitor added in parallel to the constant power load.

4.2.2 Model Reference Control Definitions and Assumptions

Thus far, it has been shown that the plant cannot be controlled satisfactorily using a traditional PD controller. Our objective is to design a controller such that the behavior of the controlled plant remains close to the behavior of a desirable reference model, $M(s)$, despite uncertainties or variations in the plant parameters. Before establishing the mathematical details, a few assumptions need to be described based upon the plant and reference model. First, the plant is a single-input, single-output, linear time-invariant system described by (4.12). Note that \hat{n}_p and \hat{d}_p are monic polynomials of order m and n , respectively. The plant is strictly proper, minimum phase, and not assumed to be stable. The gain of the plant, $k_p > 0$. Second, the reference model is described by (4.13) with numerator and denominator polynomials that are monic, coprime and of the same order as the plant. The reference model is stable, minimum phase with $k_m > 0$.

$$\frac{\hat{y}_p(s)}{\hat{u}(s)} = \hat{P}(s) = k_p \frac{\hat{n}_p(s)}{\hat{d}_p(s)} \quad (4.12)$$

$$\frac{\hat{y}_m(s)}{\hat{r}(s)} = \hat{M}(s) = k_m \frac{\hat{n}_m(s)}{\hat{d}_m(s)} \quad (4.13)$$

To achieve our control objective, we consider the controller structure found in Figure 4.10 where f_0 is a scalar, $\hat{c}(s)$, $\hat{d}(s)$, and $\hat{\lambda}(s)$ are polynomials of degrees $n-2$, $n-1$, and $n-1$, respectively.

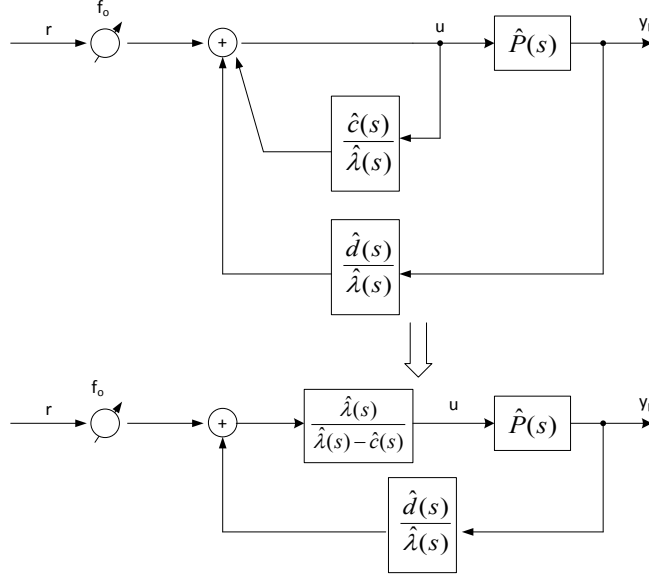


Figure 4.10: Controller Structure to Stabilize Constant Power Load [94]

The closed loop transfer function between the output, y_p , and input, r , can be shown to be (4.14). Note that (4.14b) can be obtained if (4.12) is substituted into (4.14a). It is possible to make (4.14) equal to $\hat{M}(s)$ if and only if (4.15) is satisfied. If satisfied, there exists unique f_0^* , $\hat{c}^*(s)$, and $\hat{d}^*(s)$ such that the transfer function in (4.14) equals $\hat{M}(s)$ described by (4.13), assuming that \hat{n}_p and \hat{d}_p are coprime [94].

$$\frac{y_p(s)}{r(s)} = \frac{f_0 \frac{\hat{\lambda}(s)}{\hat{\lambda}(s) - \hat{c}(s)} \hat{P}(s)}{1 - \frac{\hat{d}(s)}{\hat{\lambda}(s) - \hat{c}(s)} \hat{P}(s)} \quad (4.14a)$$

$$\frac{y_p(s)}{r(s)} = \frac{f_o k_p \hat{\lambda}(s) \hat{n}_p(s)}{(\hat{\lambda}(s) - \hat{c}(s)) \hat{d}_p(s) - k_p \hat{n}_p(s) \hat{d}(s)} \quad (4.14b)$$

$$(\hat{\lambda}(s) - \hat{c}(s))^* \hat{d}_p(s) - k_p \hat{n}_p(s) \hat{d}(s)^* = f_o \frac{k_p}{k_m} \hat{\lambda}_o(s) \hat{n}_p(s) \hat{d}_m(s) \quad (4.15)$$

The unique solutions of these polynomials can be determined with (4.16). The expression for $\hat{\lambda}_o(s)$ is an arbitrary Hurwitz polynomial of degree $n-m-l$ and $q(s)$ is the quotient obtained when dividing $\hat{\lambda}_o \hat{d}_m$ by \hat{d}_p of degree $n-m-l$.

$$\hat{d}^*(s) = \frac{1}{k_p} (\hat{q}(s) \hat{d}_p(s) - \hat{\lambda}_o(s) \hat{d}_m(s)) \quad (4.16a)$$

$$\hat{c}^*(s) = \hat{\lambda}(s) - \hat{q}(s) \hat{n}_p(s) \quad (4.16b)$$

$$f_o^* = \frac{k_m}{k_p} \quad (4.16c)$$

4.2.3 Attempt to Stabilize Second-Order Plant with Model Reference Control

Consider the second order plant associated with the output impedance of the system of Figure 4.8 listed as (4.17). The plant takes on the form of (4.18).

$$\hat{P}(s) = Z_{2,out}(s) = K_{DC} \frac{Ls - Y}{LCs^2 - YCs + 1} \quad (4.17)$$

$$\hat{P}(s) = k_p \frac{\hat{n}_p(s)}{\hat{d}_p(s)} = k_p \frac{s - q_o}{s^2 - p_1s + p_o} \quad (4.18)$$

The zero of (4.18) is not of minimum phase because the zero is located in the right half of the complex plane. The model that is chosen is listed as (4.19). One advantage of the control structure chosen (Figure 4.10) is that the forward block cancels the zeros of $\hat{P}(s)$ and replaces them with the zeros of $\hat{M}(s)$.

$$\hat{M}(s) = k_m \frac{\hat{n}_m(s)}{\hat{d}_m(s)} = k_m \frac{s + a_o}{s^2 + b_1s + b_o} \quad (4.19)$$

Utilizing the procedures outlined in the previous section, polynomials (4.20), (4.21), (4.22), and (4.23) can be written. One will notice that (4.21) introduces negative feedback terms.

$$\hat{\lambda}(s) = \hat{\lambda}_o(s)\hat{n}_m(s) = s + a_o \quad (4.20)$$

$$\begin{aligned} \hat{d}^*(s) &= \frac{1}{k_p}(\hat{q}\hat{d}_p - \hat{\lambda}_o\hat{d}_m) \\ &= \frac{-1}{k_p}[(p_1 + b_1)s + (b_o - p_o)] \\ &= d_1^*s + d_o \end{aligned} \quad (4.21)$$

$$\hat{c}^*(s) = \hat{\lambda}(s) - \hat{q}\hat{n}_p = (s + a_o) - (s - q_o) = a_o + q_o \quad (4.22)$$

The feedforward block of Figure 4.10 is listed as (4.23). Comparing (4.17) and (4.18), $q_o = Y/L$ resulting in an unstable compensator since $q_o > 0$.

$$\frac{\hat{\lambda}(s)}{\hat{\lambda}(s) - \hat{c}(s)} = \frac{s + a_o}{s - q_o} \quad (4.23)$$

4.2.4 Stabilized Third Order Plant with Model Reference Control

Utilizing the short line modeling assumption has resulted in an unstable compensator design. The third order plant model, (4.5), will be used, which introduces additional capacitance into the system (coupled pi network). Our plant is now described by (4.24).

$$\hat{P}(s) = k_p \frac{\hat{n}_p(s)}{\hat{d}_p(s)} = k_p \frac{s^2 + q_1s + q_o}{s^3 + p_2s^2 + p_1s - p_o} \quad (4.24)$$

$$k_p \equiv K_{DC} / C_1$$

$$p_o \equiv 1/(LC_1C_2Y) \quad q_o \equiv (Y - R)/(LC_2Y)$$

$$p_1 \equiv (C_1Y - RC_1 + C_2Y)/(LC_1C_2Y)$$

$$q_1 \equiv (RC_2Y - L)/(LC_2Y)$$

$$p_2 \equiv (RC_1C_2Y - LC_1)/(LC_1C_2Y)$$

In order to use model reference control, the plant needs to be minimum phase (but not necessarily stable). Therefore, both q_0 and q_1 must be greater than 0. While $q_0 > 0$ is easily satisfied as the line resistance R is usually very small or ignorable, the condition $q_1 > 0$ imposes a constraint on the use of capacitor C_2 , the value of which should be lower bounded by $L/(RY)$. When these conditions are satisfied, we can consider a reference model described by (4.25).

$$\hat{M}(s) = k_m \frac{\hat{n}_m(s)}{\hat{d}_m(s)} = k_m \frac{s^2 + a_1s + a_o}{s^3 + b_2s^2 + b_1s + b_o} \quad (4.25)$$

Using the model reference controller structure as in Figure 4.10 and following the procedures as in the previous section, we can determine $\hat{\lambda}(s)$, $\hat{d}^*(s)$ and $\hat{c}^*(s)$ to be (4.26), (4.27), and (4.28), respectively.

$$\hat{\lambda}(s) = \hat{\lambda}_o(s)\hat{n}_m(s) = s^2 + a_1s + a_o \quad (4.26)$$

$$\begin{aligned} \hat{d}^*(s) &= \frac{1}{k_p}(\hat{q}\hat{d}_p - \hat{\lambda}_o\hat{d}_m) \\ &= \frac{1}{k_p}[(p_2 - b_2)s^2 + (p_1 - b_1)s - (b_o + p_o)] \\ &= d_2^*s^2 + d_1^*s + d_o \end{aligned} \quad (4.27)$$

$$\hat{c}^*(s) = \hat{\lambda}(s) - \hat{q}\hat{n}_p = s(a_1 - q_1) + (a_o - q_o) = c_1^*s + c_o \quad (4.28)$$

The controller compensator is listed as (4.29) and is clearly stable if the parameters a_o , a_1 , b_o , b_1 , and b_2 are chosen appropriately.

$$\frac{\hat{\lambda}(s)}{\hat{\lambda}(s) - \hat{c}(s)} = \frac{s^2 + a_1s + a_o}{s^2 + q_1s + q_o} \quad (4.29)$$

4.3 COMPENSATOR DESIGN AND PARAMETER SELECTION

To select the parameters of the reference model, we consider the following criteria. First, the DC gain of the reference model equals 1, so that the output voltage is able to follow the reference voltage with no steady-state error. Second, the reference model is stable with desired transient characteristics, e.g., with sufficiently small rise time, settling time, and percentage overshoot.

To meet the first criterion, the reference model's DC gain should satisfy

$$\hat{M}(0) = k_m \frac{a_o}{b_o} = 1$$

$$\text{Stability} : a_i, b_i > 0$$

If $k_m=1$, then $a_o = b_o$. For the system to be critically damped, (4.30) must be satisfied.

To meet the second criterion, we follow the guideline of [95] and choose the pole locations as shown in Figure 4.11. The third order denominator of the reference model is chosen to be composed of a stable real pole and a complex conjugate pair as described by (4.31). We choose not to place all the poles at one point or within a very small region, because otherwise the controlled system tends to have slow response and use large control signals. Instead, we place the poles 30 degrees apart on a circle of radius ω_1 . Using (4.31), b_o , b_1 , and b_2 can be solved for as shown in (4.32).

$$a_1 = 2\sqrt{a_o} \quad (4.30)$$

$$(s + \omega_1)(s + \frac{\sqrt{3}}{2}\omega_1 + j\frac{\sqrt{3}}{2}\omega_1)(s + \frac{\sqrt{3}}{2}\omega_1 - j\frac{\sqrt{3}}{2}\omega_1) \quad (4.31)$$

$$(s + \omega_1)(s^2 + \sqrt{3}\omega_1 s + \omega_1^2) \quad (4.32)$$

$$s^3 + (\sqrt{3}\omega_1 + \omega_1)s^2 + (\omega_1^2 + \sqrt{3}\omega_1^2)s + \omega_1^3 = s^3 + b_2s^2 + b_1s + b_o$$

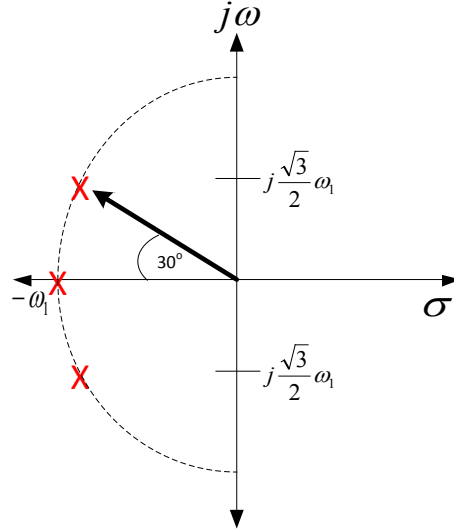


Figure 4.11: Pole Placement of the Reference Model

After determining the denominator of (4.25), we choose the numerator parameters as shown in (4.33). These parameters ensure that $\hat{\lambda}(s) = \hat{\lambda}_0(s)\hat{n}_m(s)$ is critically damped.

$$a_0 = \omega_1^3, \quad a_1 = 2\sqrt{a_0} = 2\omega_1\sqrt{\omega_1} \quad (4.33)$$

4.3.1 Simulation Results – Control Block Diagram Response

The parameters associated with the system are provided in Table 4.2. For this study, the bidirectional converter is rated for 200 kW corresponding to a transformer leakage inductance of 5.21 mH. Demanded power, P_{rms} , is 100 kW, and the DC bus ripple (ΔV_{DC}) was chosen to be +/- 4.5% of nominal DC voltage. The equivalent lumped capacitance on the output of the bidirectional DC/DC converter was calculated with (4.34), [96]. This capacitance is an electric circuit model constraint. To maintain system stability, (4.35) must be satisfied.

$$C_{eqv} > \frac{P_{rms}}{\omega_{Line} \Delta V_{dc} V_{dc}} = 3.62mF \quad (4.34)$$

$$C_2 > \frac{L}{RY} = 1.41mF \quad (4.35)$$

Table 4.2: Rated System Parameters

Parameter	Numerical Quantity
Transformer Turns, n	5
Leakage Inductance, L_T	5.208 mH
Duty Cycle, d_h	0.1464
DC Bus Voltage, V_{DC}	1 kV
Switching Frequency, f_s	3 kHz
Line Resistance, R	0.0176 Ω /km
Line Inductance, L	0.248 mH/km
Line Capacitance, $2C_{1,2}$	0.923 μ F/km
Lumped Capacitance, C_1	13.26 mF
Lumped Capacitance, C_2	5 mF
Cable Distance	0.1 km
Constant Power Load, Y	10 Ω_{DC}
Line Frequency	377 rad/s
Complex pole frequency, ω_l	3500 rad/s

With all necessary parameters defined, the pole-zero plot for the plant transfer function, (4.5), is plotted in Figure 4.12. Figure 4.12 also shows the impacts of the lumped capacitance on the overall system stability. The additional capacitance in the network helps shift the poles and zeros of the plant transfer function but doesn't completely help stabilize the plant. The pole-zero plot for the reference model, $\hat{M}(s)$, is provided in Figure 4.13. Because the zero is placed far along the real-axis, the pole placements are a bit skewed. For this reason, point identifiers are included showing that the poles conform to the design methodology found in Figure 4.11.

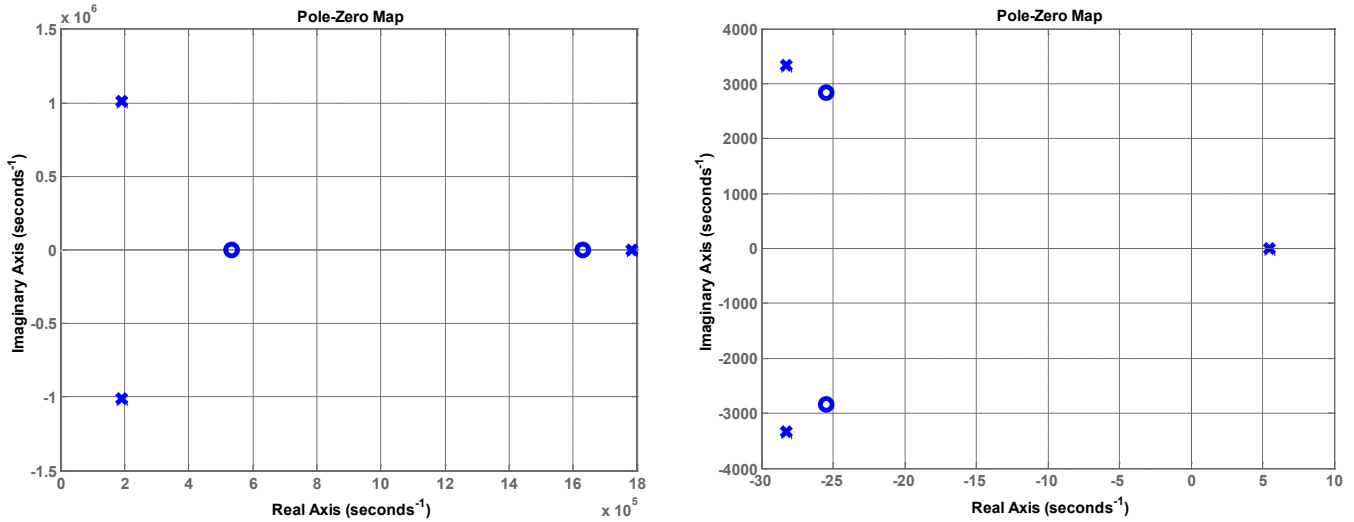


Figure 4.12: Pole-zero plot for unstable plant with lumped network capacitors (right) and neglected (left)

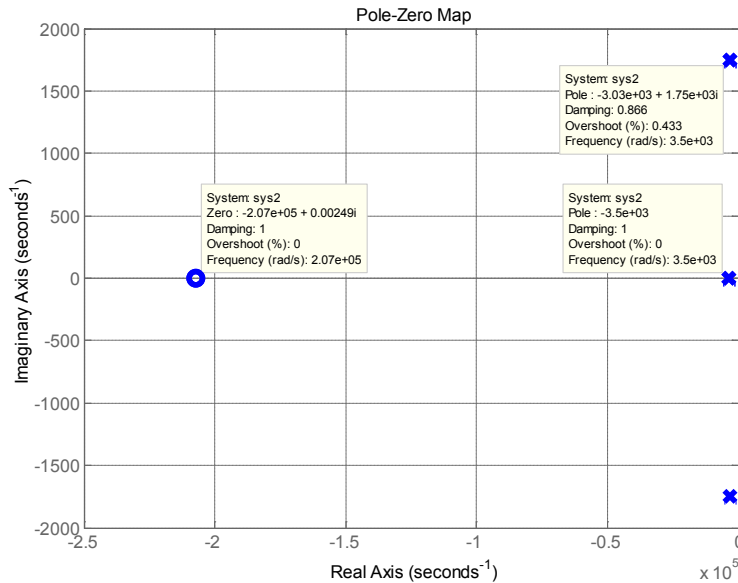


Figure 4.13: Pole-zero Plot for Model, $M(s)$

The closed loop Matlab/Simulink block diagram representation of the CPL scenario being evaluated with controller design using model reference control techniques is provided in Figure 4.14. A step response of the closed-loop block diagram response of Figure 4.14 is provided in Figure 4.15. The Matlab script used to populate the parameters associated with the block diagram is provided in Appendix B.

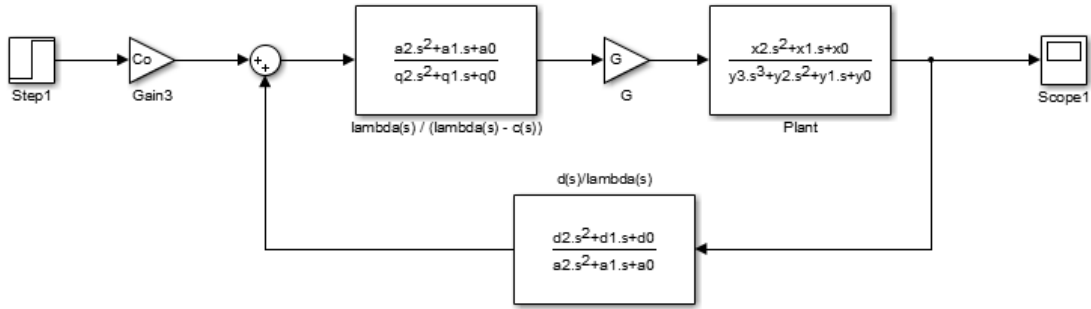


Figure 4.14: Simulation Model of Designed Control Structure Utilizing Model Reference Control

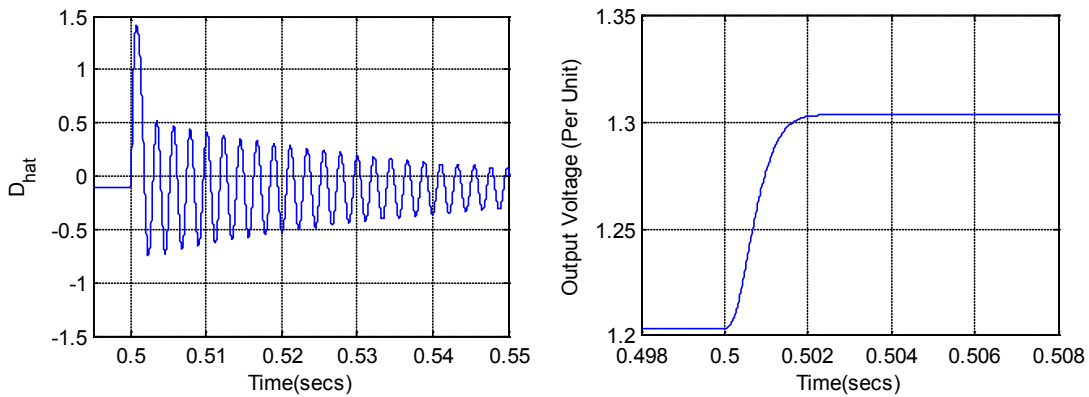


Figure 4.15: Closed Loop Controller Performance Based Upon Model Reference Control Design

As a basis of comparison, if a PD compensator were selected to regulate the plant, the expected closed loop response is provided in Figure 4.16. The noticeable observation is that the PD controller cannot stabilize the output voltage. Using model reference control design ensures that a very smooth, well performing system response is achieved.

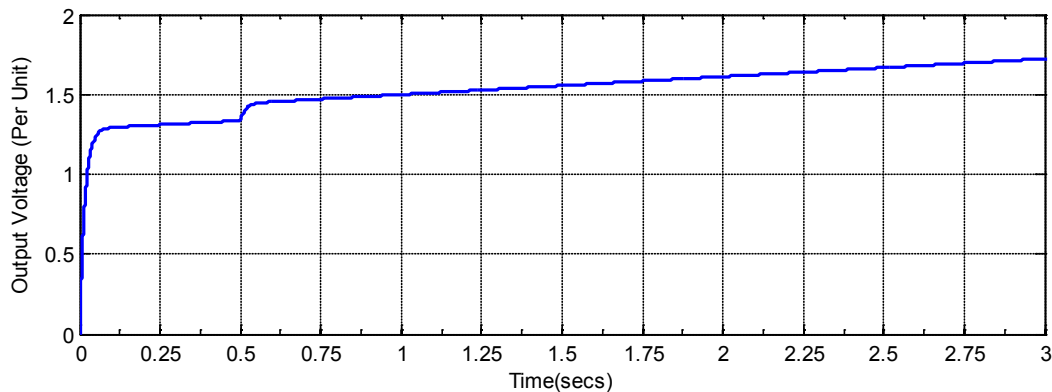


Figure 4.16: Closed Loop Controller Performance Based Upon PD Design

4.3.2 Simulation Results – Circuit Response

To ensure that the plant is adequately modelled, the model reference control design is evaluated in SimPowerSystems using the circuit layout found in Figure 4.17. Figure 4.17 is a modified version of Figure 4.5 with control blocks emphasized and the electric machine replaced with a dynamic constant power load. The DC/DC converter output voltage is regulated with the model reference controller and the inverter output voltage is regulated with a traditional dq control scheme where each axis is regulated with a PI controller. Table 4.2 provides all the parameters associated with the circuit model.

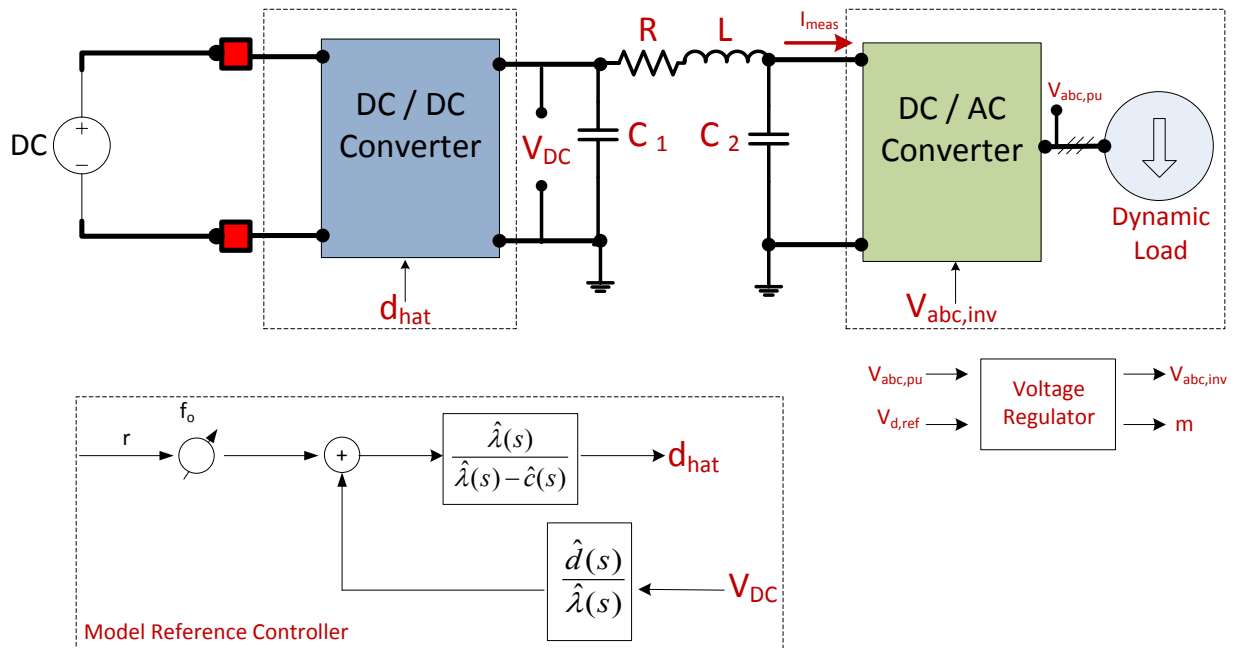


Figure 4.17: Circuit Diagram for Proving Model Reference Control Capability

Initially, the input into the controller, r , is set to 1200 V and a step change of 100 V is applied at 0.5 seconds into the simulation. The d -axis reference voltage is set to 1.0 per unit for the inverter. The DC bus voltage, DC/DC output current, power consumed by the dynamic load, and modulation index of the inverter are all provided in Figure 4.18.

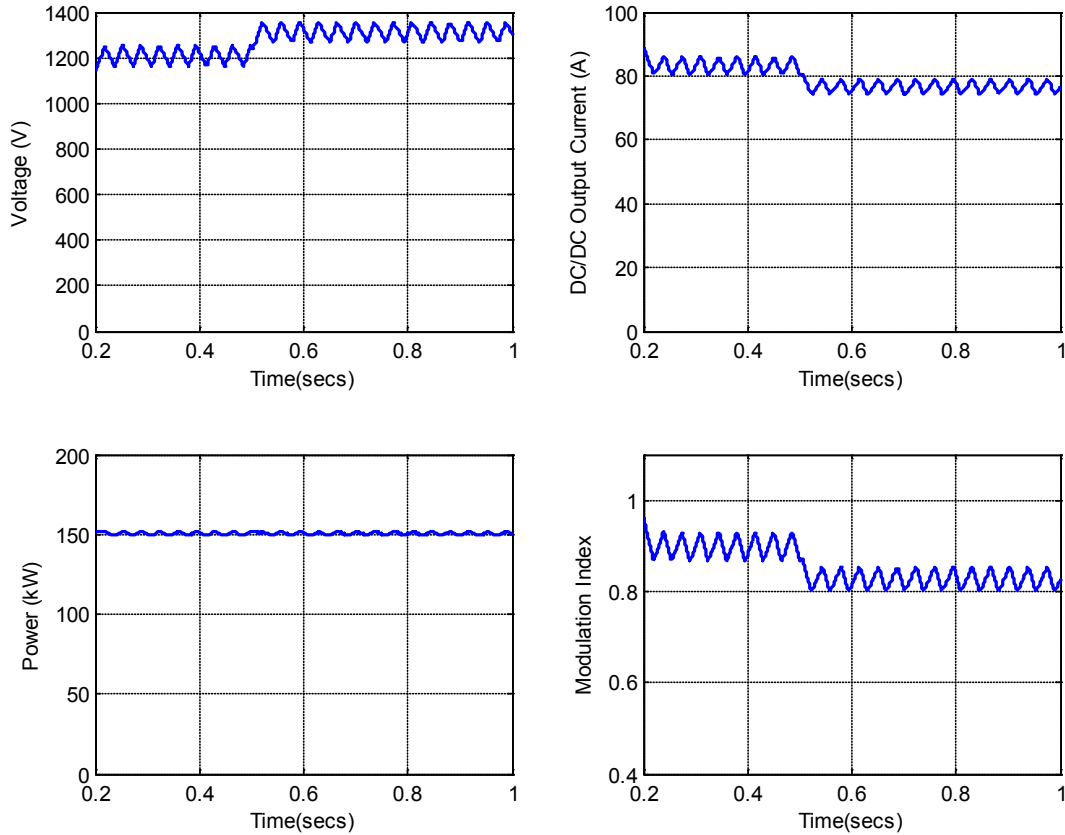


Figure 4.18: Circuit Response with Step Change in DC/DC Converter Control Input at 0.5 seconds

From the simulation results, a few observations can be observed. First, the power provided to the dynamic load is always held constant at 150 kW – if the DC bus voltage rises, the current compensates accordingly. The derivation of the output impedance, (4.5), assumed constant load impedance, Y , of 10Ω corresponding to 100 kW of DC power. This load value is with respect to the DC side of the inverter. The relationship between the DC side impedance of the inverter, R_{DC} , and AC side impedance, R_{AC} , is described by (4.36). Substituting appropriate values into (4.36), one can show that 150 kW is the appropriate AC power to be absorbed by the load at all times. This is only the case if the inverter has a neutral point clamped topology which will be described more thoroughly in the following chapter.

$$P_{DC} = P_{AC}$$

$$\frac{V_{DC}^2}{R_{DC}} = \frac{V_{LL}^2}{R_{AC}} = \frac{(0.612mV_{DC})^2}{R_{AC}} \quad (4.36)$$

$$R_{DC} = \frac{R_{AC}}{(0.612m)^2}$$

The second observation is the ripple on the voltage. The average model circuit representation of the plant under study is shown in Figure 4.19 with capacitors that impact the ripple voltage. These capacitors provide the energy storage necessary to balance instantaneous power delivered to the dynamic load. Mathematical details of these average models are provided in Chapter 5. Notice that both power converters have Norton equivalents and if transformed into Thevenin equivalents, capacitors C_1 and C_2 would be in series. With this concept in mind and from (4.34), the simulated ripple can be verified as shown in (4.37).

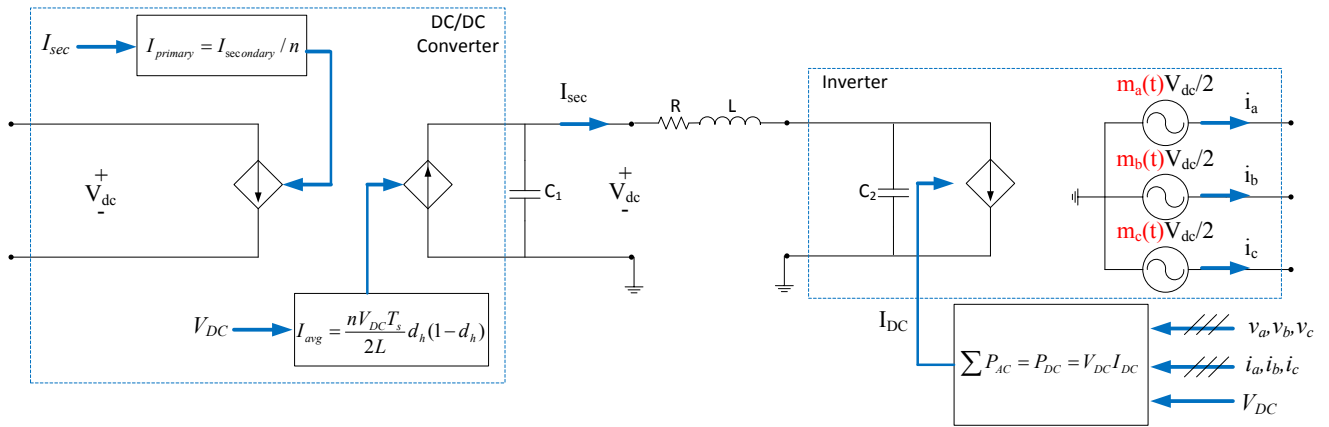


Figure 4.19: Average Circuit Model Representation of Plant Model under Study

$$\Delta V_{dc} = \frac{P_{rms}}{\omega_{Line} C_{eqv} V_{dc}} = \frac{150kW}{(377 rad / s)(3.62mF)(1200V)} = 92.10V \quad (4.37)$$

Finally, Figure 4.20 provides a comparison of the circuit simulation result and control block diagram response showing that the plant model derived adequately reflects the dynamics of the circuit behavior. The control block diagram voltage response is not a simple step change but, if zoomed around the control input step time (see Figure 4.15), one will see a very fast control response. The small signal duty cycle response between both exhibits the same transient frequency with the big difference being the observed ripple in the circuit simulation response. The average value of the small signal duty cycle for the circuit simulation converges to the control diagram response as in the case with the DC/DC converter output voltage.

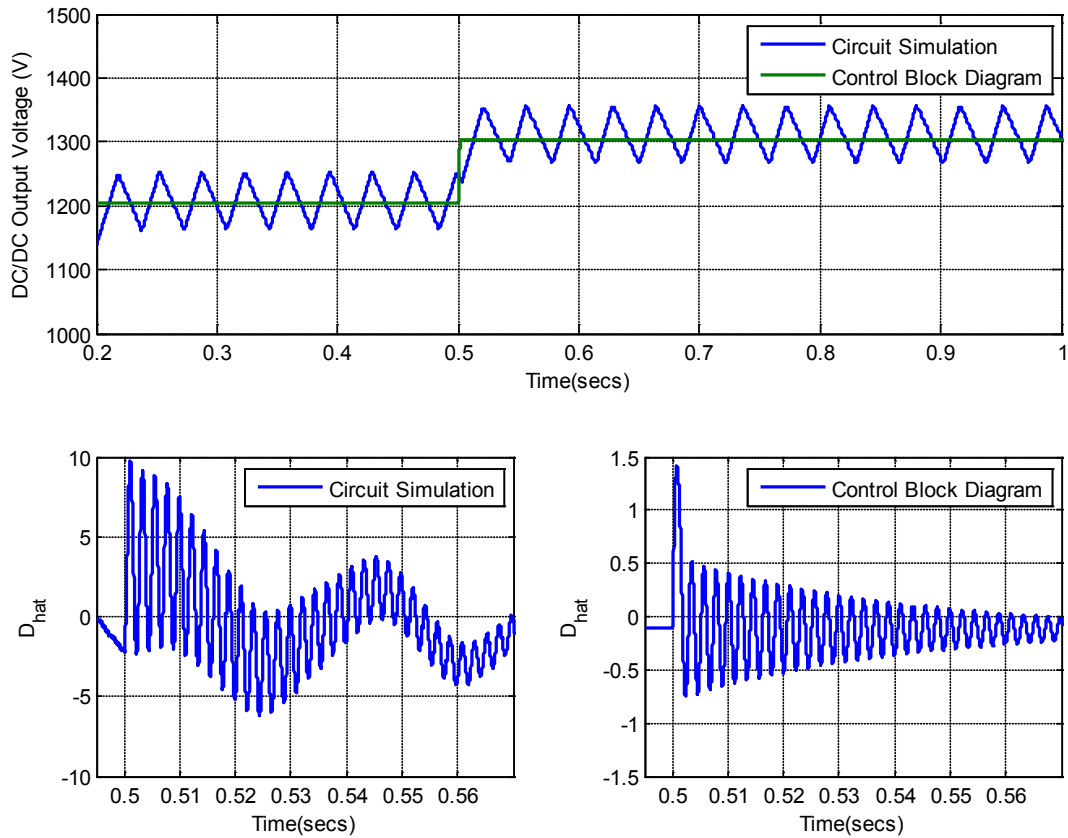


Figure 4.20: Comparison of Circuit Simulation and Control Block Diagram Response

5.0 MODELING AN OFFSHORE MEDIUM VOLTAGE DC MICROGRID

The purpose of this section is to provide the mathematical details associated with the various renewable, power electronic, and electric drive models that combine to form the overall DC microgrid model. Throughout the chapter, figures are provided in each subsection showing that the models have been adequately implemented in Matlab/Simulink. Detailed schematics of some of the Simulink models are provided in Appendix C for the curious student.

5.1 FULL CONVERTER WIND TURBINE MODEL

The wind collection system that was modeled within the Matlab/Simulink environment is composed of 1 wind turbine which will be represented by an aerodynamic model, permanent magnet synchronous generator (PMSG), and a three-level neutral point clamped rectifier that generates the required DC bus voltage. A schematic representation is found in Figure 5.1. Table 5.1 provides the wind turbine and PMSG parameters used for modeling.

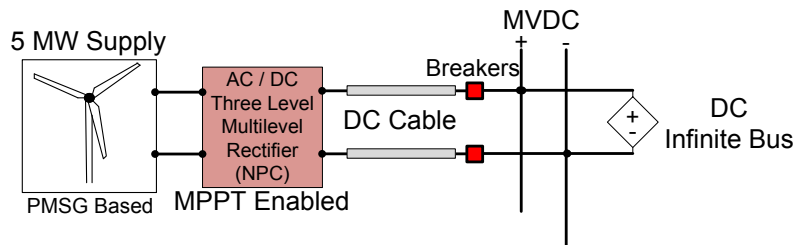


Figure 5.1: Offshore Wind Turbine Collection System

Table 5.1: Wind Turbine and Permanent Magnet Synchronous Machine Parameters [97]

Wind Turbine Parameters		PMSG parameters	
Rate power P	5 MW	Rate power P	5 MW
Rated rotor speed n_r	14.8 rpm	Rated voltage (L-L RMS)	3.3 kV
Rotor diameter D	116 m	Rated current (RMS)	0.92 kA
Hub height	138 m	Power factor	0.95
Hub height mean speed	11.8 m/s	Phase resistor R_s	50 m Ω
Cut in wind speed	2.5 m/s	d-axis inductance $L_{md}+L_\sigma$	3.5218 mH
Cut out wind speed	25 m/s	q-axis inductance $L_{mq}+L_\sigma$	3.5218 mH
Rated wind speed	11.8 m/s	PM flux	14.3522Wb
Optimum tip speed ratio	7.6179	Number of pole pairs	118
Maximum power coefficient C_p	0.4746	Inertia factor	2.5e5 kg.m ²
Air density	1.225 kg/m ³	Friction factor	2.26e4 N.m.s

5.1.1 Simplified Model of a Permanent Magnet Synchronous Machine

A standard set of electrical equations, with respect to the dq rotor reference frame, describing the permanent magnet synchronous machine are displayed as (5.1) with output torque listed as (5.2). Note that L_s is the stator leakage inductance, λ_m is the permanent magnet flux of constant magnitude, ω is the rotor speed, P is the number of pole pairs, F is a friction factor, and J the moment of inertia of the machine [98]. This model described by (5.1) and (5.2) assumes that saturation is neglected, induced emf's are sinusoidal, the Eddy currents and hysteresis losses are negligible, and there are no field current dynamics. Finally, the mechanical equation, based on Newton's second law, of the machine is listed as (5.3).

$$V_d = R_s i_d + L_s \frac{di_d}{dt} - \omega_r L_s i_q \quad (5.1a)$$

$$V_q = R_s i_q + L_s \frac{di_q}{dt} + \omega_r L_s i_d + \omega_r \lambda_m \quad (5.1b)$$

$$T_{em} = \frac{3}{2} \frac{P}{2} (\lambda_m i_q + (L_{ds} - L_{qs}) i_d i_q) \quad (5.2)$$

$$T_e - T_m - F\omega_r = J \frac{d\omega_r}{dt} \quad (5.3)$$

5.1.2 Aerodynamic Model of Wind Source

The wind source power can be computed with (5.4), which is derived from elementary fluid mechanics. Note that C_p is termed the power coefficient, ρ is the air density, A is the area swept by the turbine blades, V_W is the velocity of the wind, β is the pitch angle and λ is the tip speed ratio. The inputs into the aerodynamic model include the machine mechanical speed, the pitch angle of the wind turbine system, and wind speed. With a pitch angle of zero, the wind will generate maximum torque on the blades of the wind turbine. The rated wind speed is 11.8 m/s as indicated in Table 5.1.

$$P_T = \frac{1}{2} \rho A C_p(\beta, \lambda) V_W^3 \quad (5.4)$$

From a review of the literature, many definitions exist for the power coefficient because the term is an empirical expression [99], [100], [101], [102], [103]. The definition that was chosen for its computation comes from a laboratory validated environment and is listed as (5.5).

$$C_p(\beta, \lambda) = C_1 \left(C_2 \frac{1}{\Lambda} - C_3 \beta - C_4 \beta^x - C_5 \right) \exp(-C_6 / \Lambda) + C_7 \lambda \quad (5.5)$$

In (5.5), $C_1 = 0.5176$, $C_2 = 116$, $C_3 = 0.4$, $C_4 = 0$, $C_5 = 5$, $C_6 = 21$, and $C_7 = 0.0068$. The $1/\Lambda$ term found in (5.5) is defined by (5.6).

$$\frac{1}{\Lambda} = \frac{1}{\lambda + 0.08\beta} - \frac{0.035}{1 + \beta^3} \quad (5.6)$$

Once the power is computed, it is easy to compute the output mechanical torque by dividing by the mechanical speed of the machine. The mechanical torque generated by the turbine serves as an input into the mechanical equation of the PMSG, (5.3).

5.1.3 Maximum Power Point Tracking Control Implementation

According to [104], the optimal torque reference can be obtained using (5.7) through (5.9). Note that λ_{opt} is the optimal tip speed ratio given in Table 5.1 and C_p is computed with (5.5). The controller that implements these equations, to achieve maximum power output, is illustrated in Figure 5.2.

$$T_{ref} = K\omega_r^2 \quad (5.7)$$

$$K = \frac{1}{2}\rho AR^3 \frac{C_{p,max}}{\lambda_{opt}^3} \quad (5.8)$$

$$C_{p,max} = C_p(\beta|_{\beta=0}, \lambda_{opt}) \quad (5.9)$$

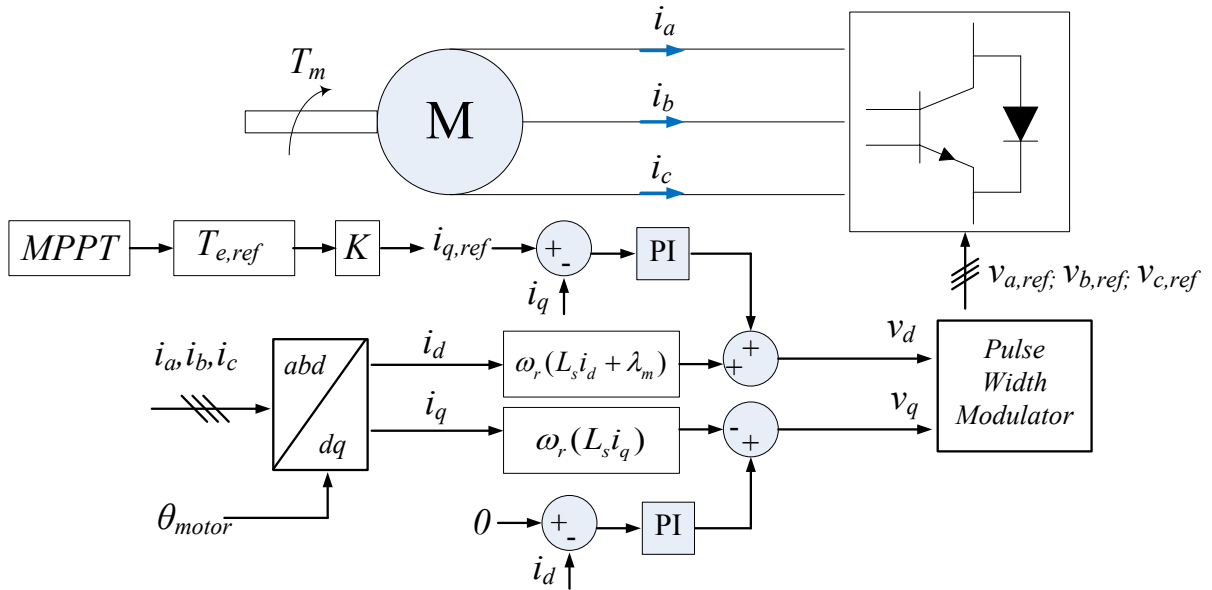


Figure 5.2: Maximum Power Point Tracking Implementation and Control of Wind Turbine

The controller uses field oriented control to perform the speed control of the PMSG by decoupling the flux linkage and torque control. The flux linkage definitions are listed as (5.10) and (5.11), [105].

$$\lambda_d = L_s i_d + \lambda_m \quad (5.10)$$

$$\lambda_q = L_s i_q \quad (5.11)$$

Three-phase power systems are conveniently modeled and controlled in the dq coordinate system. The two motivations for the change of coordinates includes (1) three variables of the original coordinate are mapped onto two variables and (2) the variables can be decoupled, analyzed, and controlled independently. For maximum torque control applications, and referring to (5.2), it's always desired to drive the d -axis current to zero and maximize the q -axis current capability. This is the reason for establishing the q -axis current reference based on the maximum torque determined with (5.7) to (5.9). The reference torque is divided by the permanent magnet flux, λ_m , and pole pairs, refer to (5.2) and note that $L_d = L_q$, to establish the q -axis reference current.

The final component in the maximum power point tracking block of Figure 5.2 is the reference signal generator output. The transformation from dq to abc components is slightly more unique compared to any other in the overall model. The relationship between the line-to-line output voltage and DC voltage for a neutral point clamped topology is described by (5.12). To obtain the desired DC voltage, it may be required to increase the fundamental line-to-line voltage by adding a third harmonic component to the three-phase sinusoidal modulating wave without causing overmodulation [77]. The reference signal generated is a combination of the three-phase sinusoidal modulated wave signal generated by the current controller based upon

$v_{d,ref}$ and $v_{q,ref}$. A third harmonic signal is superimposed onto the modulated waveform. This technique was adequately described in Chapter 3 of this dissertation.

$$V_{LL,rms} = 0.612mV_{dc} \quad (5.12)$$

5.1.4 Wind Turbine Model Validation

The expected electrical torque is calculated below from which the rated power can be obtained. Note that the machine is a wound rotor implying that L_d and L_q are the same. Figure 5.3 provides the current controller responses associated with the wind turbine. Note that the desired steady-state quantities for the quadrature axis current and direct axis current are obtained, therefore, validating that the maximum power point tracking routine is responding appropriately.

$$T_{em} = \frac{3}{2}P(\lambda_m i_q + (L_{ds} - L_{qs})i_d i_q) = \frac{3}{2}(118)((14.35)(1.3kA)) = 3.30MNm$$

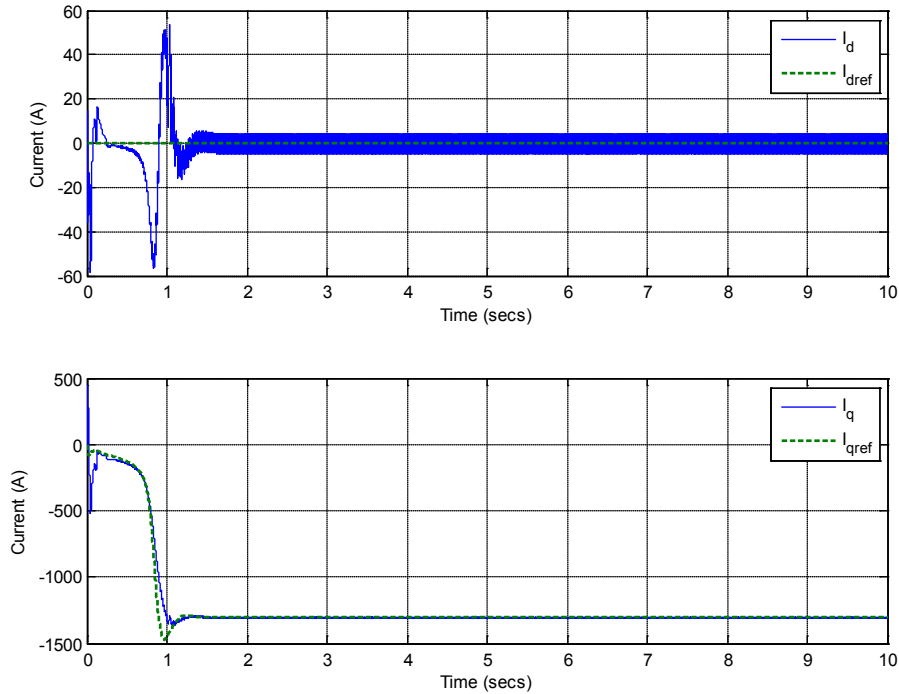


Figure 5.3: Wind Turbine Controller Responses

Figure 5.4 provides a few illustrations showing that the power coefficient and tip speed ratio achieve their optimal settings provided in Table 5.1. With all components and controls synchronized, the desired output power of the wind turbine is achieved as shown below.

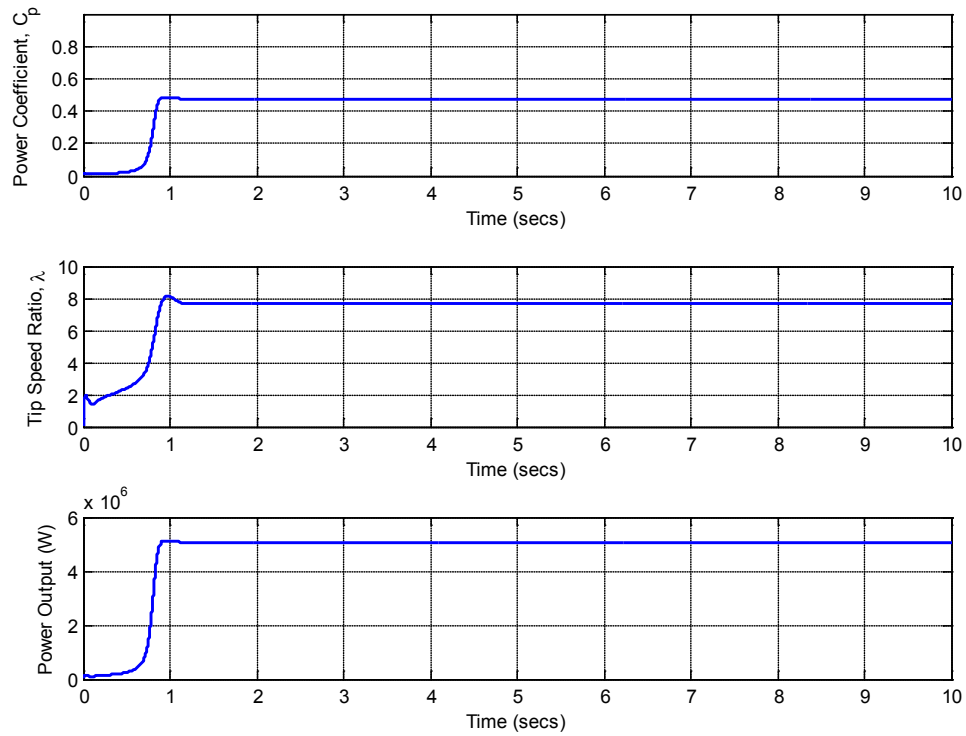


Figure 5.4: Wind Turbine Aerodynamic Responses and Output Power

5.2 POWER ELECTRONIC CONVERTER MODELING

This section develops the framework for the average models of the neutral point clamped converter, pulse width modulated boost rectifier, and the bidirectional DC/DC converter.

5.2.1 Mathematical Modeling of Power Electronic Converters: The Average Model

Figure 5.5 provides a layout of a half-bridge inverter with AC and DC side boundaries labeled in the circuit. The analysis presented on the half-bridge inverter will be valuable for understanding average model development of the neutral point clamped converter. A semiconductor switch, s , is defined as two components: (1) A high power transistor, Q , and (2) an anti-parallel diode, D . The switches are complimentary in nature as described by (5.13).

$$s_1(t) + s_2(t) \equiv 1 \quad (5.13)$$

Equations (5.14)-(5.16) describe the relationships between the half-bridge converter terminal voltages/currents and the switching functions, $s_n(t)$. The DC power, terminal power, and sending power can be described by (5.17), (5.18), and (5.19), respectively.

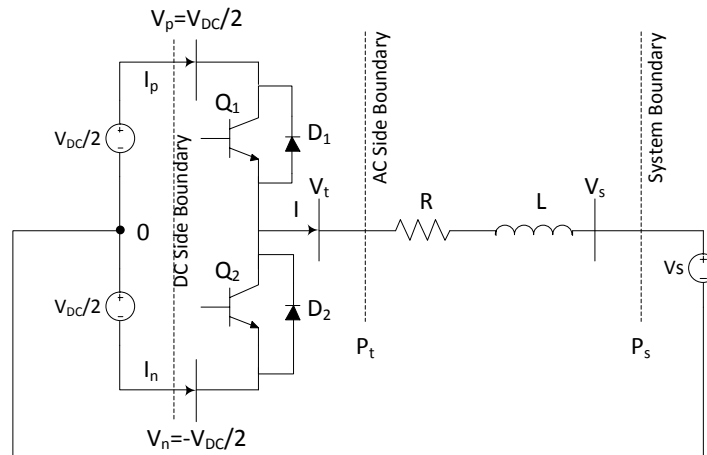


Figure 5.5: Simplified Half-Bridge Inverter

$$V_t(t) = (V_{DC}/2)s_1(t) - (V_{DC}/2)s_2(t) \quad (5.14)$$

$$i_p(t) = is_1(t) \quad (5.15)$$

$$i_n(t) = is_2(t) \quad (5.16)$$

$$P_{DC}(t) = V_p i_p + V_n i_n = \frac{V_{DC}}{2} [s_1(t) - s_2(t)] i \quad (5.17)$$

$$P_t(t) = V_t(t) i = \frac{V_{DC}}{2} [s_1(t) - s_2(t)] i \quad (5.18)$$

$$P_s(t) = V_s i \quad (5.19)$$

Equations (5.13)-(5.19) are the mathematical relationships for a switching model of the converter. The equivalent circuit utilizing these relations is provided in Figure 5.6. The *switching* model provides insight into instantaneous currents, voltages, and power quantities but does not easily show how the main control variables (one being the modulation index) impact these electrical quantities.

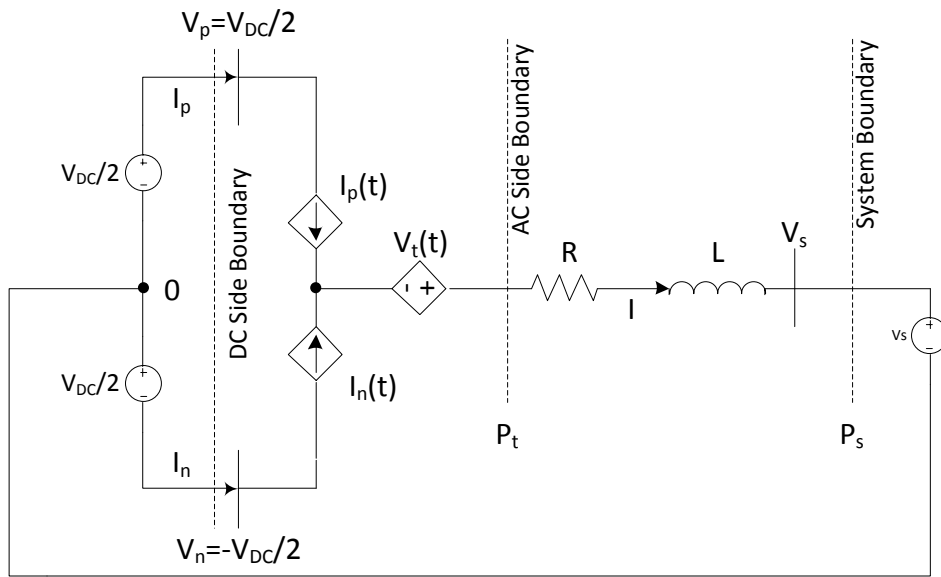


Figure 5.6: Switched Equivalent Circuit Model of the Half-Bridge Converter

The procedure for determining an average model of a circuit is straightforward. The AC side current must satisfy (5.20). The terminal voltage, because it is periodic, can be described with a Fourier series as shown with (5.21) revealing an average term and the high frequency signal components. The terminal voltage is of utmost importance because this parameter dynamically determines the amount of power flowing from the AC side boundary towards the system boundary.

$$L \frac{d}{dt} i(t) + Ri(t) = V_t(t) - V_s \quad (5.20)$$

$$V_t(t) = \frac{1}{T_s} \int_0^{T_s} V_t(\tau) d\tau + \sum_{h=1}^{\infty} [a_h \cos(h\omega_s t) + b_h \sin(h\omega_s t)] \quad (5.21)$$

Substituting (5.21) into (5.20), one arrives at (5.22). The current, $i(t)$, can be decomposed the same way. Upon doing so, (5.22) can be decomposed into a set of relationships providing the average model, (5.23a) and high frequency periodic model (5.23b). In general, any periodic signal can be averaged using (5.24). Assuming the audience is familiar with pulse width modulation routines in power electronic circuits, (5.24) is only valid if the frequency of the carrier waveform is sufficiently larger than that of the modulating waveform.

$$L \frac{d}{dt} i(t) + Ri(t) = \left(\frac{1}{T_s} \int_0^{T_s} V_t(\tau) d\tau - V_s \right) + \sum_{h=1}^{\infty} [a_h \cos(h\omega_s t) + b_h \sin(h\omega_s t)] \quad (5.22)$$

$$L \frac{d}{dt} \bar{i} + R\bar{i} = \frac{1}{T_s} \int_0^{T_s} V_t(\tau) d\tau - V_s \quad (5.23a)$$

$$L \frac{d}{dt} \tilde{i} + R\tilde{i} = \sum_{h=1}^{\infty} [a_h \cos(h\omega_s t) + b_h \sin(h\omega_s t)] \quad (5.23b)$$

$$\bar{x}(t) = \frac{1}{T_s} \int_{t-T_s}^t x_t(\tau) d\tau \quad (5.24)$$

Applying (5.24) to (5.14) through (5.19), one arrives at the averaged set of equations, (5.25)-(5.30) describing the average model of the half-bridge converter. The switching functions, s_1 and s_2 , are pulsed signals of unity amplitude and duty cycle, d , and are complimentary in nature.

$$\overline{s_1}(t) = d \quad (5.25a)$$

$$\overline{s_2}(t) = 1 - d \quad (5.25b)$$

$$\overline{V}(t) = \frac{V_{DC}}{2}(2d - 1) \quad (5.26)$$

$$\overline{i_p} = dI \quad (5.27)$$

$$\overline{i_n} = (1 - d)I \quad (5.28)$$

$$\overline{P}_{DC} = \frac{V_{DC}}{2}(2d - 1)I \quad (5.29)$$

$$\overline{P}_t = \frac{V_{DC}}{2}(2d - 1)I \quad (5.30)$$

The modulation index, m , is the amplitude ratio between the reference and carrier signals of the pulse width modulation strategy. The duty cycle, d , is related to the modulation index, m , by (5.31). Substituting (5.31) into (5.26)-(5.30), one arrives at (5.32) through (5.35).

$$m = 2d - 1 \quad (5.31)$$

$$\overline{V}_t = m \frac{V_{DC}}{2} \quad (5.32)$$

$$\overline{i_p} = \left(\frac{1+m}{2} \right) I \quad (5.33)$$

$$\overline{i_n} = \left(\frac{1-m}{2} \right) I \quad (5.34)$$

$$\overline{P}_{DC} = m \frac{V_{DC}}{2} I = \overline{P}_t \quad (5.35)$$

Utilizing the relationships previously derived, one arrives at the average circuit model of Figure 5.7. Classic references on power electronic circuit averaging are provided in the references as [76], [106], and [107].

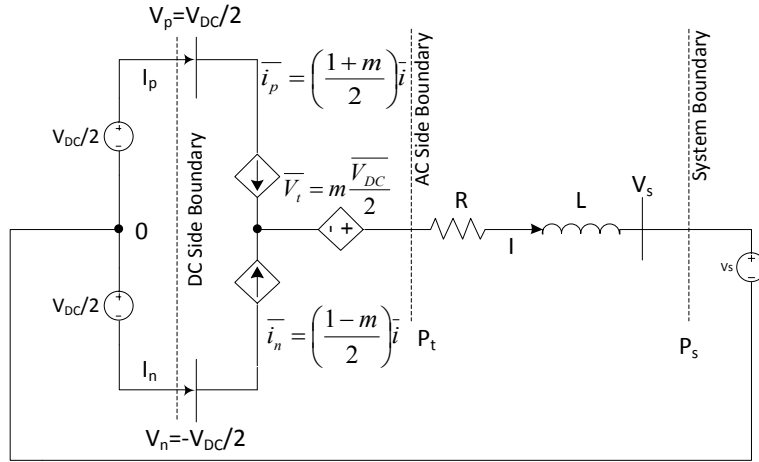


Figure 5.7: Averaged Equivalent Circuit of the Half-Bridge Converter

5.2.2 Average Model of Pulse Width Modulated Rectifier with Open Loop PQ Control

Consider the pulse width modulated boost rectifier in Figure 5.8 with power devices represented by single pole, double throw switches. Each switch, s , can take on two positions. Mathematically, two binary values are used to describe their position (1-top or 0-bottom) during circuit operation. The instantaneous voltages and currents in terms of the switch states are defined by (5.36) and (5.37).

$$\begin{bmatrix} v_{ab} \\ v_{bc} \\ v_{ca} \end{bmatrix} = \begin{bmatrix} s_a - s_b \\ s_b - s_c \\ s_c - s_a \end{bmatrix} v_{dc} = \begin{bmatrix} s_{ab} \\ s_{bc} \\ s_{ca} \end{bmatrix} v_{dc} \quad (5.36)$$

$$\dot{i}_{dc} = \begin{bmatrix} s_a \\ s_b \\ s_c \end{bmatrix}^T \cdot \begin{bmatrix} i_a \\ i_b \\ i_c \end{bmatrix} \quad (5.37)$$

Table 5.2: Operating States of Pulse Width Modulated Boost Rectifier

s_a	s_b	s_c	$s_a - s_b$	$s_b - s_c$	$s_c - s_a$	i_{dc}	v_{ab}	v_{bc}	v_{ca}
0	0	0	0	0	0	0	0	0	0
0	0	1	0	-1	1	i_c	0	$-v_{dc}$	v_{dc}
0	1	0	-1	1	0	i_b	$-v_{dc}$	v_{dc}	0
0	1	1	-1	0	1	$i_b + i_c$	$-v_{dc}$	0	v_{dc}
1	0	0	1	0	-1	i_a	v_{dc}	0	$-v_{dc}$
1	0	1	1	-1	0	$i_a + i_c$	v_{dc}	$-v_{dc}$	0
1	1	0	0	1	-1	$i_a + i_b$	0	v_{dc}	$-v_{dc}$
1	1	1	0	0	0	$i_a + i_b + i_c$	0	0	0

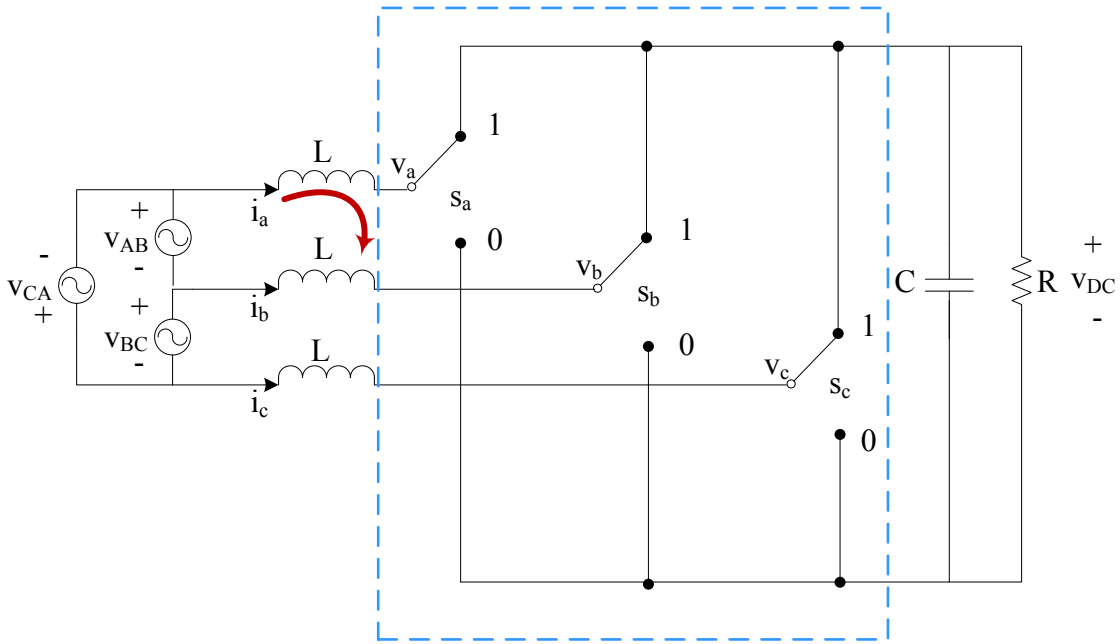


Figure 5.8: Pulse Width Modulated Boost Rectifier

The circuit states and relationships between the DC side and AC side of the rectifier given a specific switch outcome are provided in Table 5.2. Our objective is to replace the outlined region of Figure 5.8 with switch dependent current sources and, ultimately, arrive at the average circuit model. The line current and phase-to-phase current are related through (5.38).

$$i_a = i_{ab} - i_{ca} \quad i_b = i_{bc} - i_{ca} \quad i_c = i_{ca} - i_{bc} \quad (5.38)$$

If we assume balanced conditions, (5.39), we can show that the phase-to-phase current is three times the difference of any two line currents, (5.40). Writing Kirchoff's voltage law around the three phases of the circuit and applying Kirchoff's current law at the capacitor node, one can easily write the differential equations of the system listed as (5.41) and (5.42).

$$i_{ab} + i_{bc} + i_{ca} = 0 \quad (5.39)$$

$$\begin{aligned} i_a - i_b &= i_{ab} - i_{ca} - (i_{bc} - i_{ab}) = 2i_{ab} - (i_{ca} + i_{bc}) = 3i_{ab} \\ i_{ab} &= \frac{1}{3}(i_a - i_b) \end{aligned} \quad (5.40)$$

$$\begin{bmatrix} v_{AB} \\ v_{BC} \\ v_{CA} \end{bmatrix} = L \frac{d}{dt} \begin{bmatrix} i_a - i_b \\ i_b - i_c \\ i_c - i_a \end{bmatrix} + \begin{bmatrix} v_a - v_b \\ v_b - v_c \\ v_c - v_a \end{bmatrix} = 3L \frac{d}{dt} \begin{bmatrix} i_{ab} \\ i_{bc} \\ i_{ca} \end{bmatrix} + \begin{bmatrix} v_{ab} \\ v_{bc} \\ v_{ca} \end{bmatrix} \quad (5.41)$$

$$\frac{dv_{dc}}{dt} = \frac{1}{C} i_{dc} - \frac{v_{dc}}{RC} \quad (5.42)$$

If we define a few vectors by (5.43) and substitute into (5.41) and (5.42), we arrive at (5.44) and (5.45) which conveniently describe the switching model of the pulse width modulated boost rectifier.

$$\vec{v}_{LL} \equiv \begin{bmatrix} v_{AB} \\ v_{BC} \\ v_{CA} \end{bmatrix} \quad \vec{v}_{ll} \equiv \begin{bmatrix} v_{ab} \\ v_{bc} \\ v_{ca} \end{bmatrix} \quad \vec{i}_{ll} \equiv \begin{bmatrix} i_{ab} \\ i_{bc} \\ i_{ca} \end{bmatrix} \quad \vec{s}_{ll} \equiv \begin{bmatrix} s_{ab} \\ s_{bc} \\ s_{ca} \end{bmatrix} \quad (5.43)$$

$$\frac{d\vec{i}_{ll}}{dt} = \frac{1}{3L} \vec{v}_{LL} - \frac{1}{3L} \vec{s}_{LL} \cdot v_{dc} \quad (5.44)$$

$$\frac{dv_{dc}}{dt} = \frac{1}{C} \vec{s}_{LL}^T \cdot \vec{i}_{LL} - \frac{v_{dc}}{RC} \quad (5.45)$$

Recall from Fourier analysis and the earlier subsection that the average of a signal is defined by (5.46). If (5.44) and (5.45) are substituted into (5.46), the average model of the pulse width modulated rectifier can be shown to be (5.47) and (5.48).

$$\bar{x}(t) = \frac{1}{T} \int_{t-T}^t x(\tau) d\tau \quad (5.46)$$

$$\frac{d\bar{i}_{ll}}{dt} = \frac{1}{T} \int_{t-T}^t \left(\frac{1}{3L} \bar{v}_{LL}(\tau) - \frac{1}{3L} \bar{s}_{LL}(\tau) \cdot v_{dc}(\tau) \right) d\tau = \frac{1}{3L} \bar{v}_{LL} - \frac{1}{3L} \bar{d}_{LL} \cdot \bar{v}_{dc} \quad (5.47)$$

$$\frac{d\bar{v}_{dc}}{dt} = \frac{1}{C} \bar{d}_{LL}^T \cdot \bar{i}_{LL} - \frac{\bar{v}_{dc}}{RC} \quad (5.48)$$

An important integral property, (5.49), was utilized in the equation averaging and is valid if and only if the maximum frequency components of $v_{dc}(t)$ is much less than half the converter switching frequency. The average of the switching function, $s(t)$, is also defined as the duty cycle, d in (5.50).

$$\bar{v}_{ab} = \frac{1}{T} \int_{t-T}^t s_{ab}(\tau) \cdot v_{dc}(\tau) d\tau \approx \bar{s}_{ab} \cdot \bar{v}_{dc} = d_{ab} \cdot \bar{v}_{dc} \quad (5.49)$$

$$d_{ab} = \bar{s}_{ab}(t) = \frac{1}{T} \int_{t-T}^t s_{ab}(\tau) d\tau = d_a - d_b \quad (5.50)$$

Using (5.47) and (5.48), the pulse width modulated boost rectifier average model is illustrated in Figure 5.9. For further reading on the subject, consider [108].

The most straightforward way of controlling the DC voltage output of the boost rectifier resulting in modification to the real and reactive power references is through the control scheme provided in Figure 5.10. For further information, consult [109].

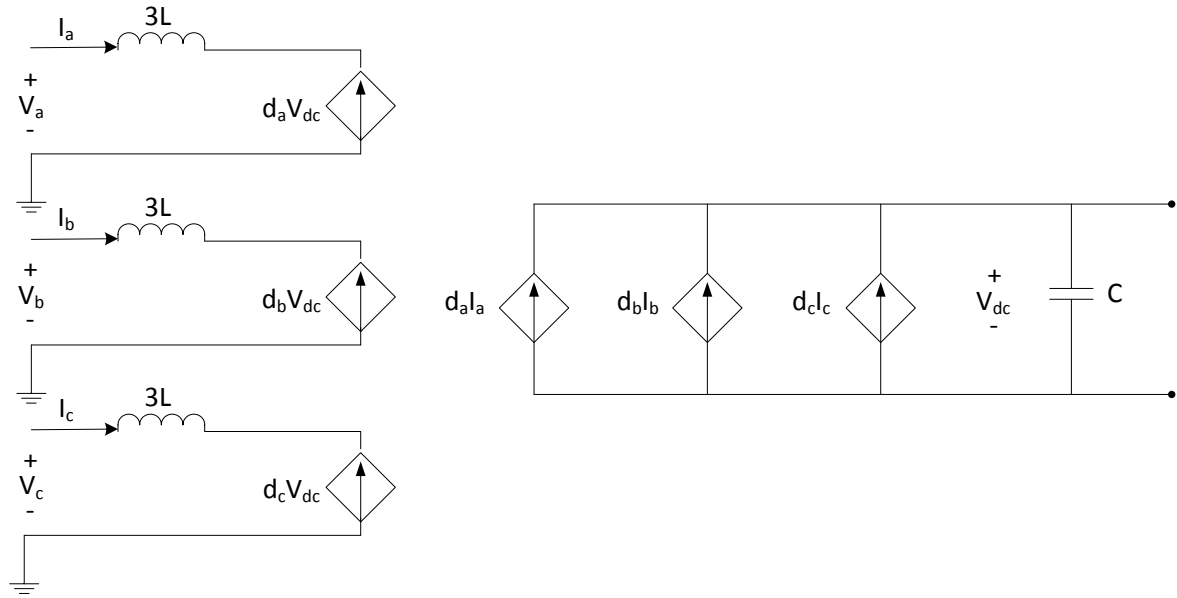


Figure 5.9: Average Model of Pulse Width Modulated Inverter/Rectifier

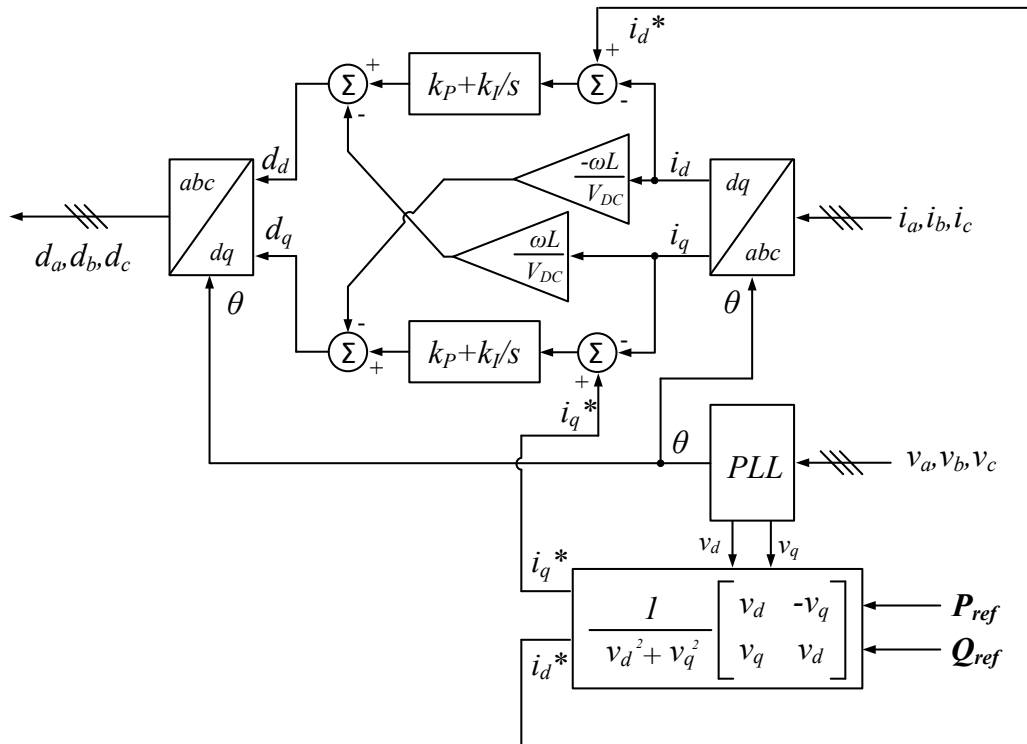


Figure 5.10: Open Loop PQ Regulator of Pulse Width Modulated Boost Rectifier

5.2.3 Average Model Implementation of Neutral Point Clamped Converter in Simulink

The half-bridge converter is a basic building block for the multilevel neutral point clamped converter. The neutral point clamped converter is utilized to interface the wind turbine to the medium voltage DC bus bar and the bidirectional DC/DC converter to the motor drive. The average model of the half-bridge converter was adequately discussed in Section 5.2.1. Using the terminal voltage of the converter described by (5.32) and noting the power balance relationship written as (5.51) that relates the AC and DC sides, Figure 5.11 provides the average circuit model of the neutral point clamped converter. The modulation index, shown in red, is dynamic whose value is adjusted by the control system.

$$i_{dc}V_{dc} = v_{ta}i_a + v_{tb}i_b + v_{tc}i_c \quad (5.51)$$

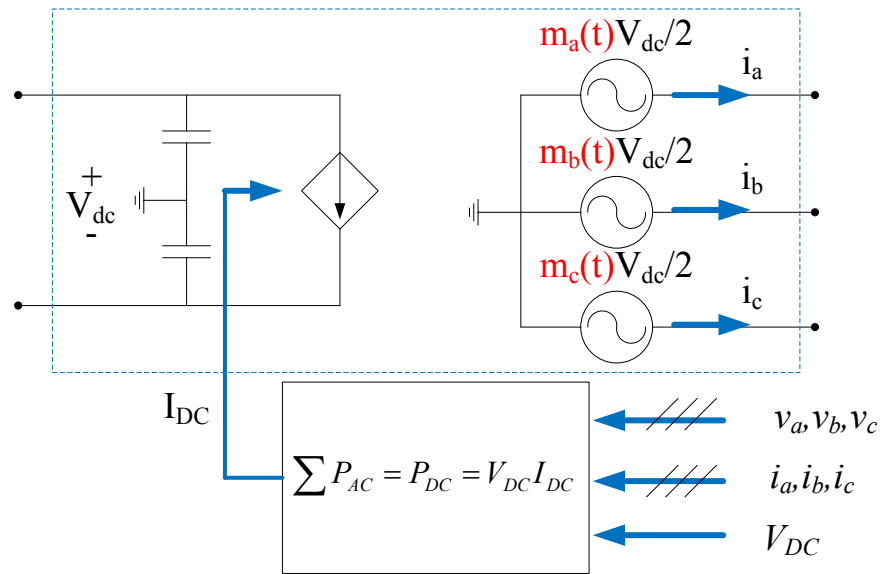


Figure 5.11: Average Model of Neutral Point Clamped Converter

Figure 5.12 shows the detailed and average output voltage responses for a three level multilevel converter – the line-to-line output has five levels as shown.

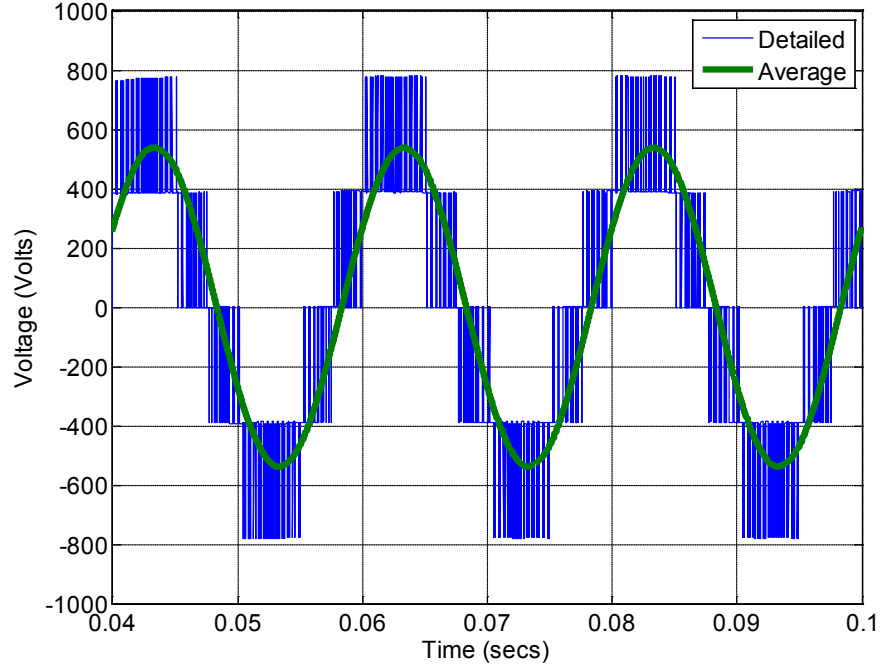


Figure 5.12: Detailed and Average Model Output Voltage Waveform of NPC Inverter

5.2.4 Average Model of Bidirectional DC/DC Converter

The average model of the dual active bridge was covered in Chapter 4. The proof of the relationships was not shown at the time. Consider the average DC input current of the dual active bridge, I_g , mathematically written as (5.52), where d is the duty cycle and I_p is the peak DC input current as was shown in Figure 4.4.

$$\bar{I}_g = I_p(1 - d) \quad (5.52)$$

Equation (5.52) is in terms of the peak DC input current, I_p . Converter equations should normally be written in terms of known parameters. Recalling that the slope of the DC input current can be written from the constitutive relationship for the voltage across an inductor, we can rewrite I_p in terms of the system input parameters (V_g, L_{Tx}, T_s, d). This relationship is listed as (5.53). Substituting (5.53) into (5.52), we arrive at the average DC input current, (5.54), for

both the primary side current and input current of the DAB converter. Comparing (5.54) and (4.2) and one will note similar expressions scaled by the transformer turns ratio. Figure 5.13 provides the circuit schematic of the DC/DC converter average model implemented in Matlab/Simulink.

$$I_p = \frac{1}{n} \frac{V_g}{L_T} \left(\frac{dT_s}{2} \right) \quad (5.53)$$

$$\bar{I}_g = \frac{1}{n} \frac{V_g}{L_T} \left(\frac{dT_s}{2} \right) (1-d) \quad (5.54)$$

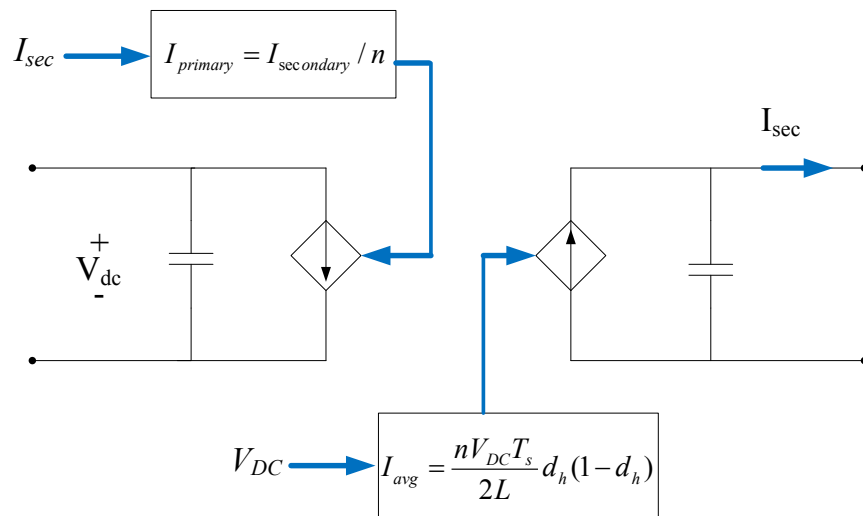


Figure 5.13: Average Model of Bidirectional DC/DC Converter

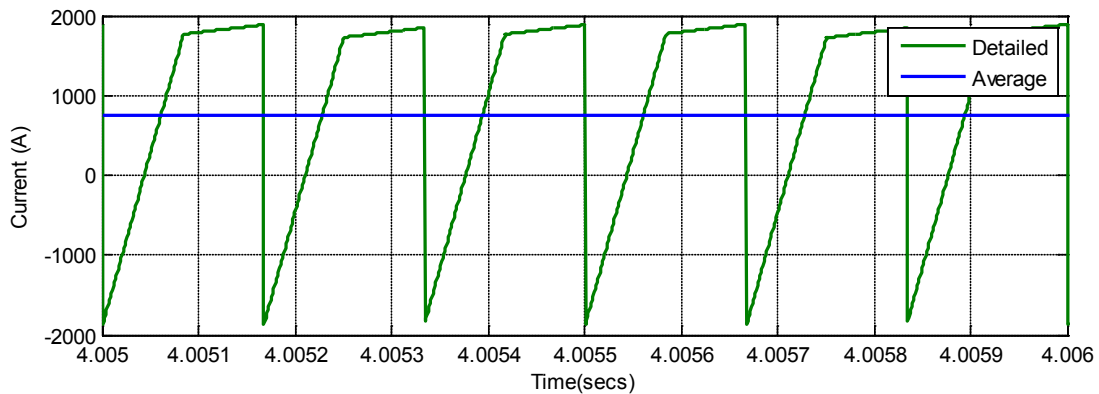


Figure 5.14: Illustration of Detailed and Average Model Currents for the Bidirectional DC/DC Converter

5.3 VARIABLE FREQUENCY DRIVE MODEL

Figure 5.15 shows a schematic diagram of a variable frequency drive used to control an induction motor/generator. The voltage sourced converter (VSC) is a three-level neutral point clamped converter mentioned in previous sections. The objective of this section is to establish the mathematical principles of how the machine is controlled with flux and current controllers. A few plots showing successful model implementation into Matlab/Simulink will be provided as done in previous sections. For a thorough treatment of the derivation refer to [76].

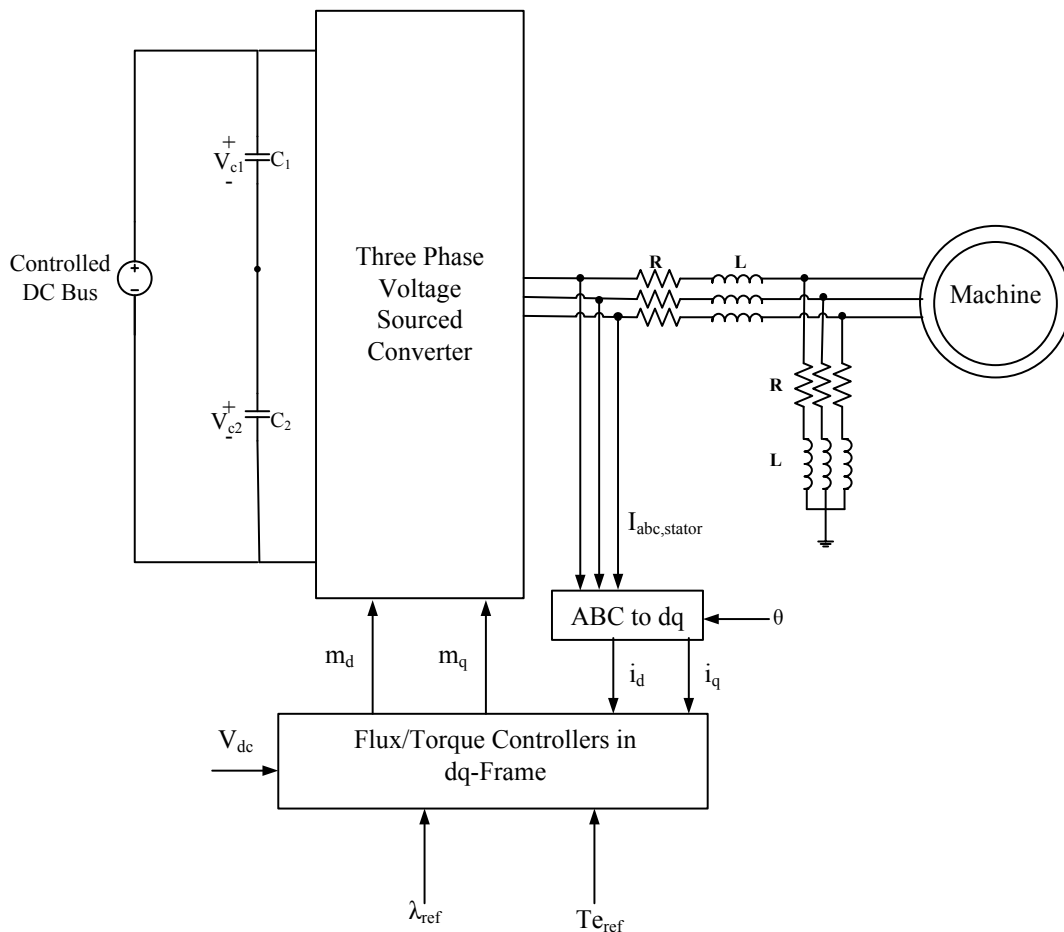


Figure 5.15: Variable-Frequency Voltage Sourced Converter for Controlling Induction Machine

The equations which govern the electrical dynamics of a symmetrical three-phase AC machine are provided in (5.55), (5.56), (5.57), and (5.58). Subscripts s , r , and m refer to the stator, rotor, and magnetization branch, respectively in all relationships. Note that all voltages, currents, and flux linkages denoted by λ are space vectors in the dq plane. The rotor position with respect to the stator is represented by variable θ_r . Traditional leakage factors denoted by σ are defined by (5.59), (5.60), and (5.61) for the stator, rotor, and total leakage factor, respectively. The stator time constant is defined by (5.62).

$$\frac{d\vec{\lambda}_s}{dt} = \vec{V}_s - R_s \vec{i}_s \quad (5.55)$$

$$\frac{d\vec{\lambda}_r}{dt} = \vec{V}_r - R_r \vec{i}_r \quad (5.56)$$

$$\vec{\lambda}_s = L_m \left[(1 + \sigma_s) \vec{i}_s + e^{j\theta_r} \vec{i}_r \right] \quad (5.57)$$

$$\vec{\lambda}_r = L_m \left[(1 + \sigma_r) \vec{i}_r + e^{-j\theta_r} \vec{i}_s \right] \quad (5.58)$$

$$\sigma_s = \frac{L_s}{L_m} - 1 \quad (5.59)$$

$$\sigma_r = \frac{L_r}{L_m} - 1 \quad (5.60)$$

$$\sigma = 1 - \frac{1}{(1 + \sigma_s)(1 + \sigma_r)} \quad (5.61)$$

$$\tau_s = \frac{L_m(1 + \sigma_s)}{R_s} \quad (5.62)$$

5.3.1 Machine Current Control

The machine flux and torque are controlled through the direct axis and quadrature axis currents. However, the VSC can only control the stator voltage. Therefore, one must relate the direct axis and quadrature axis stator currents with the stator voltages. Without sharing the mathematical abstractness of defining fictitious space phasor currents as described in [76] and [110] for the magnetization current, it can be shown that the stator current, magnetization current and stator terminal voltage are related by (5.63) where ρ is the angular position of the magnetization current with respect to the stator axis. Note that the magnetization current is aligned with the direct axis current as shown in Figure 5.16.

$$L_m \frac{d}{dt} \left[\frac{(1 + \sigma_s)(1 + \sigma_r) - 1}{1 + \sigma_r} \vec{i}_s + \frac{1}{1 + \sigma_r} \hat{i}_{mr} e^{j\rho} \right] = \vec{V}_s - R_s \vec{i}_s \quad (5.63)$$

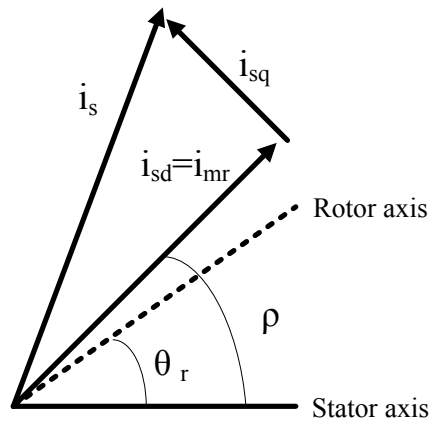


Figure 5.16: Magnetization Current Alignment in a dq Axis Frame

Substituting (5.61) and (5.62) into (5.63) and dividing through by R_s , (5.64) will be obtained. Decomposing the current and voltage space phasors into their d -axis and q -axis components, (5.65) and (5.66), using Euler's identity and substituting into (5.64), we arrive at (5.67) and (5.68).

$$\sigma\tau_s \frac{d\vec{i}_s}{dt} + (1-\sigma)\tau_s \frac{d}{dt}(\hat{i}_{mr}e^{j\rho}) = \frac{\vec{V}_s}{R_s} - \vec{i}_s \quad (5.64)$$

$$\vec{i}_s = (i_{sd} + ji_{sq})e^{j\rho} \quad (5.65)$$

$$\vec{V}_s = (V_{sd} + jV_{sq})e^{j\rho} \quad (5.66)$$

$$\sigma\tau_s \frac{di_{sd}}{dt} + i_{sd} = \sigma\tau_s \omega i_{sq} - (1-\sigma)\tau_s \frac{d\hat{i}_{mr}}{dt} + \frac{1}{R_s} V_{sd} \quad (5.67)$$

$$\sigma\tau_s \frac{di_{sq}}{dt} + i_{sq} = -\sigma\tau_s \omega i_{sd} - (1-\sigma)\tau_s \omega \hat{i}_{mr} + \frac{1}{R_s} V_{sq} \quad (5.68)$$

Equations (5.67) and (5.68) are nonlinear, coupled equations where V_{sd} and V_{sq} are inputs and I_{sd} and I_{sq} are outputs that can be decoupled if (5.69) and (5.70) are defined as new control inputs. The approach to be shared is a common technique done with three phase systems. Substituting (5.69) and (5.70) into (5.67) and (5.68), respectively, we arrive at two first order, single input, single output linear equations listed as (5.71) and (5.72) which are used for gain tuning. If the PI compensator gains are chosen based upon (5.73), the closed loop transfer function associated with (5.71) and (5.72) will contain one design variable, τ_i , to choose.

$$u_d = \sigma\tau_s \omega i_{sq} - (1-\sigma)\tau_s \frac{d\hat{i}_{mr}}{dt} + \frac{1}{R_s} V_{sd} \quad (5.69)$$

$$u_q = -\sigma\tau_s \omega i_{sd} - (1-\sigma)\tau_s \omega \hat{i}_{mr} + \frac{1}{R_s} V_{sq} \quad (5.70)$$

$$\sigma\tau_s \frac{di_{sd}}{dt} + i_{sd} = u_d \quad (5.71)$$

$$\sigma\tau_s \frac{di_{sq}}{dt} + i_{sq} = u_q \quad (5.72)$$

$$k_p = \frac{\sigma\tau_s}{\tau_i} \quad k_I = \frac{1}{\tau_i} \quad (5.73)$$

Figure 5.17 illustrates the current controller based upon (5.69) and (5.70) with flux observer, [110], establishing I_{mr} and ω setpoints. Specific features of the controller and magnetization current considerations will be discussed more thoroughly in Chapter 6.

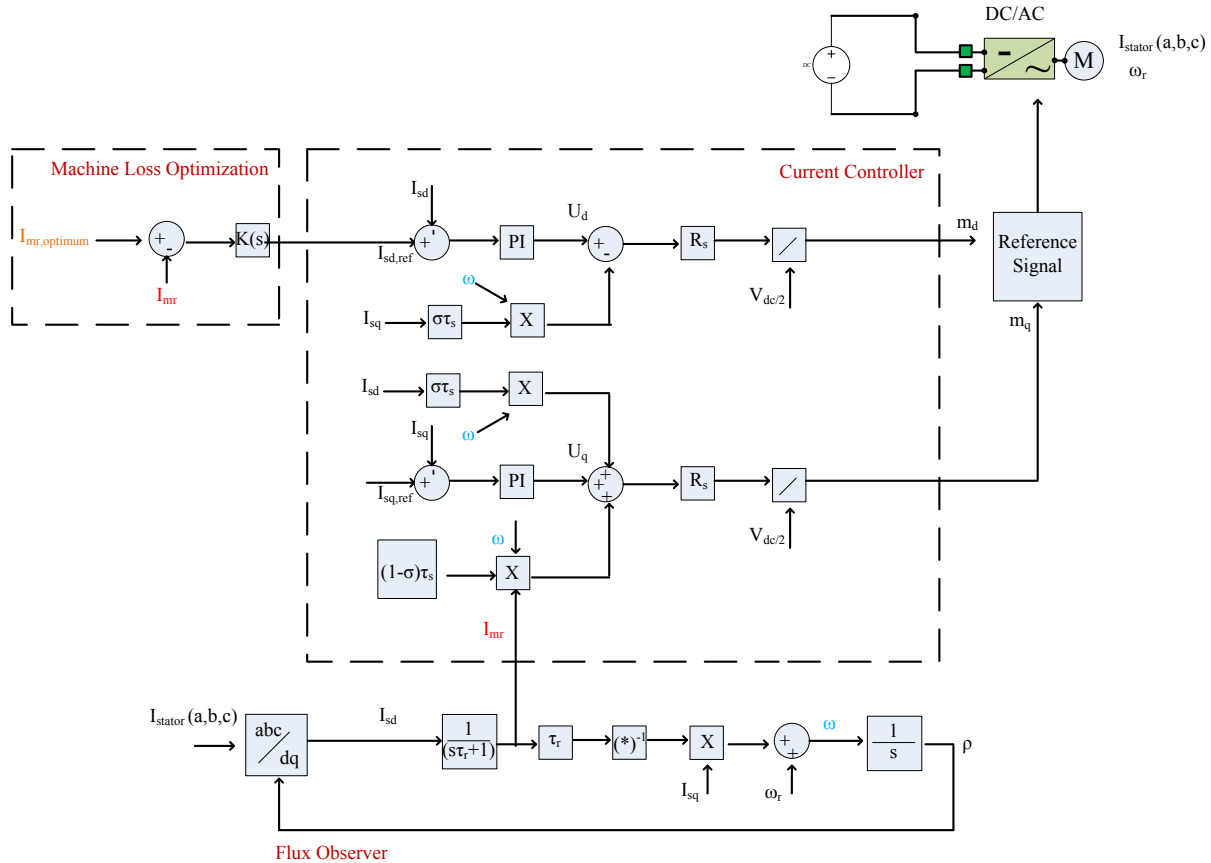


Figure 5.17: Machine Current Control

5.4 SYSTEM PARAMETERS AND ASSEMBLED DC MICROGRID VALIDATION

The DC microgrid model developed in Matlab/Simulink is found in Figure 5.18. The purpose of this section is to provide convincing arguments that the developed model is suitable for further power management studies in Chapter 6 of this dissertation. The scenario to prove model validation involves a grid disconnect at 4.0 seconds into the simulation. The only source of

generation in the model after this point comes from the wind generation and diesel generator on the platform. For our purposes, the diesel generator is modeled as an ideal three phase voltage source with uncontrolled rectifier connected to the offshore production platform low voltage bus.

At 1, 1.75, and 2.75 seconds, the motor drives rated for 1.68 MW each are connected into the network by setting their power reference controls accordingly. Also on the platform is a generic resistive load used to draw power from the diesel generator in the case for validating when the load is higher compared to the available generation (Chapter 6). For all simulations in this chapter, the wind speed is held constant at 11.8 m/s, the rated wind speed, and blade pitch set to 0 degrees to extract rated power from the generator.

One of the key takeaways from this analysis is to notice how the grid power electronics with associated controls help to isolate parts of the system network. All components are regulated except for the bidirectional DC/DC converters which are set to deliver maximum power to the loads equally. In chapter 6, the duty cycles dynamically change.

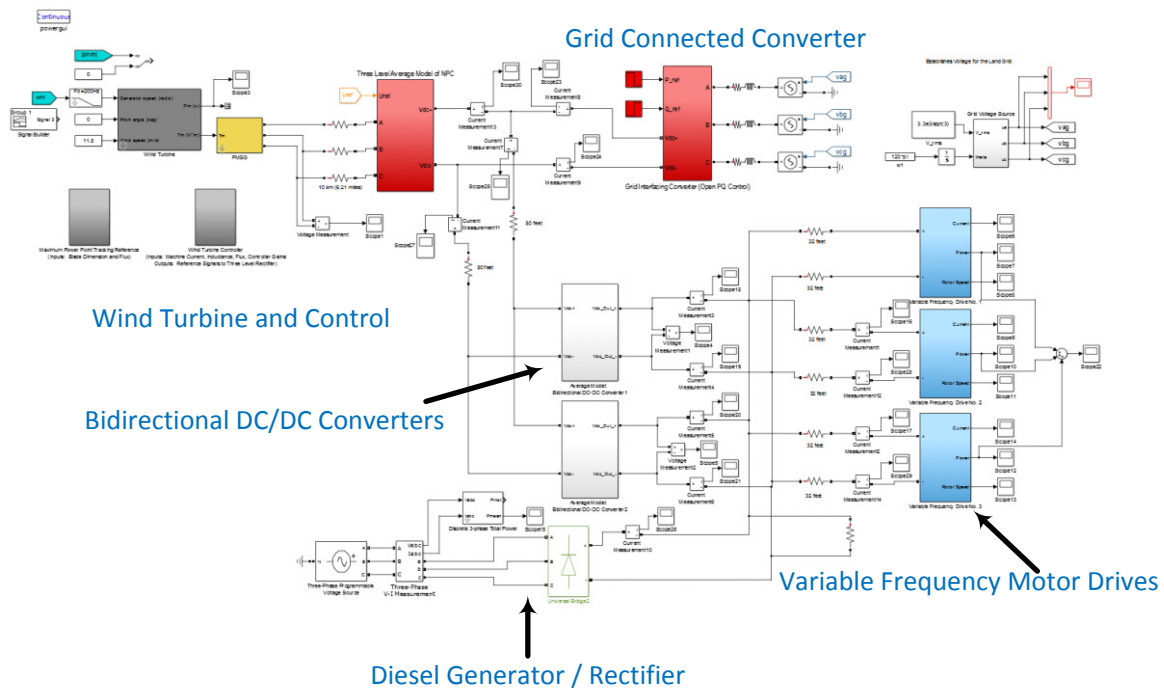


Figure 5.18: Interconnected DC Based Microgrid Computer Model

5.4.1 System Power Balance and DC/DC Converter Power Handling Capability

Figure 5.19 provides the generation source responses in the DC system. The wind turbine takes nearly 1 second of simulation time to reach full output power and maintains steady output under rated conditions even when the motors command power at 1, 1.75, and 2.75 seconds. The turbine is rated for 5 MW, 5 kV_{dc} with rectifier. The MVDC bus is slightly higher than rated as indicated in Figure 5.20 resulting in lower machine output current creating less machine torque (Equation 5.2). The wind power is also transmitted 10 km (6.2 miles) accounting for some electrical loss in the line.

The center graphic in Figure 5.19 shows the real and reactive power flowing through the grid connected, pulse width modulated rectifier. The reference power was set to 5 MW and changed to 0 MW at 4 seconds. The reference reactive power is set to zero throughout the entire simulation. The offshore platform generator supplies the remaining load on the platform if the load exceeds the total generation in the network. The load resistor is set to 1 Ω for evaluation purposes. The dynamic response of this generator is provided as the last graphic in the figure.

The currents flowing through the input of one DC/DC converter (MVDC bus side) and output of the converter are plotted in Figure 5.20. The turns ratio, $n_1 / n_2 = n$, is equal to 2. Using (4.2), we can predict the average DC current at the input and output of the converter. This calculation is provided below. The ripple on the DC current is caused by the six pulse diode bridge rectifier attached to the offshore platform DC bus. The average input current into each DC/DC converter is 823 A resulting in a total current flow of 1646 A provided by the turbine generator and grid connected converter equally.

$$I_{avg} = \frac{nV_{DC}T_s}{2L_{Tx}} d_h(1-d_h) = \frac{(2)(5481)(1/3000)}{2(208 \times 10^{-6})} (0.25)(0.75) = 1646 A$$

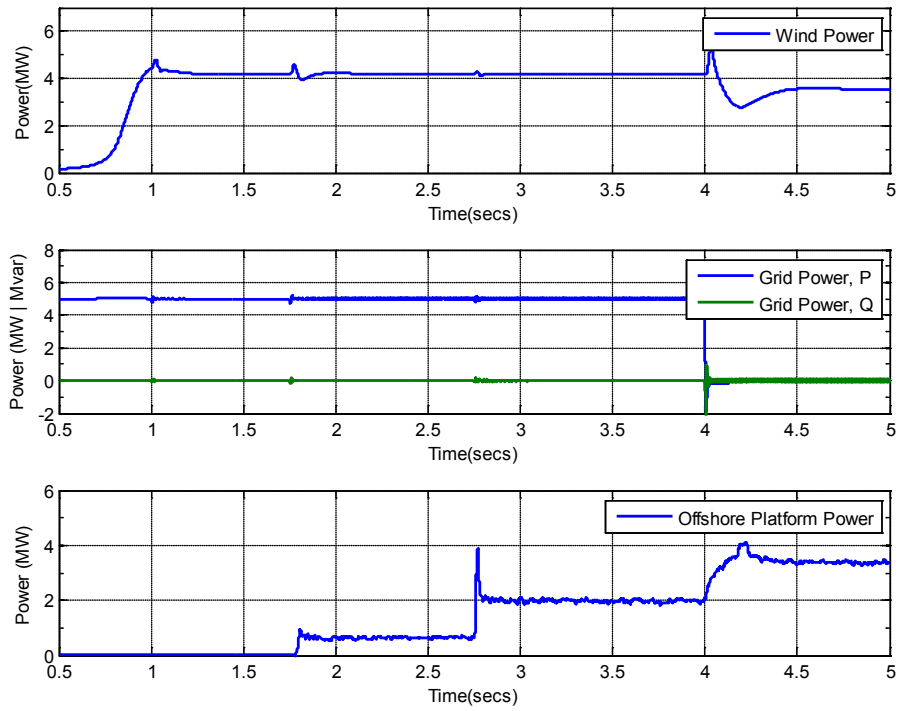


Figure 5.19: Generation Sources in Microgrid

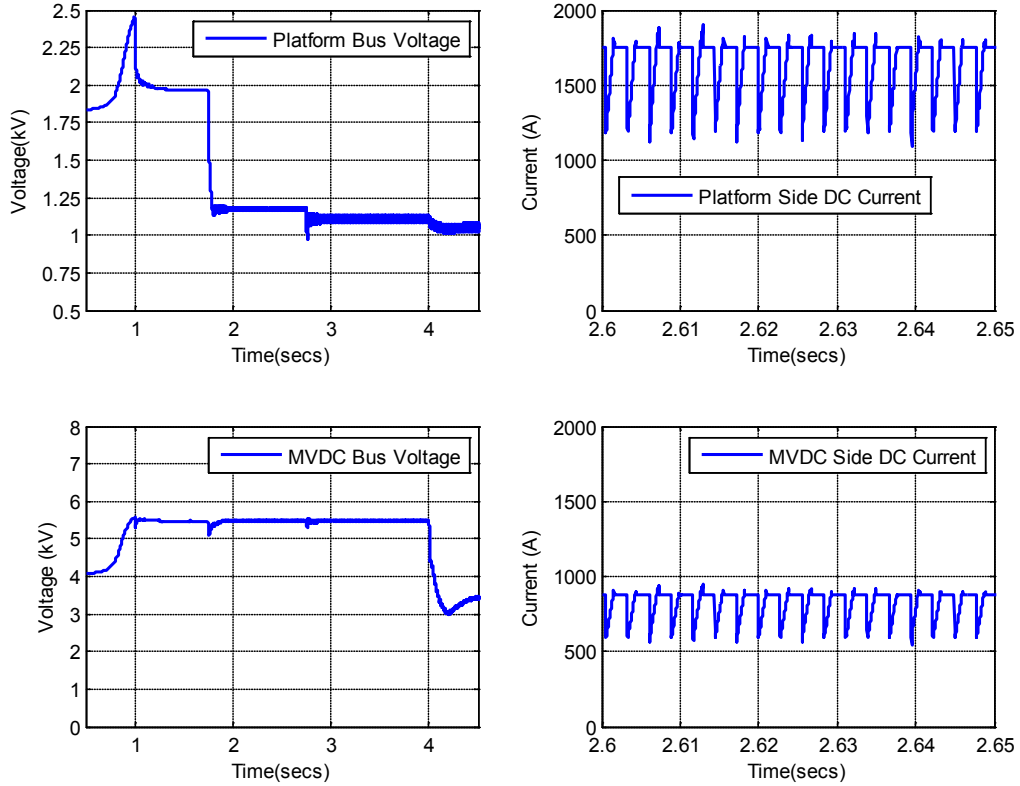


Figure 5.20: Bus DC Voltages and Currents in DC Microgrid

To explain the voltage dip that occurs at 4 seconds on the medium voltage DC bus, consider (5.1a) and (5.1b) – the equations governing the permanent magnet machine. Equations (5.74a) and (5.74b) are another form of (5.1a) and (5.1b) but in terms of flux linkage, current, and voltage. Since i_q of the wind turbine is regulated to achieve maximum power extraction, the only variable capable of changing is i_d to meet the load demand. If the d -axis current changes to something other than zero, the d -axis flux linkage is altered by decreasing – Equation (5.10) – resulting in a DC bus voltage sag as simulated. This is indeed the case as shown in Figure 5.21. *A remedy to this issue will be provided in Chapter 6 by allowing the DC/DC converter duty cycles to change, which are currently fixed in this simulation set.*

$$V_d = R_s i_d + \frac{d\lambda_d}{dt} - \omega_r \lambda_q \quad (5.74a)$$

$$V_q = R_s i_q + \frac{d\lambda_q}{dt} + \omega_r \lambda_d \quad (5.74b)$$

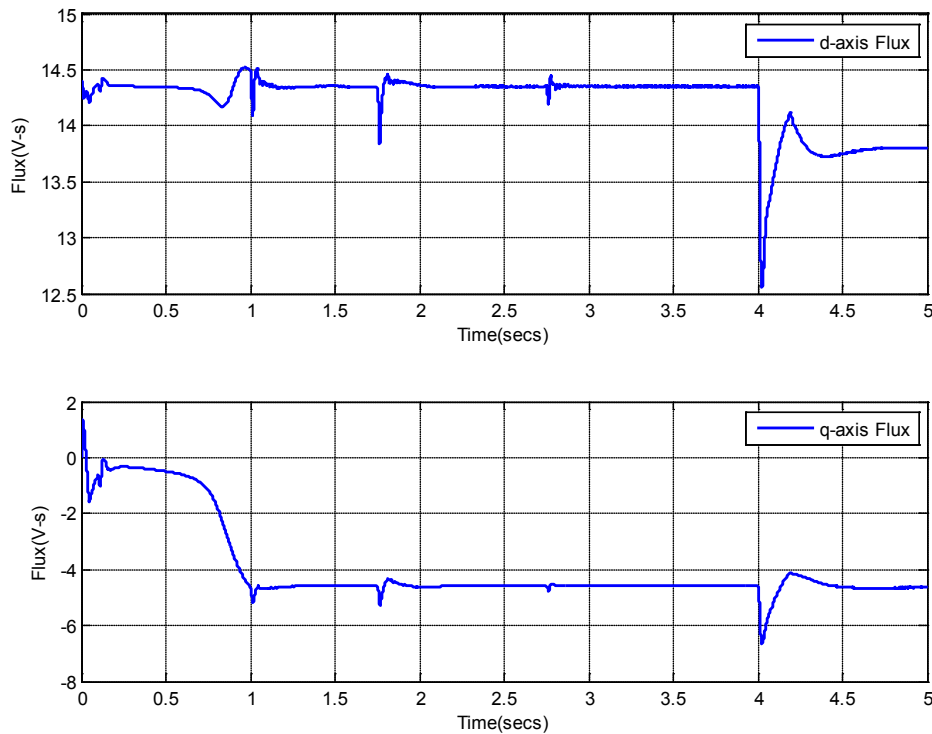


Figure 5.21: dq Flux Linkages of Wind Turbine Generator after Grid Disconnect

5.4.2 Motor Drive Responses

Regulation of the magnetization current is normally exercised during the converter start-up sequence, when the machine is at standstill, and the q -axis current is kept at zero so no machine torque is generated. Since we are dealing with larger machines on the offshore production platform, the rotor time constants are fairly large – on the order of 1 to 1.5 seconds. This implies that the currents will reach steady-state in about $5\tau_r$. To obtain a faster closed-loop response, a PI compensator, $K(s)$, is introduced to regulate the magnetization current. The drawback of a faster closed-loop response is that the d -axis current and reference point will create larger transient currents strictly due to the magnitude of the rotor time constant [76].

The machine parameters for this study are provided in Table 5.3. The reference magnetization current can be set using (5.75) under the assumption that the rotor speed regulates closely to the rated mechanical speed which is often the case to generate maximum efficiency out of the induction machine ($\eta \approx 1 - s$). Figure 5.22 provides the regulated d -axis current of 141 A and q -axis current of 7.3 kA for each machine. Knowing the rated torque and the machine speed held constant at 32 rad/s, the q -axis current can be predicted with (5.76).

$$i_{mr,ref} = \sqrt{\frac{2}{3}} \frac{V_{LL}}{(1 + \sigma_s)L_m \omega_o} \quad (5.75)$$

$$T_e = \frac{3}{2} \left(\frac{L_m}{1 + \sigma_r} \right) i_{mr} i_{sq} \quad (5.76)$$

Classic texts on machine reference theory such as [111] often designate the q -axis on the real axis and d -axis on the imaginary axis and this is how the induction machine model in Matlab/Simulink orients itself. For the derivation provided for the motor drive current regulator,

the d -axis is along the real axis and q -axis aligned to the imaginary axis. The axes orientations are provided in Figure 5.23. This will become important when interpreting the torque direction.

Table 5.3: Induction Machine Parameters [76]

Parameter	Numerical Quantity
Nominal Power, P	1.678 MW
Pole Pairs	12
Nominal Voltage, V_{LL}	2300 V
Nominal Frequency, ω_o	377 rad/s
Stator Resistance, R_s	29 m Ω
Rotor Resistance, R_r	22 m Ω
Magnetizing Inductance, L_m	34.6 mH
Stator Inductance, L_s	35.2 mH
Rotor Inductance, L_r	35.2 mH
Stator Leakage Factor, σ_s	0.0173
Stator Leakage Factor, σ_r	0.0173
Total Leakage Factor, σ	0.0337
Stator Time Constant, τ_s	1.213 secs
Rotor Time Constant, τ_r	1.6 secs
Controller Constant, τ_i	3 milliseccs
Controller Gains, $K_p; K_I$	13.67, 333 sec ⁻¹
i_{mr} Controller Gains	79.6, 50 sec ⁻¹

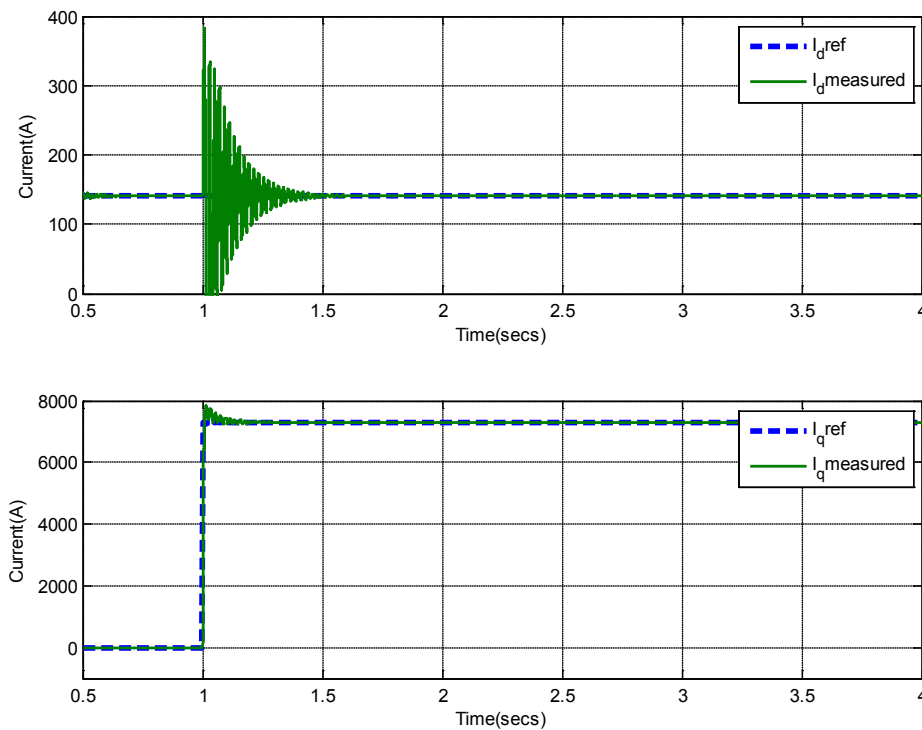


Figure 5.22: dq Current Regulation of Induction Motors

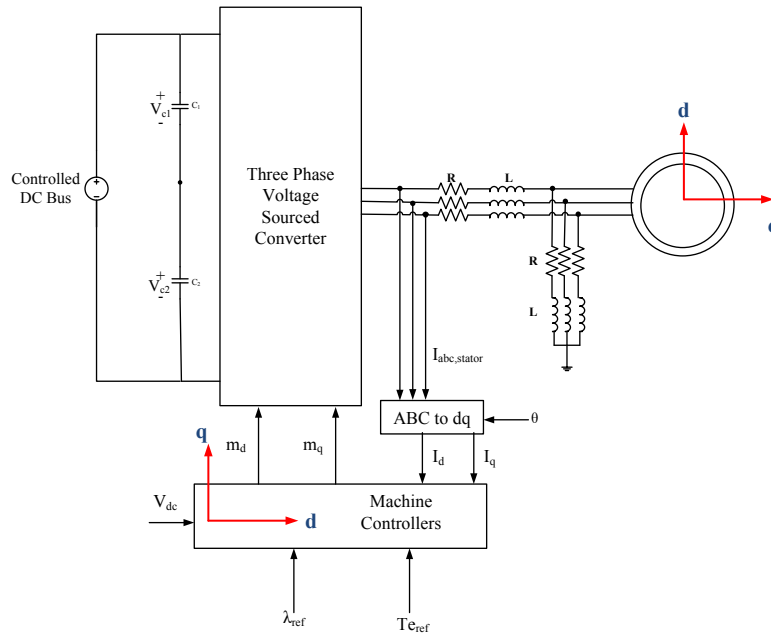


Figure 5.23: Axes Orientation for Current Controller and Motor

Our job now is to map the chosen dq controller axes onto the dq machine axes. For clarity, we will designate a subscript m for motor axis and subscript c for controller axis. Consider Figure 5.24 with our attention on graphic (a) – representative axis for the current controller – and graphic (c), representative axis for the motor. From this illustration we can write (5.77) where f is either AC voltage or current.

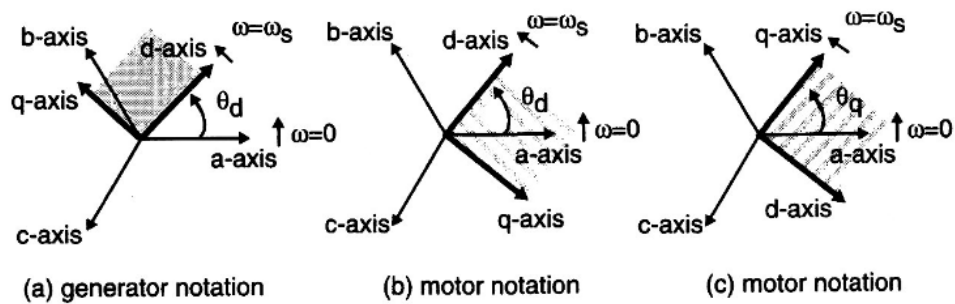


Figure 5.24: Relationship between the dq and abc Quantities for Generating and Motoring Operation[98]

$$\begin{bmatrix} f_{d,c} \\ f_{q,c} \end{bmatrix} = \begin{bmatrix} 1 & 0 \\ 0 & -1 \end{bmatrix} \begin{bmatrix} f_{q,m} \\ f_{d,m} \end{bmatrix} \quad (5.77)$$

Another expression for the induction machine torque expressed in terms of the d_m -axis and q_m -axis currents is listed as (5.78).

$$T_{e,m} = \frac{3}{2}P(\lambda_{ds,m}i_{qs,m} - \lambda_{qs,m}i_{ds,m}) \quad (5.78)$$

Substituting (5.77) into (5.78), we arrive at a torque expression for the motor mapped into the controller dq axis orientation.

$$T_{e,c} = \frac{3}{2}P(-\lambda_{qs,c}i_{ds,c} + \lambda_{ds,c}i_{qs,c}) \quad (5.79)$$

Recall that the controller d -axis is aligned with the magnetization current (see Figure 5.16) and because the stator leakage inductance, L_{ls} , is much smaller in comparison to the magnetizing inductance, L_m , we are able to simplify (5.79) to (5.80), [112].

$$T_{e,c} = \frac{3}{2}P(\lambda_{ds,c}i_{qs,c}) = \frac{3}{2}P(L_m i_{ds,c}i_{qs,c}) = -\frac{3}{2}P(L_m i_{qs,m}i_{ds,m}) \quad (5.80)$$

Table 5.4 provides the predicted steady-state results of the motor drive. Figure 5.25 shows the d -axis and q -axis simulated stator currents and machine electrical torque in the motor dq frame described earlier. For motor operation, the q -axis current must lead the d -axis current, Figure 5.24, which is indeed the case. The expected flux magnitude can be calculated with (5.81), which is a result of equating (5.80) with (5.76). Finally, Figure 5.26 provides the total demanded power by the motors as they command power at 1, 1.75, and 2.75 seconds. The dynamic behavior of the inverter modulation index for one motor is also plotted. As the offshore DC bus voltage drops due to increased load, the modulation index increases to maintain system currents (see Figure 5.11).

$$\lambda_{ds} = \frac{1}{P} \frac{L_m^2}{L_r} i_{mr} \quad (5.81)$$

Table 5.4: Predicted Motor Simulation Results

P_{rated}	ω	T_e	i_{sqLL}	$i_{sd} = i_{mr}$	λ_{ds}
1.678 MW	31.42 rad/s	53.4 kN	7.42 kA	141 A	0.4 V-s

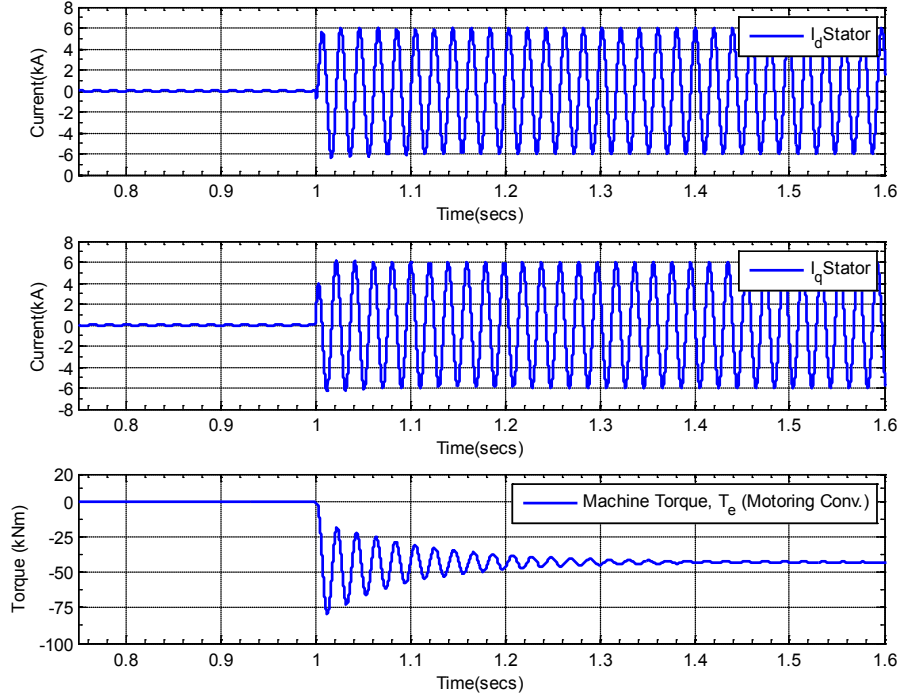


Figure 5.25: dq Stator Currents and Motor Torque

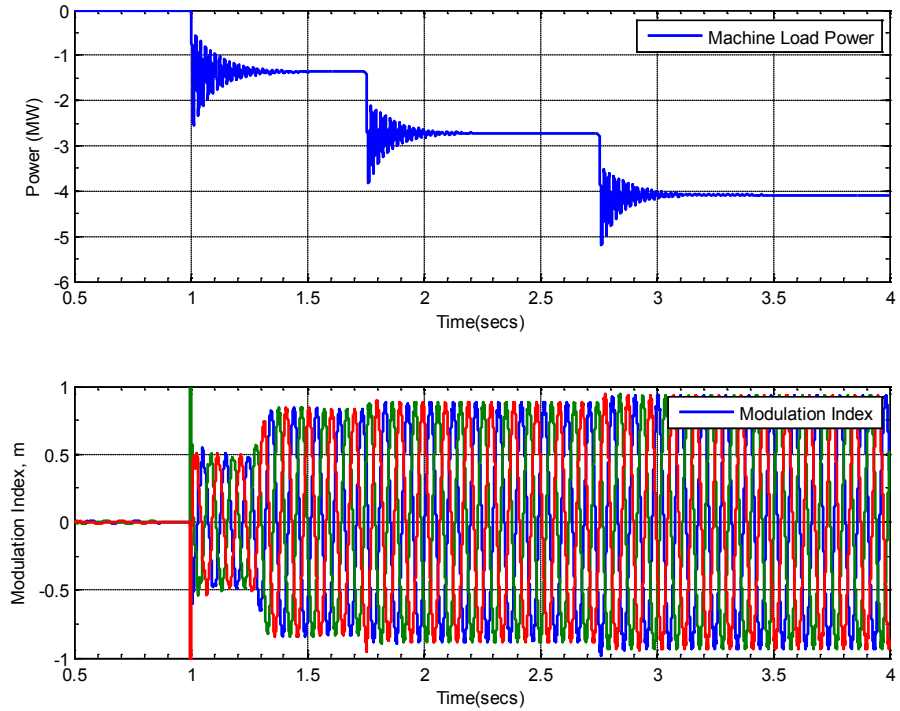


Figure 5.26: Motor Load Power and Modulation Index of Motor Inverters

6.0 DYNAMIC POWER MANAGEMENT AND DC/DC CONVERTER CURRENT SHARING EVALUATION UNDER VARIOUS MODE TRANSITIONS

In traditional AC systems, power management is critical to ensure that system generation and load are balanced so stability issues are not of concern. System frequency deviation in AC architectures from the intended set-point (50 or 60 Hz) has often been the indicator that an issue is arising – lower system frequency implies load is greater than available generation and high system frequency implies available generation is greater than total load.

As mentioned in previous sections, future microgrids will have hierarchical control structures for monitoring deviations and managing power. Figure 6.1 provides the role a central computer will play in the microgrid studied throughout this dissertation. Available power generation and power absorbed by the loads are measured and sent back to the central computer in order to coordinate power flows in the network. Power flows can be altered by adjusting the blade pitch of the wind turbine, duty cycles of the bidirectional DC/DC converters, or power reference of the grid connected converter.

In this chapter, we will focus on the power management of the microgrid assuming ideal communications. We will also study two mode transitions in this chapter including (1) main grid connected to being disconnected and (2) grid disconnected to grid connected. A low voltage ride through scenario associated within the microgrid setting is left as future work. Dynamic behavior of the real-time DC/DC converter duty cycle adjustments is of most interest to the

research team and will be emphasized. The power management routine also has the capability of scaling the amount of power flowing through each DC/DC converter. Since both converters are sized to handle 10 MW of power in the case of converter failure, simulations can be run showing that the power does not need to be equally shared between both components. In practice, it's not always guaranteed that the converters are always manufactured by the same vendor.

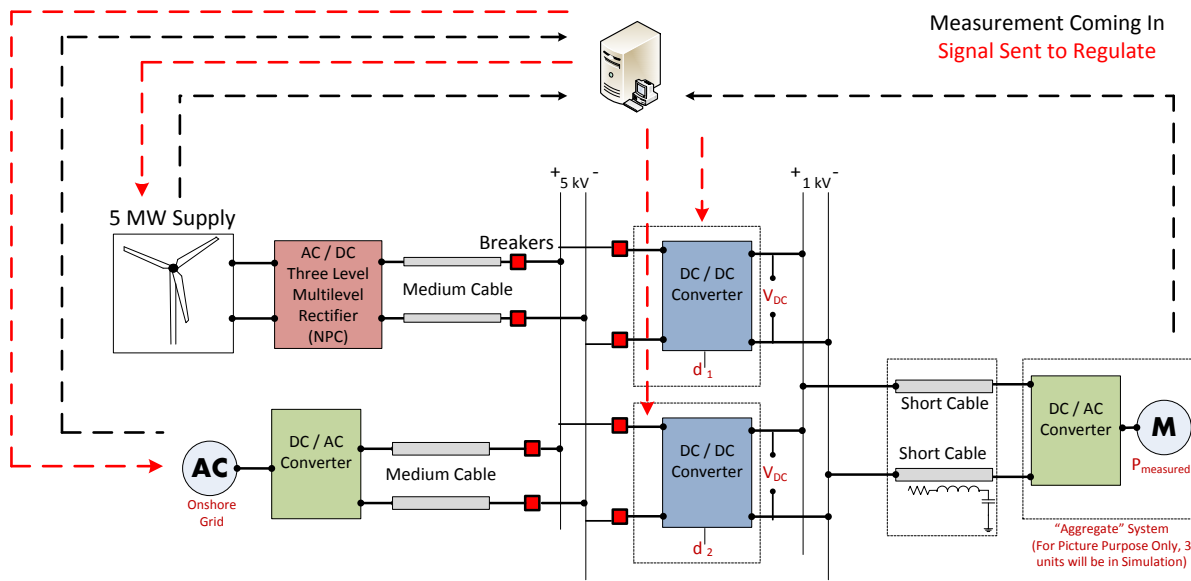


Figure 6.1: Power Signals and Coordination through Centralized Computer

6.1.1 Power Management Routine

The power flowing through the DC/DC converters is described by (6.1), where V_H is the medium voltage DC bus and V_L is the offshore production platform bus voltage. P_{tot} is the total power the converter is rated to handle – 10 MW for our system studies – and α is a scaling factor between 0 and 1. For converter sizing, this factor is set to 0.5 since two converters are assumed to be in operation at all times.

$$\alpha P_{tot} = \frac{nV_H V_L T_s}{2L_{Tx}} d_h (1 - d_h) \quad (6.1)$$

If (6.1) is solved for the duty cycle, d_h , we arrive at (6.2). If P_{tot} is 10 MW; V_H is 5 kV; V_L is 1 kV; f_s is 3 kHz; L_{Tx} is 208 μ H; and α is 0.5 then n must be set to 5 to have a positive real root as a solution to the quadratic equation. Equation (6.2) is a critical expression that is continuously solved for to adjust the DC/DC converter duty cycles as system conditions change. *In Chapter 5, the duty cycle was fixed to validate system operation.* The previous discussion is critical to ensure that the duty cycle is below 0.5 for power to flow from generation to load.

$$d_h^2 - d_h + \left[\frac{2\alpha P_{tot} L_T f_s}{nV_H V_L} \right] = 0 \quad (6.2)$$

With the approach to be presented, we assume one directional power flow in the direction of the offshore production platform and ideal communication between the central computer and diesel generator. The inputs from the primary control into the secondary power management scheme strictly include the machine electrical power and current, DC bus voltages, and all system generation. The power management architecture is found in Figure 6.2.

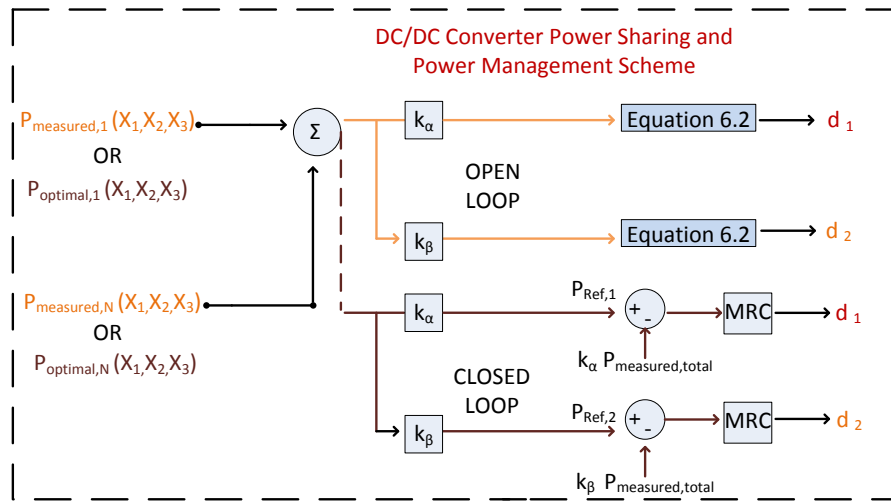


Figure 6.2: Power Management Routine for Adjusting DC/DC Converters in Microgrid

Starting from left to right in Figure 6.2, the total power generation on the MVDC side of the microgrid is summed (based on system measurements) and scaled by factors k_α and k_β . These weights range from 0 to 1 depending on the power rating of the bidirectional converter. There is one weight for each DC/DC converter. Utilizing (6.2), the duty cycle, d_h , is determined and adjusts the DC/DC converter output power. The later description can be argued to be open loop in nature with future efforts put forth into implementing the model reference control (MRC) design of Chapter 4 as shown in Figure 6.2. The power management routine is simple Matlab code programmed and communicates directly with the Simulink model as shown in Figure 6.3 – bottom left of the diagram shows a white bin with several inputs and two outputs corresponding to the duty cycles of the DC/DC converter.

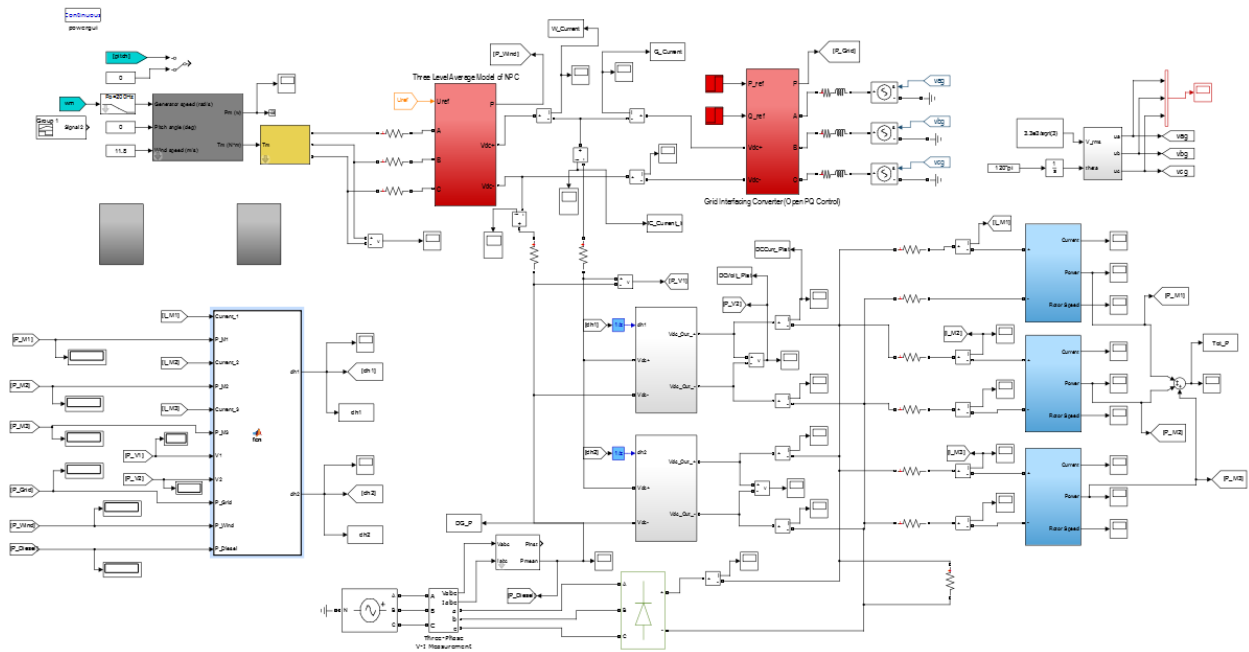


Figure 6.3: Microgrid Computer Model with Implementation of Power Management Scheme

6.1.1 DC/DC Converter Dynamic Response under a Grid Disconnection

The case under study in this section is very similar to the case studied in Chapter 5 but the DC/DC converters are able to adjust their duty cycles to allow or suppress power flow depending on load demand. The wind turbines always produce maximum power, the grid supplies 5 MW and disconnects at 4 seconds into the simulation. The motor drives command power at 1 second, 1.75 seconds, and 2.75 seconds and are all rotating at a fixed speed of 32 rad/s (rated mechanical speed). A 0.25 Ω resistor is attached to the offshore platform bus. The bidirectional DC/DC converter No. 1 (closest to the generation) has a scaling factor, k_α , equal to 0.6 and converter No. 2 has a scaling factor, k_β set to 0.4. This implies that 60% of the power generation will flow through No.1 and 40% through No. 2.

Figure 6.4 provides the generation profiles as a function of time. Because the generation supplied through the pulse width modulated rectifier completely diminishes to zero, there is not enough power generation to supply the motor drives and the resistive load in the network, thus, resulting an increased output from the diesel generation in the system. The dynamic behavior of the DC/DC converter duty cycles is provided in Figure 6.5 adjusting with changes in system load and available power generation. Sample calculations for the first time interval of Figure 6.5 are provided below.

$$d_h^2 - d_h + \left[\frac{2\alpha P_{tot} L_T f_s}{n V_H V_L} \right] = d_h^2 - d_h + \left[\frac{2(0.6)(5MW + 4.2MW)(208\mu)(3000)}{(5)(7442)(1516)} \right] = 0$$

$$d_{h,No.1} = 0.1422 \text{ or } 0.8577$$

$$d_h^2 - d_h + \left[\frac{2\alpha P_{tot} L_T f_s}{n V_H V_L} \right] = d_h^2 - d_h + \left[\frac{2(0.4)(5MW + 4.2MW)(208\mu)(3000)}{(5)(7442)(1516)} \right] = 0$$

$$d_{h,No.2} = 0.089 \text{ or } 0.910$$

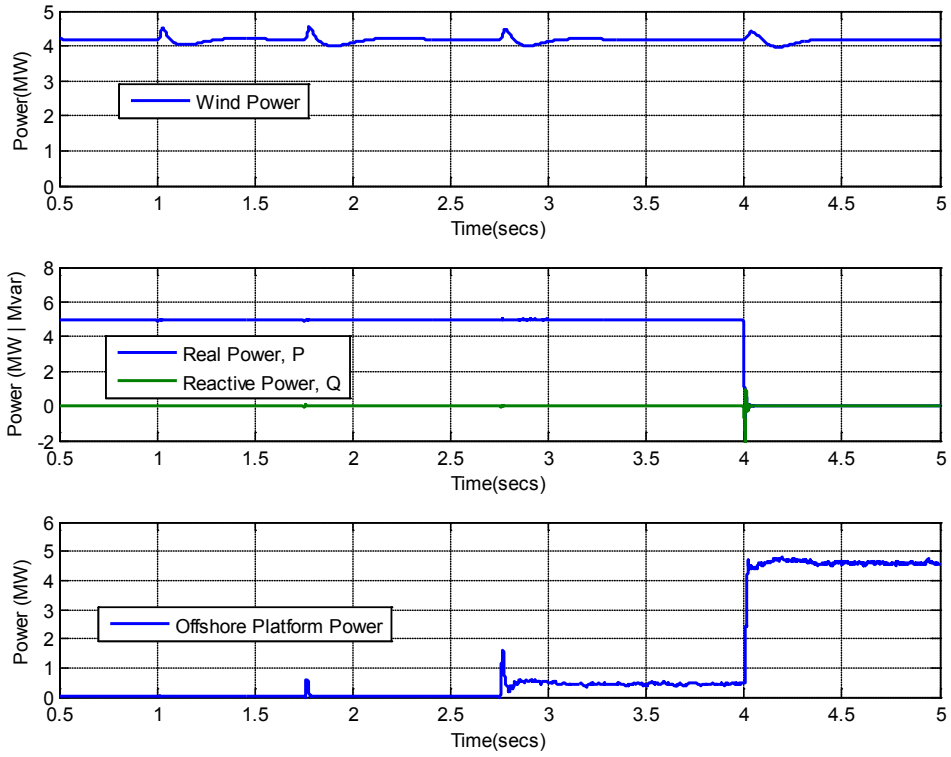


Figure 6.4: System Generation Response During a Grid Disconnect

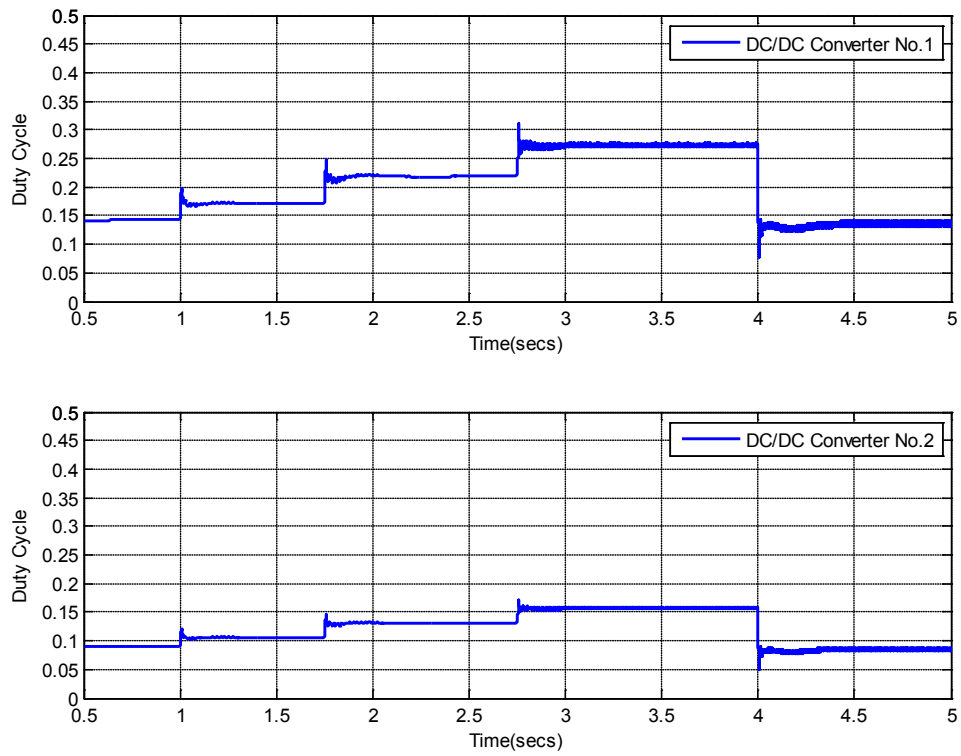


Figure 6.5: DC/DC Converter Duty Cycle Response

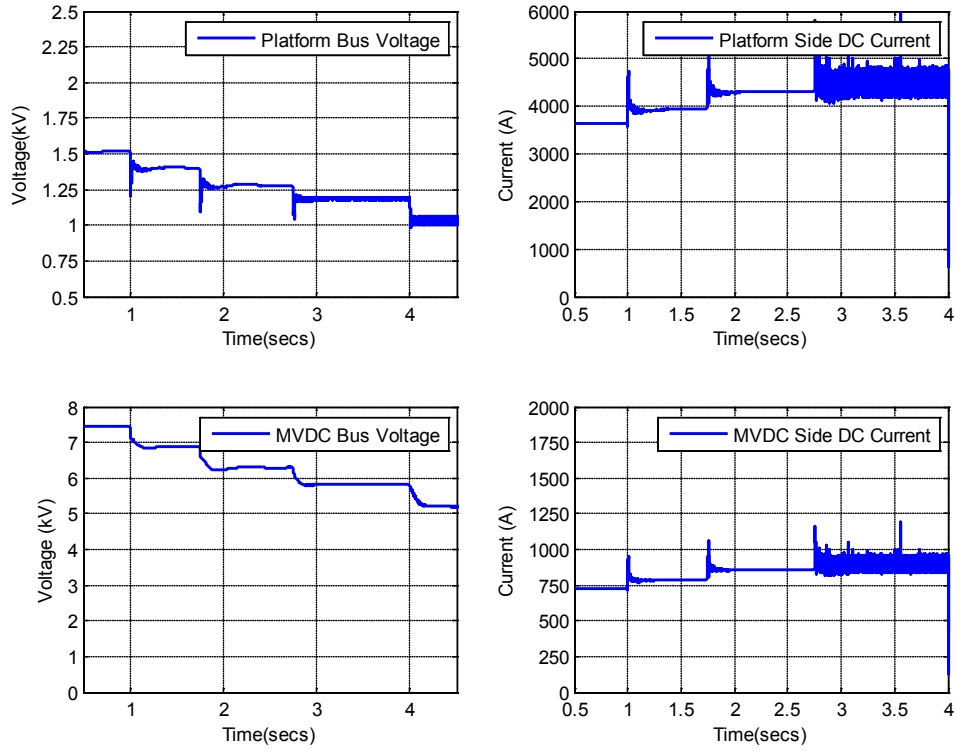


Figure 6.6: DC Bus Voltages and Current Flows in Case of Grid Disconnect

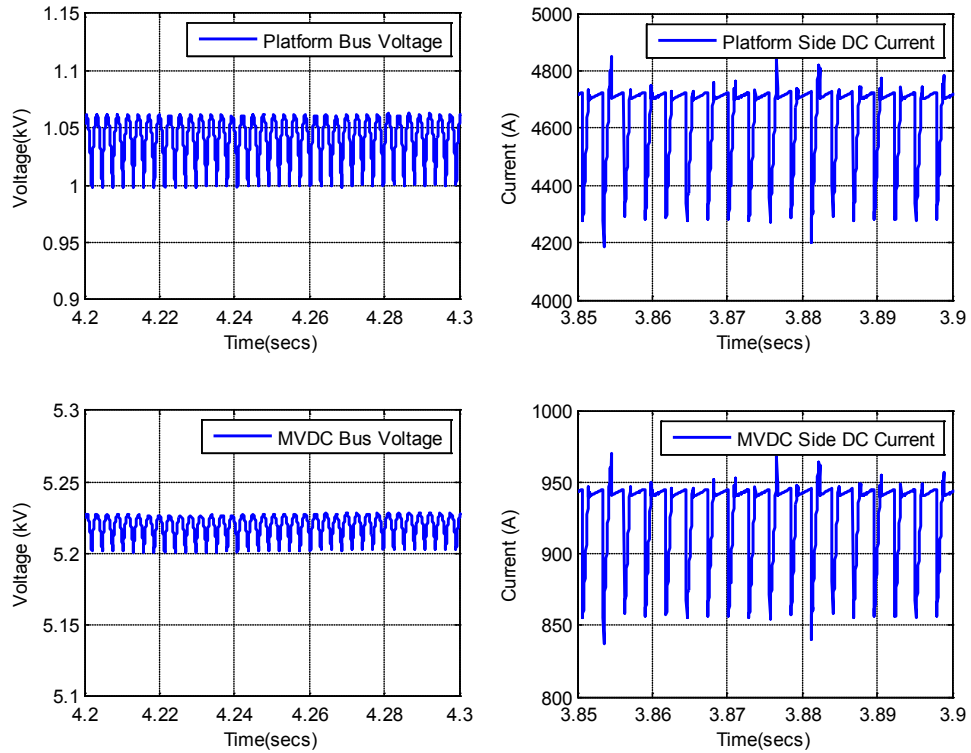


Figure 6.7: Zoomed-In Intervals of Figure 6.6 Providing Finer Electrical Characteristics

Figure 6.6 provides DC bus voltages on the medium voltage bus bar and offshore production platform bus bar as well as current flows along the rails of these busses. Constant power load characteristics are also observed. As voltage drops because power is commanded by the motor drives, current increases to maintain desired power to the motors. High ripple is observed in the current as full load is brought into service at 2.75 seconds into the simulation. Zoomed-in regions of the currents and voltages at points beyond 2.75 seconds are provided in Figure 6.7. The characteristic pulses generated by the rectifier attached to the low voltage DC bus are observed, which are naturally reflected onto the medium voltage DC bus through the interfacing DC/DC converters. The scaled currents through each of the DC/DC converters are provided in Figure 6.8. Remember, the duty cycles are a function of k_α and k_β .

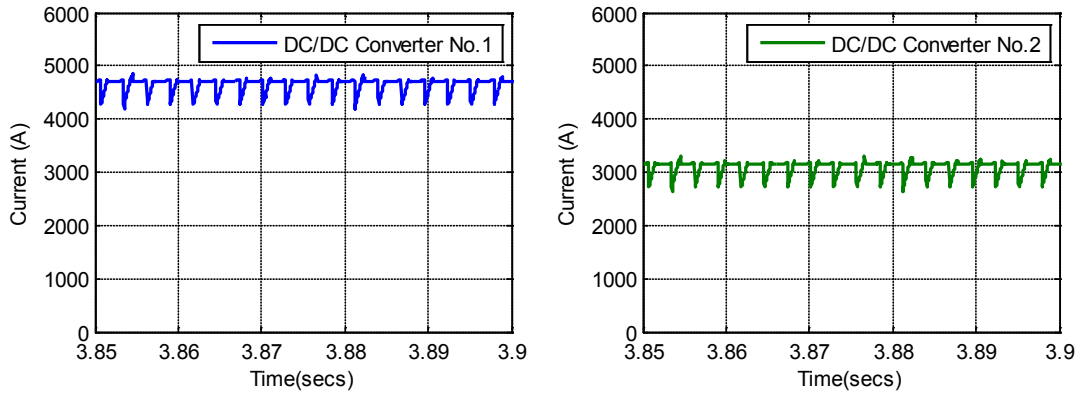


Figure 6.8: Output Currents of DC/DC Converters for Grid Disconnect Scenario – 60% / 40 % Weighting

$$I = \frac{nV_H T_s}{2L_T} d_h (1 - d_h) = \frac{(5)(5832)(1/3000)}{2(208\mu)} (0.273)(1 - 0.273) = 4.64kA$$

$$I = \frac{nV_H T_s}{2L_T} d_h (1 - d_h) = \frac{(5)(5832)(1/3000)}{2(208\mu)} (0.1572)(1 - 0.1572) = 3.10kA$$

Finally, for completeness, Figure 6.9 provides the dynamic response of the wind generator currents, wind generator current controller, and current supplied by the grid up until

grid disconnection. The high ripple wind generator current is noticeable at 2.75 seconds and, when noticed at a finer resolution, takes on similar characteristics as those shown in Figure 6.7.

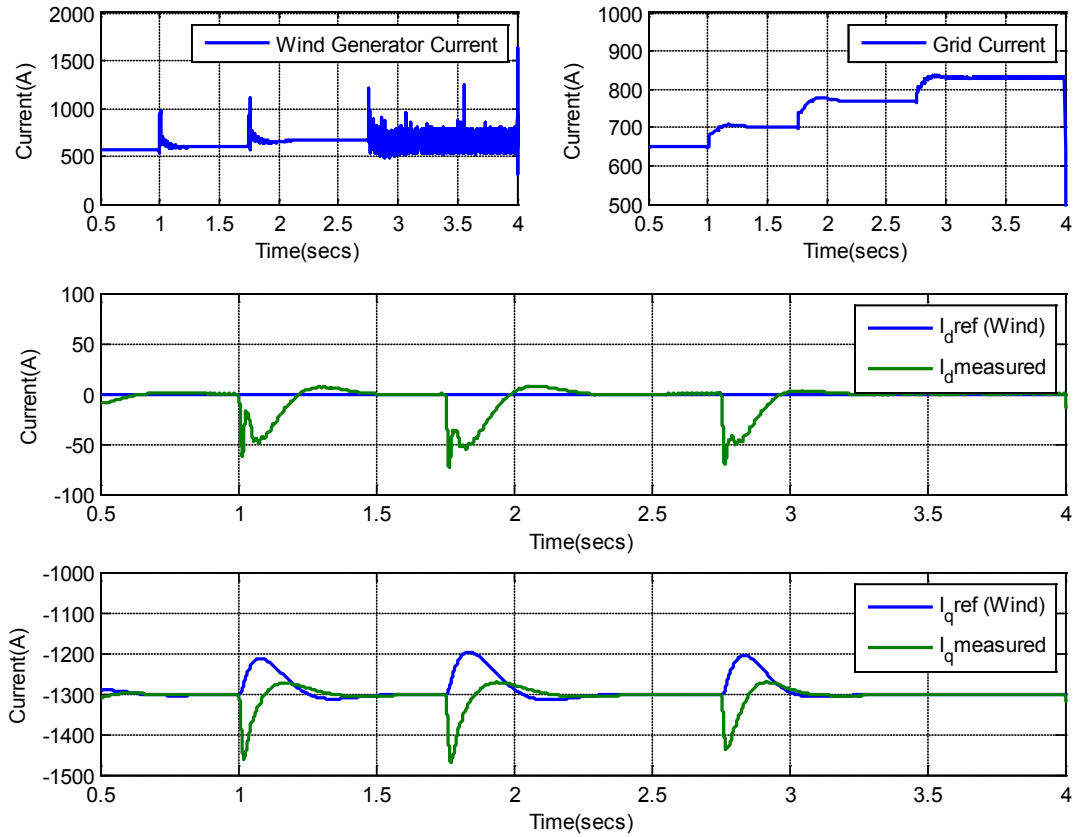


Figure 6.9: Wind Generator Currents and Grid Connected Converter Current for Grid Disconnect Scenario

At the time this dissertation is being written, research attention has been focused upon sharing power between parallel connected converters as presented in [113]. Future efforts will for sure be centered upon the microgrid case, as was done in this chapter, and with a nicely written article starting the trend in [114].

6.1.2 DC/DC Converter Dynamic Response under a Grid Connection

For the grid connected scenario, we consider the case when the total generation in the system becomes much larger in comparison to the total load when the grid interfacing converter is commanded to deliver 5 MW of power. This converter essentially transitions from a disconnected to grid connected state. The wind turbine is continuously feeding maximum rated power into the network and only one motor drive is active in the circuit at all times with the other two out of service. The generic load of 0.25Ω remains in the circuit. With this simulation study, one can postulate that the dynamic behavior of the DC/DC converters act as an aid for improving system stability as compared to the time to mechanically alter the blade pitch of the wind turbines. DC/DC converter No.1 and No.2 are set to share 60% and 40% of the total current, respectively, as in the previous section.

Figure 6.10 provides the generation profiles of the wind, power flowing through the grid connected converter, and diesel generation power on the offshore production platform. Notice that once the grid connected converter commands power at four seconds, the diesel generation is no longer needed to supply the offshore load – truly an economic benefit. Figure 6.11 shows the dynamic behavior of the DC/DC converter duty cycles. The duty cycles are initially low and, once more generation becomes available, the duty cycles increase allowing more generation to flow through the converter to meet the desired load. Finally, the detailed current waveforms of each of the DC/DC converters are provided in Figure 6.11.

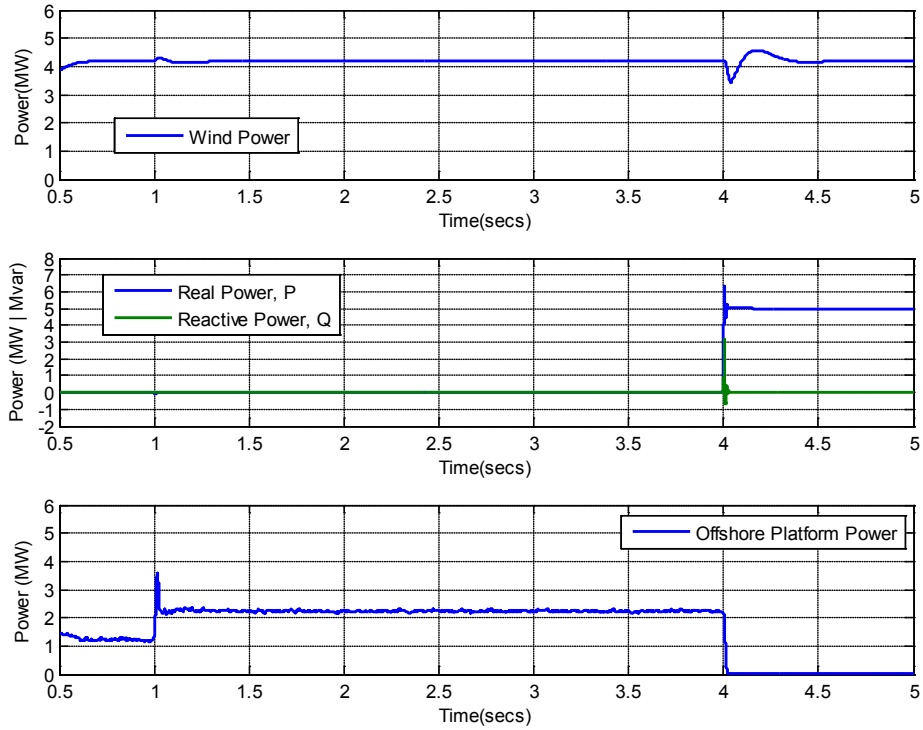


Figure 6.10: System Generation Response During a Grid Connection

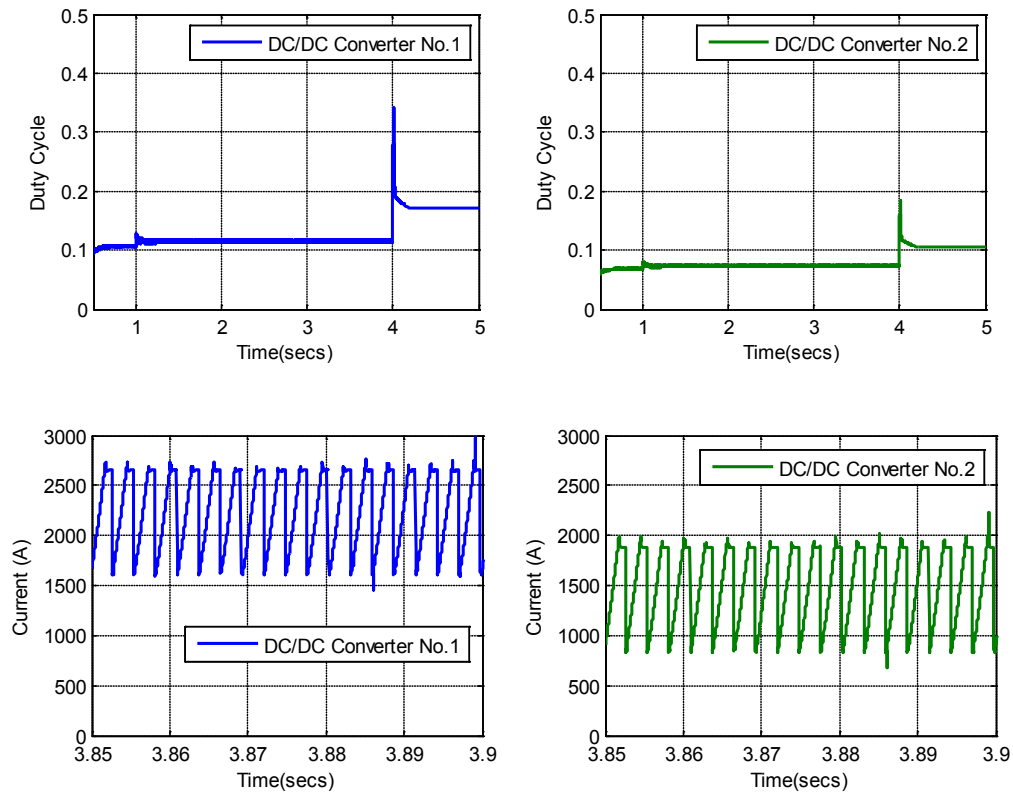


Figure 6.11: Duty Cycles and Output Currents of DC/DC Converters – 60% / 40% Weighting

7.0 CONSIDERATIONS FOR DESIGNING THE COMMUNICATION NETWORK ARCHITECTURE OF THE OFFSHORE DC MICROGRID

Emphasis has been placed on the electrical design of the offshore microgrid to this point. The electrical system also needs to work in tight synchronization with the signaling system provided by the telecommunication subsystem. Fast cooperation of those systems is dependent upon scalable and intelligently designed co-existent architectures. As discussed in previous chapters, the microgrid control architectures can be summarized by three layers: primary, secondary, and tertiary control. Each one of these layers is a separate physical entity that may or may not be owned by the same operator. Each control layer must function in unison with each other in a scalable and highly efficient manner. Designing the communication network architecture to meet the stringent real-time operation requirements of the control layers is the focus of this chapter.

This chapter will provide an overview of the distributed control architecture, including the microgrid and wide-area communication networks. Telecommunication technological options, security, and addressing protocols for the microgrid architecture will also be conveyed. This chapter is published in [115].

7.1 COMMUNICATION NETWORKS

Communication network architectures are described in terms of the seven layer OSI Model [116]. For the purposes of the following discussion, the focus is on layers two and three – Media Access Level (MAC) and Internet Protocol (IP). The MAC layer provides the functionality to send and receive data between a transmitter and a receiver, within the bounds of the same network. Basic transmission error checking is provided. The IP layer builds upon, adding intra-network addressing, substantially improved error checking, retransmission capabilities for lost packets, congestion control, and session management (via Transmission Control Protocol (TCP) and User Datagram Protocol (UDP)). In-depth discussion of the OSI Model and above mentioned protocols is out of the scope of this chapter, with additional resources provided [117].

Due to the real-time, and safety critical nature of the drilling operation, the communication network has to provide above all fast, reliable and secure service. The entire communication network can be envisioned as two separate networks: (1) microgrid network and (2) wide-area communication network. The microgrid network includes the DC/DC converters, induction machines, diesel generator and respective primary and secondary controllers. The wide-area network includes the secondary control associated with the wind turbines and tertiary control, with the secondary control functioning as a bridge between the two networks. The geographical distance between the elements of the wide area network can be quite high depending on how far the wind turbines are installed from the offshore platform.

7.1.1 Microgrid Communication Network

The frequency of messages in the microgrid network is determined by the fastest cycle of a subsystem element. There are three logical channels in the network including (1) induction machine / primary controller to the secondary controller, (2) secondary controller to the DC/DC converters, (3) secondary controller to diesel generator. These channels are pictorially shown in Figure 7.1.

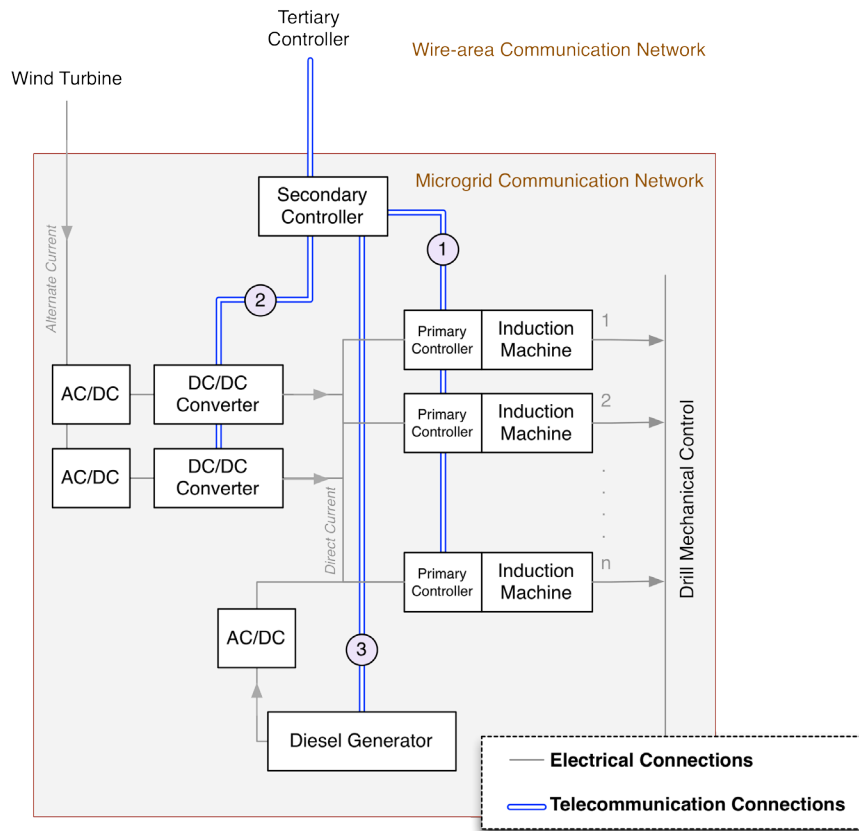


Figure 7.1: Architecture of Microgrid Communication Networks

The primary controller functions as an independent local control. The channel between the induction machine and secondary controller has the highest frequency of messages. The induction machine would provide torque and rotor speed measurements every 10 to 25 μs [118]. This rate is necessary to capture and address transient phenomenon due to grid islanding. The

two measurements provided are float values and the payload of every message is not extensive. However, the high update rate means that the number of messages received each second is quite high. Each measurement pair is unique to the induction machine and the number of measurements is proportional to the number of motors in the microgrid. Given the update cycle, the estimated number is between 5,000 and 10,000 messages per motor per second. Once the secondary controller receives the measured values from each motor, the control calculates the appropriate duty cycles for each of the two DC/DC converters (for this case) to alter the demanded power flow to the machine loads. The latency between a measured torque and motor speed and reception of the corrected control command by each DC/DC converter constitutes the control loop delay experienced by the power system.

The secondary control would contribute significantly to the delay budget. The controller would have to interface with the wide-area control network, employing IP addressing, resulting in full IP Stack included in the real-time operating system and a slower runtime cycle. One way of preventing slower runtime cycles is to have two execution cycles running in the embedded real-time operating systems of the controller. The processes should run on two physically separated processors communicating via shared memory channels as shown in Figure 7.2. This would allow the inside electrical loop controller to operate at a much higher rate by only implementing MAC layer addressing and omitting encryption/decryption operations – Steps (2) and (6) in Figure 7.2.

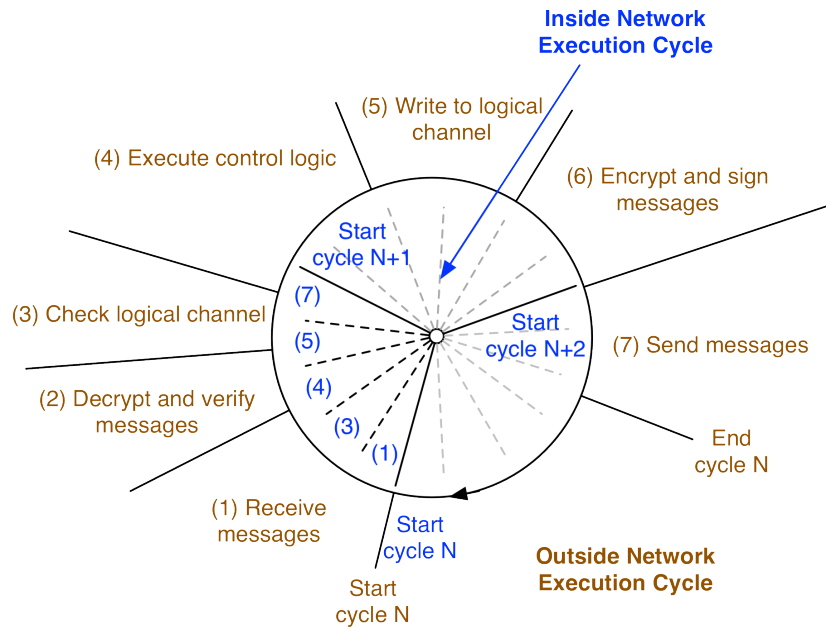


Figure 7.2: Secondary Controller's Inside and Outside Communication Cycles

The outside network application would (1) query the outside interface (IP Layer), (2) decrypt information, (3) read the logical channel for any message from inside the microgrid, (4) execute control logic, (5) write to the logical channel, (6) encrypt data, and (7) write to the outside interface at the end of its cycle. The inside loop controller would (1) receive network messages, (3) check the logical channel for any control instruction from the tertiary controller, (4) execute logic, (5) write messages to the tertiary controller, (7) and output messages to the appropriate local microgrid network port.

Even by separating the controllers in order to gain performance, it is unlikely that the inside communication cycle would be able to keep up with the 10 to 20 μ s message frequency. Without loss of generality, we assume that the inside communication execution cycle would be of at least 10 millisecond and the outside communication cycle would be around 20 millisecond.

7.1.2 Wide-Area Control Network

The tertiary controller is in charge of balancing energy supply and demand between the onshore grid, wind turbines, and one or more microgrids. In the event of insufficient wind generation, the tertiary control would initialize the diesel generators located in various microgrids in order to continue non-interrupted drilling operations. The tertiary controller would be distributed in nature with each microgrid having a dedicated top level controller as illustratively shown in Figure 7.3.

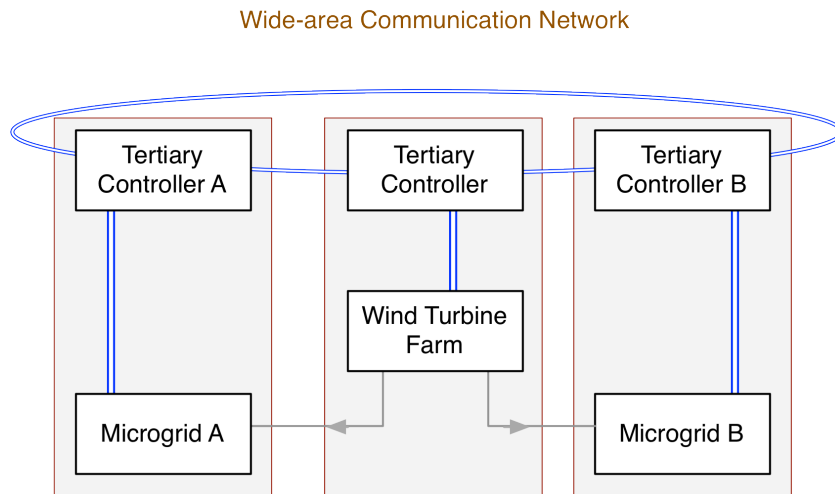


Figure 7.3: Architecture of Wide-Area Communication Network

Due to the large geographical area, the communication network would require IP addressing and significant security protocols. Contrary to the local microgrid control network, which creates messages at a deterministic high rate, the wide-area control network would be non-deterministic in nature. Two major types of messages would be present: (1) keep alive between different sub-systems, and command/failure notifications. The keep alive message would range between milliseconds to seconds. The control and failure messages are stochastic in nature, which may be a result of wind patterns or other natural phenomena as well as hardware and software failures.

Due to the size of the wide-area communication network, security becomes an issue as well as interconnectivity and scalability. One wind farm may be connected to two or more offshore platforms and a tertiary control may communicate between multiple wind farms and platforms as illustrated. Functionality provided by the IP layer would be needed here for session establishment and maintenance. Data encryption and authentication is vital for security protection. The network is assumed to be using UDP and not TCP as transmission protocol. Retransmissions are not employed. In case of a lost packet, the receiver would take into account the follow up packet. A retransmit packet will contain stale information (data too old to be acted upon) by the time it is received. In the case of TCP, it is possible to flood the network with retransmitted packets, creating congestion. TCP uses principle design to avoid loss in non-critical networks. The protocol tends to be over active and too aggressive in time-critical networks. Hence, the applications at the end points need to be robust enough in order to tolerate packet losses, up to a safe predefined number, and continue normal operation.

7.2 PERFORMANCE ANALYSIS OF THE DISTRIBUTED COMMUNICATION ARCHITECTURE

Communication networks are evaluated in terms of four factors – efficiency, latency, availability and reliability, and security. In the following section, we discuss each communication technology and evaluate its performance based on those parameters. A summary of all communication parameters and suggested numerical quantities associated with the microgrid power system being study are provided in Table 7.1.

Table 7.1: Telecommunication Protocols and Media Options for Microgrid and Wide-Area Networks [115]

	Microgrid Network		Wide-area Grid Protocol		
	Ethernet	Fiber	Wimax	Satellite	Microwave
Addressing	MAC		IP		
Message Packet Type	MAC		UDP		
Retransmissions	-		-		
Range	250 Miles [8]	100's of Miles [8]	10 Miles [9]	(Up to 100's of miles) [10]	30 miles [11]
Security	Physical		Public and Private Key Encryption, Message Authentication		
Payload	42 bytes (minimum)		512 bytes (minimum)		
Overhead per Message	42 bytes (MAC)		42 bytes (MAC) + 20 bytes (IP) + 8 bytes (UDP)		
Transmission Rate (bits/sec)	1 Gbps	1 Gbps	40 Mbps	1 Mbps	45 Mbps
Message Transmission Delay	0.6 μ sec/link	4.6 μ sec/link	120 μ sec/link	>10 msec/link [10]	100 μ sec/link
Link Availability	0.99999 [8]	0.9999 [8]	0.99	0.95 [12]	0.99 [11]
Protocols Oneway End-to-End Availability	0.99998 (2 links)	0.999 ¹	0.9 ¹	0.59 ¹	0.9 ¹
Protocols End-to-End Delay	\approx 10 msec (2 links)	\approx 100 msec ¹	\approx 100 msec ¹	> 150 msec ¹	\approx 100 msec ¹

7.2.1 Availability and Reliability

Availability in communication networks is the percentage of time which the network is in a specified operational state. A simple representation of availability, shown by (7.1), is the product of all link and equipment availability, A_i , on the communication path assuming a series arrangement. Equation (7.1) is applied for a communication network that does not have built-in back-up paths. For networks with more than one path between source and destination pair, availability is determined with (7.2), where A_{pi} is the availability of the i th path.

$$A_{series} = \prod_{i=1}^n A_i \quad (7.1)$$

$$A_{parallel} = 1 - \prod_{i=1}^n (1 - A_{pi}) \quad (7.2)$$

In general, parallel networks are always more reliable, however they are much more expensive to implement. For the availability calculation in the microgrid and wide-area communication networks, we assume single path networks. Unlikely in reality, it is important to analyze this base case in order to gain understanding of media options and their suitability.

7.2.2 Packet Size and Overhead

Efficiency is defined as the fraction of useful data bits out of the total bits transmitted. The extra bits are control information and they are referred to as overhead. There are two communication protocols employed in the network design: (1) inside the microgrid and (2) outside the microgrid/inside the wide-area. The goal of the former protocol is speed and reliability, however, some performance is sacrificed for the purposes of interoperability and security. In the communication protocol within the microgrid we assume Ethernet is adopted and 42 bytes are used for the payload. This is the minimum allowed by the MAC protocol. There are an additional 42 bytes of mandatory MAC header. The overall efficiency is 50%, which is low, and a result of the small payload of every packet. This can be corrected by buffering some measurements, and sending them in a single packet. This however goes against the real-time principle of the applications. Low efficiency is typical of such applications (real time audio and video). In the wide-area network, the payload would be 512 bytes (the minimum for UDP Packets) with additional 70 bytes of headers. The payload would also be encrypted but private key encryption does not expand the data it encrypts. The overall efficiency is much higher, around 90% but, with larger packet size, there would be large transmission delay.

7.2.3 Transmission Delays

There would be a number of sources of delay in the network – transmission delay, processing delay in the intermediate nodes, and encryption/decryption delay (only for the wide-area network). From these sources, the transmission delay would be the least significant, and the processing delay most significant. In the wide-area network, there would be a 13 μ s delay for private key encryption per message (assuming low level field programmable gate array

implementation of AES/Rijndael [119]), and another 4 millisecond delay [120] for authentication of the data. Assuming the real-time system has reasonable performance, 10 milliseconds per cycle for the inside interface [121], 15 milliseconds for the outside interface plus an additional 5 milliseconds for encryption and authentication. This would result in 10 to 11 milliseconds of delay for one hop end-to-end delay for the microgrid network and 100 milliseconds for the wide-area network.

7.2.4 Security

As stated previously, security results in too much overhead and delay and is unlikely to be used in the microgrid network. The assumption here is that the microgrid network would be contained in one physical location – the offshore platform. As such, the cyber security is replaced by physical security (locked cabinets for the equipment and steel cable enclosures as an example).

In the tertiary network, encryption is necessary because the network has a large geographical span, possibly connecting multiple networks owned by different operators, and potential use of wireless communication technology. Wireless signals are easily intercepted and fabricated and have to be encrypted to prevent malicious behavior.

There exists two encryption paradigms – public and private key encryption. The advantage of public key encryption is that two parties communicating with each other have their own separate keys. Such data encrypted by a party is also signed by that party and cannot be later denied or produced by a third party. The downside of public key encryption is that it has quite slow decryption and especially slow encryption procedures. For the latter reason, it is not used for large data streams. In comparison, private key cryptography is significantly faster, up to

speeds of 3 Gbps [119], but both parties share the same key. Data is not signed and can be denied or knowledge of the secret key allows a third party to join the communication undetected.

A common practice in security protocols is to use public key encryption in the initial communication set-up, agree upon a private key, and switch to private key encryption. Since public keys are individual, there is a need for key management intermediary, a Certificate Authority that is in charge of distributing, renewing and retiring keys. The microgrid communication network would have to be protected by a firewall and an intrusion detection system (IDS). This is especially important, since inside the microgrid network there is no data encryption. Under no conditions should an outside communication channel be allowed in those non-encrypted networks. The secondary controller should be the only channel of communication inside and outside the microgrid network. Deviation of this rule could result in adversary issuing plain text control commands to the DC/DC converters and damaging the induction machines.

8.0 CONCLUSIONS AND FUTURE WORK

As mentioned earlier, this dissertation body is multi-faceted focusing on many areas of electrical engineering including communications, electric motor drives and machines, microgrid design, power magnetics, power electronics modeling and control, power system analysis, and renewable generation. The microgrid design presented is truly multi-disciplinary requiring a diverse set of skillsets. However, adequate engineering will not be enough to make microgrids a reality. State incentives, scalable and economical microgrid controllers, and cheap forms of storage will help to drive microgrid developments into the marketplace. Future natural disasters equivalent to Superstorm Sandy could/will cause scientists and engineers, government leaders, and policy developers to think differently about grid design to ensure grid resiliency, [122].

Various contributions can be found throughout the dissertation body and only the main drivers of each chapter will be elaborated here. First, the case was made for a unique offshore DC microgrid using renewable generation as its main source of power generation. The offshore microgrid is composed of electric machines and transformers that can consume significant space on the platforms as well as weigh down the overall structure. New classes of nanocomposite magnetic materials that operate at high frequency/ high power have been shown with ANSYS to reduce the magnetic volume for bidirectional DC/DC converters, power transformers, and electric machines. Only the electrical performance has been evaluated. Further study in the mechanical behavior of these materials is essential for electric machine applications.

Second, an argument was made to show that the offshore microgrid is inherently a multi-terminal network. Multi-terminal HVDC is currently an attractive topic in the industry. A modular multilevel converter with associated controls was simulated in PSCAD/EMTDC and a component sensitivity analysis on peak DC fault currents showed that the bypass switch speed and transformer impedance contribute greatly to the peak currents. Power converter scaling methods for performing simulation studies have also been provided for other research teams.

Third, the electric motor drives in the microgrid design behave as constant power loads, which are inherently unstable. Proportional derivative control techniques that most power engineers are accustomed too are not adequate for stabilizing these loads and a new control approach using model reference control design principles was shown to stabilize and dampen the unstable plant model used in the analysis.

Fourth, a completely validated Matlab/Simulink computer model of the offshore microgrid composed of wind turbines that maximum power point track, average power electronic models for DC/DC converters; multilevel inverters; and rectifiers with associated control, and variable speed electric motor drives was described. Fifth, related to the fourth takeaway, a preliminary power management scheme was implemented that dynamically adjusts the duty cycles of the bidirectional DC/DC converters to main balance between generation and loads. For AC systems, frequency is an indicator of system balance. For DC systems, one could argue that the DC/DC duty cycle serves as a similar indicator. Finally, the dissertation presented a communication network architecture for managing power in the offshore microgrid providing a number of technological options with theoretical bounds.

Many future work efforts are in-store for the proposed model reference control design in Chapter 4. First, the research team wants to validate the concepts experimentally and we can do this with the facilities in the university. The university is equipped with a new, state-of-the-art electric power systems lab with all equipment donated by Eaton. Figure 8.1 shows a few pictures of the lab. Experiments can be isolated with set-ups as shown in the left of Figure 8.1 for stability evaluation. Power management routines for larger systems can be proven using the motor control center (MCC), equipped with six, 5 hp variable frequency motor drives. The motors are permanently mounted in the back of the MCC and not shown in the picture. All motors are connected to a common AC bus as the case in the simulation models.



Figure 8.1: Portable Motor Units (Left) and Motor Control Center (Right)

The model reference control design was analytically determined using small signal analysis to linearize the design. Our next approach, which is becoming a speciality of the group, is to use adaptive controllers to continuously update controller parameters as a result of disturbances or changes in grid conditions. The difficulty and challenge is obtaining an adequate adaptation rule for common microgrid events.

Wind turbines are required to abide by Low Voltage Ride Through (LVRT) criteria established through the Federal Energy Regulatory Commission (FERC) Large Generator

Interconnection Agreement (LGIA) in current AC system designs [123]. The LVRT profile is shown in Figure 8.2. Meeting these requirements can be troublesome for vendors in stiff, meshed AC architectures and might be even more challenging in future microgrid designs. Remember, microgrids were first proposed to help meet the renewable integration targets set by the United States government and will need to abide by these regulations unless standards are adjusted for microgrids in particular. The Matlab/Simulink model does not have the capability of investigating LVRT. As the system voltage falls in the computer model, current from the wind turbine converter increases to meet the constant power load demands. In LVRT scenarios, the converter current cannot feed system disturbances, like faults.

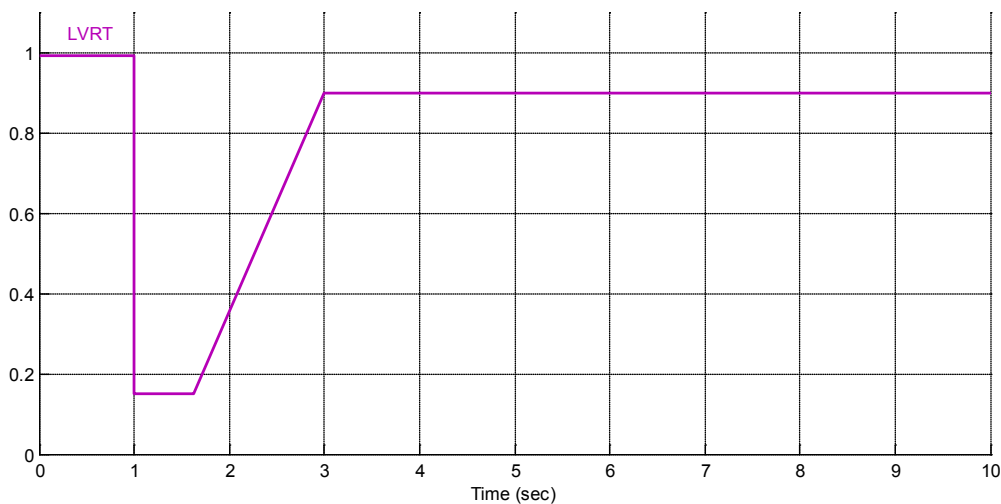


Figure 8.2: LVRT Requirement per Appendix G of FERC's LGIA

Throughout the dissertation, the author assumed ideal communication constraints. In practice, this will definitely not be the case and diesel generators will not respond as quickly as the profiles have shown in the simulation results. In fact, communication delays are another root cause of a system becoming unstable – information is not received in order for the controllers to take action. Electrical engineers and telecommunication engineers at Pitt will be heavily investigating these communication constraints in the future timeframe.

APPENDIX A

MATLAB CODE TO EVALUATE SWITCHING FREQUENCY IMPACTS ON TRANSFORMER POWER DENSITY

```

function [c,ceq] = XfmrConstraints1(x)
% Lead Graduate Student Researcher: Brandon Grainger
% Undergraduate Research Assistant: Zachary Smith
% January 2014

%% Objective of Function XfmrConstraints
% The objective of this function is to calculate the amount of flux in the
% transformer, losses in the core and windings, and temperature rise.

%% Initial Conditions:
%a = .028m
%b = .110m
%d = .028m
%h = .205m
%N = 32

f = 1000;           % Operating frequency of transformer (Hz)
Bmax = 0.75;       % Maximum Flux Density (Tesla)
Bmin = 0.65;       % Minimum Flux Density (Tesla)
Tmax = 150;        % Maximum allowed temperature (Celsius)

%% Declaration of Physical Properties
% Geometric Properties
a = x(1);           % Property a in meters
b = x(2);           % Property b in meters
d = x(3);           % Property d in meters
h = x(4);           % Property h in meters
N = x(5);           % Number of turns in Primary

Ac = a*d;           % Cross Sectional Area (m^2)
Aw = 2*b*h;         % Window Area (m^2)
l0 = 2*(a+b+d);     % Mean Length per Turn (m)
l1 = 2*a+2*b;       % Transformer Width (m)
l2 = d+b;           % Transformer Thickness (m)
l3 = 2*a+2*h;       % Transformer Height (m)
V = l1*l2*l3;       % Transformer Core (m^3)
Vc = (2*a+b)*(2*a+2*h)*d-2*h*b*d; % Core Volume (m^3)
At = 2*(l1*l2+l1*l3+l2*l3); % Transformer Thermal Area (m^2)

%% Variables
%%%%%%%%%% Transformer Parameters %%%%%%%%%%
circuit = 8;        % Number of circuits in primary
PowerT = 128340;    % Power rating of the transformer W
PowerFactor = 0.93; % Minimum allowable power factor
STrans = PowerT/PowerFactor; % Maximum kVA of the transformer
omega = 2*pi*f;     % Radial Frequency
Erms = 13.8*10^3;   % Voltage of the transformer (Volts)
Ermspri = Erms;     % RMS voltage - primary winding (Volts)
Irmspri = STrans/Ermspri/circuit; % RMS curr. - primary winding (Amperes)
Ermssec = Ermspri*0.5580; % RMS voltage - second. winding (Volts)
% (utility side)
Irmsec = PowerT/Ermssec; % RMS curr. - secondary winding (Amps)
% (utility side)

%%%%%%%%%% Pcore Variables %%%%%%%%%%%
alpha = 1.6945;
beta = 1.967;
k = 0.787;          % W/kg

%%%%%%%%%% Pwinding Variables %%%%%%%%%%%
rho = 23*10^(-9);   % Electrical resistivity of copper
% Ohm*m at 100degC
km = 2;             % Coil numbers in the transformer
kAC = 1;            % AC Resistance Coefficient
kw = 0.1;           % Fill factor of the window area

mu0 = 4*pi*10^(-7); % Permeability constant (H/m)
n = 420;            % Number of strands in Litz wire
dc = 0.00010160;   % Strand diameter (m)
kf = 1;             % Factor accounting for field
% distribution in multiwinding TXs
Rs = 0.323;         % Resistance of secondary wire (Ohms)

```

```

% 22 AWG wire
Rdc = 0.0104; % DC Resistance of primary wire (Ohms)
% 12 AWG wire

%% Calculation of Cost Function, Losses, and Temperature Rise
%%%%%%%%%%%%%%%%%%%%%%%%%%%%%%%%%%%%%%%%%%%%%%%%%%%%%%%%%%%%%%%%%%%%%%%%
Vcore = 11*12*13; % Cost Function (Volume in m^3)
weight = 15*0.453592; % Weight of transformer in kg
origVcore = 0.0177; % Initial value of transformer (m^3)
density = weight/origVcore; % Density of core

%%% Magnetix Flux in the Transformer %%%

% Flux Density of the Core (T) (V*s/(m^2))
BTx= sqrt(2)*Erms/(2*pi*f*N*circuit*a*d);

%%%%%%%%%%%%%%%%%%%%%%%%%%%%%%%%%%%%%%%%%%%%%%%%%%%%%%%%%%%%%%%%%%%%%%%%
%% Calculation of Core Loss (W)
Pcore = density*Vcore*(k*(f/1000)^(alpha)*BTx^(beta));

% Alternative Core Loss Equation
% Pcore = Vcore*(0.0277419*(f)^(alpha)*BTx^(beta));

%%%%%%%%%%%%%%%%%%%%%%%%%%%%%%%%%%%%%%%%%%%%%%%%%%%%%%%%%%%%%%%%%%%%%%%%
%% Power Loss in the Windings %%%
Pwinding = kAC*km*kw*rho*N^2*l0/Aw;
Fr = 1 + (pi*omega*mu0*N*n)^2*dc^6/(768*rho^2*b^2);
Pwp = (Fr*Irmspri^2*Rdc)*circuit; % Litz Wire Winding Loss (Primary)
Pws = Irmsec^2*Rs; % Solid Copper Wire Loss (Secondary)
Pwinding = Pwp+Pws; % Total Winding Loss

%%%%%%%%%%%%%%%%%%%%%%%%%%%%%%%%%%%%%%%%%%%%%%%%%%%%%%%%%%%%%%%%%%%%%%%%
%% Temperature Rise %%%
Trise = 450*((Pcore+Pwinding)/(At*100*100))^(0.826);
% Average Temperature Rise of the Transformer.
%"At" in the Trise equation is multiplied by 10000 to get units cm^2.

c(1) = BTx - Bmax;
c(2) = Trise - Tmax;
c(3) = -BTx + Bmin;
ceq = [];

%%%%%%%%%%%%%%%%%%%%%%%%%%%%%%%%%%%%%%%%%%%%%%%%%%%%%%%%%%%%%%%%%%%%%%%%
%% Variables of Interest to Display %%%
BTx
Trise
Irmspri
Pcore
Pwinding
Powerloss = (Pcore + Pwinding)
efficiency = (STrans-Powerloss)/STrans
a
b
d
h
N
disp('excel results')
disp(BTx)
disp(Trise)
disp(Irmspri)
disp(Pcore)
disp(Pwinding)
disp(Powerloss)
disp(efficiency)
disp(a)
disp(b)
disp(d)
disp(h)
disp(N)
disp(Vcore)
disp(f)
end

```

```

function [Vcore] = XfmrCost1( x )
% Lead Graduate Student Researcher: Brandon Grainger
% Undergraduate Research Assistant: Zachary Smith
% January 2014

%% Objective of Function XfmrCost
% The objective of this function is to calculate the cost (volume) of the
% transformer.

%% Initial Conditions:
%a = .028m
%b = .110m
%d = .028m
%h = .205m
%N = 32
%Solver: fmincon - Constrained nonlinear minimization
%Algorithm: Interior point
%Frequency 1000Hz
%Start Point [0.028 0.110 0.028 0.205 32]
%Lower Bound [0.0075 0.04 0.075 0.09 25]
%Upper Bound [0.08 0.36 0.08 0.51 32]
% Bmax = 0.75;           % Maximum Flux Density (Tesla)
% Bmin = 0.65;           % Minimum Flux Density (Tesla)
% Tmax = 150;           % Maximum allowed temperature (Celsius)
%% Declaration of Physical Properties
% Geometric Properties
a = x(1);                % Property a in meters
b = x(2);                % Property b in meters
d = x(3);                % Property d in meters
h = x(4);                % Property h in meters

l1 = 2*a+2*b;            % Transformer Width (m)
l2 = d+b;                % Transformer Thickness (m)
l3 = 2*a+2*h;            % Transformer Height (m)

%% Calculation of Cost Function
%%%%%%%%%% Volume of the Core %%%%%%%%%%%
Vcore = l1*l2*l3;        % Cost Function (Volume in m^3)

end

```

APPENDIX B

MATLAB CODE TO EVALUATE MODEL REFERENCE CONTROLLER DESIGN FOR CONSTANT POWER LOAD SCENARIO

```

% Brandon Grainger
% June 2014
% Sponsored: ABB Corporate Research
% Purpose - Stability Assessment of MRC Controller

%-----
% Cable Parameters
% 3.6/6(7.2)kV - Single Core, XLPE Insultated, PVC Sheathed, Screened
% Unarmoured cables - IEC 60502-2

% Nominal Cross Section: 1000mm^2
% Current Rating: 1340 A - Copper wire / Duct
%-----
clc;
clear
%----- Cable Characteristics -----

% Distance
d= 0.1;

% DC Resistance at 20 degrees
R_m = 0.0176; %ohm/km
R = R_m*d; %ohm

% Trefoil Formation
L_m = 0.248e-3; %H/km
L = L_m*d; %H

% Nominal Capacity
C_m = 0.923e-6; %F/km
C = C_m/2*d;

%%----- Converter Characteristics -----

n = 5;
Vdc = 1000;
Ts = 1/3000;
L_conv = 5.208e-3;
dh= 0.1464;

Y = (Vdc)^2/100e3
C1 = (C + (100e3/(Vdc*0.1*Vdc*377)));
C1 = 13.2e-3
C2 = [(L/(R*Y))+2e-3];
C2 = 5e-3

%----- Pole Placement of M(s) -----

wn = 5000;
wn = 3500; % Tuned for Slower Control Response

Kp_PD = 1/(Y+1); % Kp < 1/Y (Constraint)
Kd_PD = 1;

%-----
% Transfer Function Characteristics of Plant (3rd Order System)
% x coefficients for numerator; y coefficients for denominator

x2 = Y*C2*L;
x1 = R*C2*Y-L;
x0 = Y-R;
y3 = L*C1*C2*Y;
y2 = R*C1*C2*Y-L*C1;
y1 = C1*Y-R*C1 + C2*Y;
y0 = -1;
G = n*Vdc*Ts*(1-2*dh)/(2*L_conv);
sys=G*tf([x2 x1 x0],[y3 y2 y1 y0])

%-----
% Adaptive Controller Transfer Function Characteristics

```

```

km = 1;
G = G/100;
kp = G/C1;
Co = km/kp;

% Compensator: Lambda / (Lambda - C_hat)
w1 = sqrt(wn^3/km)           % w1 is numerator coefficient of M(s)

a2 = 1                       % Lambda Coefficients
a1 = 2*w1
a0 = w1^2

q2 = 1;                      % Lambda - C_hat Coefficients
q1 = (R*C2*Y-L)/(L*C2*Y);    % Plant Transfer Function numerator
q0 = (Y-R)/(L*C2*Y);

% Feedback: d_hat / Lambda

b2 = sqrt(3)*wn+wn
b1 = wn*wn + sqrt(3)*wn*wn
b0 = km*wn*wn*wn

p2 = (R*C1*C2*Y-L*C1)/(L*C1*C2*Y)
p1 = (C1*Y-R*C1+C2*Y)/(L*C1*C2*Y)
p0 = -1/(L*C1*C2*Y)

d2 = (p2-b2)/kp             % d_hat Coefficients
d1 = (p1-b1)/kp
d0 = -(b0+p0)/kp

%-----

% Zero/Pole Placement for M(s) and P(s) on Same Mapping

sys2=tf([1 a1 a0],[1 b2 b1 b0])
figure
iopzplot(sys)
figure
iopzplot(sys2)

%-----

% Testing Matching Equality: Variable "Right" = Variable "Left"

np=tf([1 q1 q0], 1);
dm = tf([1 b2 b1 b0],1);

Right = np*dm

aaa = -tf([1 q1 q0],1)*tf([(p2-b2) (p1-b1) -(b0+p0)],1);
bbb = (tf([1 a1 a0], 1)-tf([(a1-q1) (a0-q0)], 1))*tf([1 p2 p1 -p0],1);

Left = aaa+bbb

%-----

```

APPENDIX C

MODELING THE WIND TURBINE IN SIMULATION PLATFORMS

This appendix was written to provide an intuitive understanding of the wind turbine model developed in this dissertation.

Permanent Magnet Synchronous Generator (PMSG) Implementation in Simulators

The outputs of the machine module shown in Figure AC.1 include the machine mechanical and electrical speeds, measured *abc* currents and rotor displacement angle. These variables are extensively used to coordinate the control between the machine and three-level, neutral point clamped rectifier.

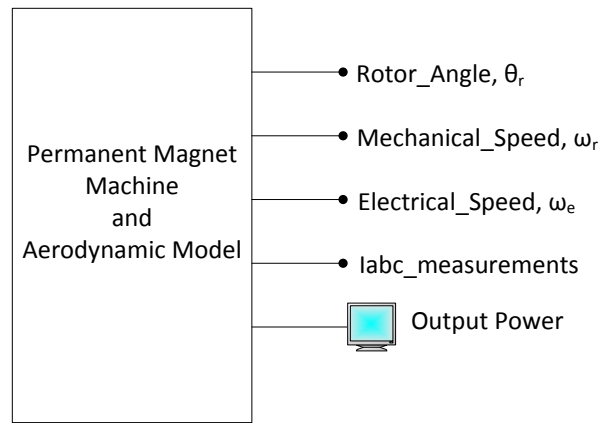


Figure AC.1: PMSG and Aerodynamic Model Module with Outputs

The blocks connected together in Figure AC.2, which are embedded in Figure AC.1, are used to solve the mechanical equation of the machine described by (5.3). The inputs to the equation are the mechanical torque coming from the aerodynamic model and the electromagnetic torque coming from the electrical model of Figure AC.3. The moment of inertia of the machine, J , is $2.5 \times 10^5 \text{ kgm}^2$, the friction factor, F , is $2.26 \times 10^4 \text{ Nm-s}$, and the number of pole pairs was chosen to be 118. Once the mechanical speed of the machine is solved for in the inner loop, the electrical speed can be determined by multiplying by the number of pole pairs. The mechanical speed is also integrated using the discrete time integrator, $1/s$, to obtain the rotor angular position. Three of the four outputs of Figure AC.1 come from the mechanical equation.

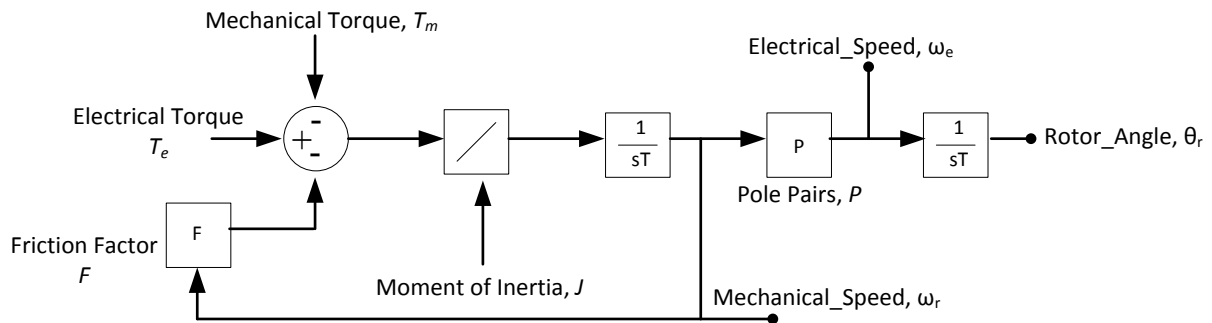


Figure AC.2: Mechanical Equation Implementation of PMSG

Figure AC.3 provides a technique for solving the two coupled electrical equations listed as (5.1a) and (5.1b). This set of blocks requires three inputs, which include the rotor angular position, electrical machine speed, and the abc line-to-ground voltage measurements from the terminals of the machine. The three-phase voltage measurement is transformed into dq components by means of a standard Park's transformation, listed as (A1). The block in Figure AC.3 labeled, *Script ABC to dq0 Rotor Reference*, is a script that performs the transformation.

Note that the following trigonometric identities listed as (A2a) through (A2d) are convenient expressions for computing the 3x3 matrix in a computer.

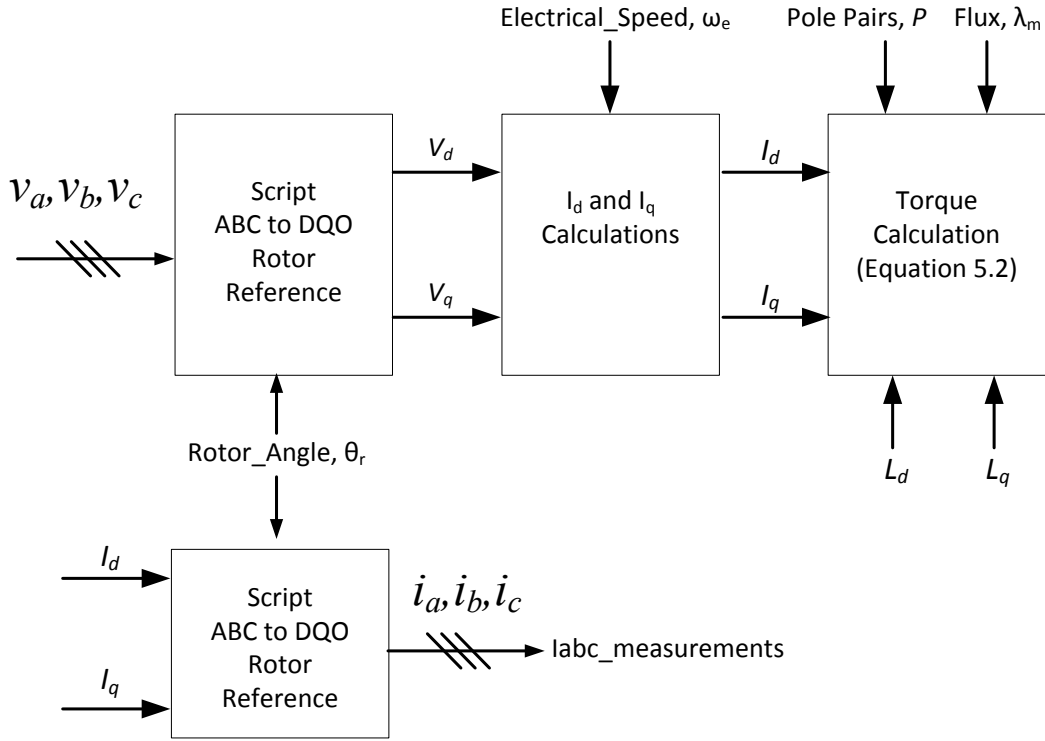


Figure AC.3: Electrical Model Implementation of PMSG

$$[T_{dqo}(\theta_r)] = \frac{2}{3} \begin{bmatrix} \cos \theta_r & \cos(\theta_r - \frac{2\pi}{3}) & \cos(\theta_r + \frac{2\pi}{3}) \\ -\sin(\theta_r) & -\sin(\theta_r - \frac{2\pi}{3}) & -\sin(\theta_r + \frac{2\pi}{3}) \\ 1/2 & 1/2 & 1/2 \end{bmatrix} \quad (\text{A1})$$

$$\cos(\theta_r - \frac{2\pi}{3}) = \frac{\sqrt{3}}{2} \sin(\theta_r) - \frac{1}{2} \cos(\theta_r) \quad (\text{A2a})$$

$$\cos(\theta_r + \frac{2\pi}{3}) = \frac{\sqrt{3}}{2} \sin(\theta_r) + \frac{1}{2} \cos(\theta_r) \quad (\text{A2b})$$

$$-\sin(\theta_r - \frac{2\pi}{3}) = \frac{1}{2} \sin(\theta_r) + \frac{\sqrt{3}}{2} \cos(\theta_r) \quad (\text{A2c})$$

$$-\sin(\theta_r + \frac{2\pi}{3}) = \frac{1}{2} \sin(\theta_r) - \frac{\sqrt{3}}{2} \cos(\theta_r) \quad (\text{A2d})$$

The heart of the computations occurs in the I_d and I_q Calculations block found in Figure AC.3. The inputs to this block include the dq components of the abc line-to-ground voltage measurements as well as the calculated electrical speed from the mechanical equation of Figure AC.2. A subsystem exists within the I_d and I_q Calculations block that solves the coupled differential equations of the electrical system listed as (5.1a) and (5.1b). The details of the underlining system are found in Figure AC.4. The next step in the process is to compute the electromagnetic torque of the machine. With the dq current components calculated, the torque can be calculated using (5.2). This electromagnetic torque, T_e , is fed back into the mechanical equation model to complete the coupling between the electrical and mechanical relationships.

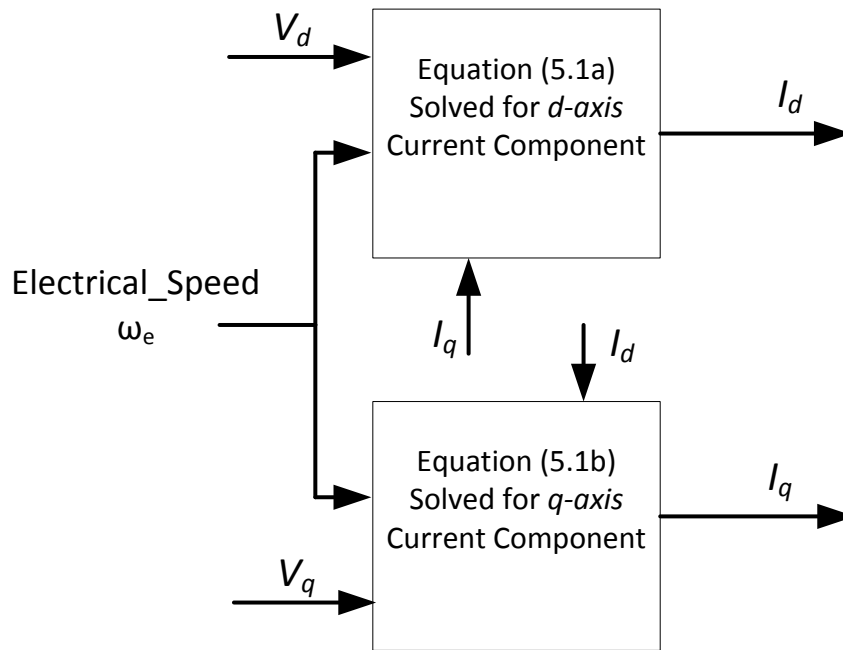


Figure AC.4: Illustration for Solving Electrical System Differential Equations

The last step in the process is to send the dq current components through an inverse Park's transformation described by (A3) to obtain the abc currents. These currents are then fed into programmable current sources, as shown in Figure AC.5, which serve as the main source of power for the physical MVDC wind collection system. Recall that most distributed resources

can be modeled current fed components, [25]. The audience will notice three voltage measurements being made in Figure AC.5. These measurements are fed into the electrical model system equations (Figure AC.3).

$$[T_{dqo}(\theta_r)]^{-1} = \frac{2}{3} \begin{bmatrix} \cos \theta_r & -\sin(\theta_r) & 1 \\ \cos(\theta_r - \frac{2\pi}{3}) & -\sin(\theta_r - \frac{2\pi}{3}) & 1 \\ \cos(\theta_r + \frac{2\pi}{3}) & -\sin(\theta_r + \frac{2\pi}{3}) & 1 \end{bmatrix} \tag{A3}$$

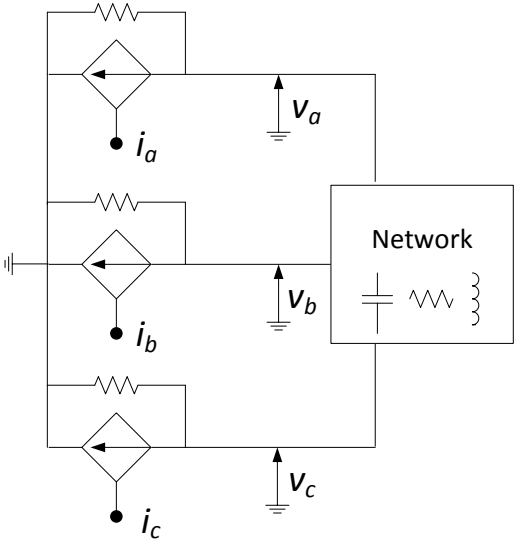


Figure AC.5: Physical Machine Interconnection to the MVDC Collection System

APPENDIX D

SCRIPTS FOR MONITORING AND ADJUSTING POWER EXCHANGE THROUGHOUT THE DC MICROGRID

```

% Brandon Grainger
% Parameters for System Model
% Sponsored: ABB Corporate Research Center
% March 2014

%-----
% Simulation Convergence Parameters
%-----

Ts=5e-5;
Ts_Control=50e-6;
Ts_Power=Ts;

%-----
% Wind Turbine System and Control Parameters
%-----
Radius = 58;                % Unit: Meters
Pairs = 118;                % Unit: N/A
M_Flux = 14.3522;          % Unit: Webers (Vs)
L_machine = 3.5218e-3;     % Unit: Henry

% Control Parameters
Kp_Wind = 0.3;
Ki_Wind = 10;

%-----
% Bidirectional DC/DC Converter
%-----
fs_DCDC = 3000;
Ts_DCDC = 1/fs_DCDC;
L_DCDC = 208e-6;
n = 5000/7500;

%-----
% Bidirectional DC/DC Converter
%-----

% Motor Drive No.1 Parameters
Rs = 29e-3;
Rr = 22e-3;
Lm = 34.6e-3;
Lls = 0.6e-3;
Llr = 0.6e-3;
Ls = Lls + Lm;
Ls = 35.2e-3;
Lr = Llr + Lm;
Lr = 35.2e-3;
Prated = 1.678e6;
Vrated = 2300;
wo = 377;
sigma_s = (Ls/Lm)-1;
sigma_r = (Lr/Lm)-1;
sigma = 1 - (1/((1+sigma_r)*(1+sigma_s)));
Imr_ref = (sqrt(2/3)*Vrated)/(wo*Lm*(sigma_s+1));
tau_s = Lm*(1+sigma_s)/Rs;
tau_r = Lm*(1+sigma_r)/Rr;
tau_i = 3e-3;

Kp = 1*sigma*tau_s/tau_i;
Ki = 1/tau_i;

% Motor Drive No.2 Parameters
Rs_2 = 29e-3;
Rr_2 = 22e-3;
Lm_2 = 34.6e-3;
Lls_2 = 0.6e-3;
Llr_2 = 0.6e-3;
Ls_2 = Lls_2 + Lm_2;
Ls_2=35.2e-3;

```

```

Lr_2 = Llr_2 + Lm_2;
Lr_2=35.2e-3;
Prated_2 = 1.678e6;
Vrated_2 = 2300;
wo = 377;
sigma_s_2 = (Ls_2/Lm_2)-1;
sigma_r_2 = (Lr_2/Lm_2)-1;
sigma_2 = 1 - (1/((1+sigma_r_2)*(1+sigma_s_2)));
Imr_ref_2 = (sqrt(2/3)*Vrated_2)/(wo*Lm_2*(sigma_s_2+1));
tau_s_2 = Lm*(1+sigma_s_2)/Rs_2;
tau_r_2 = Lm*(1+sigma_r_2)/Rr_2;
tau_i_2 = 3e-3;

Kp_2 = 1*sigma_2*tau_s_2/tau_i_2;
Ki_2 = 1/tau_i_2;

% Motor Drive No.3 Parameters
Rs_3 = 29e-3;
Rr_3 = 22e-3;
Lm_3 = 34.6e-3;
Lls_3 = 0.6e-3;
Llr_3 = 0.6e-3;
Ls_3 = Lls_3 + Lm_3;
Ls_3=35.2e-3;
Lr_3 = Llr_3 + Lm_3;
Lr_3=35.2e-3;
Prated_3 = 1.678e6;
Vrated_3 = 2300;
wo = 377;
sigma_s_3 = (Ls_3/Lm_3)-1;
sigma_r_3 = (Lr_3/Lm_3)-1;
sigma_3 = 1 - (1/((1+sigma_r_3)*(1+sigma_s_3)));
Imr_ref_3 = (sqrt(2/3)*Vrated_3)/(wo*Lm_3*(sigma_s_3+1));
tau_s_3 = Lm*(1+sigma_s_3)/Rs_3;
tau_r_3 = Lm*(1+sigma_r_3)/Rr_3;
tau_i_3 = 3e-3;

Kp_3 = 1*sigma_3*tau_s_3/tau_i_3;
Ki_3 = 1/tau_i_3;

```

BIBLIOGRAPHY

- [1] G. F. Reed, B. M. Grainger, A. R. Sparacino, R. J. Kerestes, and M. J. Korytowski, "Advancements in medium voltage DC architecture development with applications for powering electric vehicle charging stations," in *2012 IEEE Energytech*, 2012, pp. 1–8.
- [2] H. Mirzaee, S. Dutta, and S. Bhattacharya, "A medium-voltage DC (MVDC) with series active injection for shipboard power system applications," in *2010 IEEE Energy Conversion Congress and Exposition*, 2010, pp. 2865–2870.
- [3] M. Bash, R. R. Chan, J. Crider, C. Harianto, J. Lian, J. Neely, S. D. Pekarek, S. D. Sudhoff, and N. Vaks, "A Medium Voltage DC Testbed for ship power system research," in *2009 IEEE Electric Ship Technologies Symposium*, 2009, pp. 560–567.
- [4] T. Ericson, "The ship power electronic revolution: Issues and answers," in *2008 55th IEEE Petroleum and Chemical Industry Technical Conference*, 2008, pp. 1–11.
- [5] G. Reed, B. Grainger, A. Sparacino, and Z.-H. Mao, "Ship to Grid: Medium-Voltage DC Concepts in Theory and Practice," *IEEE Power Energy Mag.*, vol. 10, no. 6, pp. 70–79, Nov. 2012.
- [6] ABB in the United States, "U.S. Department of Energy to fund major Offshore Wind Grid Interconnection study," 2011. [Online]. Available: <http://www.abb.us>.
- [7] I. C. Evans and R. Limpaecher, "High power clean DC bus generation using AC-link AC to DC power voltage conversion, DC regulation, and galvanic isolation," in *2009 IEEE Electric Ship Technologies Symposium*, 2009, pp. 290–301.
- [8] F. Falco, "Subsea Technologies at the Heart of Future Oilfields," 2014. [Online]. Available: <http://www.gepowerconversion.com/inspire>.
- [9] E. Ibanez, T. Mai, and L. Coles, "Analyzing the Deployment of Large Amounts of Offshore Wind to Design an Offshore Transmission Grid in the United States," in *11th Annual International Workshop on Large-Scale Integration of Wind Power into Power Systems*, 2012.
- [10] Siemens AG Energy Sector, "The Offshore Way: WIPOS-Wind Power Offshore Substation," 2011. [Online]. Available: <http://www.siemens.com/energy/wipos>.

- [11] P. Lundberg, M. Callavik, M. Bahrman, and P. Sandeberg, "Platforms for Change: High-Voltage DC Converters and Cable Technologies for Offshore Renewable Integration and DC Grid Expansions," *IEEE Power Energy Mag.*, vol. 10, no. 6, pp. 30–38, Nov. 2012.
- [12] R. H. Lasseter and P. Paigi, "Microgrid: a conceptual solution," in *2004 IEEE 35th Annual Power Electronics Specialists Conference (IEEE Cat. No.04CH37551)*, 2004, vol. 6, pp. 4285–4290.
- [13] T. S. Basso and R. DeBlasio, "IEEE 1547 Series of Standards: Interconnection Issues," *IEEE Trans. Power Electron.*, vol. 19, no. 5, pp. 1159–1162, Sep. 2004.
- [14] L. M. Tolbert, "Power Conversion Systems for Microgrids," ECCE 2012 Rap Session, Raleigh, NC, 2012.
- [15] S. Krishnamurthy, T. M. Jahns, and R. H. Lasseter, "The operation of diesel gensets in a CERTS microgrid," in *2008 IEEE Power and Energy Society General Meeting - Conversion and Delivery of Electrical Energy in the 21st Century*, 2008, pp. 1–8.
- [16] J. M. Guerrero, J. Matas, L. Garcia de Vicuna, M. Castilla, and J. Miret, "Decentralized Control for Parallel Operation of Distributed Generation Inverters Using Resistive Output Impedance," *IEEE Trans. Ind. Electron.*, vol. 54, no. 2, pp. 994–1004, Apr. 2007.
- [17] R. Teodorescu and F. Blaabjerg, "Flexible Control of Small Wind Turbines With Grid Failure Detection Operating in Stand-Alone and Grid-Connected Mode," *IEEE Trans. Power Electron.*, vol. 19, no. 5, pp. 1323–1332, Sep. 2004.
- [18] D. Chen, Chien-Liang Wang, Yubin Lai, Jih-Sheng(Jason) Lee, Yuang-Shung Martin, "Design of Parallel Inverters for Smooth Mode Transfer Microgrid Applications," *IEEE Trans. Power Electron.*, vol. 25, no. 1, pp. 6–15, Jan. 2010.
- [19] J. C. Vasquez, J. M. Guerrero, A. Luna, P. Rodriguez, and R. Teodorescu, "Adaptive Droop Control Applied to Voltage-Source Inverters Operating in Grid-Connected and Islanded Modes," *IEEE Trans. Ind. Electron.*, vol. 56, no. 10, pp. 4088–4096, Oct. 2009.
- [20] M. A. Zamani, A. Yazdani, and T. S. Sidhu, "A Control Strategy for Enhanced Operation of Inverter-Based Microgrids Under Transient Disturbances and Network Faults," *IEEE Trans. Power Deliv.*, vol. 27, no. 4, pp. 1737–1747, Oct. 2012.
- [21] L. Xu and D. Chen, "Control and Operation of a DC Microgrid With Variable Generation and Energy Storage," *IEEE Trans. Power Deliv.*, vol. 26, no. 4, pp. 2513–2522, Oct. 2011.
- [22] K. De Brabandere, B. Bolsens, J. Van den Keybus, A. Woyte, J. Driesen, and R. Belmans, "A Voltage and Frequency Droop Control Method for Parallel Inverters," *IEEE Trans. Power Electron.*, vol. 22, no. 4, pp. 1107–1115, Jul. 2007.

- [23] Jung-Won Kim, Hang-Seok Choi, and Bo Hyung Cho, “A novel droop method for converter parallel operation,” *IEEE Trans. Power Electron.*, vol. 17, no. 1, pp. 25–32, 2002.
- [24] J. M. Guerrero, N. Berbel, J. Matas, L. G. de Vicuna, and J. Miret, “Decentralized Control for Parallel Operation of Distributed Generation Inverters in Microgrids Using Resistive Output Impedance,” in *IECON 2006 - 32nd Annual Conference on IEEE Industrial Electronics*, 2006, pp. 5149–5154.
- [25] J. Rocabert, A. Luna, F. Blaabjerg, and P. Rodríguez, “Control of Power Converters in AC Microgrids,” *IEEE Trans. Power Electron.*, vol. 27, no. 11, pp. 4734–4749, Nov. 2012.
- [26] I. Batarseh, K. Siri, and H. Lee, “Investigation of the output droop characteristics of parallel-connected DC-DC converters,” in *Proceedings of 1994 Power Electronics Specialist Conference - PESC'94*, 1994, pp. 1342–1351.
- [27] A. Bidram and A. Davoudi, “Hierarchical Structure of Microgrids Control System,” *IEEE Trans. Smart Grid*, vol. 3, no. 4, pp. 1963–1976, Dec. 2012.
- [28] J. M. Guerrero, J. C. Vasquez, J. Matas, L. G. de Vicuna, and M. Castilla, “Hierarchical Control of Droop-Controlled AC and DC Microgrids—A General Approach Toward Standardization,” *IEEE Trans. Ind. Electron.*, vol. 58, no. 1, pp. 158–172, Jan. 2011.
- [29] J. Liang, T. Jing, O. Gomis-Bellmunt, J. Ekanayake, and N. Jenkins, “Operation and Control of Multiterminal HVDC Transmission for Offshore Wind Farms,” *IEEE Trans. Power Deliv.*, vol. 26, no. 4, pp. 2596–2604, Oct. 2011.
- [30] D. Salomonsson, L. Soder, and A. Sannino, “An Adaptive Control System for a DC Microgrid for Data Centers,” *IEEE Trans. Ind. Appl.*, vol. 44, no. 6, pp. 1910–1917, 2008.
- [31] C. Abbey, D. Cornforth, N. Hatziargyriou, K. Hirose, A. Kwasinski, E. Kyriakides, G. Platt, L. Reyes, and S. Suryanarayanan, “Powering Through the Storm: Microgrids Operation for More Efficient Disaster Recovery,” *IEEE Power Energy Mag.*, vol. 12, no. 3, pp. 67–76, May 2014.
- [32] A. Kwasinski, V. Krishnamurthy, J. Song, and R. Sharma, “Availability Evaluation of Micro-Grids for Resistant Power Supply During Natural Disasters,” *IEEE Trans. Smart Grid*, vol. 3, no. 4, pp. 2007–2018, Dec. 2012.
- [33] “Power Electronics Research and Development Program Plan,” Office of Electricity Delivery and Energy Reliability, Washington, DC, 2011.
- [34] R. Ram, “Power Electronics,” ARPA-E Pre-Summit Workshop, Washington, DC, Mar. 2010.

- [35] A. M. Leary, P. R. Ohodnicki, and M. E. McHenry, "Soft Magnetic Materials in High-Frequency, High-Power Conversion Applications," *J. Met.*, vol. 64, no. 7, pp. 772–781, Jul. 2012.
- [36] W. Kramer, S. Chakraborty, B. Kroposki, and H. Thomas, "Advanced Power Electronic Interfaces for Distributed Energy Systems Part 1: Systems and Topologies," National Renewable Energy Laboratory, 2008.
- [37] Q. Li, M. Lim, J. Sun, A. Ball, Y. Ying, F. C. Lee, and K. D. T. Ngo, "Technology road map for high frequency integrated DC-DC converter," in *2010 Twenty-Fifth Annual IEEE Applied Power Electronics Conference and Exposition (APEC)*, 2010, pp. 533–539.
- [38] M. Schaefer, G. Dietzmann, and H. Wirth, "Magnetic losses in ferrites and nanocrystalline ribbons for power applications," *J. Magn. Magn. Mater.*, vol. 101, no. 1–3, pp. 95–96, Oct. 1991.
- [39] R. Hasegawa, "Applications of amorphous magnetic alloys in electronic devices," *J. Non. Cryst. Solids*, vol. 287, no. 1–3, pp. 405–412, Jul. 2001.
- [40] R. Hasegawa, "Applications of amorphous magnetic alloys," *Mater. Sci. Eng. A*, vol. 375–377, pp. 90–97, Jul. 2004.
- [41] M. E. McHenry, M. A. Willard, and D. E. Laughlin, *Amorphous and nanocrystalline materials for applications as soft magnets*, vol. 44, no. 4. 1999, pp. 291–433.
- [42] R. W. A. A. De Doncker, D. M. Divan, and M. H. Kheraluwala, "A three-phase soft-switched high-power-density DC/DC converter for high-power applications," *IEEE Trans. Ind. Appl.*, vol. 27, no. 1, pp. 63–73, 1991.
- [43] A. Pressman and K. Billings, *Switching Power Supply Design*. McGraw-Hill; 3rd edition, 2009.
- [44] Y. Xie, J. Sun, and J. S. Freudenberg, "Power Flow Characterization of a Bidirectional Galvanically Isolated High-Power DC/DC Converter Over a Wide Operating Range," *IEEE Trans. Power Electron.*, vol. 25, no. 1, pp. 54–66, Jan. 2010.
- [45] D. Segaran, D. G. Holmes, and B. P. McGrath, "Comparative analysis of single and three-phase dual active bridge bidirectional DC-DC converters." pp. 1–6, 2008.
- [46] J. Xue, F. Wang, D. Boroyevich, and Z. Shen, "Single-phase vs. three-phase high density power transformers," in *2010 IEEE Energy Conversion Congress and Exposition*, 2010, pp. 4368–4375.
- [47] M. Pavlovsky, S. W. H. de Haan, and J. A. Ferreira, "Concept of 50 kW DC/DC converter based on ZVS, quasi-ZCS topology and integrated thermal and electromagnetic design," in *2005 European Conference on Power Electronics and Applications*, 2005, p. 9.

- [48] I.-Y. Chung, W. Liu, M. Andrus, K. Schoder, D. A. Cartes, and M. Steurer, "Integration of a bi-directional dc-dc converter model into a large-scale system simulation of a shipboard MVDC power system," in *2009 IEEE Electric Ship Technologies Symposium*, 2009, pp. 318–325.
- [49] D. Costinett, D. Maksimovic, and R. Zane, "Design and Control for High Efficiency in High Step-Down Dual Active Bridge Converters Operating at High Switching Frequency," *IEEE Trans. Power Electron.*, vol. 28, no. 8, pp. 3931–3940, Aug. 2013.
- [50] "Gallium-Nitride Switch Technology for Bi-Directional Battery-to-Grid Charger Applications." [Online]. Available: <http://arpa-e.energy.gov/?q=arpa-e-projects/compact-interactive-electric-vehicle-charger>.
- [51] J. Xue, "Single-phase vs. Three-phase High Power High Frequency Transformers," Virginia Tech, 2010.
- [52] R. Prieto, J. A. Oliver, J. A. Cobos, J. Uceda, and M. Christini, "Errors obtained when 1D magnetic component models are not properly applied," in *APEC '99. Fourteenth Annual Applied Power Electronics Conference and Exposition. 1999 Conference Proceedings*, 1999, vol. 1, pp. 206–212 vol.1.
- [53] W. McLyman, *Transformer and Inductor Design Handbook, Fourth Edition*. CRC Press; 4th edition, 2012.
- [54] "0P44125UC MAGNETICS Core." [Online]. Available: <http://www.mag-inc.com/File Library/Product Datasheets/Ferrite/New Ferrite data sheets/0P44125UC.pdf>.
- [55] "P Material," 2014. [Online]. Available: <http://www.mag-inc.com/products/ferrite-cores/p-material>.
- [56] "0P44949EC ETD Core," 2014. [Online]. Available: <http://www.mag-inc.com/File Library/Product Datasheets/Ferrite/New Ferrite data sheets/0P44949EC.pdf>.
- [57] B. M. Grainger, O. Scioscia, T. E. McDermott, G. F. Reed, and E. Lin, "Prediction and experimental verification of core loss and temperature distribution for geometrically scaled finemet toroids using finite element analysis," in *2014 IEEE Applied Power Electronics Conference and Exposition - APEC 2014*, 2014, pp. 2615–2620.
- [58] W. Shen, F. Wang, D. Boroyevich, and C. W. Tipton IV, "High-Density Nanocrystalline Core Transformer for High-Power High-Frequency Resonant Converter," *IEEE Trans. Ind. Appl.*, vol. 44, no. 1, pp. 213–222, 2008.
- [59] J. M. Silveyra, a. M. Leary, V. DeGeorge, S. Simizu, and M. E. McHenry, "High speed electric motors based on high performance novel soft magnets," *J. Appl. Phys.*, vol. 115, no. 17, p. 17A319, May 2014.

- [60] Cogent Surahammars Burks AB, “Typical Data for SURA M600-50A,” 2008. [Online]. Available: <http://www.sura.se>.
- [61] European Steel and Alloy Grades, “Properties of Grade M600-50A,” 2013. [Online]. Available: <http://www.steelnumber.com>.
- [62] M. Dems and K. Komezca, “Performance Characteristics of a High-Speed Energy-Saving Induction Motor With an Amorphous Stator Core,” *IEEE Trans. Ind. Electron.*, vol. 61, no. 6, pp. 3046–3055, Jun. 2014.
- [63] M. J. Melfi, “Optimum pole configuration of AC induction motors used on adjustable frequency power supplies,” in *Industry Applications Society 42nd Annual Petroleum and Chemical Industry Conference*, 1995, pp. 237–242.
- [64] W. A. Reass, D. M. Baca, and R. F. Gribble, “Multi-Megawatt High Frequency Polyphase Nanocrystalline Transformers,” 2007. [Online]. Available: http://www.nist.gov/pml/high_megawatt/upload/2007_Reass-II.pdf.
- [65] C. R. Sullivan, “Cost-constrained selection of strand diameter and number in a litz-wire transformer winding,” *IEEE Trans. Power Electron.*, vol. 16, no. 2, pp. 281–288, Mar. 2001.
- [66] G. F. Reed, B. M. Grainger, H. Bassi, E. Taylor, Z.-H. Mao, and A. K. Jones, “Analysis of high capacity power electronic technologies for integration of green energy management,” in *IEEE PES T&D 2010*, 2010, pp. 1–10.
- [67] W. Breuer, D. Retzmann, and K. Uecker, “Highly Efficient Solutions for Smart and Bulk Power Transmission of ‘Green Energy,’” Siemens AG, Energy Sector - Power Transmission Division, 2011.
- [68] J. Rodriguez, L. G. Franquelo, S. Kouro, J. I. Leon, R. C. Portillo, M. A. M. Prats, and M. A. Perez, “Multilevel Converters: An Enabling Technology for High-Power Applications,” *Proc. IEEE*, vol. 97, no. 11, pp. 1786–1817, Nov. 2009.
- [69] B. Gemmell, J. Dorn, D. Retzmann, and D. Soerangr, “Prospects of multilevel VSC technologies for power transmission,” in *2008 IEEE/PES Transmission and Distribution Conference and Exposition*, 2008, pp. 1–16.
- [70] J. Wang, R. Burgos, and D. Boroyevich, “A survey on the modular multilevel converters — Modeling, modulation and controls,” in *2013 IEEE Energy Conversion Congress and Exposition*, 2013, pp. 3984–3991.
- [71] M. Saedifard and R. Iravani, “Dynamic Performance of a Modular Multilevel Back-to-Back HVDC System,” *IEEE Trans. Power Deliv.*, vol. 25, no. 4, pp. 2903–2912, Oct. 2010.

- [72] X. Li, Q. Song, W. Liu, H. Rao, S. Xu, and L. Li, "Protection of Nonpermanent Faults on DC Overhead Lines in MMC-Based HVDC Systems," *IEEE Trans. Power Deliv.*, vol. 28, no. 1, pp. 483–490, Jan. 2013.
- [73] J. Peralta, H. Saad, S. Denetiere, J. Mahseredjian, and S. Nguefeu, "Detailed and Averaged Models for a 401-Level MMC–HVDC System," *IEEE Trans. Power Deliv.*, vol. 27, no. 3, pp. 1501–1508, Jul. 2012.
- [74] U. N. Gnanarathna, A. M. Gole, and R. P. Jayasinghe, "Efficient Modeling of Modular Multilevel HVDC Converters (MMC) on Electromagnetic Transient Simulation Programs," *IEEE Trans. Power Deliv.*, vol. 26, no. 1, pp. 316–324, Jan. 2011.
- [75] M. Guan and Z. Xu, "Modeling and Control of a Modular Multilevel Converter-Based HVDC System Under Unbalanced Grid Conditions," *IEEE Trans. Power Electron.*, vol. 27, no. 12, pp. 4858–4867, Dec. 2012.
- [76] A. Yazdani and R. Iravani, *Voltage-Sourced Converters in Power Systems: Modeling, Control, and Applications*. Hoboken: Wiley, 2010.
- [77] B. Wu, *High-Power Converters and AC Drives*. Wiley, 2006.
- [78] A. Yazdani and R. Iravani, "A Unified Dynamic Model and Control for the Voltage-Sourced Converter Under Unbalanced Grid Conditions," *IEEE Trans. Power Deliv.*, vol. 21, no. 3, pp. 1620–1629, Jul. 2006.
- [79] D. W. Novotny and T. A. Lipo, *Vector Control and Dynamics of AC Drives*. Oxford University Press, USA, 1996.
- [80] H. Saad, J. Peralta, S. Denetiere, J. Mahseredjian, J. Jatskevich, J. A. Martinez, A. Davoudi, M. Saeedifard, V. Sood, X. Wang, J. Cano, and A. Mehrizi-Sani, "Dynamic Averaged and Simplified Models for MMC-Based HVDC Transmission Systems," *IEEE Trans. Power Deliv.*, vol. 28, no. 3, pp. 1723–1730, Jul. 2013.
- [81] K. Ilves, S. Norrga, L. Harnefors, and H.-P. Nee, "On Energy Storage Requirements in Modular Multilevel Converters," *IEEE Trans. Power Electron.*, vol. 29, no. 1, pp. 77–88, Jan. 2014.
- [82] T. M. Blooming and D. J. Carnovale, "Application of IEEE STD 519-1992 Harmonic Limits," in *Conference Record of 2006 Annual Pulp and Paper Industry Technical Conference*, 2006, pp. 1–9.
- [83] H. Maekawa, Y. Watanabe, K. Murata, Y. Hirota, "Research and Development of DC +/- 500 kV Extruded Cables," in *Cigre Session 2002*, 2002.
- [84] ATCO Electric Group, "Eastern Alberta Transmission Line," 2013. [Online]. Available: <http://www.atcoelectric.com/Projects/HVDC/Eastern-Alberta-Transmission-Line>.

- [85] P. Cairoli, I. Kondratiev, and R. A. Dougal, "Coordinated Control of the Bus Tie Switches and Power Supply Converters for Fault Protection in DC Microgrids," *IEEE Trans. Power Electron.*, vol. 28, no. 4, pp. 2037–2047, Apr. 2013.
- [86] A. Emadi, A. Khaligh, C. H. Rivetta, and G. A. Williamson, "Constant Power Loads and Negative Impedance Instability in Automotive Systems: Definition, Modeling, Stability, and Control of Power Electronic Converters and Motor Drives," *IEEE Trans. Veh. Technol.*, vol. 55, no. 4, pp. 1112–1125, Jul. 2006.
- [87] A. Kwasinski and C. N. Onwuchekwa, "Dynamic Behavior and Stabilization of DC Microgrids With Instantaneous Constant-Power Loads," *IEEE Trans. Power Electron.*, vol. 26, no. 3, pp. 822–834, Mar. 2011.
- [88] C. N. Onwuchekwa and A. Kwasinski, "Analysis of Boundary Control for Buck Converters With Instantaneous Constant-Power Loads," *IEEE Trans. Power Electron.*, vol. 25, no. 8, pp. 2018–2032, Aug. 2010.
- [89] D. Costinett, H. Nguyen, R. Zane, and D. Maksimovic, "GaN-FET based dual active bridge DC-DC converter," in *2011 Twenty-Sixth Annual IEEE Applied Power Electronics Conference and Exposition (APEC)*, 2011, pp. 1425–1432.
- [90] H. K. Krishnamurthy and R. Ayyanar, "Building Block Converter Module for Universal (AC-DC, DC-AC, DC-DC) Fully Modular Power Conversion Architecture," in *2007 IEEE Power Electronics Specialists Conference*, 2007, pp. 483–489.
- [91] International Electrotechnical Commission, "Power cables with extruded insulation and their accessories for rated voltages from 1 kV ($U_m = 1,2$ kV) up to 30 kV ($U_m = 36$ kV) - Part 2: Cables for rated voltages from 6 kV ($U_m = 7,2$ kV) up to 30 kV ($U_m = 36$ kV)," 2014.
- [92] A. Emadi, B. Fahimi, and M. Ehsani, "On the Concept of Negative Impedance Instability in the More Electric Aircraft Power Systems with Constant Power Loads," Aug. 1999.
- [93] J. Glover, M. Sarma, and T. Overbye, *Power System Analysis and Design*, 4th ed. Thomas Learning, 2008.
- [94] S. Sastry and M. Bodson, *Adaptive Control: Stability, Convergence and Robustness*. New York: Dover Publications, 2011.
- [95] C.-T. Chen, *Linear System Theory and Design*, 4th ed. Oxford, UK: Oxford University Press, 2013.
- [96] L. Xue, D. Diaz, Z. Shen, F. Luo, P. Mattavelli, and D. Boroyevich, "Dual active bridge based battery charger for plug-in hybrid electric vehicle with charging current containing low frequency ripple," in *2013 Twenty-Eighth Annual IEEE Applied Power Electronics Conference and Exposition (APEC)*, 2013, pp. 1920–1925.

- [97] J. Li, A. Q. Huang, S. Bhattacharya, and W. Jing, "Application of active NPC converter on generator side for MW direct-driven wind turbine," in *2010 Twenty-Fifth Annual IEEE Applied Power Electronics Conference and Exposition (APEC)*, 2010, pp. 1010–1017.
- [98] C.-M. Ong, *Dynamic Simulations of Electric Machinery: Using Matlab/Simulink*. Prentice-Hall, 1998.
- [99] F. Deng and Z. Chen, "Power control of permanent magnet generator based variable speed wind turbines," in *2009 International Conference on Electrical Machines and Systems*, 2009, pp. 1–6.
- [100] A. M. Howlader, N. Urasaki, T. Senjyu, A. Uehara, A. Yona, and A. Y. Saber, "Output power smoothing of wind turbine generation system for the 2-MW permanent magnet synchronous generators." pp. 452–457, 2010.
- [101] M. Fatu, C. Lascu, G.-D. Andreescu, R. Teodorescu, F. Blaabjerg, and I. Boldea, "Voltage Sags Ride-Through of Motion Sensorless Controlled PMSG for Wind Turbines," in *2007 IEEE Industry Applications Annual Meeting*, 2007, pp. 171–178.
- [102] S. A. Diaz, C. Silva, J. Juliet, and H. A. Miranda, "Indirect sensorless speed control of a PMSG for wind application," in *2009 IEEE International Electric Machines and Drives Conference*, 2009, pp. 1844–1850.
- [103] M. Arifujjaman, "Modeling, simulation and control of grid connected Permanent Magnet Generator (PMG)-based small wind energy conversion system," in *2010 IEEE Electrical Power & Energy Conference*, 2010, pp. 1–6.
- [104] K. Johnson, L. Fingersh, M. Balas, and L. Pao, "Methods for Increasing Region 2 Power Capture on a Variable Speed HAWT," Golden, Colorado, 2004.
- [105] R. Burgos, P. Kshirsagar, A. Lidozzi, F. Wang, and D. Boroyevich, "Mathematical Model and Control Design for Sensorless Vector Control of Permanent Magnet Synchronous Machines," in *2006 IEEE Workshops on Computers in Power Electronics*, 2006, pp. 76–82.
- [106] R. D. Middlebrook and S. Cuk, "A general unified approach to modelling switching-converter power stages," *Power Electron. Spec. Conf.*, vol. -1, pp. 18–34, 1976.
- [107] S. R. Sanders, J. M. Noworolski, X. Z. Liu, and G. C. Verghese, "Generalized averaging method for power conversion circuits," *IEEE Trans. Power Electron.*, vol. 6, no. 2, pp. 251–259, Apr. 1991.
- [108] S. Hiti, D. Boroyevich, and C. Cuadros, "Small-signal modeling and control of three-phase PWM converters," in *Proceedings of 1994 IEEE Industry Applications Society Annual Meeting*, 1994, pp. 1143–1150.

- [109] R. Teodorescu, M. Liserre, and P. Rodriguez, *Grid Converters for Photovoltaic and Wind Power Systems*. John Wiley and Sons, 2011.
- [110] W. Leonhard, *Control of Electrical Drives*, 3rd ed. Springer-Verlag, 2001.
- [111] P. Krause, O. Wasynczuk, and S. Sudhoff, *Analysis of Electric Machinery and Drive Systems*, 2nd ed. Wiley/IEEE Press, 2002.
- [112] G. O. Garcia, J. C. M. Luis, R. M. Stephan, and E. H. Watanabe, “An efficient controller for an adjustable speed induction motor drive,” *IEEE Trans. Ind. Electron.*, vol. 41, no. 5, pp. 533–539, 1994.
- [113] M. N. Marwali, J.-W. Jung, and A. Keyhani, “Control of Distributed Generation Systems— Part II: Load Sharing Control,” *IEEE Trans. Power Electron.*, vol. 19, no. 6, pp. 1551–1561, Nov. 2004.
- [114] A. D. Paquette, M. J. Reno, R. G. Harley, and D. M. Divan, “Sharing Transient Loads : Causes of Unequal Transient Load Sharing in Islanded Microgrid Operation,” *IEEE Ind. Appl. Mag.*, vol. 20, no. 2, pp. 23–34, Mar. 2014.
- [115] V. Kounev, B. Grainger, G. Reed, and D. Tipper, “Analysis of an Offshore Medium Voltage DC Microgrid Environment Part II: Communication Network Architecture,” in *IEEE PES T&D 2014*, 2014, pp. 1–5.
- [116] D. Wetteroth, *OSI Reference Model for Telecommunications*. McGraw-Hill, 2001.
- [117] B. A. Forouzan, *TCP/IP Protocol Suite*, 2nd ed. New York: McGraw-Hill, 2002.
- [118] P. Vas, *Sensorless Vector and Direct Torque Control*. New York: Oxford University Press, 1998.
- [119] Ç. K. Koç and C. Paar, Eds., *Cryptographic Hardware and Embedded Systems — CHES 2000*, vol. 1965. Berlin, Heidelberg: Springer Berlin Heidelberg, 2000.
- [120] Q. Wang, H. Khurana, Y. Huang, and K. Nahrstedt, “Time Valid One-Time Signature for Time-Critical Multicast Data Authentication,” in *IEEE INFOCOM 2009 - The 28th Conference on Computer Communications*, 2009, pp. 1233–1241.
- [121] W. Yen, T.-Y., Wolf, “Performance estimation for real-time distributed embedded systems,” *IEEE Trans. Parallel Distrib. Syst.*, vol. 9, no. 11, pp. 1125–1136, 1998.
- [122] M. Klemun, “5 Market Trends that Will Drive Microgrids into the Mainstream,” *Green Tech Grid*, 2014. [Online]. Available: <http://www.greentechmedia.com/articles/read/5-Market-Trends-That-Will-Drive-Microgrids-Into-the-Mainstream>.

- [123] P. Tenca, A. A. Rockhill, and T. A. Lipo, "Low Voltage Ride-Through Capability for Wind Turbines based on Current Source Inverter Topologies," in *2007 7th International Conference on Power Electronics and Drive Systems*, 2007, pp. 1115–1122.